UNIVERSITY OF ROCHESTER
LABORATORY FOR LASER ENERGETICS

Volume 116
July–September 2008
DOE/NA/28302-866

LLE Review

Quarterly Report

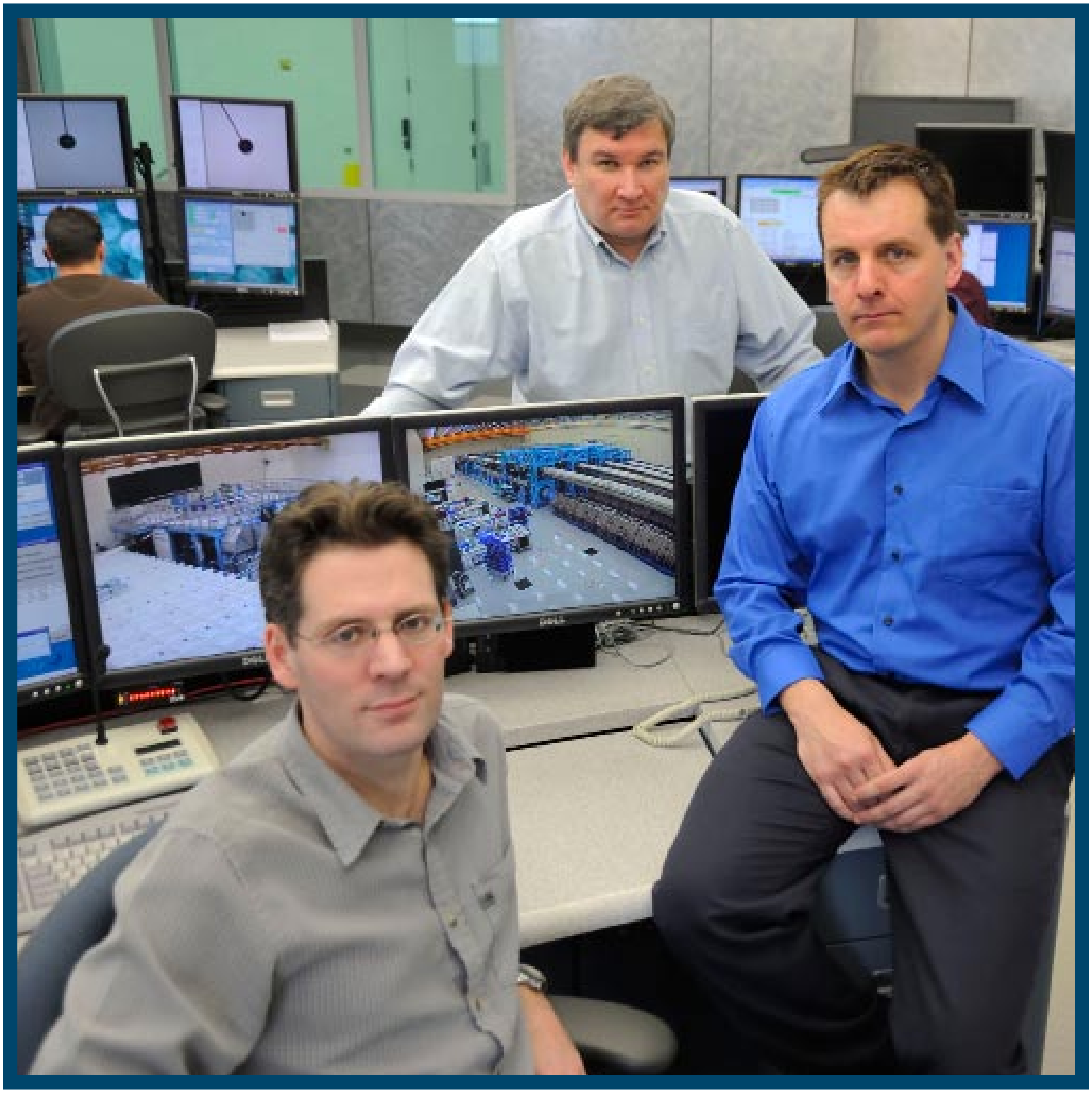

About the Cover:

Kilojoule-class high-intensity lasers offer the promise of generating a relativistic electron–positron pair plasma for the first time in controlled laboratory experiments (see "Optimizing Electron–Positron Pair Production on kJ-Class High-Intensity Lasers for the Purpose of Pair-Plasma Creation" on p. 161). Graduate student Michael Storm (The Institute of Optics) (right) and LLE scientists Jason Myatt (seated) and Andrei Maximov are shown in the OMEGA EP Control Room. Four beamlines of OMEGA EP can be seen in the display monitor to the right of Dr. Myatt. Two of these beamlines can be compressed in the grating compressor chamber (white structure seen in the monitor to the left of Dr. Myatt) to "relativistic intensities." These scientists describe how pair production can be optimized for irradiation conditions achievable on these two high-intensity beamlines. They also estimate the likelihood of successful pair-plasma creation.

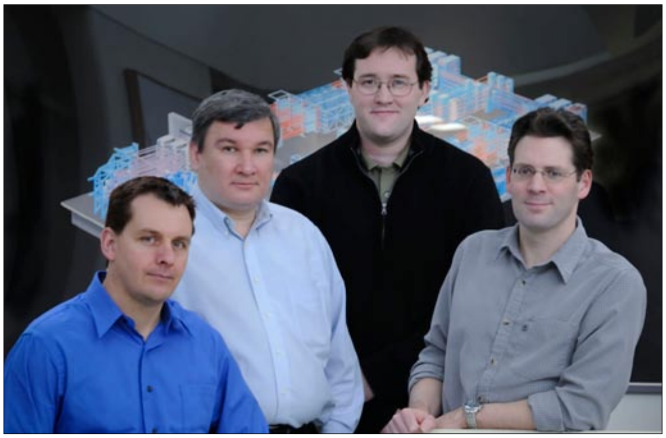

The inside cover photo shows (from left to right) graduate student Michael Storm (experimental), scientist Andrei Maximov (plasma/theory), scientist Philip Nilson (experimental), and scientist Jason Myatt (plasma/theory). These researchers are currently exploring the implications of the new physical regimes that have recently become accessible with the OMEGA/OMEGA EP Laser Facilities, particularly those related to volumetric heating and energetic particle production.

The work described in this volume includes current research at the Laboratory for Laser Energetics, which is supported by New York State Energy Research and Development Authority, the University of Rochester, the U.S. Department of Energy Office of Inertial Confinement Fusion under Cooperative Agreement No. DE-FC52-08NA28302, and other agencies.

Printed in the United States of America
Available from
National Technical Information Services
U.S. Department of Commerce
5285 Port Royal Road
Springfield, VA 22161
Price codes: Printed Copy A06
Microfiche A01

For questions or comments, contact John A. Marozas, Editor, Laboratory for Laser Energetics, 250 East River Road, Rochester, NY 14623-1299, (585) 273-5605.

Worldwide-Web Home Page: http://www.lle.rochester.edu/

UNIVERSITY OF ROCHESTER
LABORATORY FOR LASER ENERGETICS

Volume 116
July–September 2008
DOE/NA/28302-866

LLE Review

Quarterly Report

Contents

In Brief

This volume of the LLE Review, covering July–September 2008, features "Optimizing Electron–Positron Pair Production on kJ-Class High-Intensity Lasers for the Purpose of Pair-Plasma Creation" by J. Myatt, J. A. Delettrez, A. V. Maximov, D. D. Meyerhofer, R. W. Short, C. Stoeckl, and M. Storm. In this article, the authors report that expressions for the yield of electron–positron pairs, their energy spectra, and production rates have been obtained in the interaction of multi-kJ pulses of high-intensity laser light interacting with solid targets (p. 161). The Bethe–Heitler conversion of hard x-ray bremsstrahlung is shown to dominate over direct production (trident process). The yields and production rates have been optimized as a function of incident laser intensity, by the choice of target material and dimensions, indicating that up to 5×10^{11} pairs can be produced on the OMEGA EP Laser System. The corresponding production rates are sufficiently high that the possibility of pair-plasma creation is shown to exist.

Additional highlights of recent research presented in this issue include the following:

- S. X. Hu, P. B. Radha, J. A. Marozas, R. Betti, T. J. B. Collins, R. S. Craxton, J. A. Delettrez, D. H. Edgell, R. Epstein, V. N. Goncharov, I. V. Igumenshchev, F. J. Marshall, R. L. McCrory, P. W. McKenty, D. D. Meyerhofer, S. P. Regan, T. C. Sangster, S. Skupsky, V. A. Smalyuk (LLE), and D. Shvarts (Nuclear Research Center, Negev) describe neutron yields of direct-drive, low-adiabat ($\alpha \simeq 2$ to 3) cryogenic D_2 target implosions on OMEGA have been systematically investigated using the two-dimensional (2-D) radiation hydrodynamics code *DRACO* (p. 172). Low-mode ($\ell \leq 12$) perturbations, including initial target offset, ice-layer roughness, and laser-beam imbalance, were found to be the primary source of yield reduction in implosions for thin-shell (5-μm), low-α, cryogenic targets. Overall, our 2-D simulations of thin-shell implosions track experimental measurements for different target conditions and peak laser intensities ranging from 2.5×10^{14} to 6×10^{14} W/cm^2. Simulations also indicate that fusion yield is sensitive to the relative phases between the target offset and the ice-layer perturbations. These 2-D numerical results provide a reasonably good guide to understanding the yield degradation in direct-drive, low-adiabat, cryogenic, thin-shell-target implosions. Thick-shell (10-μm) implosions generally give lower yield over clean (YOC) than low-ℓ-mode *DRACO* simulation predictions. Simulations including the effect of laser-beam nonuniformities indicate that high-ℓ-mode perturbations caused by laser imprinting play a role in further degrading the neutron yield of thick-shell implosions. Finally, for obtaining meaningful implosions to study ICF compression physics, these results suggest a target specification with a $\leq$30-μm offset and ice-roughness of $\sigma_{\rm rms} < 3$ μm.

- H. Sawada, S. P. Regan, P. B. Radha, R. Epstein, D. Li, V. N. Goncharov, S. X. Hu, D. D. Meyerhofer, J. A. Delettrez, P. A. Jaanimagi, V. A. Smalyuk, T. R. Boehly, T. C. Sangster, B. Yaakobi (LLE), and R. C. Mancini (Department of Physics, University of Nevada, Reno, Nevada) present a time-resolved Al 1*s*–2*p* absorption spectroscopy used to diagnose direct-drive, shock-wave heating and compression of planar targets having nearly Fermi-degenerate plasma conditions ($T_{\rm e} \sim 10$ to 40 eV, ~3 to 11 g/cm^3) on the OMEGA Laser System (p. 185). A planar plastic foil with a buried Al tracer layer was irradiated with peak intensities of 10^{14} to 10^{15} W/cm^2 and probed with the pseudocontinuum M-band emission from a point-source Sm backlighter in the range of 1.4 to 1.7 keV. The laser-ablation processes launch 10- to 70-Mbar shock waves into the CH/Al/CH target. The Al 1*s*–2*p* absorption spectra were analyzed using the atomic physics code *PrismSPECT* to infer $T_{\rm e}$ and in the Al layer, assuming uniform plasma conditions during shock-wave heating, to determine when the heat front penetrated the Al layer. The drive foils were simulated with the 1-D hydrodynamics code *LILAC* using a flux-limited ($f = 0.06$

and $f = 0.1$), nonlocal thermal-transport model. The predictions of simulated shock-wave heating and the timing of heat-front penetration are compared with the observations. The experimental results for a wide variety of laser-drive conditions and buried depths have shown that the *LILAC* predictions using $f = 0.06$ and the nonlocal model accurately model the shock-wave heating and timing of the heat-front penetration while the shock is transiting the target. The observed discrepancy between the measured and simulated shock-wave heating at late times of the drive can be explained by the reduced radiative heating caused by lateral heat flow in the corona.

- C. D. Zhou (LLE and the Fusion Science Center for Extreme States of Matter and Fast Ignition Physics) and R. Betti (LLE, the Departments of Mechanical Engineering and Physics and Astronomy, and the Fusion Science Center for Extreme States of Matter and Fast Ignition Physics) describe how the ignition condition (Lawson criterion) for inertial confinement fusion can be cast in a form dependent on the only two measurable parameters of the compressed fuel assembly: the hot-spot ion temperature $\left(T_i^h\right)$ and the total areal density (ρR_{tot}) that includes the cold shell contribution (p. 204). A marginal ignition curve is derived in the $\rho R_{\text{tot}}, T_i^h$ plane and current implosion experiments are compared with the ignition curve. On this plane, hydrodynamic equivalent curves show how a given implosion would perform with respect to the ignition condition when scaled up in the laser-driver energy. An approximate form of the ignition condition (typical of laser-driven ICF) is $\left\langle T_i^{\text{no}\,\alpha}\right\rangle_{\text{n}}^{2.6} \times \left\langle \rho R_{\text{tot}}\right\rangle_{\text{n}} > 50\ \text{keV}^{2.6} \times \text{g/cm}^2$, where $\left\langle \rho R_{\text{tot}}\right\rangle_{\text{n}}$ and $\left\langle T_i^{\text{no}\,\alpha}\right\rangle_{\text{n}}$ are the neutron-averaged total areal density and hot-spot ion temperature without accounting for α-particle energy deposition, respectively. Such a criterion can be used to determine how surrogate D_2 and sub-ignited DT target implosions perform with respect to the one-dimensional ignition threshold.

- X. L. Cross, X. Zheng, P. D. Cunningham, L. M. Hayden, Š. Chromik, M. Sojkova, V. Štrbík, P. Odier, and R. Sobolewski (LLE) present an ultrafast THz-pulse time-domain spectroscopy (TDS) and femtosecond optical-pump THz-probe (OPTP) studies of Hg-Ba-Ca-Cu-O (HBCCO) high-temperature, superconducting thin films (p. 219). Our 500-nm-thick films were prepared by rf-magnetron sputtering of Re-Ba-Ca-Cu-O precursor films, followed by an *ex-situ*, high-temperature mercuration process. The resulting films were *c*-axis oriented with a predominant Hg-1212 (plus some Hg-1223) phase. Their transition temperature T_{c} had an onset at 123 K and zero resistance at 110 K. The THz TDS measurements demonstrated a sharp drop in the transmitted THz signal when the sample temperature was decreased below T_{c}, which we directly related to a change in the imaginary component of the film's complex conductivity. Simultaneously, the peak of the temperature-dependent real part of the conductivity was shifted toward lower frequencies at lower temperatures. The time-resolved OPTP spectroscopy experiments showed that the quasiparticle relaxation process exhibited an intrinsic single-picosecond dynamics with no phonon bottleneck, which is a unique feature among superconductors and makes the HBCCO material very promising for ultrafast radiation detector applications.

- This volume concludes with a summary of LLE's Summer High School Research Program (p. 224), the FY08 Laser Facility Report (p. 226), and the National Lasers Users' Facility and External Users' Programs (p. 228).

John A. Marozas
Editor

Optimizing Electron–Positron Pair Production on kJ-Class High-Intensity Lasers for the Purpose of Pair-Plasma Creation

Introduction

The creation of a relativistically hot electron–positron plasma in the laboratory is an ambitious experimental challenge that has yet to be realized. Electron–positron pair plasmas are theoretically interesting because of the mass symmetry between the plasma components. For example, this symmetry results in the absence of both acoustic modes and Faraday rotation.[1,2] Waves and instabilities in electron–positron plasmas differ significantly from asymmetric electron–ion plasmas and have been discussed theoretically in Refs. 1 and 2. Electron–positron plasmas are important in astrophysical settings;[3] new insights into astrophysical phenomena such as black holes, pulsar magnetospheres, active galactic nuclei, bipolar outflows (jets), and gamma-ray bursts (GRB) may be gained by appropriate laboratory investigations.[4]

The main difficulty in creating an electron–positron plasma arises because terrestrial positron sources are typically very weak; e.g., source rates of ~10^6 positrons s^{-1} are obtained using radioactive sources[5,6] and (10^8 to 10^9) positrons s^{-1} using accelerator-based sources.[7] To date, classical single-component, positron-plasma charge clouds have been created and confined, with cloud sizes slightly exceeding the Debye length, by storing and cooling positrons created through radioactive decay in electrostatic Penning traps.[5,6,8] Penning traps cannot, however, simultaneously confine significant numbers of both positive and negative species.[2] In principle, the simultaneous confinement of electrons and positrons in non-neutral stellerators[9] or mirror machines[10] appears possible, but it has yet to be achieved. An alternative to the above schemes is proposed that uses ultra-intense laser pulses as an intense positron source.[11–17] The first step toward producing a pair plasma is to optimize the pair-production rate. Calculations in this article indicate that source rates approaching 10^{24} positrons s^{-1} are attainable with the generation of petawatt laser systems either recently completed, such as OMEGA EP,[18] or currently under construction, e.g., NIF-ARC.[19] Such source rates are shown to be high enough that the density of pairs approaches that required for the formation of a pair plasma.

The following sections of this article (1) present calculations of the direct and indirect yield as a function of laser intensity and target geometry; (2) analyze the results, optimizing the yields, and the production rates; (3) estimate the likelihood of pair–plasma production; and (4) summarize our conclusions.

Calculation of Positron Yield in Laser–Target Interactions

High-energy petawatt lasers, such as LLE's recently completed OMEGA EP Laser Facility,[18] deliver kilojoules of laser energy at focused laser intensities of $I_0 \lesssim 10^{20}$ W/cm^2. Such intensities are still several orders of magnitude below the level required to create electron–positron pairs from the vacuum.[20–22] However, laser–matter interaction at intensities $I_0 \gtrsim 10^{18}$ W/cm^2 efficiently produce hot electrons with characteristic energies in the MeV range,[23] which may be approximated by the ponderomotive (Wilks) scaling for the hot-electron "temperature"[24]

$$\Theta_{\text{hot}} = 0.511\left[\left(1 + I_{18}\lambda_{\mu\text{m}}^2 \big/ 1.37\right)^{1/2} - 1\right] \text{MeV}, \qquad (1)$$

where I_{18} is the laser intensity in units of 10^{18} W/cm^2 and $\lambda_{\mu\text{m}}$ is the laser wavelength in μm (= 1.053 μm for OMEGA EP). This scaling predicts temperatures ranging from $\Theta_{\text{hot}} \sim 1$ MeV at $I_{\text{L}} = 1 \times 10^{19}$ W/cm^2 to $\Theta_{\text{hot}} \sim 15$ MeV at $I_{\text{L}} = 1 \times 10^{21}$ W/cm^2. Electrons with kinetic energies exceeding the threshold value, $T_{\text{th,e}} \approx 2m_{\text{e}}c^2 = 1.022$ MeV (neglecting the small correction due to recoil of the nucleus), have a finite probability of creating an electron–positron pair in matter. A significant uncertainty exists in the scaling of hot-electron temperature with laser intensity. An alternative scaling, the so-called Beg scaling,[25] has been proposed $\left[\Theta_{\text{hot}} = 0.46\left(I_{19}\lambda_{\mu\text{m}}^2\right)^{1/3} \text{MeV}\right]$, which seems to give better agreement with a certain class of high-contrast experiments.[26] The Beg scaling predicts significantly lower temperatures for a given laser intensity leading to less-favorable pair-production rates.

Several mechanisms lead to the production of pairs: Pairs can be created directly (trident process) by energetic electrons interacting with the Coulomb field of the atomic nucleus (or with the field of an atomic electron) or pairs can be created indirectly.

Indirect production first requires the production of a bremsstrahlung photon followed by pair production by the photon in the nuclear (or atomic-electron) field (photo-pair production). The reaction rate for direct production in the nuclear (electron) field is of the order of $Z^2 n_{\mathrm{hot}} n_i \alpha^2$ ($n_{\mathrm{hot}} n_{\mathrm{e}} \alpha^2$), while bremsstrahlung is of the order of $Z^2 n_{\mathrm{hot}} n_i \alpha$ and pair production is $Z^2 n_\gamma n_i \alpha$. Here, $\alpha \approx 1/137$ is the fine-structure constant, Z is the atomic number, and n_{hot}, n_i, n_{e}, and n_γ are the hot-electron, atomic, atomic-electron, and photon number densities, respectively. Two-photon-pair production is the lowest-order process in α (zeroth), but it can be ignored because the (bremsstrahlung) photon density is orders of magnitude lower than the hot-electron number density. The reverse of this process, pair annihilation, is expected to occur and will provide a characteristic annihilation radiation signature of back-to-back photons at ~511 keV, which can be used to diagnose the presence of pairs.[27,28]

The ratio of the cross sections for direct and photoproduction, with energy dependence, has been given in Ref. 29:

$$\frac{\sigma_T}{\sigma_{\gamma \to \mathrm{e}^+\mathrm{e}^-}} = \frac{\alpha}{\pi}\left[\log\left(\frac{E_0}{m_{\mathrm{e}}c^2}\right)\log\left(\frac{E_0}{2.137\, m_{\mathrm{e}}c^2 Z^{-1/3}}\right) + \frac{1}{3}\log^2\left(2.137\, Z^{-1/3}\right)\right], \tag{2}$$

where E_0 is the total energy of the incident electron (photons are assumed to have the same energy), m_{e} is the electron mass, and c is the speed of light. From this expression it can be seen that pair production is more efficient (at 5 MeV the ratio is $\sigma_T / \sigma_{\gamma \to \mathrm{e}^+\mathrm{e}^-} = 0.017$), but there is an additional inefficiency associated with first creating the hard bremsstrahlung photons. In the following subsections, the efficiencies of each process are carefully computed. The cross sections (per atom) for both direct production σ_T and photon-pair production $\sigma_{\gamma \to \mathrm{e}^+\mathrm{e}^-}$ are proportional to Z^2. The production efficiency will be greatest using a target material that optimizes the product of Z^2 and the atomic number density n_i. In this article we assume the target to be Au ($Z = 79$), which is close to optimal $\left(Z^2 n_i = Z^2 \rho N_{\mathrm{A}} / A \sim 3.66 \times 10^{26}\ \mathrm{cm}^{-3}\right)$, where A is the atomic weight, ρ is the mass density, and N_{A} is the Avogadro number.

The threshold kinetic energy for the production of muons is $T_{\mathrm{th},\mu} = 212$ MeV and $T_{\mathrm{th},\pi} \approx 280$ MeV for pions.[30] It is unlikely that muons or pions can be created with any significant efficiency with the current generation of petawatt-class lasers.

1. Direct Pair Production by Electrons (Trident Production)

Trident production(a),[29,31,32] of electron–positron pairs by fast electrons colliding with the Coulomb field of an atomic nucleus has been approximated by either the Bhabha cross section[29] or various forms valid at high energy.[33] The Bhabha cross section is not entirely satisfactory since the uncertainties over the range of electron energies considered here (ranging roughly from threshold to a few tens of MeV) are hard to determine.[11] More recently Gryaznykh[34] numerically evaluated the integrals arising from the three lowest-order diagrams that have been computed by Baĭer *et al.*[35] Reference 34 provides a fitting formula for the total cross section σ_T, which is valid from threshold to ~100 MeV,

$$\sigma_T = 5.22\, Z^2 \log^3\left[\frac{2.30 + T_0(\mathrm{MeV})}{3.52}\right]\mu\mathrm{b}, \tag{3}$$

together with limiting forms near threshold

$$\sigma_T = \frac{7\, Z^2 r_0^2 \alpha^2}{2304} \frac{\left(T_0 - 2m_{\mathrm{e}}c^2\right)^3}{\left(m_{\mathrm{e}}c\right)^3}, \tag{4}$$

and at high energies

$$\sigma_T = \frac{28\pi Z^2 r_0^2 \alpha^2}{27} \log^3\left(\frac{T_0}{m_{\mathrm{e}}c^2}\right). \tag{5}$$

Here, T_0 is the kinetic energy of the incident electron, $r_0 \equiv e^2/m_{\mathrm{e}}c^2 = 2.82 \times 10^{-13}\ \mathrm{cm}^2$ is the classical electron radius, and e is the elementary charge. In an infinite target, the trident yield $Y_{+,T}$ can be computed for a given probability distribution of incident electron kinetic energies, $f_0(T_0)$, by integrating along the electron path, running down in kinetic energy from the initial value T_0 assuming the continuous slowing-down approximation (CSDA),

$$\begin{aligned} Y_{+,T} &= \eta_r N_{\mathrm{e}} \int_0^\infty \mathrm{d}T_0 f_0(T_0) \int_0^{T_0} \mathrm{d}T n_i \sigma_T(T) \left|\frac{\mathrm{d}T}{\mathrm{d}s}\right|^{-1} \\ &= \eta_r N_{\mathrm{e}} \int_0^\infty \mathrm{d}T_0 f_0(T_0) \int_0^{s(T_0)} \mathrm{d}s' n_i \sigma_T\left[T(T_0, s')\right]. \end{aligned} \tag{6}$$

(a) In general, "trident" and "quartets" refer to the production of lepton pairs by virtual photons in the Coulomb fields of nuclei and atomic electrons, respectively. "Pairs" and "triplets" refer to the corresponding process induced by real photons.

Here N_e is the total number of hot electrons, s' is the path length variable for an electron of initial kinetic energy T_0 of CSDA range $s(T_0)$, and $\eta_r = 1$. The yield in a thin target, significantly thinner than the hot-electron practical range, can be estimated by introducing the "refluxing efficiency" $\eta_r \lesssim 1$ (Ref. 36). The refluxing efficiency represents the fraction of hot electrons that are trapped by the space charge of the target relative to the total number, which can be close to unity for a range of target interaction conditions.[36,37] The electron stopping power $-(\mathrm{d}T/\mathrm{d}s)$, from which $T(T_0,s) = T_0 + \int_0^s \mathrm{d}s'\left(\mathrm{d}T/\mathrm{d}s'\right)$ is computed, has been taken from Ref. 38.

The yield computed according to Eq. (6), per kJ of hot electrons, is shown as the dashed line in Fig. 116.1 for a range of hot-electron temperatures, perfect refluxing efficiency $\eta_r = 1$, and an exponential hot-electron energy distribution function $f_0(T_0) = \left(1/\Theta_{\mathrm{hot}}\right)\exp\left(-T_0/\Theta_{\mathrm{hot}}\right)$. The average positron kinetic energy $\overline{T}_+$ for an incident electron of energy T_0 is calculated by the formula $\overline{T}_+ = T_0\left\{1/3 - b\log\left[T_0/\left(3m_e c^2\right)\right]\right\}$. The dimensionless parameter b (= 0.0565) has been found in Ref. 34 by fitting to the results of numerical computation of the integrals. The average positron energy produced for a distribution of hot electrons, $f_0(T_0)$, can be estimated by

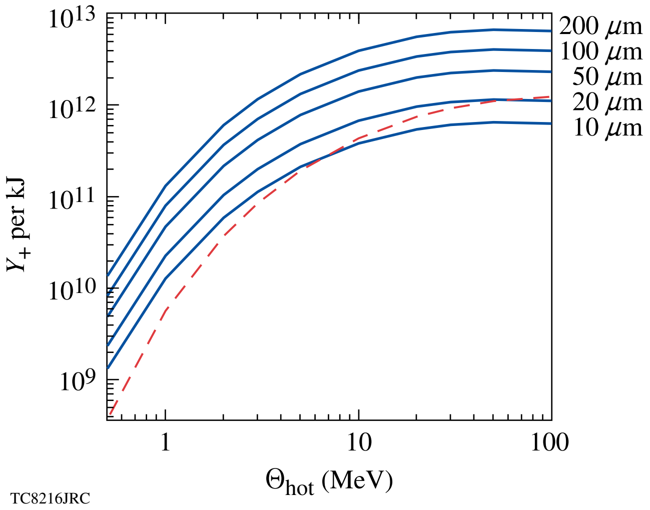

Figure 116.1
The solid curves show the photo-produced positron yield (number of pairs per kJ of hot electrons) as a function of hot-electron temperature (in MeV) for targets of thickness ranging from 10 μm to 200 μm. The dashed curve shows the direct (trident) yield from Eq. (6).

$$\left\langle T_+\right\rangle_T = \int_0^\infty \mathrm{d}T_0 f_0(T_0)\frac{1}{\Xi(T_0)} \times \int_0^{s(T_0)} \mathrm{d}s'\,\overline{T}_+\left[T(T_0,s')\right]\sigma_T\left[T(T_0,s')\right], \qquad (7)$$

where $\Xi(T_0) \equiv \int_0^{s(T_0)} \mathrm{d}s'\sigma_T$.

2. Indirect Photo-Pair Production

a. Hard x-ray production. To compute the indirect yield, one must first calculate the hard component of the bremsstrahlung. This can be estimated using the Bethe–Heitler cross section[39]

$$\sigma_\gamma(E_0,k)\mathrm{d}k = Z^2 r_0^2\alpha\frac{\mathrm{d}k}{kE_0^2}\left\{\left(E_0^2+E^2\right)\left[\phi_1(\gamma)-\frac{4}{3}\log Z\right] - \frac{2}{3}EE_0\left[\phi_2(\gamma)-\frac{4}{3}\log Z\right]\right\}. \qquad (8)$$

This represents the cross section for an incident electron of total energy $E_0 = (T_0 + m_e c^2)$ to produce a bremsstrahlung photon, in the field of an atomic nucleus, with energy between k and $k + \mathrm{d}k$ (the scattered electron has energy $E = E_0 - k$). The screening factors $\phi_1(\gamma)$ and $\phi_2(\gamma)$ have their usual definitions,[40] with the screening parameter γ given by $\gamma = 100\, m_e c^2 k/\left(E_0 E Z^{1/3}\right)$.

The photon energy spectrum, differential in photon energy, produced by electrons with an initial energy spectrum $f_0(T_0)$ that run down their energy completely in the target is given by

$$N_\gamma(k)\mathrm{d}k = \left(\eta_r N_e\right)\int_0^\infty \mathrm{d}T_0 f_0(T_0) \times \int_0^{T_0}\mathrm{d}T n_i\sigma_\gamma(E,k)\mathrm{d}k\left|\frac{\mathrm{d}T}{\mathrm{d}s}\right|^{-1}$$

$$= \left(\eta_r N_e\right)\int_0^\infty \mathrm{d}T_0 f_0(T_0) \times \int_0^{s(T_0)}\mathrm{d}s' n_i\sigma_\gamma\left[E(E_0,s')k\right]\mathrm{d}k. \qquad (9)$$

The energy contained in bremsstrahlung photons, ϵ_γ, may be computed by multiplying Eq. (9) by photon energy k and integrating, to give

$$\epsilon_{\gamma\{0,>\}} = \left(\eta_r N_{\mathrm{e}}\right)\int_0^\infty \mathrm{d}T_0 f_0\left(T_0\right) T_0 Y_{\{0,>\}}\left(T_0\right), \qquad (10)$$

where $Y_{\{0,>\}}$ has the definition

$$Y_{\{0,>\}}\left(T_0\right) \equiv \frac{n_i}{T_0}\int_{\left\{0,2mc^2\right\}}^\infty \mathrm{d}kk\sigma_\gamma\left[E\left(T_0,s'\right)k\right]. \qquad (11)$$

In the above definitions of ϵ_γ and Y, the symbol "0" or ">" in the subscript indicates if the photon energy k in the k integration is either unrestricted or restricted to be greater than the threshold for pair production, $k > 2m_{\mathrm{e}}c^2$ (= 1.022 MeV), respectively. The quantity Y_0 is the usual "radiation yield."[38] This is the fraction of an incident electron's kinetic energy T_0 that is converted into radiation as the electron thermalizes within an infinite medium of a given material. Likewise, $Y_>$ measures the fraction of this energy that is above threshold for pair production. For convenience, the "bremsstrahlung efficiency" $\eta_{\gamma,\{0,>\}} \equiv \epsilon_{\gamma,\{0,>\}}/\left(N_{\mathrm{e}}\Theta_{\mathrm{hot}}\right)$ has been introduced. It is defined as the ratio of bremsstrahlung energy to hot-electron kinetic energy for hot electrons described by the probability distribution $f_0(T_0)$.

Figure 116.2 shows a plot of the bremsstrahlung efficiency $\eta_{\gamma,0}$, radiation yield Y_0, and a comparison with the Koch and Motz scaling,[39]

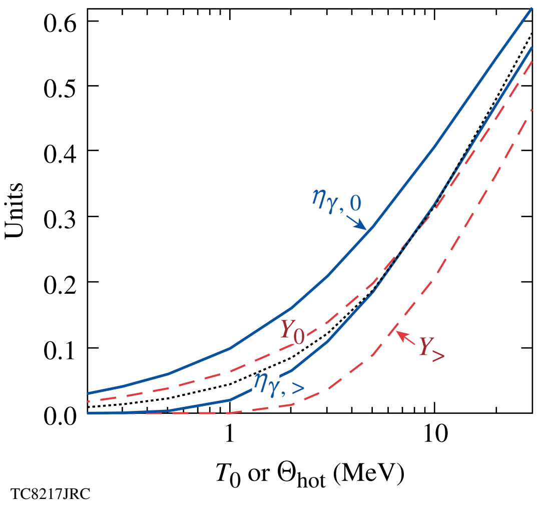

Figure 116.2
Solid curves show the bremsstrahlung efficiency $\eta_{\gamma,0} \equiv \epsilon_{\gamma,0}/\left(N_{\mathrm{e}}\Theta_{\mathrm{hot}}\right)$ and bremsstrahlung efficiency above threshold $\eta_{\gamma,>}$ as functions of hot-electron temperature from Eq. (10). The dashed curves show the radiation yield Y_0 and radiation yield above threshold $Y_>$ [Eq. (11)] as functions of electron kinetic energy. The dotted curve is the Koch and Motz thick-target bremsstrahlung scaling.[39]

$$\left(Y_0\right)_{\mathrm{K-M}} = 3\times10^{-4} Z\mathcal{T}_0' \Big/ \left(1+3\times10^{-4} Z\mathcal{T}_0'\right),$$

where $\mathcal{T}_0'$ is the electron kinetic energy in mass units, $\mathcal{T}_0' \equiv T_0/m_{\mathrm{e}}c^2$. The quantities $\eta_{\gamma,>}$ and $Y_>$ are also shown. In these calculations the best-available tabulated differential bremsstrahlung cross sections have been used (from Ref. 41) rather than the Bethe–Heitler expression [Eq. (8)].

Two important loss mechanisms preclude the *extraction* of an amount of bremsstrahlung energy equal to the radiation yield in practical laser–foil interaction experiments. These are (a) the escape of high-energy electrons from the foil (i.e., $\eta_r < 1$) and (b) the self-absorption of a portion of the bremsstrahlung generated in the foil. In this application, however, self-absorption is desired—the dominant contribution to the attenuation coefficient being pair production for photon energies $\gtrsim$5 MeV (Ref. 42). High refluxing efficiency $\eta_r \sim 1$ is observed in experiments conducted at laser energies $E_{\mathrm{L}} \sim 500$ J (Refs. 37 and 43). Future experiments are planned to test the extrapolation to kJ laser energies.[37] Another potentially important consideration for higher target energy densities is target expansion caused by the hot-electron pressure.[44] This represents an additional energy sink for the hot electrons.

b. Pair production. If the bremsstrahlung energy spectrum $N_\gamma(k)$ is known, either experimentally[23] or as computed by Eq. (9), the resulting photo-pair yield is readily computed assuming isotropy and homogeneity of the bremsstrahlung emission. In a foil where Compton scattering is negligible, the number of photo-produced positrons in the (total) energy range $E_+ + dE_+$, produced in a foil of thickness d, is given by

$$\begin{aligned} N_{\mathrm{e}^+}\left(E_+\right)dE_+ = \frac{N_{\mathrm{A}}}{A}\int_0^\infty \mathrm{d}k\int \mathrm{d}\Omega\Bigg(\int_0^d \rho \mathrm{d}t\Bigg\{\int_0^t \mathrm{d}s\frac{1}{|\cos\theta|} \\ \times n_\gamma^-(k,t,\theta)\exp\left[-\mu(k)\frac{(t-s)}{|\cos\theta|}\right] \\ + \int_t^d \mathrm{d}s\frac{1}{|\cos\theta|}n_\gamma^+(k,t,\theta) \\ \times \exp\left[-\mu(k)\frac{(s-t)}{|\cos\theta|}\right]\Bigg\}\Bigg) \\ \times \sigma_{\gamma\to\mathrm{e}^+\mathrm{e}^-}\left(k,E_+\right)dE_+, \end{aligned} \qquad (12)$$

where E_+ is the (total) positron energy and $\mu(k) = n_i\sigma_{\text{tot}}(k)$ is the linear attenuation coefficient for x rays of energy k.[(b)] The total cross section σ_{tot} has contributions from coherent and incoherent Compton scattering, photo-electric absorption, pair production, and photo-nuclear absorption, $\sigma_{\text{tot}} = \sigma_{\text{scat}} + \sigma_{p-\text{e}} + \sigma_{\gamma\to\text{e}^+\text{e}^-} + \sigma_{p-\text{n}}$. For photon energies $k \gtrsim 5$ MeV, pair production dominates, while close to threshold, $k \sim 1$ MeV, pair production competes with Compton scattering, $\sigma_{\gamma\to\text{e}^+\text{e}^-} \sim \sigma_{\text{scat}}$. In gold at solid density, the Compton-scattering cross section $\sigma_{\text{scat}} \lesssim 10$ barns translates into a probability of ~0.06 scattering events mm^{-1}. Since it will be verified *a posteriori* that optimal target thicknesses will not exceed the millimeter scale, the assumptions leading to Eq. (12) are justified. In Eq. (12), a new quantity $n_\gamma^\pm(k,t,\theta)\text{d}k\text{d}t\text{d}\Omega$, has been introduced. It represents the number of photons of energy between k and $k + \text{d}k$ that are born with a propagation direction falling into the solid angle between Ω and $\Omega + \text{d}\Omega$, originating at a depth between t and $t + \text{d}t$ in the target, and propagating in the forward/backward (+/–) direction. The simplifying assumption that bremsstrahlung photons are isotropic and produced homogeneously throughout the foil volume, perhaps as a result of hot-electron refluxing,[37,43] allows $n_\gamma^\pm$ to be written simply in terms of $N_\gamma(k)$, i.e.,

$$n_\gamma^\pm(k,t,\theta)\text{d}k\text{d}t\text{d}\Omega = \frac{1}{2}N_\gamma(k)\text{d}k\left(\frac{\text{d}t}{d}\right)\left(\frac{\text{d}\Omega}{2\pi}\right)H[\pm\cos(\theta)],$$

where H is the Heaviside step function. Equation (12) becomes

$$N_{\text{e}^+}(E_+)dE_+ = \frac{N_{\text{A}}}{A}\int_0^\infty \text{d}kN_\gamma(k)\sigma_{\gamma\to\text{e}^+\text{e}^-}(k,E_+)dE_+ \times \int\frac{d\Omega}{4\pi}(\rho L)_{\text{eff}}, \tag{13}$$

where $(\rho L)_{\text{eff}}$ is an "effective depth" in the target (in g/cm^2) for photons of energy k with birth angle θ. This can be written as the product of the average depth in the absence of attenuation, $\rho d/(2|\cos\theta|)$, and an attenuation correcting factor C,

$$(\rho L)_{\text{eff}} = \frac{\rho d}{2|\cos\theta|}\cdot C\left[\frac{\mu(k)d}{|\cos\theta|}\right], \tag{14}$$

where $C(w) = 2/w^2\,[\exp(-w)-(1-w)]$. This correction factor ranges from unity, when attenuation along the path w is small, to $C \sim 2|\cos\theta|/(\mu d)$ when the attenuation is large, giving $(\rho L)_{\text{eff}} \approx \rho/\mu$. For solid-density gold, $\rho/\mu = (19.3)(0.79) = 15.3\ \text{g/cm}^2$ at threshold photon energy ($k = 1.022$ MeV). The angle-average effective depth for photons of energy k required by Eq. (13) becomes

$$\langle\rho L\rangle_\Omega \equiv \frac{1}{4\pi}\int\text{d}\Omega(\rho L)_{\text{eff}} \tag{15}$$

$$= \rho d\int_0^1 \text{d}x\,\min\left\{\frac{1}{2x}C\left(\frac{\mu d}{x}\right),\frac{r}{d}\right\}. \tag{16}$$

The replacement of $(\rho L)_{\text{eff}}$ by $(\rho L)_{\text{eff}} \longrightarrow \min\{(\rho L)_{\text{eff}}, \rho r\}$ takes into account the effect of finite target radius r (transverse dimensions). The integral in Eq. (16) can be readily performed, yielding

$$\begin{aligned}\langle\rho L\rangle_\Omega = {}& \frac{1}{2}\frac{\rho}{\mu}\left[1+\left(1-\frac{1}{\mu d}\right)\left(1-e^{-\mu d}\right)-\mu d\ Ei(-\mu d)\right] \\ & -\frac{x^*}{2}\frac{\rho}{\mu}\left[1+\left(1-\frac{x^*}{\mu d}\right)\left(1-e^{-\mu d/x^*}\right)-\frac{\mu d}{x^*} \times Ei\left(-\frac{\mu d}{x^*}\right)\right]+x^*\rho r,\end{aligned} \tag{17}$$

where $Ei(x)$ is the "exponential integral"[45] and x^* is given by the solution to $x^*/(\mu d)\left(1-e^{-\mu d/x^*}\right) = 1x^*\mu r$, if $r < 1/\mu$, or $x^* = 0$ otherwise. In the case of most interest to experiment, that of weak attenuation $d < r \ll 1/\mu$, Eq. (17) can be approximated as

$$\langle\rho L\rangle_\Omega \approx \frac{\rho d}{2}\log\left(\frac{2.516}{\mu d}\right), \qquad \mu d \ll 1, \mu r \ge 1 \tag{18}$$

$$\langle\rho L\rangle_\Omega \approx \frac{\rho d}{2}\log\left(5.437\frac{r}{d}\right), \qquad \mu d \ll 1, \mu r \ll 1 \tag{19}$$

In the case of strong attenuation, Eq. (17) can be approximated as

$$\langle\rho L\rangle_\Omega \approx \frac{\rho}{\mu}, \qquad \mu d \gg 1, r > d/2. \tag{20}$$

Intermediate cases $\mu d \lesssim 1$ and $\mu r \lesssim 1$ require the numerical evaluation of Eq. (17). The origin of the logarithmic dependence on either foil radius r or absorption $1/\mu$ in Eqs. (18) and (19) is because these serve to regularize the otherwise logarithmically divergent integral, Eq. (16).

[(b)] Usually called the mass attenuation coefficient when expressed in cm^2/g.

With the above results, the positron energy spectrum is given by

$$N_{\mathrm{e}^+}(E_+)dE_+ = \frac{N_\mathrm{A}}{A}\int_0^\infty \mathrm{d}k N_\gamma(k) \times \sigma_{\gamma\to\mathrm{e}^+\mathrm{e}^-}(k,E_+)dE_+\langle\rho L\rangle_\Omega , \quad (21)$$

and the total photo-produced positron yield is given by $Y_{+,\gamma} = \int_{mc^2}^\infty N_{\mathrm{e}^+}(E_+)dE_+$. The yield can be computed directly from the *total* pair cross section

$$\sigma_{\gamma\to\mathrm{e}^+\mathrm{e}^-}(k) = \int dE_+\sigma_{\gamma\to\mathrm{e}^+\mathrm{e}^-}(k,E_+),$$

(the tabulated total cross section is more readily available) according to

$$Y_{+,\gamma} = \frac{N_\mathrm{A}}{A}\int_0^\infty \mathrm{d}k N_\gamma(k)\sigma_{\gamma\to\mathrm{e}^+\mathrm{e}^-}(k)\langle\rho L\rangle_\Omega . \quad (22)$$

In Eq. (21), the bremsstrahlung spectrum $N_\gamma(k)$ is given by Eq. (9) and the angle-average effective depth $\langle\rho L\rangle_\Omega$ by Eq. (17), while the differential pair cross-section[41] $\sigma_{\gamma\to\mathrm{e}^+\mathrm{e}^-}(k,E_+)$ is obtained from the bremsstrahlung cross section [Eq. (8)]. This is achieved by making the substitution $E_0 \longrightarrow -E_+$, $E \longrightarrow E_-$, $k \longrightarrow -k$ and multiplying by $E_+^2 dE_+/(k^2\mathrm{d}k)$ to take care of the change in density of final states (general substitution rule[46]), where E_- is the energy of the pair electron. In general, this expression for the cross section is accurate only for high energies, so we normalize this differential expression to yield a total cross section $\sigma_{\gamma\to\mathrm{e}^+\mathrm{e}^-}(k)$ that agrees with those tabulated by Hubbell *et al.*[42] The total cross sections of Hubbell *et al.* represent the most-recent systematic computations and tabulations. The same reference provides the mass attenuation coefficient.

Analysis of the Positron-Yield Calculations

1. Dependence of Positron Yield and Positron Spectrum on Interaction Conditions

Figure 116.1 shows the photo-produced positron yield $Y_{+,\gamma}$ per kilojoule of hot-electron energy as a function of hot-electron temperature for foil thicknesses ranging between 10 μm and 200 μm and a radius $r = 1$ mm. Photo-produced pairs dominate over trident pairs for targets of thickness $d \gtrsim 20$ μm for hot-electron temperatures $0.5 \lesssim \Theta_\mathrm{hot} \lesssim 100$ MeV. For pair production in "showers,"[30] it is known that production by virtual photons becomes negligible compared with production by real photons if the target thickness is much more than 1/25 of a radiation length (i.e., for $d \gtrsim 135$ μm in Au). Hot-electron refluxing is responsible for the dominance of photo-produced pairs in thinner-than-expected targets. Refluxing leads to higher photon production for a given foil thickness, i.e., it is the difference between thin- and thick-target bremsstrahlung yields.[37,43]

Figure 116.3 shows the average positron kinetic energy $\langle T_+\rangle_\gamma$ and the average hot-electron kinetic energy Θ_hot as a function of laser intensity I_L. In Fig. 116.3, the hot-electron temperature corresponding to a particular laser intensity has been determined by two different scalings: the ponderomotive scaling [Eq. (1)] and the Beg intensity scaling.[25] Unlike transformed Eq. (8), the cross section $\sigma_{\gamma\to\mathrm{e}^+\mathrm{e}^-}$ is asymmetric in the energy distribution of the pair for high-*Z* elements near threshold.[40] Accounting for this effect would lead to a slightly higher positron temperature by an amount of the order of the binding energy, which is considered to be negligible.

For a fixed target thickness, the pair creation efficiency (Fig. 116.1) increases with hot-electron temperature, with energetic efficiencies of $E_{\mathrm{e}^+}/E_\mathrm{hot} \sim 1.6 \times 10^{-4}$ achieved for $\Theta_\mathrm{hot} \sim 2$ MeV. The optimal hot-electron temperature for the creation of pairs by the Bethe–Heitler process is $(\Theta_\mathrm{hot})_\mathrm{opt} \approx 50$ MeV, corresponding to an optimal laser intensity of $(I_\mathrm{L})_\mathrm{opt} \sim 10^{22}$ W/cm^2, based on the ponderomotive scaling, or $(I_\mathrm{L})_\mathrm{opt} \sim 10^{25}$ W/cm^2 for the Beg scaling. This enormous variation in optimal laser intensity reflects the degree of uncertainty of the hot-electron temperature scaling with laser intensity in the regime $I_\mathrm{L} \gtrsim 10^{21}$ W/cm^2. The

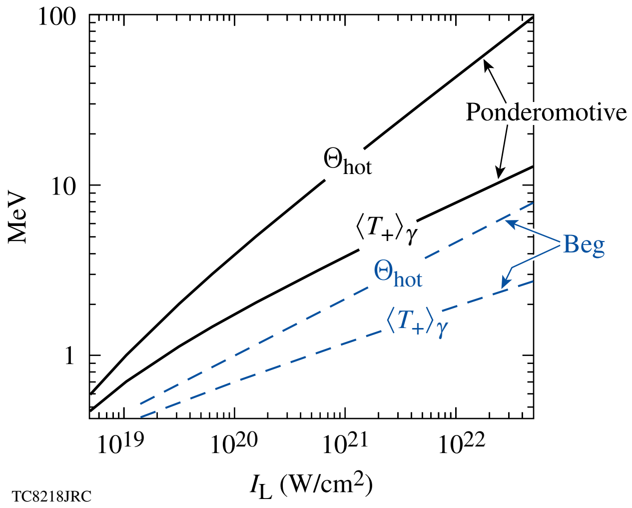

Figure 116.3
The solid curves show the hot-electron temperature (upper curve) and mean positron kinetic energy $\langle T_+\rangle_\gamma$ (lower curve), resulting from the energy spectrum computed in Eq. (21) as functions of laser intensity, assuming the ponderomotive scaling. The dashed curves show the same quantities, but for Beg intensity scaling.

scalings used in Fig. 116.3 have been extrapolated beyond the tested regime $10^{18} \lesssim I_L \lesssim 10^{21}$ W/cm^2. The Beg scaling, which predicts far fewer energetic electrons, was originally based on experiments in the intensity range $I_L \lesssim 10^{19}$ W/cm^2 (Ref. 25). For higher hot-electron temperatures $\Theta_{hot} \gtrsim 50$ MeV, the positron production efficiency $Y_{+,\gamma}$, expressed per kJ of hot-electron energy, decreases ($E_{hot} = N_e\Theta_{hot}$ is the energy content of the hot electrons) because the bremsstrahlung spectrum becomes too hard. The pair-production cross section has a very weak energy dependence above photon energies of $k \sim 10$ MeV, and, as far as maximizing the number of pairs is concerned, it is more efficient to have two photons at half the energy.

For a given laser intensity and small x-ray attenuation μd, the production efficiency increases with target thickness by Eq. (18) or Eq. (19), depending on the ratio of the target radius to the photon linear attenuation length μr. For $\mu d \gg 1$, the efficiency is independent of target thickness and $Y_{+,\gamma} \approx \rho/\mu \int \mathrm{d}k N_\gamma(k)\sigma_{\gamma\to e^+e^-}(k)$. The attenuation length varies weakly over the photon energy range of $1 < k < 100$ MeV and has the approximate value $1/\mu \leq 0.8$ cm.

2. Optimized Useful Positron Yield

The long-term goal of this work is to create a pair plasma in the space surrounding the foil target where one can conduct experiments, and not in its interior. The "useful" pair yield (i.e., the number of pairs able to escape the target per kJ of hot-electron energy) must therefore be optimized. For a given laser intensity it might seem that the target should be made as thick as possible, up to an x-ray attenuation length $d \sim 1/\mu \sim 0.8$ cm. The target thickness is more tightly constrained, however, since only positrons within a range $r_0(E_+)$ of the surface will be able to escape and the positron range is typically much less than the x-ray attenuation length $r_0 \ll 1/\mu$. The optimal target thickness $d = d_{opt}(\langle T_+\rangle)$ is a function of the positron energy, determined by the hot-electron spectrum and depends on the scaling of the hot-electron temperature with laser intensity. Unfortunately, the latter represents a source of considerable uncertainty because such scalings are imprecisely known and are extrapolated from significantly smaller laser systems $E_L \lesssim 500$ J.

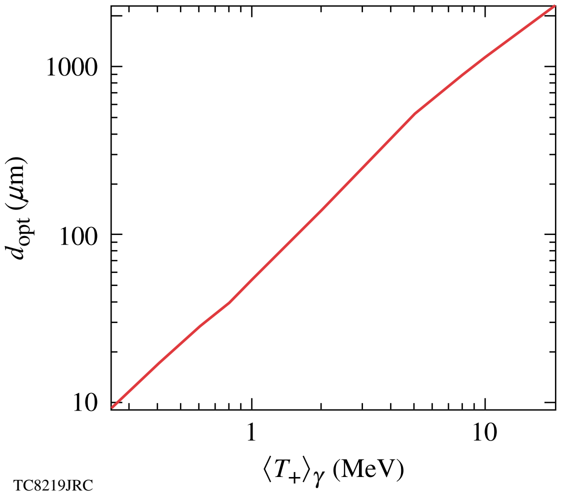

Figure 116.4
The solid curve shows an estimate for the optimal target thickness d_{opt} in μm as a function of average positron energy $\langle T_+\rangle$ in MeV (positron energy is shown as a function of incident laser intensity in Fig. 116.3).

Figure 116.4 shows an estimate for the optimal target thickness d_{opt} as a function of average positron energy $\langle T_+\rangle$. Taken with Fig. 116.3, Fig. 116.4 allows one to estimate the optimal target thickness to be made for a given incident laser intensity. This estimate has been obtained by setting the target thickness d equal to the thickness that is known, experimentally, to transmit only 50% of a normally incident monoenergetic electron beam of energy T, where T is set to the average positron energy $T = \langle T_+\rangle$. This thickness is substantially less than the CSDA range due to the path-length straggling caused by multiple scattering of electrons (and positrons) in the Coulomb field of high-Z nuclei (such as Au). This calculation provides a useful "rule of thumb" that will be refined by future detailed Monte Carlo modeling for a more-precise optimization. For a given thickness d, the transmission Tr(T,Z,d) is computed from the "empirical transmission equation" $\mathrm{Tr}(T,Z,d) = \exp\left[-\alpha\left(d/R_{ex}\right)^\beta\right]$ of Ebert *et al.*,[47] where T is the incident electron energy (the differences between electron and positron stopping and scattering in matter are neglected). The "extrapolated range" R_{ex} is approximated by $R_{ex} = 0.565\,[125/(Z+112)]\,T - 0.423\,[175/(Z+162)]$ g/cm^2, where $\alpha = (1-1/\beta)^{1-\beta}$ and the parameter β is given by $\beta = [387\ T/Z\ (1 + 7.5 \times 10^{-5}\ ZT^2)]^{0.25}$, with T in MeV. The regime of validity for this expression for Tr(T,Z,d) has been expanded from 4 MeV < T < 12 MeV (Ref. 47) to $T \sim 0.25$ MeV by using the extrapolated ranges of Tabata *et al.*[48] in the regime 0.25 MeV < T < 4 MeV.

Figure 116.5 shows the "optimized useful yield" as a function of laser intensity for both Beg and ponderomotive scalings. It is apparent that at intensities of $I_L \sim 5 \times 10^{19}$ W/cm^2,(c) there is an uncertainty in the pair yield of almost two orders of magnitude. This is a result of the strong temperature dependence of the yield for electron temperatures close to the threshold

---

(c)Multikilojoule pulses have not been achieved at higher intensity.

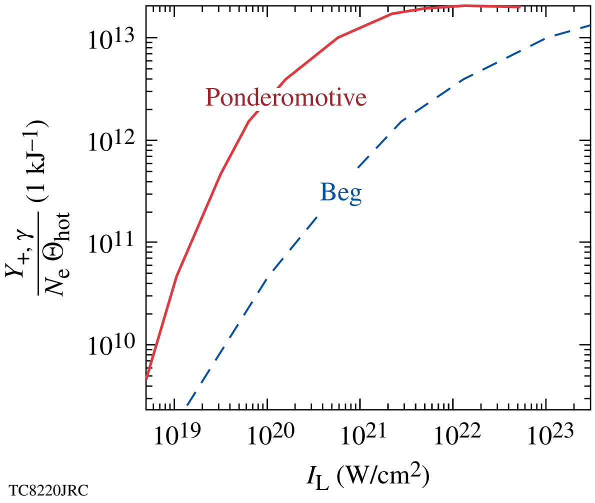

Figure 116.5
The solid curve shows the optimum pair yield per kJ of hot electrons $Y_{+,\gamma}/(N_\mathrm{e}\Theta_\mathrm{hot})$ as a function of incident laser intensity I_L, assuming ponderomotive scaling. The dashed curve shows the same quantity, but for Beg intensity scaling.

for pair production, $\Theta_\mathrm{hot} \sim 1$ MeV, and the current uncertainty in hot-electron energy scaling with laser intensity. At $I_\mathrm{L} = 5 \times 10^{19}$ W/cm^2, the Beg scaling predicts a hot-electron temperature of $\Theta_\mathrm{hot} \approx 0.8$ MeV and an optimized yield of $Y_{+,\gamma} = 1.5 \times 10^{10}$ pairs per kJ of hot electrons, achieved with a foil of thickness $d = 40\ \mu$m. At the same laser intensity, the ponderomotive scaling predicts $T_\mathrm{hot} = 2.5$ MeV and a yield of $Y_{+,\gamma} = 1 \times 10^{12}$ per kJ at $d = 200\ \mu$m. This extreme sensitivity will make measurements of the pair yield a good diagnostic for hot-electron temperature in the regime of importance for advanced inertial confinement fusion (ICF) designs, such as fast ignition.[49,50]

A reasonable upper bound for the optimized pair yield on OMEGA EP, and similar future laser systems, can be determined: Assuming the ponderomotive scaling [Eq. (1)], which is more consistent with experiments with significant preplasma,[26] a laser energy of $E_\mathrm{L} = 2.5$ kJ delivered at an intensity of $I_\mathrm{L} = 5 \times 10^{19}$ W/cm^2, a hot-electron conversion efficiency of $\eta_{\mathrm{L}\rightarrow\mathrm{e}} = 0.2$ (Ref. 51), and perfect refluxing efficiency $\eta_r = 1$ (Refs. 37, 43, and 51), the expected yield is $Y_{+,\gamma} = 5 \times 10^{11}$ pairs. This corresponds to 0.4×10^{10} pairs per steradian, assuming isotropic emission.

3. Optimized Pair-Production rates

The pair-production rate $\dot{Y}_{+,\gamma}$ is estimated by $\dot{Y}_{+,\gamma} \approx Y_{+,\gamma}/\tau^*$, where τ^* is the characteristic production time. Here, τ^* is the time required for the initial hot-electron distribution $f_0(T)$ to slow down so that the relative fraction of particles above threshold,

$$\phi_>(t) \equiv \int_{T_\mathrm{th,e}}^{\infty} \mathrm{d}T\, f(T,t) \Big/ \int_{T_\mathrm{th,e}}^{\infty} \mathrm{d}T\, f_0(T)\,,$$

has fallen by $1/e$, i.e., $\phi_>(\tau^*) = 1/e$. The slowing-down distribution at time t, $f(T,t)$ is computed according to the CSDA approximation: $f(T,t) = f_0(T + \Delta T)$, where $\Delta T = -c\int_{t_0}^{t} \mathrm{d}t\beta(T)\left|\mathrm{d}t/\mathrm{d}s\right|$, $\beta = (1-1/\gamma^2)^{1/2}$, and $\gamma = 1 + T/(m_\mathrm{e}c^2)$. This assumes that the production time τ^* is longer than the laser pulse duration. If this is not the case, it must be factored into the calculation.

Figure 116.6 shows the pair-production rate $\dot{Y}_{+,\gamma}$ as a function of laser intensity, for both Beg and ponderomotive scalings. For the case of ponderomotive scaling, the production rate rises rapidly for intensities around $I_\mathrm{L} \sim 1 \times 10^{19}$ W/cm^2 ($\Theta_\mathrm{hot} = 0.96$ MeV) and reaches a maximum at $(I_\mathrm{L})_\mathrm{max} = 1.5 \times 10^{21}$ W/cm^2 ($\Theta_\mathrm{hot} = 16.4$ MeV). The maximum-achievable production rate of $\dot{Y}_{+,\gamma} \approx 10^{24}\mathrm{s}^{-1}\,\mathrm{kJ}^{-1}$ greatly exceeds any known terrestrial source; indeed, such a high rate is normally encountered only in astrophysical and cosmological settings.[3]

The maximum in pair-production rate is very broad, with 50% of the maximum value achieved at the moderate intensity of $I_\mathrm{L} = 1 \times 10^{20}$ W/cm^2 ($\Theta_\mathrm{hot} = 3.9$ MeV). This implies that highly useful experiments can be conducted at $I_\mathrm{L} \ll (I_\mathrm{L})$max. High production rates can be obtained by virtue of the large available energy $E_\mathrm{L} \sim 5$ kJ on currently available systems (OMEGA EP) with the practical possibility of high-intensity short-pulse lasers with $E_\mathrm{L} \sim 100$ kJ in the near future (e.g., the

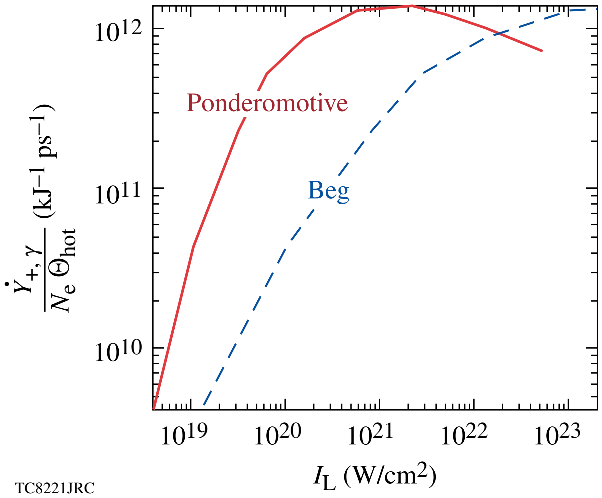

Figure 116.6
The solid curve shows the optimized pair-production rate per kJ of hot electrons $\dot{Y}_{+,\gamma}/(N_\mathrm{e}\Theta_\mathrm{hot})$ as a function of laser intensity for the ponderomotive scaling. The dashed curve shows the same quantity for the Beg intensity scaling.

proposed "HiPER" facility[52,53]). The corresponding intensities for Beg scaling are easily obtained from ponderomotive intensities by making the approximate transformation

$$(I_{20})_{\mathrm{Beg}} \approx 87.9\,(I_{20})^{3/2}_{\mathrm{pond}} \times \left[1 - 0.35\,(I_{20})^{-1/2}_{\mathrm{pond}} + 0.08\,(I_{20})^{-1}_{\mathrm{pond}} - \ldots\right],$$

which is useful for $(I_{20})_{\mathrm{pond}} \gtrsim 1$. Here, I_{20} is the laser intensity I_{L} expressed in units of 10^{20} W/cm^2.

4. Relativistic Pair-Plasma Production

As shown in Fig. 116.3, the expanding cloud of pair particles will have a temperature characteristic of the hot electrons and γ rays that created it. Unless confined, the relativistic electron–positron pairs will expand into the space surrounding the target at approximately the speed of light.

Although, in general, the expansion into the vacuum can be expected to be quite complicated,[(d)] the expected plasma parameters can be estimated by assuming free expansion at the speed of light from an infinitesimal source, starting at time $t = 0$, combined with a constant source rate $\dot{Y}_{+,\gamma}$. On this basis, the positron density n_+ at radius r and time t is

$$n_+(r,t) = \frac{1}{4\pi r^2}\frac{\dot{Y}_{+,\gamma}}{c} \qquad \text{for } c\left(t-\tau^*\right) < r < ct\,; \tag{23}$$

$$\text{otherwise,} \qquad n_+(r,t) = 0. \tag{24}$$

This gives in practical units

$$n_+(r,t) \approx 0.7 \times 10^{16}\left(\frac{0.03\ \mathrm{cm}}{r}\right)^2 \times \frac{\dot{Y}_{+,\gamma}}{10^{12}\ \mathrm{kJ}^{-1}\ \mathrm{ps}^{-1}}\,\frac{E_{\mathrm{hot}}}{2.5\ \mathrm{kJ}}\ \mathrm{cm}^{-3}. \tag{25}$$

The Coulomb coupling parameter $\Gamma_+ = e^2\big/\left(a\langle T_+\rangle_\gamma\right)$, where the ion-sphere radius $a = \left(4\pi n_+/3\right)^{-1/3}$ expresses the ratio of Coulomb energy of the particles to their thermal energy. This parameter is much less than unity,

$$\Gamma_+ = 5 \times 10^{-8}\left(n_+\big/10^{16}\ \mathrm{cm}^{-3}\right)^{1/3}\left(\langle T_+\rangle_\gamma\big/1\ \mathrm{MeV}\right)^{-1} \ll 1,$$

because the particles are dilute and their temperature is high. The number of particles in a Debye sphere $N_{\mathrm{D}} = (3\Gamma_+)^{-3/2}$ is correspondingly high,

$$N_{\mathrm{D}} = 1.7 \times 10^{10}\left(n_+\big/10^{16}\ \mathrm{cm}^{-3}\right)^{-1/2}\left(\langle T_+\rangle_\gamma\big/1\ \mathrm{MeV}\right)^{3/2}.$$

The expanding cloud may appear to be a classical weakly coupled plasma.[54] For collective excitation to be supported, however, the cloud size must exceed the Debye length,

$$\lambda_{\mathrm{D}} = \sqrt{4\pi n_+ e^2\big/\langle T_+\rangle_\gamma} \approx 7.4 \times 10^3 \times \left(n_+\big/10^{16}\ \mathrm{cm}^{-3}\right)^{-1/2}\left(\langle T_+\rangle_\gamma\big/1\ \mathrm{MeV}\right)^{1/2}\ \mathrm{cm}.$$

The ratio of density scale length $L_n = \left|\mathrm{d}\log n_+\big/\mathrm{d}r\right|^{-1}$ to the Debye length, for the expansion given by Eq. (23), is

$$\frac{L_n}{\lambda_{\mathrm{D}}} = \frac{1}{2}\left(\frac{\dot{Y}_{+,\gamma}e^2}{c\langle T_+\rangle_\gamma}\right)^{1/2}. \tag{26}$$

This ratio is independent of r, assuming that the expansion is isothermal,

$$\frac{L_n}{\lambda_{\mathrm{D}}} = 1.7\left(\frac{\dot{Y}_{+,\gamma}}{10^{12}\ \mathrm{ps}^{-1}\ \mathrm{kJ}^{-1}}\right)^{1/2}\left(\frac{E_{\mathrm{hot}}}{2.5\ \mathrm{kJ}}\right)^{1/2}\left(\frac{\langle T_+\rangle_\gamma}{1\ \mathrm{MeV}}\right)^{-1/2}. \tag{27}$$

Adiabatic expansion would give a more favorable ratio for larger radii.

From the above estimate [Eq. (27)], the rate of positron production $\dot{Y}_{+,\gamma}$ is probably insufficient to guarantee the production of a pair plasma for laser energies of several kJ. The chances for success can be greatly improved, however, by limiting the expansion of the cloud.

Confinement of the pairs, such as might be obtained in a magnetic mirror,[10] is not necessary. Radial confinement of the order of 100 μm with free expansion in the remaining dimension will lead to a cloud that is several tens of Debye lengths in size[55]

[(d)] Electrostatic sheath fields and large-scale, self-generated dc magnetic fields will modify the expansion.

and has many particles in a Debye sphere; i.e., the cloud will form a classical weakly coupled plasma. Radial confinement may be obtained in several ways, e.g., by using one of the OMEGA EP beams to magnetize the positron-generation foil using a "magnetic trap" target,[55] or by the application of an externally generated magnetic field of the type used in the Magneto-Inertial Fusion Electrical Discharge System (MIFEDS).[56]

Summary

The yield of electron–positron pairs caused by both direct and indirect processes resulting from the interaction of laser-accelerated hot electrons with target atoms has been calculated. Indirect production is the dominant process for practical target interaction conditions.

Calculation of the indirect yield required two steps: First, an expression for the hard x-ray spectrum and yield was obtained [Eqs. (9) and (10)]. This was computed in the limit in which the majority of fast electrons are confined to the target by space-charge effects (the so-called "refluxing limit"). Second, convenient expressions were obtained for the pair spectrum [Eq. (21)] and pair yield [Eq. (22)]. These are given in terms of the photon spectrum $N_\gamma(k)$ and an angle-average effective depth for photons $\langle \rho L \rangle_\Omega$, which is dependent on the photon energy and target geometry [Eqs. (17–20)]. Predictions of bremsstrahlung yield [Eq. (10)] and spectrum [Eq. (9)] are experimentally verifiable and might prove useful for other applications.

For a given target thickness, the efficiency of pair creation (pairs per kJ of hot electrons) was shown to increase with the temperature Θ_{hot} of the laser-excited electrons, with maximum production efficiency obtained at a hot-electron temperature of $\Theta_{\text{hot}} = 50$ MeV. Energetic efficiencies of $\sim 1.6 \times 10^{-4}$ are shown to be achievable at $\Theta_{\text{hot}} = 2$ MeV. The corresponding laser intensity for optimal yield could optimistically be as low as $I_{\text{L}} \sim 10^{22}$ W/cm^2.

The optimal "useful" yield is limited by the range of the pairs in the target material. It has been maximized by matching the target thickness to the expected penetration distance of the pairs as a function of laser intensity and Θ_{hot} scaling (see Fig. 116.5). It was demonstrated that a yield of $Y_{+,\gamma} = 5 \times 10^{11}$ pairs might be generated on OMEGA EP, provided that the hot-electron temperature is consistent with the ponderomotive scaling. More unfavorable yields are obtained with Beg scaling.

Pair-production rates were calculated and shown to have a very broad maximum of $\dot{Y}_{+,\gamma} = 1 \times 10^{24}\ \text{s}^{-1}\ \text{kJ}^{-1}$, obtained at $I_{\text{L}} = 1.5 \times 10^{21}$ W/cm^2 ($\Theta_{\text{hot}} = 16.4$ MeV), which is a significantly lower Θ_{hot} than that required for maximizing the yield. The rate displays little sensitivity to the hot-electron temperature over a wide range. This implies that, as far as production rates are concerned, increasing laser intensities above the currently attainable levels is less important than increasing available laser energy, which does not rely on further technological advances.

An estimate of plasma parameters, assuming free expansion of the pairs into the vacuum, indicates that current kJ-class, high-intensity lasers may come close to producing a pair plasma with a physical size similar to, or slightly smaller than, the Debye length. A successful demonstration will probably require efforts to confine or limit the expansion of the expanding pairs. Possible confinement schemes, such as externally applied magnetic fields, are suggested. The yields, production rates, and energy spectra that have been computed in this article will be useful for particle-in-cell (PIC) or implicit-hybrid PIC calculations of the dynamics of expansion and pair-plasma production.

ACKNOWLEDGMENT

This work was supported by the U.S. Department of Energy Office of Inertial Confinement Fusion under Cooperative Agreement No. DE-FC52-08NA28302, the University of Rochester, and the New York State Energy Research and Development Authority. The support of DOE does not constitute an endorsement by DOE of the views expressed in this article.

REFERENCES

1. V. Tsytovich and C. B. Wharton, Comments Plasma Phys. Control. Fusion **4**, 91 (1978).
2. G. P. Zank and R. G. Greaves, Phys. Rev. E **51**, 6079 (1995).
3. M. L. Burns, A. K. Harding, and R. Ramaty, eds. *Positron-Electron Pairs in Astrophysics, AIP Conference Proceedings 101* (American Institute of Physics, New York, 1983).
4. B. A. Remington *et al.*, Science **284**, 1488 (1999).
5. C. M. Surko, M. Leventhal, and A. Passner, Phys. Rev. Lett. **62**, 901 (1989).
6. C. M. Surko and T. J. Murphy, Phys. Fluids B **2**, 1372 (1990).
7. T. Kurihara *et al.*, Nucl. Instrum. Methods Phys. Res. B **171**, 164 (2000).
8. C. M. Surko *et al.*, Nucl. Instrum. Methods Phys. Res. B **171**, 2 (2000).
9. T. S. Pedersen *et al.*, J. Phys. B **36**, 1029 (2003).
10. G. Gibson, W. C. Jordan, and E. J. Lauer, Phys. Rev. Lett. **5**, 141 (1960).
11. J. W. Shearer *et al.*, Phys. Rev. A **8**, 1582 (1973).

12. E. P. Liang, S. C. Wilks, and M. Tabak, Phys. Rev. Lett. **81**, 4887 (1998).
13. D. A. Gryaznykh, Ya. Z. Kandiev, and V. A. Lykov, JETP Lett. **67**, 257 (1998).
14. T. E. Cowan *et al.*, in *High-Field Science*, edited by T. Tajima, K. Mima, and H. Baldis (Kluwer Academic, New York, 2000), pp. 145–156.
15. C. Gahn *et al.*, Appl. Phys. Lett. **77**, 2662 (2000).
16. K. Nakashima and H. Takabe, Phys. Plasmas **9**, 1505 (2002).
17. S. C. Wilks *et al.*, Astrophys. Space Sci. **298**, 347 (2005).
18. L. J. Waxer, D. N. Maywar, J. H. Kelly, T. J. Kessler, B. E. Kruschwitz, S. J. Loucks, R. L. McCrory, D. D. Meyerhofer, S. F. B. Morse, C. Stoeckl, and J. D. Zuegel, Opt. Photonics News **16**, 30 (2005).
19. M. H. Key, Phys. Plasmas **14**, 055502 (2007).
20. J. Schwinger, Phys. Rev. **82**, 664 (1951).
21. E. Brezin and C. Itzykson, Phys. Rev. D **2**, 1191 (1970).
22. H. Nitta *et al.*, Phys. Rev. Lett. **93**, 180407 (2004).
23. S. P. Hatchett, C. G. Brown, T. E. Cowan, E. A. Henry, J. S. Johnson, M. H. Key, J. A. Koch, A. B. Langdon, B. F. Lasinski, R. W. Lee, A. J. MacKinnon, D. M. Pennington, M. D. Perry, T. W. Phillips, M. Roth, T. C. Sangster, M. S. Singh, R. A. Snavely, M. A. Stoyer, S. C. Wilks, and K. Yasuike, Phys. Plasmas **7**, 2076 (2000).
24. S. C. Wilks *et al.*, Phys. Rev. Lett. **69**, 1383 (1992).
25. F. N. Beg *et al.*, Phys. Plasmas **4**, 447 (1997).
26. M. G. Haines, Imperial College, private communications (2008).
27. T. E. Cowan, M. Roth, J. Johnson, C. Brown, M. Christl, W. Fountain, S. Hatchett, E. A. Henry, A. W. Hunt, M. H. Key, A. MacKinnon, T. Parnell, D. M. Pennington, M. D. Perry, T. W. Phillips, T. C. Sangster, M. Singh, R. Snavely, M. Stoyer, Y. Takahashi, S. C. Wilks, and K. Yasuike, Nucl. Instrum. Methods Phys. Res. A **455**, 130 (2000).
28. H. Chen *et al.*, Rev. Sci. Instrum. **77**, 10E703 (2006).
29. H. J. Bhabha, Proc. R. Soc. Lond. A, Math. Phys. Sci. **152**, 559 (1935).
30. Y.-S. Tsai, Rev. Mod. Phys. **46**, 815 (1974).
31. G. Racah, Nuovo Cimento **14**, 93 (1937).
32. B. B. Rossi, *High-Energy Particles*, Prentice-Hall Physics Series (Prentice-Hall, New York, 1952).
33. T. Murota, A. Ueda, and H. Tanaka, Prog. Theor. Phys. **16**, 482 (1956).
34. D. A. Gryaznykh, Phys. At. Nucl. **61**, 394 (1998).
35. V. N. Baĭer and V. S. Fadin, Sov. Phys.-JETP **34**, 253 (1972).
36. J. Myatt, W. Theobald, J. A. Delettrez, C. Stoeckl, M. Storm, T. C. Sangster, A. V. Maximov, and R. W. Short, Phys. Plasmas **14**, 056301 (2007).
37. P. M. Nilson, W. Theobald, J. F. Myatt, C. Stoeckl, M. Storm, J. D. Zuegel, R. Betti, D. D. Meyerhofer, and T. C. Sangster, "Bulk Heating of Dense Plasma High-Intensity Laser-Plasma Interactions," submitted to Physical Review E.
38. H. O. Wyckoff, *ICRU Report*, **37**, International Commission on Radiation Units and Measurements, Inc., Bethesda, MD (1984).
39. H. W. Koch and J. W. Motz, Rev. Mod. Phys. **31**, 920 (1959).
40. H. A. Bethe and J. Ashkin, in *Experimental Nuclear Physics*, edited by E. Sergrè (Wiley, New York, 1953), Vol. I, pp. 166–357.
41. S. M. Seltzer and M. J. Berger, Nucl. Instrum. Methods Phys. Res. B **12**, 95 (1985).
42. J. H. Hubbell, H. A. Gimm, and I. Øverbø, J. Phys. Chem. Ref. Data **9**, 1023 (1980).
43. S. D. Baton *et al.*, High Energy Density Phys. **3**, 358 (2007).
44. M. Tabak, Bull. Am. Phys. Soc. **52**, 284 (2007).
45. M. Abramowitz and I. A. Stegun, eds. *Handbook of Mathematical Functions with Formulas, Graphs, and Mathematical Tables*, Applied Mathematics Series 55 (U.S. Government Printing Office, Washington, DC, 1964).
46. J. D. Bjorken and S. D. Drell, *Relativistic Quantum Mechanics*, International Series in Pure and Applied Physics (McGraw-Hill, New York, 1964).
47. P. J. Ebert, A. F. Lauzon, and E. M. Lent, Phys. Rev. **183**, 422 (1969).
48. T. Tabata, R. Ito, and S. Okabe, Nucl. Instrum. Methods **103**, 85 (1972).
49. N. G. Basov, S. Yu. Gus'kov, and L. P. Feokistov, J. Sov. Laser Res. **13**, 396 (1992).
50. M. Tabak *et al.*, Phys. Plasmas **1**, 1626 (1994).
51. P. M. Nilson, W. Theobald, J. Myatt, C. Stoeckl, M. Storm, O. V. Gotchev, J. D. Zuegel, R. Betti, D. D. Meyerhofer, and T. C. Sangster, Phys. Plasmas **15**, 056308 (2008).
52. M. Dunne, Nat. Phys. **2**, 2 (2006).
53. S. Atzeni *et al.*, Phys. Plasmas **15**, 056311 (2008).
54. S. Ichimaru, *Statistical Plasma Physics. Volume I, Basic Principles*, Frontiers in Physics (Addison-Wesley, Redwood City, CA, 1992).
55. J. Myatt, A. V. Maximov, R. W. Short, and D. D. Meyerhofer, Bull. Am. Phys. Soc. **52**, 66 (2007).
56. O. V. Gotchev, N. W. Jang, J. P. Knauer, M. D. Barbero, R. Betti, C. K. Li, and R. D. Petrasso, J. Fusion Energy **27**, 25 (2008).

Neutron Yield Study of Direct-Drive, Low-Adiabat Cryogenic D_2 Implosions on OMEGA

Introduction

As a viable path to energy production, inertial confinement fusion (ICF) has been actively pursued over the past decades.[1] In a standard ICF design, a thin-shell capsule containing a solid DT (ice) layer and low-density DT gases is imploded as symmetrically as possible, either directly driven by high-energy lasers[2] or indirectly driven by x rays in a hohlraum.[3] The high-speed, inward-moving shell compresses the low-density DT gases, thereby creating a "hot spot" during the stagnation of the implosion. Thermonuclear reactions in this high-temperature hot spot can trigger a burn wave that ignites the assembled, surrounding high-density fuel. To obtain energy gain, the imploding DT fuel must be compressed to thousands of times its solid density.[4] On one hand, a properly created hot spot, with certain density and temperature, provides the alpha (α) particles for subsequent heating of the assembled, surrounding high-density, low-temperature fuels. On the other hand, the fuel areal density (ρR) must be high enough to stop the heating particles for efficient burn-wave propagation. It is clear that proper hot-spot formation and high-density fuel assembly must be attained simultaneously to guarantee a successful ignition. Any target perturbations can grow exponentially via Rayleigh–Taylor (RT) instability[5–9] to disrupt the hot-spot formation as well as the high-density fuel assembly.

Cryogenic implosions with high adiabats of $\alpha \geq 4$ (α is defined as the ratio of fuel pressure to the Fermi-degenerate pressure) have been previously investigated in OMEGA experiments[10] and simulations.[11] To efficiently compress ICF targets to high densities, the fuel must maintain a low adiabat of $\alpha \simeq 2$ during a direct-drive implosion.[12] Low-adiabat implosions are very sensitive, however, to RT instability growth. Mitigation of RT growth has been proposed and conducted using a laser picket in front of the main pulse, which shapes the fuel adiabat to be low at the back surface and high at the ablation front.[13,14] A series of such shaped low-adiabat ($\alpha \simeq 2$ to 3) cryogenic targets have been imploded at the OMEGA Laser Facility.[15–17] Since efficient diagnostic methods for ρR measurement of DT implosions are not yet fully implemented, most cryogenic implosions on OMEGA are currently performed with D_2 targets. For D_2 implosions, the compression has been successfully measured up to $\rho R \sim 200$ mg/cm^2 by secondary proton scattering.[15–17] As discussed above, assembly of high-density fuels is extremely crucial, but getting the predicted fusion yield from the formed hot spot is equally important to the success of ICF; after all, it provides the "trigger" for ignition burn propagation to occur. A variety of perturbations can significantly reduce the fusion yield. This article is devoted to understanding the perturbation sources and how they affect the neutron yield in low-adiabat cryogenic D_2 implosions conducted on OMEGA.

The next two sections give a brief description of the two-dimensional (2-D) numerical simulations and experimental basics, respectively. Subsequent sections (1) present simulation results that examine in detail the effects of both individual and combined perturbation sources on the implosion yield degradation; (2) discuss the absolute experimental neutron yield and neutron rate measurements, when compared to our modelings; and (3) summarize our results.

Two-Dimensional *DRACO* Simulations

The 2-D radiation hydrodynamics code *DRACO* has been developed at LLE for both implosion and planar target simulations.[18] *DRACO* can be run in either Lagrangian, Eulerian, or Arbitrary–Lagrangian–Eulerian (ALE) mode, but this study uses only the ALE version. For spherical implosion simulations, the *DRACO* coordinates are defined by the cylindrical axis z and radius R, with the assumption of azimuthal symmetry. The laser absorption of plasmas through inverse bremsstralung is implemented by three-dimensional (3-D) ray tracing with the exact port geometry of OMEGA.[19] Although *DRACO* has the option of using different equations of state (EOS's) in hydro-simulations, the *SESAME* EOS table[20] is used throughout this study. The *SESAME* EOS of direct-drive ICF shell material has recently been verified by compressibility measurements.[21,22] Agreements were found for a variety of drive conditions related to direct-drive ICF. The radiation transport in *DRACO* has used the multigroup diffusion model, in which the Astrophysics Opacity Table (AOT)[23] is applied.

Since the laser energy absorbed near the critical-density region must be transported to the ablation surface by electrons, the thermal-transport model in direct-drive ICF is crucial for properly simulating the target drive. There has been a long history of using flux-limited Spitzer thermal conductivity in laser–plasma fluid modelings.[24] Previous experiments with both planar and spherical targets[25,26] have shown that a flux limiter of $f = 0.06$ works well for low/middle laser intensities (up to ~6×10^{14} W/cm^2) of square pulses; however, there was also evidence that a time-dependent flux limiter[27] or a nonlocal heat-transport model[16] is required to better simulate implosions driven by high-intensity lasers and/or sophisticated pulse shapes. In principle, we can perform our 2-D simulations with a time-dependent flux limiter, which partially accounts for the nonlocal effects. However, since the purpose of this study is to explore the perturbation effects on the neutron-yield degradation of implosions, we have confined our simulations to those shots that are insensitive to the heat-transport model. Namely, we have studied mostly cryogenic D_2 implosions with low/middle laser intensities ranging from 2.5 to 6×10^{14} W/cm^2. For those implosions, the local and nonlocal 1-D *LILAC*[28] simulations show less sensitivity to shock timing; therefore, a normal flux limiter of $f = 0.06$ was adopted for these studies.

DRACO's capability to simulate Rayleigh–Taylor instability growth has recently been demonstrated with intense laser-driving planar-target experiments on OMEGA.[29] For low-mode perturbations similar to those investigated here, the code properly predicts their growth rate at the relevant laser-intensity range. Generally, we have examined an ice-layer roughness mode up to $\ell = 12$. The higher modes of ice-layer perturbations are found to be less important to yield degradation in thin-shell (~5-μm) implosions.

D_2 Implosion Experiments on OMEGA

The 60-beam OMEGA Laser Facility delivers up to 30-kJ, 351-nm UV energies on target.[30] A typical laser pulse used for low-adiabat D_2 implosions is shown in Fig. 116.7(b), in which the Gaussian-like laser picket is used to shape the target adiabat.[13,14] Each laser beam, coming from ports in 3-D geometry, is equipped with an SG-4 phase plate. Standard beam-smoothing techniques were used, including distributed phase plates,[31] polarization smoothing,[32] and smoothing by spectral dispersion (SSD).[33] The power imbalance (PI) among beams has an rms (root mean square) of ~2.6%, while the mistiming (MT) is typically within ~12-ps rms. The mispointing of each beam has an uncertainty of ~12-μm rms. All of these low-mode laser nonuniformities have been implemented in our 3-D ray-tracing laser-absorption package. We have separately examined the effect of each of these nonuniformities and their combined effects on the performance of a uniform target. The simulation results are summarized in Table 116.I. Compared to the uniform irradiation, it was found that mistiming among beams is the dominant effect to the total yield-over-clean (YOC) degradation, while other low-mode laser perturbations change the YOC only a few percent around that of the symmetric implosion. The "clean" yield is defined as the neutron yield from a 2-D simulation with uniform laser irradiation and

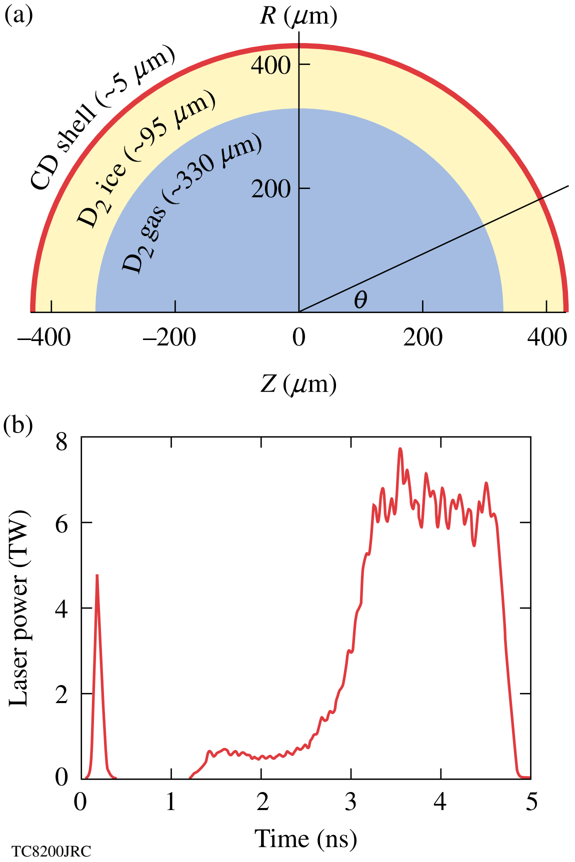

Figure 116.7
(a) The schematic diagram of a typical thin-shell cryogenic D_2 target imploded on OMEGA; (b) the shaped low-adiabat ($\alpha \simeq 2$ to 3) laser pulse with a picket.

Table 116.I: YOC dependence on low-mode laser nonuniformities.

Low-mode laser nonuniformity	$YOC_{2\text{-}D}$
3-D port geometry only	96.7%
Geometry + mispointing (~12 μm)	98.0%
Geometry + power imbalance (~2.6%)	102%
Geometry + mistiming (~12 ps)	82.2%
Full nonuniformity (including all)	83.3%

a symmetric target. It shows that all of these combined illumination nonuniformities reduce the YOC to a level of ~83% for a uniform target. All of the following studies have included these low-ℓ-mode laser nonuniformities since they are always present in OMEGA experiments.

Detailed descriptions of cryogenic targets formed for OMEGA implosions can be found in Refs. 34 and 35. Basically, the targets are D_2 filled, with a CD shell having an outer diameter of ~860 μm and a shell thickness of 5 to 10 μm. The targets are permeation filled with high-pressure D_2 gas and cooled to below the triple point (~18.7 K). They are then transported to a characterization station for layer formation and finally to the OMEGA target chamber for implosion. The ice-layer roughness is measured in experiment before implosion. The actual low-mode spectrum of ice roughness is used in our simulations.

A typical target [shown schematically in Fig. 116.7(a)] has an ice layer of ~95-μm thickness. Figure 116.8 illustrates the irradiation nonuniformity in the case of non-zero target offset. The target offset is caused by oscillation when the shroud is pulled before implosion. This initial target offset is measured through an x-ray pinhole camera image at the beginning of corona plasma formation.[10] The fusion yield is measured by a combination of activation, scintillation, and track recorder. When compared to the predicted symmetric implosion yield, the YOC provides a direct measurement of target performance.

The low-adiabat cryogenic implosion campaign conducted on OMEGA used a wide range of peak laser intensities up to ~10^{15} W/cm^2. For high intensities near ~10^{15} W/cm^2, the compression is somewhat degraded with respect to the standard 1-D prediction due to different mechanisms.[15,16,36] Thus, this study of neutron-yield degradation will focus on those low- to mid-intensity shots that obtained $\langle \rho R \rangle_{\text{exp}}$ better than 60% of the standard 1-D prediction. They are generally in the range of $\langle \rho R \rangle_{\text{exp}} \simeq 100$ to 200 mg/cm^2.

Results and Discussions

Using the laser pulse shown in Fig. 116.7(b) throughout this general study, we will first address, separately, the effects induced by pure offset and pure ice roughness on the YOC degradation. We then discuss their combined effects on reducing the neutron yield. Finally, we compare the simulation results to experiments. The absolute neutron yields and rates from *DRACO* simulations are also compared with measurements for individual shots. Note that the laser nonuniformities discussed above have been included in all of the following studies since they are always present in OMEGA experiments.

1. Pure Offset

For the target and pulse shape characterized in Fig. 116.7, we simulated implosions with different initial target offsets but no ice roughness present (symmetric target). The offset is along the positive z axis, thereby leading to more irradiation on the "left" side than on the "right" side of the target. This can be

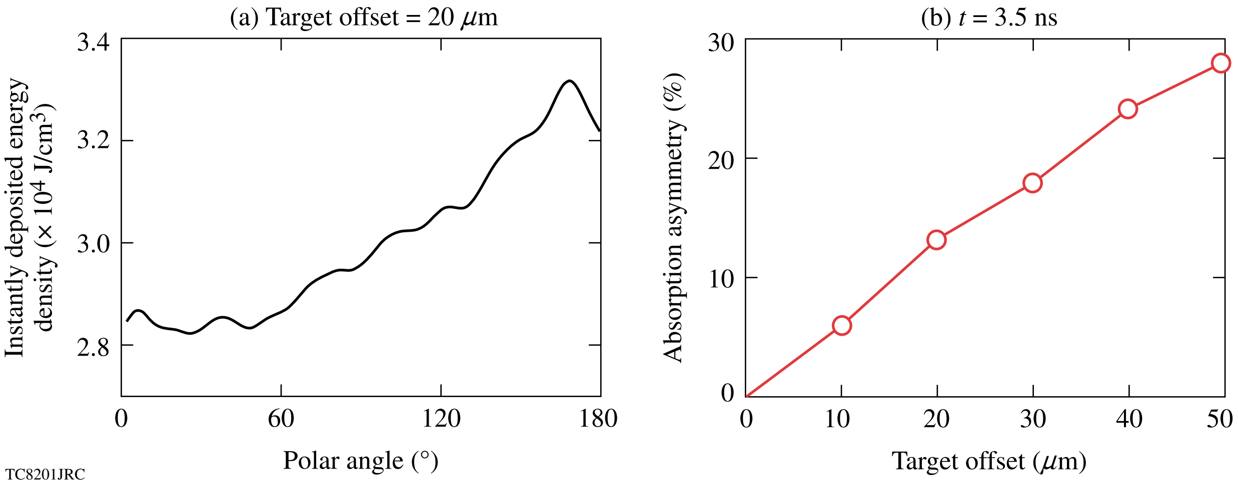

Figure 116.8
(a) The deposited energy density at t = 3.5 ns versus the angle θ (relative to the +z axis) for a target offset of 20 μm; (b) the absorption asymmetry plotted as a function of target offset.

seen in Fig. 116.8(a) for the case of a 20-μm offset, in which is plotted the instantly absorbed laser energy density (ED) at time $t = 3.5$ ns as a function of the polar angle θ [defined in Fig. 116.7(a)]. The $\theta = 0°$ line is along the positive z axis, while $\theta = 180°$ is for the negative z axis. The absorption asymmetry is defined as

$$\text{absorption symmetry} = \frac{\text{ED}_{\text{max}} - \text{ED}_{\text{min}}}{\text{ED}_{\text{avg}}}, \qquad (1)$$

where ED_{max}, ED_{min}, and ED_{avg} are the temporal maximum, minimum, and averaged energy-density depositions in the full range of polar angle θ. For the case of zero offset, the symmetric illumination gives no absorption asymmetry, while it reaches to ~13% at a 20-μm offset. In Fig. 116.8(b), the absorption asymmetry is plotted at $t = 3.5$ ns as a function of the initial target offset. Approximately 30% more laser absorption is seen on the left side than on the right side of the target in the case of a 50-μm offset. The uneven drive compresses the target asymmetrically, thereby reducing the final hot-spot temperature and density, which leads to neutron-yield degradation. As examples, the density contours are plotted at the peak compression time ($t = 4.9$ ns) for the cases of 20-μm and 40-μm offset in Figs. 116.9(a) and 116.9(b) and the neutron rates as a function of time in Fig. 116.9(c). It can be seen that the larger the offset, the more asymmetric the compression. Consequently, the hot-spot ion temperature and density decrease from $T_i \simeq 1.8$ keV and $\rho \simeq 9$ g/cm^3 to $T_i \simeq 1.5$ keV and $\rho \simeq 7$ g/cm^3 as the target offset increases from 20 μm [Fig. 116.9(a)] to 40 μm [Fig. 116.9(b)]. Compared to the symmetric case, a non-zero target offset has caused the "burn" to truncate early and has resulted in a relatively lower peak rate, thereby leading to an overall reduction in neutron yield, as shown in Fig. 116.9(c). The resulting $\text{YOC}_{\text{2-D}}$ decreases from 43% to 13.8% for these two cases, respectively.

Figure 116.10 explores the detailed hydrodynamics of how the offset affects hot-spot formation. Density snapshots at different times of (a) $t = 4.55$ ns, (b) $t = 4.65$ ns, (c) $t = 4.75$ ns, and (d) $t = 4.85$ ns are shown during shell stagnation for the case of 20-μm offset. Since the absorption on the target's left side is constantly higher, the shock from the left side is stronger than that from the right side. The asymmetric shock converges and shifts to the right side, away from the core center. At $t = 4.55$ ns, the asymmetrically converged shock starts to bounce back. As evidence of the bounced shock asymmetry, the unevenly formed high-pressure region on the inner surface of the right side of the target is indicated by Fig. 116.10(b). This asymmetrically bounced shock acting with a continuously uneven drive makes the target convergence unequal from both sides. As time goes on, convergence is stronger on the left side of the target (opposite to the initial target offset direction), thereby leading to high compression along that side. All these features are presented in the simulations in Fig. 116.10.

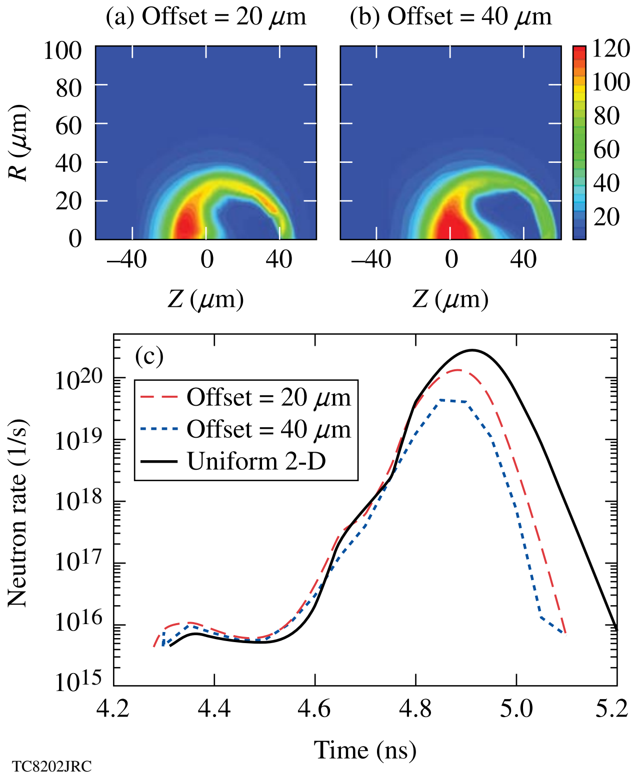

Figure 116.9
The density contour plots at peak compression for target offset of (a) 20 μm and (b) 40 μm. The corresponding neutron rates are plotted in (c) for the two offset situations as well as the symmetric case.

Pure-offset simulations up to 50 μm have been performed with the pulse shape and uniform target characterized in Fig. 116.7; the results are summarized in Fig. 116.11. It is noted that at zero offset the laser illumination nonuniformities degrade the $\text{YOC}_{\text{2-D}}$ to ~83%, as was addressed above. Overall, the $\text{YOC}_{\text{2-D}}$ monotonically decreases as the offset increases. For a target offset of 20 μm, the simulation gives a YOC ~40%, which is three to four times higher than experimental observations. Thus, the target offset alone cannot explain the YOC degradation in experiments.

2. Ice Roughness Only

The ice-layer roughness has been characterized in experiments.[34] As an example, the low-ℓ-mode spectrum of ice roughness for a typical cryogenic D_2 target is shown in Fig. 116.12, with $\sigma_{\text{rms}} \simeq 3.2$ μm. Approximating the ice-layer

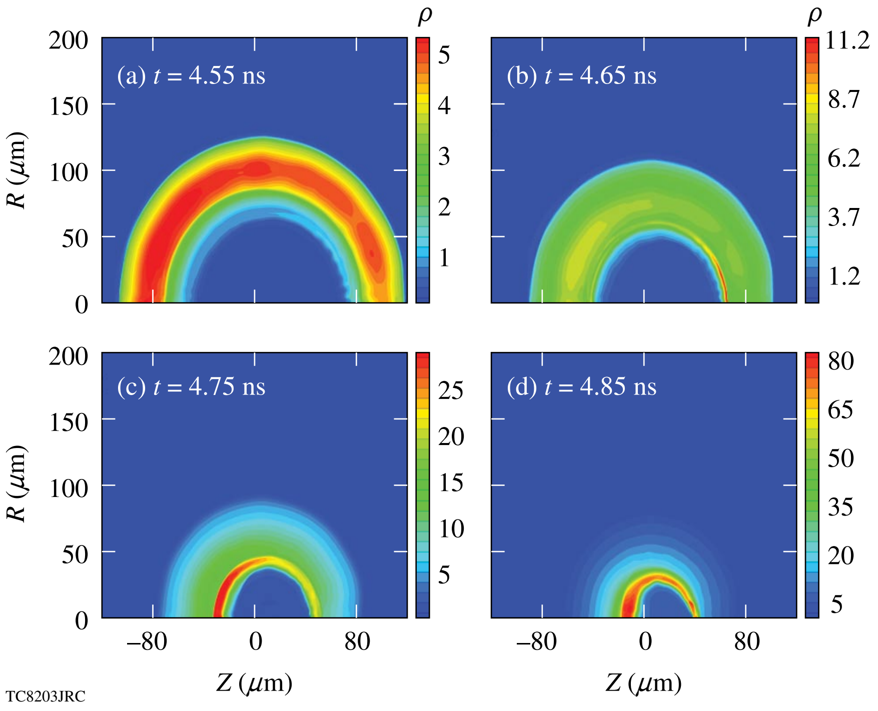

Figure 116.10
The density contour plots of a uniform target implosion with 20-μm offset, during the deceleration phase at times (a) $t = 4.55$ ns, (b) $t = 4.65$ ns, (c) $t = 4.75$ ns, and (d) $t = 4.85$ ns.

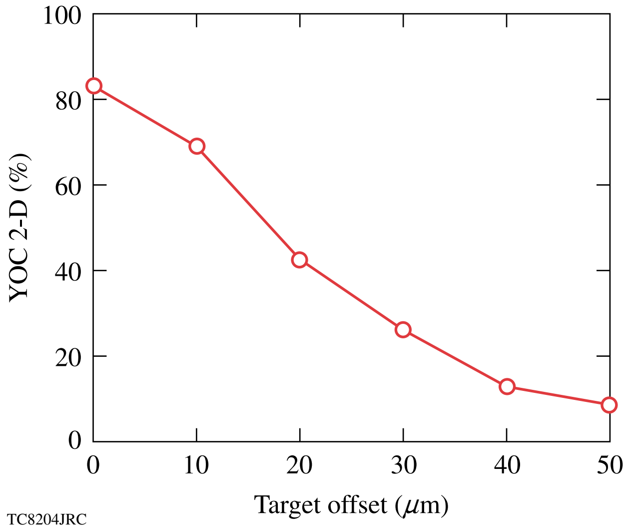

Figure 116.11
The $YOC_{2\text{-}D}$ as a function of target offset only.

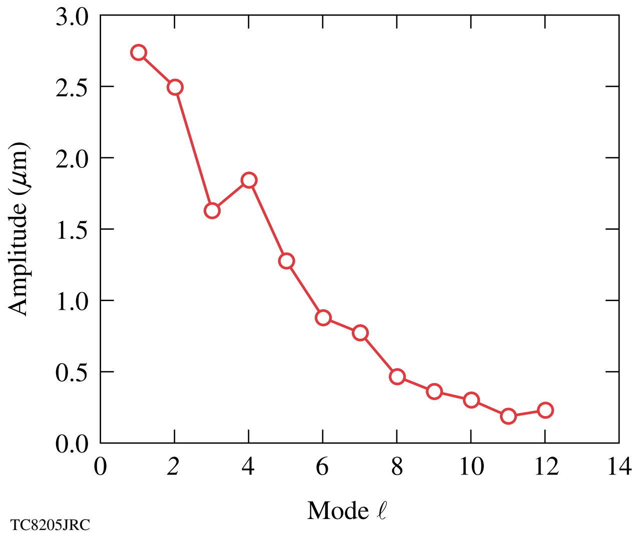

Figure 116.12
The low-ℓ-mode spectrum of ice-layer roughness for a typical cryogenic D_2 target imploded on OMEGA.

perturbation as a sum of *cosine* modes, we construct the ice-layer thickness (ΔR) for our *DRACO* simulations. Namely,

$$\Delta R(\theta) = \Delta R_0 + \sum_{\ell=1}^{n} \pm A_\ell \cos(\ell\theta), \tag{2}$$

where ΔR_0 is the average thickness of the ice layer and A_ℓ is the perturbation amplitude of the ℓth mode. Due to the hydro-boundary conditions imposed in *DRACO*, the phase among different modes can only be either 0 or π radian. This gives a plus (+) or minus (–) sign in the superposition of each mode. Different combinations of these signs provide various phases of the ice layer, which give different perturbed shell thicknesses along the polar angle θ. For instance, three such phases are drawn in Fig. 116.13. We mark the shell thickness at

$\theta = 0°$, $\theta = 90°$, and $\theta = 180°$ for each target condition. For the phase-1 target shown in Fig. 116.13(a), the thinnest ice layer is along the $\theta = 0°$ axis, while the thickest portion is at $\theta = 90°$. Figures 116.13(b) and 116.13(c) indicate the other two cases, of which the thinnest ice layer is along $\theta = 90°$, but different conditions are indicated along the z axis.

Without target offset, simulations were performed for these three target conditions characterized in Fig. 116.13. The simulated results are presented in Figs. 116.14(a)–116.14(c) for density contours at peak compression and in Fig. 116.14(d) for neutron rates. Depending on which part is the thinnest ice layer, the shock will first break out there. For example, the shock breaks out early from the right side ($\Delta R = 90\ \mu$m at $\theta = 0°$) of the target in the phase-1 condition. The asymmetrically converged shock will push the core toward the left side (along the $\theta = 180°$ direction). For targets in phases 2 and 3, the thinnest ice layer is along the $\theta = 90°$ direction. When the shock breaks out early from there, it makes the final hot spot more elongated along the z axis as illustrated in Figs. 116.14(b) and 116.14(c). Consequently, we observe that the compressed core of the phase-1 target shifts to $z \simeq -10\ \mu$m at stagnation, while the center of mass moves roughly to $z \simeq +10\ \mu$m for phases 2 and 3. The phase-1 target gives a better performance than the other two targets. The $\mathrm{YOC}_{2\text{-D}}$ is about 31% on average and varies within ~3% for these three phases. The yield performance is not sensitive to different phases in the case of zero offset, but this observation can be largely changed when combined to nonzero target offset. Even though an ice roughness of $\sigma \simeq 3.2\ \mu$m could significantly reduce the $\mathrm{YOC}_{2\text{-D}}$ to a level of ~30%, these simulations indicate that the ice roughness alone cannot explain the experimental YOC measurements. They are generally two to

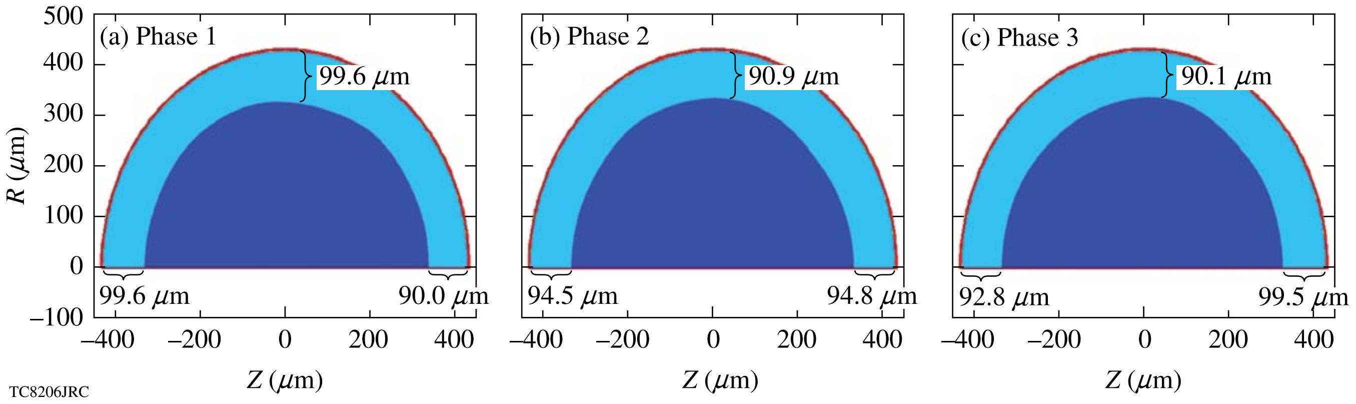

Figure 116.13
Different target conditions depending on the phases among low modes of the ice-layer roughness.

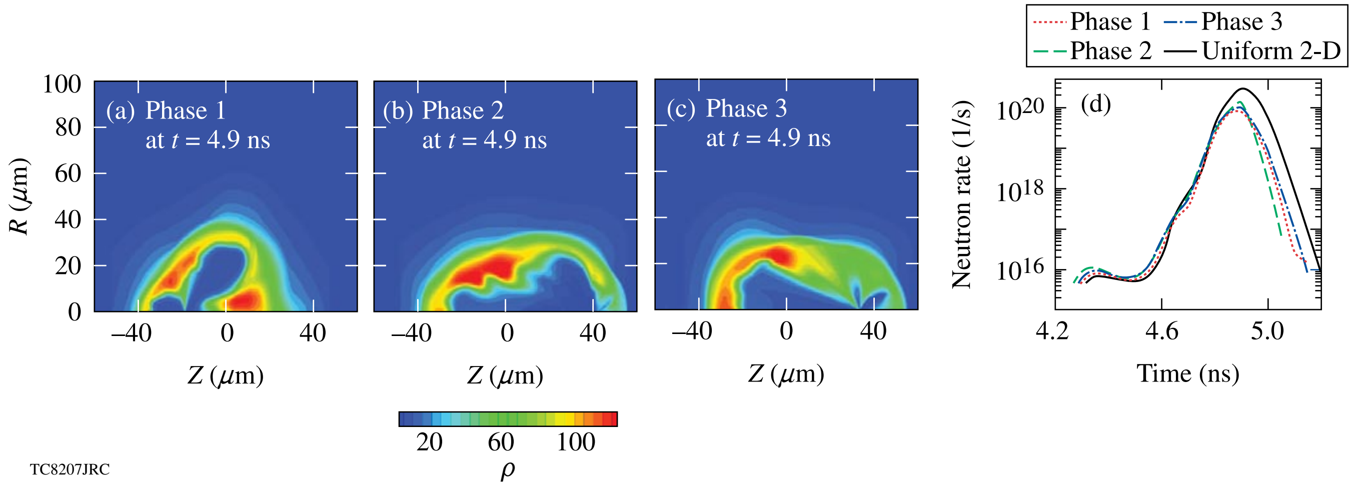

Figure 116.14
The density plots at peak neutron production, respectively, for the three different target conditions [(a), (b), and (c)] in Fig. 116.13. The corresponding neutron rates are shown in (d).

three times higher than the experimental YOC measurements, which have both ice roughness and nonzero target offset.

3. Combination of Target Offset and Ice Roughness

From here on, we examine the combined perturbation effects of both the target offset and the ice-layer roughness on the neutron-yield degradation of D_2 target implosions. Numerical examples are shown in Fig. 116.15 in the case of a 30-μm offset for the target ice-layer conditions illustrated in Fig. 116.13. In these figures, the density contours are plotted at the time of their peak neutron production. Overall, the offset acts like a dominant $\ell = 1$ mode that compresses the shell more on the left side (e.g., along the "anti-offset" direction). However, the detailed core configurations vary significantly for different phases of ice roughness. As seen in Fig. 116.14(a), the pure ice roughness in phase 1 gives a final compressed core shifted to $Z = -10$ μm, referred to here as the "equivalent offset" to the ice roughness. This equivalent offset is opposite the real target offset, which is set along the positive z direction. Namely, the two perturbation effects are "out of phase" as the hard-driven side (along θ = 180°) encounters a thicker ice layer [see Fig. 116.13(a)], so that the shocks breaking out from both sides are somewhat more balanced in phase 1. Thus, when combining the real target offset of $z = +30$ μm with the phase-1 ice roughness, the final compressed core moves roughly to $z \simeq +30–10 \simeq 20$ μm as indicated by Fig. 116.15(a). It therefore gives a better performance and results in more neutron production, shown as the thick, solid curve in Fig. 116.15(d). While for phases 2 and 3, the ice-roughness effect is "in phase" with the target offset perturbation. In other words, both perturbations constructively cause the target to perform less satisfactorily. Figures 116.15(b) and 116.15(c) show that the final cores shift to distances larger than their initial target offset of 30 μm; therefore, both cases perform less satisfactorily than the phase-1 target. With the extra perturbation of offset, the target performance is now more sensitive to the phase of ice roughness. The final target performance actually depends on whether the target offset is in phase or out of phase with the ice roughness. We have also explored other phases and found that phases 1 and 2 shown here are the two extremes.

To characterize the hot-spot condition, the quantity of $\rho^2 T_i^4$ is plotted in Fig. 116.16 for the three cases shown in Fig. 116.15, where ρ and T_i are the D_2 density and the ion temperature, respectively. Since the fusion rate is proportional to this quantity,[1] these plots indicate where neutrons are probably generated and what portion of the core volume contributes to neutron production during peak compression. Bearing in mind the azimuthal symmetry imposed in *DRACO*, one can see from Fig. 116.16 that the core condition of the phase-1 target is much better (having more volume with higher $\rho^2 T_i^4$) than the other two cases, which is consistent with the higher neutron production from the phase-1 target.

By varying the target offset and the ice roughness, the effects of different combinations of the two on the implosion neutron yield have been numerically examined. The results are summarized in Fig. 116.17, which plots the YOC$_{2\text{-D}}$ versus the initial target offset for ice roughnesses of $\sigma_{\text{rms}} = 1.0$ μm and $\sigma_{\text{rms}} = 3.2$ μm. All phases explored for each point have been averaged; also indicated is the YOC$_{2\text{-D}}$ range that each target phase could possibly reach. Figure 116.17 shows that, as the

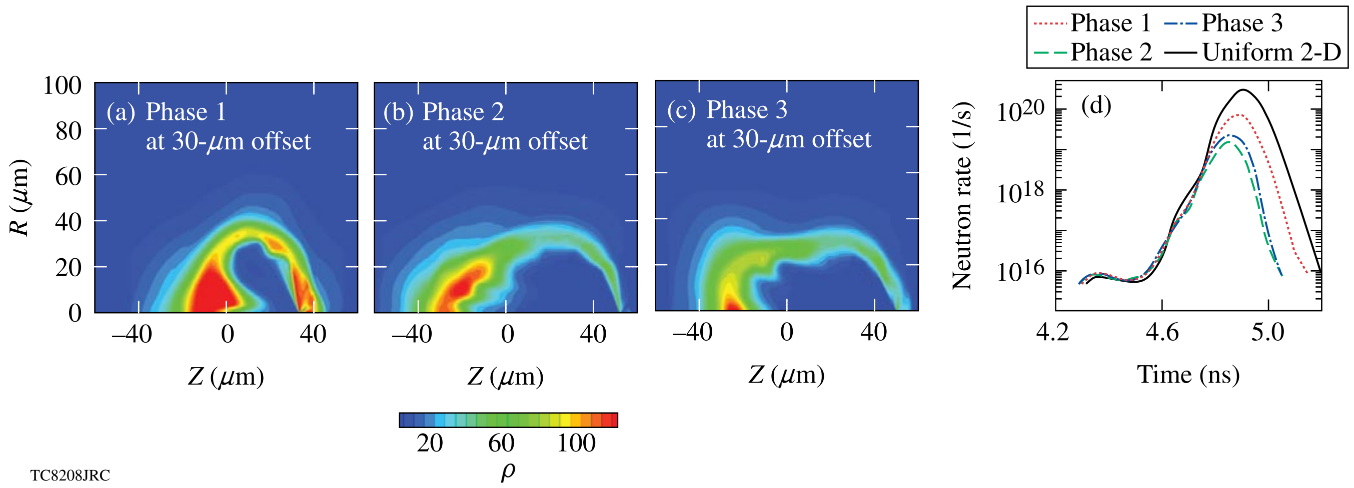

Figure 116.15
Similar to Fig. 116.14, but the targets are now offset by 30 μm.

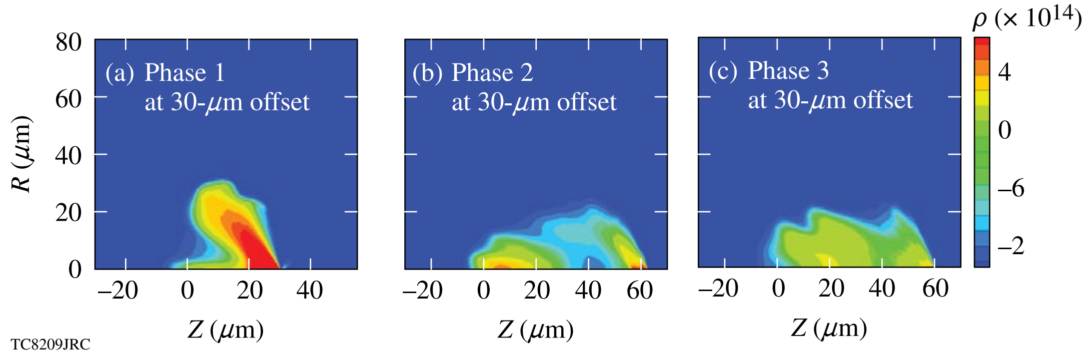

Figure 116.16
The contour plots of $\rho^2 T_i^4$ on the z–r plane, for the corresponding cases [(a), (b), and (c)] in Fig. 116.15. The images indicate where most of the neutrons are probably generated, as the fusion cross section is proportional to $\rho^2 T_i^4$.

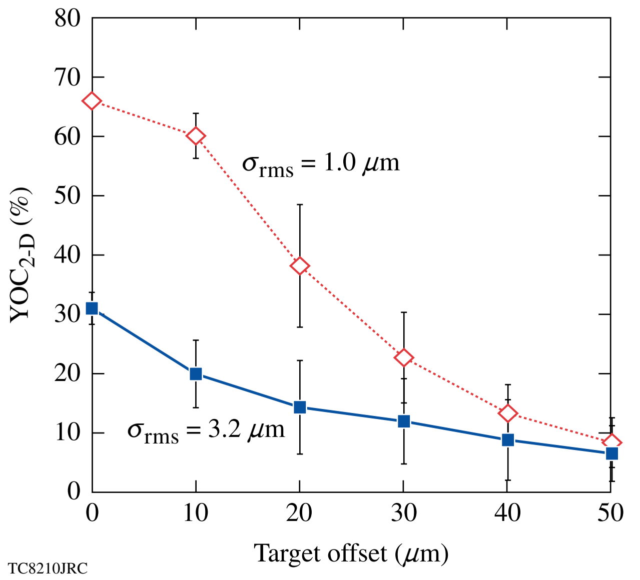

Figure 116.17
$YOC_{2\text{-}D}$ versus target offset for ice roughnesses $\sigma_{\rm rms}$ = 1.0 μm and $\sigma_{\rm rms}$ = 3.2 μm. The points are obtained by averaging different phases, where the possible $YOC_{2\text{-}D}$ range is also marked for each condition.

target offset increases beyond ~10 μm, the $YOC_{2\text{-}D}$ drops more dramatically in the case of $\sigma_{\rm rms}$ = 1 μm than that of $\sigma_{\rm rms}$ = 3.2 μm. For both cases, the phase-dependent YOC range is significant at a target offset of 20 to 40 μm. When the target offset increases to 50 μm, it becomes the dominant effect and the yield is no longer sensitive to the ice roughness.

4. Comparison to Experiments

In this subsection, we first compare the overall YOC performance as a function of target offset and ice roughness. Secondly, we focus on individual shots by using the actual experimental conditions in our simulations.

The general studies presented in Fig. 116.17 were performed for the case of low-adiabat, thin-CD-shell (5-μm) D_2 implosions. Similar-condition experiments have been conducted on OMEGA.[15–17] Shots that resulted in a compression of $\langle\rho R\rangle_{\rm exp} / \langle\rho R\rangle_{\rm 1\text{-}D} \geq 60\%$ are plotted in comparison with our *DRACO* simulations ($\sigma_{\rm rms}$ = 3.2 μm) in Fig. 116.18. The shots are divided into two groups according to their target ice roughness, i.e., $\sigma_{\rm rms} < 3.5$ μm (circles) and $\sigma_{\rm rms} > 3.5$ μm (triangles). We find reasonably good agreement between our *DRACO* simulation and experiments at an ice-roughness level of $\sigma_{\rm rms} \sim 3$ μm. Shots with a larger ice roughness ($\sigma_{\rm rms} >$ 3.5 μm) constantly give a lower YOC, which is reasonably below our simulations of $\sigma_{\rm rms}$ = 3.2 μm.

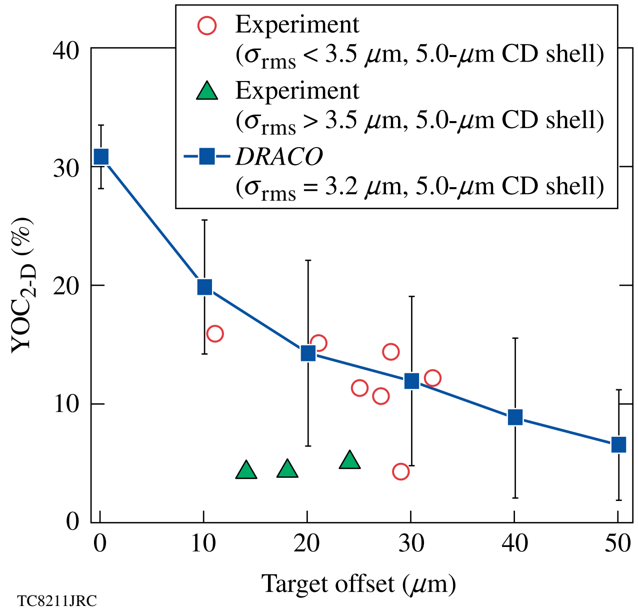

Figure 116.18
A comparison of simulated $YOC_{2\text{-}D}$ with experimental measurements for low-adiabat ($\alpha \simeq 2$ to 3), thin-shell (~5-μm) D_2 implosions on OMEGA.

D_2 targets having thick (~10-μm) CD shells were also imploded with the shaped pulse indicated in Fig. 116.19(a). For the thick-shell targets that we studied, the ice layer had a thickness of ~95 μm. The peak laser intensity now increases to ~5×10^{14} W/cm^2. In this case, the laser continuously ablates the CD shell during the entire implosion, and there is no ablation transition from CD to D_2. Compared to the thin-shell implosions, the 10-μm-thick-shell targets give a constantly lower YOC ≤ 7%. To understand the yield performance in thick-shell implosions, a general study was also performed through low-ℓ-mode *DRACO* simulations. The comparison is made in Fig. 116.19(b). The numerical prediction of YOC$_{2\text{-D}}$ from low-ℓ-mode *DRACO* simulations is higher overall than the experimental measurements by a factor of ~3. In contrast to the thick-shell situation, high-ℓ-mode perturbation growth in thin-shell implosions is probably stabilized when the laser ablation transits into D_2 (high ablation velocity). We speculate that for thick-shell targets, high-mode perturbations such as laser imprinting[37,38] may become more important since the high-density CD shell stays intact at the ablation surface during the laser irradiation. To that end, we performed simulations to resolve high modes up to $\ell_{\max} \simeq 200$. The results indicate that a factor of 2 reduction is observed, which brings the high-ℓ-mode simulation results close to experimental measurements for thick-shell implosions.

To get a sense of how YOC degrades when ice roughness increases, we have collected those shots with usual target offsets between ~10 μm and ~40 μm. The results are plotted in Fig. 116.20 and compared with low-ℓ-mode *DRACO* simulations. For thin-shell (5-μm) targets, our simulations are performed with an average target offset of 25 μm. The numerical results provide an upper limit for these experiments. The overall trend of YOC degradation with increased ice roughness is reasonably well reproduced by *DRACO* simulations. The 10-μm-thick-shell targets consistently give a lower YOC

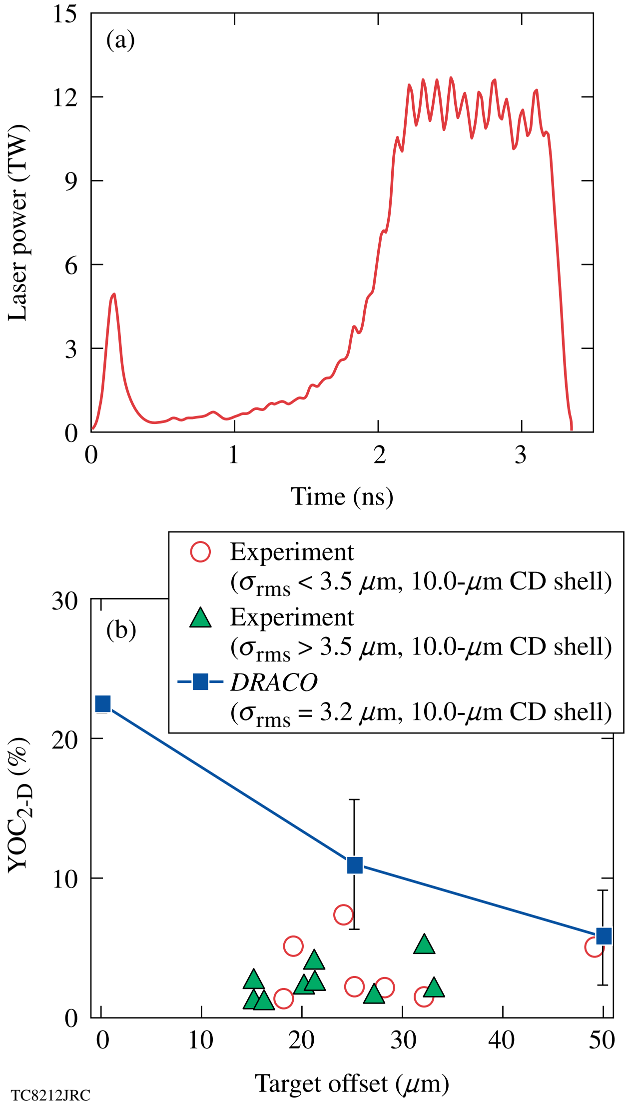

Figure 116.19
(a) A shaped pulse for low-adiabat ($\alpha \simeq 2$ to 3), thick-shell (~10-μm) D_2 implosions on OMEGA; (b) low-ℓ-mode *DRACO* simulated YOC compared with experimental measurements.

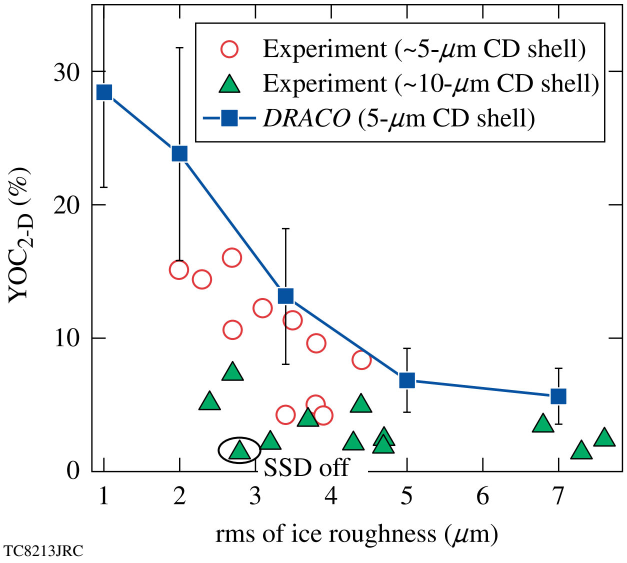

Figure 116.20
The simulated thin-shell YOC$_{2\text{-D}}$ as a function of the ice roughness σ_{rms} at a target offset of 25 μm, which is compared to experimental YOC measurements for both 5-μm- and 10-μm-CD-shell implosions at an offset range of 10 to 40 μm. The laser peak intensity (2.5 to 6.0×10^{14} W/cm^2) and pulse shape vary for different experimental shots.

than thin-shell targets. One shot with SSD off is marked in the figure, which shows a very low YOC level.

Finally, we discuss *DRACO* simulations for several individual shots in different conditions. The measured absolute neutron yields, which span two orders of magnitude, are plotted in comparison with *DRACO* simulations in Fig. 116.21. Different low-adiabat pulse shapes are used for these shots with peak intensities varying from 2.5×10^{14} W/cm^2 to ~6×10^{14} W/cm^2. For most thin-shell (5-μm) targets, the simulated neutron yields reasonably track the measurements (within a factor of 2). One shot (46864) labeled "shock timing" in Fig. 116.21 has shown a big difference between simulation and experiment. Our constant flux-limiter (f = 0.06) simulation gives three-to-four-times-higher neutron yield. For this shot, we noticed that the laser pulse has a higher picket so that the yield and compression performance was sensitive to the thermal transport modeling. Shock timing has played a significant role in target performance. There is also significant discrepancy between the low-ℓ-mode *DRACO* simulation and the experiment for a 10-μm-thick-shell implosion, which is also labeled in Fig. 116.21. Again, high-ℓ-mode perturbations not included in simulations may have further degraded the neutron yield in experiments.

Besides the total neutron yield, we have also compared the calculated time-resolved neutron rates to those observed in thin-shell experiments. Examples of such comparisons are illustrated in Fig. 116.22. The simulated neutron rate has been broadened somewhat to account for the time dispersion (due to thermal broadening and/or 3-D effects) in experiments. Good agreement is reached when the Gaussian broadening is done with a width of $\sigma \simeq 100$ ps. We noticed that the thermal broadening contributes only to $\sigma \sim 40$ ps; it is not yet clear about other sources of broadening, although 3-D effect may be the major player. For the low-intensity (~3×10^{14} W/cm^2) shot (50267) in which the simulated total yield agrees with the experiment, the measured neutron rate is reproduced by a *DRACO* simulation with a broadening of ~100 ps, as shown in Fig. 116.22(a). While, for the mid-intensity (~6×10^{14} W/cm^2) shot (49937) illustrated by Fig. 116.22(b), the simulated neutron rate is wider and higher than measurement, the total neutron

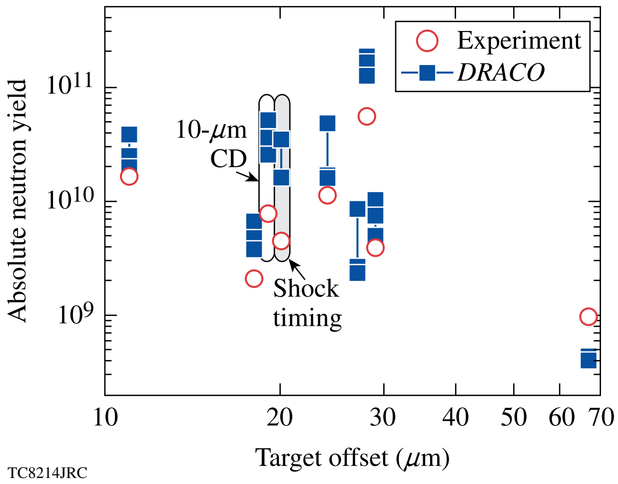

Figure 116.21
The absolute neutron yields are compared between experiments and *DRACO* simulations. Different phases are explored in the simulations. The two shots that are labeled are sensitive to either shock timing or thick-shell implosion for which high-ℓ-mode nonuniformities may be important.

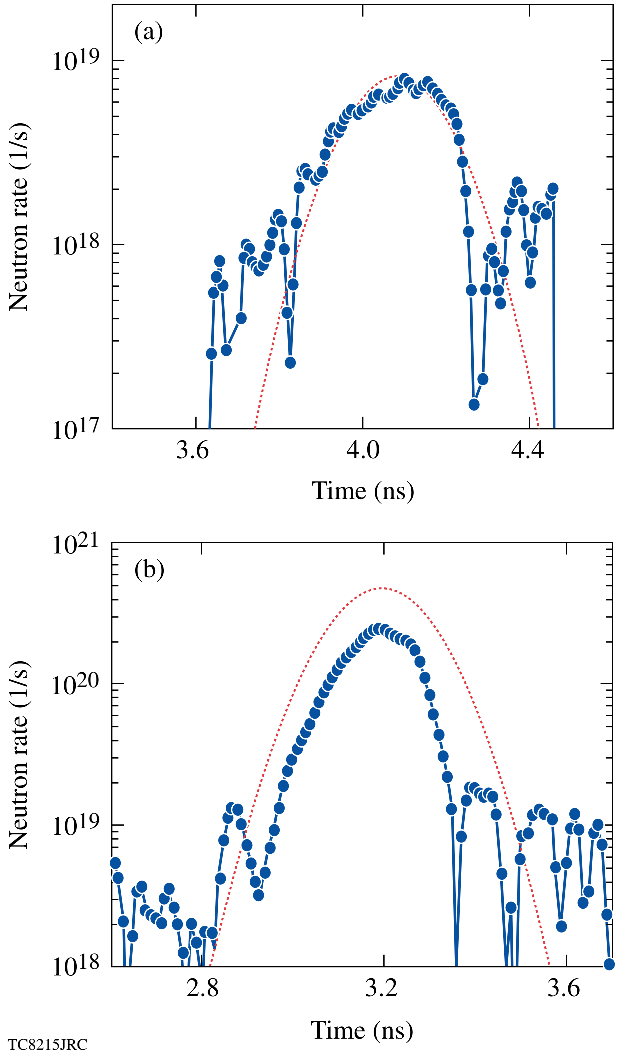

Figure 116.22
The neutron-rate comparison between experiments (circles) and simulations (lines) for (a) low-intensity (~3×10^{14} W/cm^2) shot 50267 and (b) mid-intensity (~6×10^{14} W/cm^2) shot 49937.

yield in the 2-D simulation is larger than the experimental value by almost a factor of 2. We believe that such a discrepancy may be within the uncertainties that the approximation of a 2-D code may cause in approaching the 3-D reality.

Conclusion

Using 2-D *DRACO* simulations, we have systematically investigated low-ℓ-mode perturbation effects on the neutron-yield degradation of direct-drive, low-adiabat ($\alpha \simeq 2$ to 3) cryogenic D_2 implosions on OMEGA. Despite the limitation of reduced dimensionality, our 2-D simulations show that for thin-shell (5-μm) targets, the yield degradation can be reasonably explained by the combined perturbations from the target offset, the low-ℓ-mode ice roughness, and low-ℓ-mode laser illumination nonuniformities. In terms of YOC, thick-shell targets generally do not perform as well as thin-shell targets using similar pulse shapes. We show that high-ℓ-mode perturbations such as laser imprinting may play a role in further reducing neutron yields in thick-shell cryogenic implosions. Besides the total neutron yield, the broadened neutron rates from 2-D simulations are also reasonably comparable to measurements, especially for low-intensity and thin-shell implosions. It should also be important to directly carry out such studies for DT implosions because extrapolating these D_2 results to the DT case is not straightforward since shock timing may play a different role. So far fewer DT shots have been conducted on OMEGA than D_2 shots. For these reasons, we leave such a similar investigation of DT implosions for future studies.

ACKNOWLEDGMENT

This work was supported by the U.S. Department of Energy Office of Inertial Confinement Fusion under Cooperative Agreement No. DE-FC52-08NA28302, the University of Rochester, and the New York State Energy Research and Development Authority. The support of DOE does not constitute an endorsement by DOE of the views expressed in this article.

REFERENCES

1. S. Atzeni and J. Meyer-ter-Vehn, *The Physics of Inertial Fusion: Beam Plasma Interaction, Hydrodynamics, Hot Dense Matter*, International Series of Monographs on Physics (Clarendon Press, Oxford, 2004); J. D. Lindl, *Inertial Confinement Fusion: The Quest for Ignition and Energy Gain Using Indirect Drive* (Springer-Verlag, New York, 1998).
2. S. E. Bodner *et al.*, Phys. Plasmas **7**, 2298 (2000).
3. J. D. Lindl, Phys. Plasmas **2**, 3933 (1995).
4. P. W. McKenty, V. N. Goncharov, R. P. J. Town, S. Skupsky, R. Betti, and R. L. McCrory, Phys. Plasmas **8**, 2315 (2001).
5. S. E. Bodner, Phys. Rev. Lett. **33**, 761 (1974); H. Takabe *et al.*, Phys. Fluids **28**, 3676 (1985); H. J. Kull and S. I. Anisimov, Phys. Fluids **29**, 2067 (1986); A. B. Bud'ko and M. A. Liberman, Fluids B **4**, 3499 (1992); V. V. Bychkov, S. M. Goldberg, and M. A. Liberman, Phys. Plasmas **1**, 2976 (1994); J. Sanz, Phys. Rev. Lett. **73**, 2700 (1994); J. G. Wouchuk and A. R. Piriz, Phys. Plasmas **2**, 493 (1995).
6. R. Betti, V. N. Goncharov, R. L. McCrory, P. Sorotokin, and C. P. Verdon, Phys. Plasmas **3**, 2122 (1996); R. Betti, V. N. Goncharov, R. L. McCrory, and C. P. Verdon, Phys. Plasmas **5**, 1446 (1998); V. N. Goncharov, P. McKenty, S. Skupsky, R. Betti, R. L. McCrory, and C. Cherfils-Clérouin, Phys. Plasmas **7**, 5118 (2000).
7. B. A. Remington *et al.*, Phys. Rev. Lett. **73**, 545 (1994); K. Shigemori *et al.*, Phys. Rev. Lett. **78**, 250 (1997); S. G. Glendinning, S. N. Dixit, B. A. Hammel, D. H. Kalantar, M. H. Key, J. D. Kilkenny, J. P. Knauer, D. M. Pennington, B. A. Remington, R. J. Wallace, and S. V. Weber, Phys. Rev. Lett. **78**, 3318 (1997); M. M. Marinak *et al.*, Phys. Rev. Lett. **80**, 4426 (1998); C. J. Pawley *et al.*, Phys. Plasmas **6**, 565 (1999).
8. D. L. Tubbs, C. W. Barnes, J. B. Beck, N. M. Hoffman, J. A. Oertel, R. G. Watt, T. Boehly, D. Bradley, P. Jaanimagi, and J. Knauer, Phys. Plasmas **6**, 2095 (1999); C. Cherfils *et al.*, Phys. Rev. Lett. **83**, 5507 (1999).
9. V. A. Smalyuk, T. R. Boehly, D. K. Bradley, V. N. Goncharov, J. A. Delettrez, J. P. Knauer, D. D. Meyerhofer, D. Oron, and D. Shvarts, Phys. Rev. Lett. **81**, 5342 (1998); J. P. Knauer, R. Betti, D. K. Bradley, T. R. Boehly, T. J. B. Collins, V. N. Goncharov, P. W. McKenty, D. D. Meyerhofer, V. A. Smalyuk, C. P. Verdon, S. G. Glendinning, D. H. Kalantar, and R. G. Watt, Phys. Plasmas **7**, 338 (2000); O. Sadot, V. A. Smalyuk, J. A. Delettrez, D. D. Meyerhofer, T. C. Sangster, R. Betti, V. N. Goncharov, and D. Shvarts, Phys. Rev. Lett. **95**, 265001 (2005); H. Azechi *et al.*, Phys. Rev. Lett. **98**, 045002 (2007).
10. F. J. Marshall, R. S. Craxton, J. A. Delettrez, D. H. Edgell, L. M. Elasky, R. Epstein, V. Yu. Glebov, V. N. Goncharov, D. R. Harding, R. Janezic, R. L. Keck, J. D. Kilkenny, J. P. Knauer, S. J. Loucks, L. D. Lund, R. L. McCrory, P. W. McKenty, D. D. Meyerhofer, P. B. Radha, S. P. Regan, T. C. Sangster, W. Seka, V. A. Smalyuk, J. M. Soures, C. Stoeckl, S. Skupsky, J. A. Frenje, C. K. Li, R. D. Petrasso, and F. H. Séguin, Phys. Plasmas **12**, 056302 (2005).
11. P. W. McKenty, T. C. Sangster, M. Alexander, R. Betti, R. S. Craxton, J. A. Delettrez, L. Elasky, R. Epstein, A. Frank, V. Yu. Glebov, V. N. Goncharov, D. R. Harding, S. Jin, J. P. Knauer, R. L. Keck, S. J. Loucks, L. D. Lund, R. L. McCrory, F. J. Marshall, D. D. Meyerhofer, S. P. Regan, P. B. Radha, S. Roberts, W. Seka, S. Skupsky, V. A. Smalyuk, J. M. Soures, K. A. Thorp, M. Wozniak, J. A. Frenje, C. K. Li, R. D. Petrasso, F. H. Séguin, K. A. Fletcher, S. Padalino, C. Freeman, N. Izumi, J. A. Koch, R. A. Lerche, M. J. Moran, T. W. Phillips, G. J. Schmid, and C. Sorce, Phys. Plasmas **11**, 2790 (2004).
12. R. Betti, K. Anderson, J. Knauer, T. J. B. Collins, R. L. McCrory, P. W. McKenty, and S. Skupsky, Phys. Plasmas **12**, 042703 (2005); J. P. Knauer, K. Anderson, R. Betti, T. J. B. Collins, V. N. Goncharov, P. W. McKenty, D. D. Meyerhofer, P. B. Radha, S. P. Regan, T. C. Sangster, V. A. Smalyuk, J. A. Frenje, C. K. Li, R. D. Petrasso, and F. H. Séguin, Phys. Plasmas **12**, 056306 (2005).
13. V. N. Goncharov, J. P. Knauer, P. W. McKenty, P. B. Radha, T. C. Sangster, S. Skupsky, R. Betti, R. L. McCrory, and D. D. Meyerhofer, Phys. Plasmas **10**, 1906 (2003).

14. K. Anderson and R. Betti, Phys. Plasmas **10**, 4448 (2003).

15. T. C. Sangster, V. N. Goncharov, P. B. Radha, V. A. Smalyuk, R. Betti, R. S. Craxton, J. A. Delettrez, D. H. Edgell, V. Yu. Glebov, D. R. Harding, D. Jacobs-Perkins, J. P. Knauer, F. J. Marshall, R. L. McCrory, P. W. McKenty, D. D. Meyerhofer, S. P. Regan, W. Seka, R. W. Short, S. Skupsky, J. M. Soures, C. Stoeckl, B. Yaakobi, D. Shvarts, J. A. Frenje, C. K. Li, R. D. Petrasso, and F. H. Séguin, Phys. Rev. Lett. **100**, 185006 (2008).

16. V. N. Goncharov, T. C. Sangster, P. B. Radha, R. Betti, T. R. Boehly, T. J. B. Collins, R. S. Craxton, J. A. Delettrez, R. Epstein, V. Yu. Glebov, S. X. Hu, I. V. Igumenshchev, J. P. Knauer, S. J. Loucks, J. A. Marozas, F. J. Marshall, R. L. McCrory, P. W. McKenty, D. D. Meyerhofer, S. P. Regan, W. Seka, S. Skupsky, V. A. Smalyuk, J. M. Soures, C. Stoeckl, D. Shvarts, J. A. Frenje, R. D. Petrasso, C. K. Li, F. Séguin, W. Manheimer, and D. G. Colombant, Phys. Plasmas **15**, 056310 (2008).

17. R. L. McCrory, D. D. Meyerhofer, R. Betti, R. S. Craxton, J. A. Delettrez, D. H. Edgell, V. Yu Glebov, V. N. Goncharov, D. R. Harding, D. W. Jacobs-Perkins, J. P. Knauer, F. J. Marshall, P. W. McKenty, P. B. Radha, S. P. Regan, T. C. Sangster, W. Seka, R. W. Short, S. Skupsky, V. A. Smalyuk, J. M. Soures, C. Stoeckl, B. Yaakobi, D. Shvarts, J. A. Frenje, C. K. Li, R. D. Petrasso, and F. H. Séguin, Phys. Plasmas **15**, 055503 (2008).

18. P. B. Radha, T. J. B. Collins, J. A. Delettrez, Y. Elbaz, R. Epstein, V. Yu. Glebov, V. N. Goncharov, R. L. Keck, J. P. Knauer, J. A. Marozas, F. J. Marshall, R. L. McCrory, P. W. McKenty, D. D. Meyerhofer, S. P. Regan, T. C. Sangster, W. Seka, D. Shvarts, S. Skupsky, Y. Srebro, and C. Stoeckl, Phys. Plasmas **12**, 056307 (2005); D. Keller, T. J. B. Collins, J. A. Delettrez, P. W. McKenty, P. B. Radha, B. Whitney, and G. A. Moses, Bull. Am. Phys. Soc. **44**, 37 (1999).

19. J. A. Marozas, F. J. Marshall, R. S. Craxton, I. V. Igumenshchev, S. Skupsky, M. J. Bonino, T. J. B. Collins, R. Epstein, V. Yu. Glebov, D. Jacobs-Perkins, J. P. Knauer, R. L. McCrory, P. W. McKenty, D. D. Meyerhofer, S. G. Noyes, P. B. Radha, T. C. Sangster, W. Seka, and V. A. Smalyuk, Phys. Plasmas **13**, 056311 (2006).

20. B. I. Bennett *et al.*, Los Alamos National Laboratory, Los Alamos, NM, Report LA-7130 (1978).

21. S. X. Hu, V. A. Smalyuk, V. N. Goncharov, J. P. Knauer, P. B. Radha, I. V. Igumenshchev, J. A. Marozas, C. Stoeckl, B. Yaakobi, D. Shvarts, T. C. Sangster, P. W. McKenty, D. D. Meyerhofer, S. Skupsky, and R. L. McCrory, Phys. Rev. Lett. **100**, 185003 (2008).

22. R. Cauble *et al.*, Phys. Rev. Lett. **80**, 1248 (1998).

23. W. F. Huebner *et al.*, Los Alamos National Laboratory, Los Alamos, NM, Report LA-6760-M (1977).

24. R. C. Malone, R. L. McCrory, and R. L. Morse, Phys. Rev. Lett. **34**, 721 (1975).

25. S. P. Regan, R. Epstein, V. N. Goncharov, I. V. Igumenshchev, D. Li, P. B. Radha, H. Sawada, W. Seka, T. R. Boehly, J. A. Delettrez, O. V. Gotchev, J. P. Knauer, J. A. Marozas, F. J. Marshall, R. L. McCrory, P. W. McKenty, D. D. Meyerhofer, T. C. Sangster, D. Shvarts, S. Skupsky, V. A. Smalyuk, B. Yaakobi, and R. C. Mancini, Phys. Plasmas **14**, 056305 (2007).

26. T. R. Boehly, E. Vianello, J. E. Miller, R. S. Craxton, T. J. B. Collins, V. N. Goncharov, I. V. Igumenshchev, D. D. Meyerhofer, D. G. Hicks, P. M. Celliers, and G. W. Collins, Phys. Plasmas **13**, 056303 (2006).

27. A. Sunahara, J. A. Delettrez, C. Stoeckl, R. W. Short, and S. Skupsky, Phys. Rev. Lett. **91**, 095003 (2003).

28. J. Delettrez, Can. J. Phys. **64**, 932 (1986); J. Delettrez, R. Epstein, M. C. Richardson, P. A. Jaanimagi, and B. L. Henke, Phys. Rev. A **36**, 3926 (1987).

29. V. A. Smalyuk, S. X. Hu, V. N. Goncharov, D. D. Meyerhofer, T. C. Sangster, D. Shvarts, C. Stoeckl, B. Yaakobi, J. A. Frenje, and R. D. Petrasso, Phys. Rev. Lett. **101**, 025002 (2008); V. A. Smalyuk, S. X. Hu, V. N. Goncharov, D. D. Meyerhofer, T. C. Sangster, C. Stoeckl, and B. Yaakobi, Phys. Plasmas **15**, 082703 (2008).

30. T. R. Boehly, D. L. Brown, R. S. Craxton, R. L. Keck, J. P. Knauer, J. H. Kelly, T. J. Kessler, S. A. Kumpan, S. J. Loucks, S. A. Letzring, F. J. Marshall, R. L. McCrory, S. F. B. Morse, W. Seka, J. M. Soures, and C. P. Verdon, Opt. Commun. **133**, 495 (1997).

31. Y. Lin, T. J. Kessler, and G. N. Lawrence, Opt. Lett. **20**, 764 (1995).

32. T. R. Boehly, V. A. Smalyuk, D. D. Meyerhofer, J. P. Knauer, D. K. Bradley, R. S. Craxton, M. J. Guardalben, S. Skupsky, and T. J. Kessler, J. Appl. Phys. **85**, 3444 (1999).

33. S. Skupsky, R. W. Short, T. Kessler, R. S. Craxton, S. Letzring, and J. M. Soures, J. Appl. Phys. **66**, 3456 (1989); J. E. Rothenberg, J. Opt. Soc. Am. B **14**, 1664 (1997); S. P. Regan, J. A. Marozas, J. H. Kelly, T. R. Boehly, W. R. Donaldson, P. A. Jaanimagi, R. L. Keck, T. J. Kessler, D. D. Meyerhofer, W. Seka, S. Skupsky, and V. A. Smalyuk, J. Opt. Soc. Am. B **17**, 1483 (2000).

34. D. H. Edgell, W. Seka, R. S. Craxton, L. M. Elasky, D. R. Harding, R. L. Keck, and M. D. Wittman, Fusion Sci. Technol. **49**, 616 (2006).

35. T. C. Sangster, R. Betti, R. S. Craxton, J. A. Delettrez, D. H. Edgell, L. M. Elasky, V. Yu. Glebov, V. N. Goncharov, D. R. Harding, D. Jacobs-Perkins, R. Janezic, R. L. Keck, J. P. Knauer, S. J. Loucks, L. D. Lund, F. J. Marshall, R. L. McCrory, P. W. McKenty, D. D. Meyerhofer, P. B. Radha, S. P. Regan, W. Seka, W. T. Shmayda, S. Skupsky, V. A. Smalyuk, J. M. Soures, C. Stoeckl, B. Yaakobi, J. A. Frenje, C. K. Li, R. D. Petrasso, F. H. Séguin, J. D. Moody, J. A. Atherton, B. D. MacGowan, J. D. Kilkenny, T. P. Bernat, and D. S. Montgomery, Phys. Plasmas **14**, 058101 (2007).

36. V. A. Smalyuk, D. Shvarts, R. Betti, J. A. Delettrez, D. H. Edgell, V. Yu. Glebov, V. N. Goncharov, R. L. McCrory, D. D. Meyerhofer, P. B. Radha, S. P. Regan, T. C. Sangster, W. Seka, S. Skupsky, C. Stoeckl, B. Yaakobi, J. A. Frenje, C. K. Li, R. D. Petrasso, and F. H. Séguin, Phys. Rev. Lett. **100**, 185005 (2008).

37. D. H. Kalantar, M. H. Key, L. B. Da Silva, S. G. Glendinning, B. A. Remington, J. E. Rothenberg, F. Weber, S. V. Weber, E. Wolfrum, N. S. Kim, D. Neely, J. Zhang, J. S. Wark, A. Demir, J. Lin, R. Smith, G. J. Tallents, C. L. S. Lewis, A. MacPhee, J. Warwick, and J. P. Knauer, Phys. Plasmas **4**, 1985 (1997); M. Nakai *et al.*, Phys. Plasmas **9**, 1734 (2002); V. A. Smalyuk, O. Sadot, J. A. Delettrez, D. D. Meyerhofer, S. P. Regan, and T. C. Sangster, Phys. Rev. Lett. **95**, 215001 (2005); V. A. Smalyuk, V. N. Goncharov, K. S. Anderson, R. Betti, R. S. Craxton, J. A. Delettrez, D. D. Meyerhofer, S. P. Regan, and T. C. Sangster, Phys. Plasmas **14**, 032702 (2007).

38. R. J. Taylor, A. L. Velikovich, J. P. Dahlburg, and J. H. Gardner, Phys. Rev. Lett. **79**, 1861 (1997); A. L. Velikovich *et al.*, Phys. Plasmas **5**, 1491 (1998); V. N. Goncharov, S. Skupsky, T. R. Boehly, J. P. Knauer, P. McKenty, V. A. Smalyuk, R. P. J. Town, O. V. Gotchev, R. Betti, and D. D. Meyerhofer, Phys. Plasmas **7**, 2062 (2000); P. B. Radha, V. N. Goncharov, T. J. B. Collins, J. A. Delettrez, Y. Elbaz, V. Yu. Glebov, R. L. Keck, D. E. Keller, J. P. Knauer, J. A. Marozas, F. J. Marshall, P. W. McKenty, D. D. Meyerhofer, S. P. Regan, T. C. Sangster, D. Shvarts, S. Skupsky, Y. Srebro, R. P. J. Town, and C. Stoeckl, Phys. Plasmas **12**, 032702 (2005).

Al 1*s*–2*p* Absorption Spectroscopy of Shock-Wave Heating and Compression in Laser-Driven Planar Foil

Introduction

A physical understanding of the shock-wave heating, radiative heating, and heating by energetic electrons in direct-drive inertial confinement fusion (ICF) is required to control the pressure in the main fuel layer.[1] A direct-drive hot-spot ignition ICF target consists of a spherical cryogenic fuel shell of deuterium and tritium surrounded by a thin plastic layer.[2] It is illuminated by symmetrically arranged intense laser beams having a temporal laser shape of a low-intensity foot followed by the gradual increase to a high-intensity main drive. The foot intensity launches a weak shock into the target, and the ramp of the laser intensity launches multiple shock waves with increasing strengths (compression wave) to isentropically compress the shell and implode the target to form a central hot spot with sufficient fuel areal density and temperature for ignition. The shell entropy or adiabat (α), defined as the ratio of the pressure in the fuel layer to the Fermi pressure, relates to the ICF target performance and the stabilization of Rayleigh–Taylor (RT) hydrodynamic instabilities.[3] The minimum energy required for ignition scales to $E_{\mathrm{ig}} \sim \alpha^{1.88}$, while the ablation velocity that stabilizes the RT growth is proportional to $V_a \sim \alpha^{3/5}$ (Ref. 3). Therefore, a successful direct-drive ICF implosion design with energy gain creates an adiabat in the shell that strikes a balance between the laser-energy requirement and the target stability.

The shock wave launched by laser ablation is the dominant heating mechanism that sets the shell adiabat. After a coronal plasma is formed, the ablation process is driven by the energy flow via electron thermal transport from the critical density and the ablation surface (conduction zone). The incident laser can propagate into the plasma up to the critical density where the laser frequency is equal to the plasma frequency $\left(n_{\mathrm{c}} = 1.1 \times 10^{21} / \lambda_{\mu\mathrm{m}}^2\right)$. The laser energy that is absorbed near the critical-density surface is thermally transported by electrons to the ablation surface where the outer surface of the target is ablated and a shock wave is launched inward. The shell accelerates via the rocket effect. Modeling of electron thermal transport in the conduction zone is challenging because the steep temperature gradient in the plasma causes the classical Spitzer–Härm thermal conductivity[4] to break down. The 1-D hydrodynamics code *LILAC*[5] uses a flux-limited thermal transport model[6] to calculate the heat flux. It takes the minimum value of the heat flux calculated with either the classical Spitzer–Härm thermal conductivity ($q_{\mathrm{SH}} = \kappa \nabla T_{\mathrm{e}}$, where κ is the Spitzer conductivity)[4] or an artificially inhibited, free-streaming heat flux ($q_{\mathrm{FS}} = n_{\mathrm{e}} T_{\mathrm{e}} v_{\mathrm{th}}$, where v_{th} is the thermal electron velocity) [i.e., $q = \min\left(q_{\mathrm{SH}}, f \bullet q_{\mathrm{FS}}\right)$, where f is the empirically determined flux limiter]. The typical value of f for simulations of direct-drive experiments is $0.04 < f < 0.1$. Although simulations with a constant flux limiter and experiments agree well, simulations with the same value of f do not consistently match to the all experimental data.[7] For instance, shock-velocity measurements in CH foils on OMEGA[8] agree with the simulation with $f = 0.06$, while the Richtmyer–Meshkov-growth measurements are in agreement with $f = 0.1$ (Ref. 9). A nonlocal electron-transport model developed by Goncharov[10] has shown consistent agreement between these two experiments and the simulations.[9] The nonlocal model acts like a time-dependent flux limiter and includes the transport of high-energy electrons in the tail of the electron-velocity distribution. X-ray radiation from the corona and suprathermal (energetic) electrons generated from two-plasmon-decay (TPD) instability[11] have been identified as possible target-heating sources.[12] These mechanisms could preheat the target before the shock-wave heating occurs. This preheating could increase the shell adiabat, reduce the compressibility of the fuel, and lead to a degradation of the ICF target performance.

The plasma conditions of a direct-drive, shock-wave–heated, compressed target are predicted to be in a warm-dense-matter (WDM)[13] regime where the degree of degeneracy and the electron–electron coupling parameter[14] are of the order of unity and the ion–ion coupling parameter exceeds 1 (Ref. 15). The electron–electron coupling parameter Γ_{ee} is defined as the ratio of Coulomb potential between free electrons to the average kinetic energy of the free electrons [$\Gamma_{\mathrm{ee}} = e^2/dk_{\mathrm{B}}T_{\mathrm{e}}$, where $d = (3/4\pi n_{\mathrm{e}})^{1/3}$ is the average interparticle spacing]. The degree of degeneracy Θ is the ratio of the Fermi temperature to the electron temperature $\left(\Theta = T_{\mathrm{F}} / T_{\mathrm{e}}\right)$. Diagnostic techniques to probe plasma conditions in the WDM regime are limited because the electron temperature of the plasma is too low for it to emit x rays and its density (above solid density) is too high to be probed with optical lasers for Thomson-scattering measurements.[16] These extreme conditions have been diagnosed with x-ray scattering[17,18] and x-ray absorption spectroscopy.[19,20] Spectrally resolved x-ray scattering has been demonstrated to probe these plasmas created with radiative heating[17,21] and direct-drive, shock-wave heating.[22] Scattering experiments require a relatively large amount of matter to scatter a sufficient number of incident x rays, limiting its spatial resolution. Although it requires a buried mid-Z tracer layer in the shock-wave–heated foil, x-ray absorption spectroscopy measurements can provide time-resolved local measurements. The temporal and spatial resolution of the time-resolved x-ray absorption spectroscopy is sufficient to resolve the shock-wave heating from heat-front penetration.

Local plasma conditions during shock-wave heating and compression, as well as the timing of heat-front penetration, are diagnosed with time-resolved Al 1*s*–2*p* absorption spectroscopy of planar plastic foils with a buried tracer layer of Al. Plastic foils are surrogates for cryogenic fuel layers. The objective of this article is to test electron-thermal-transport models in *LILAC* by comparing the predicted shock-wave–heated plasma conditions with measurements and to determine if additional heating due to energetic electrons or x-ray radiation from the coronal plasma is significant. The CH/Al/CH drive foil was directly irradiated with peak intensities of 10^{14} to 10^{15} W/cm^2 and probed with a point source of Sm backlighter irradiated with laser intensities of ~10^{16} W/cm^2 (Ref. 19). The measured Al 1*s*–2*p* spectra were analyzed with the atomic physics code *PrismSPECT*[23] to infer T_e and ρ in the buried Al layer, assuming uniform plasma conditions during the shock-wave heating and compression, and to determine when the heat front penetrated the Al layer. Strong shock waves and isentropic compression were studied. This is the first observation of plasma conditions created with a compression wave.[24] The level of shock-wave heating and timing of heat-front penetration inferred from the experiments were compared with the post-processed *LILAC* simulations using the time-dependent atomic physics code *Spect3D*.[25] The shock-wave heating and heat-front penetration predicted by *LILAC* using $f = 0.06$ or the nonlocal model agree with experimental results for times when the shock is transiting the foil. At late times in the drive, observed discrepancies between the predicted and measured plasma conditions in the Al layer are attributed to reduced radiative heating due to lateral heat flow in the corona. Therefore, preheat due to energetic electrons near the end of the laser drive could not be resolved in this experiment.

The following sections of this article (1) describe the setup of the x-ray absorption spectroscopy experiment on OMEGA; (2) present 1-D *LILAC* simulations and absorption spectra calculated from the post-processed *LILAC* using *Spect3D*; (3) present measured streak spectra and analyses of Al 1*s*–2*p* absorption spectra with *PrismSPECT*; (4) discuss and present results for square and shaped laser drives; (5) briefly mention future work; and (6) summarize results.

Experiment

The experiment consists of three main components: a point-source Sm backlighter, a CH/Al/CH drive foil, and a Bragg crystal spectrometer, with a schematic (not drawn to scale) shown in Fig. 116.23. The relative alignment of these three components is crucial for the success of the experiment. A 50-μm planar CH foil with a 1- or 2-μm buried Al layer was irradiated with up to 21 OMEGA laser beams[8] that were smoothed with distributed phase plates (DPP's),[26] 1-THz, 2-D smoothing by spectral dispersion (SSD),[27] and polarization smoothing (PS).[28] The overlapped intensity was uniform

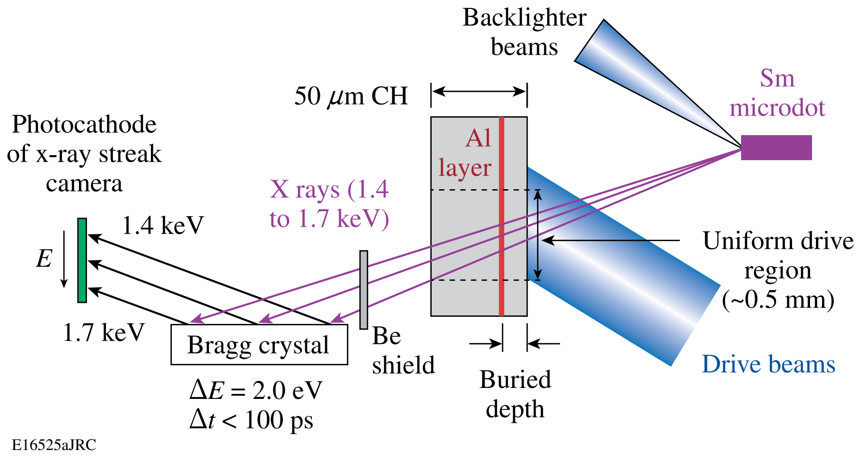

Figure 116.23
A schematic of the Al 1*s*–2*p* absorption spectroscopy experiment showing a point-source Sm backlighter, a plastic drive foil with a buried Al layer, a Be blast shield, and a Bragg crystal spectrometer coupled to an x-ray streak camera.

over a 0.5-mm-diam spot and peak intensities in the range of 10^{14} to 10^{15} W/cm^2. The overall thickness of the drive foil was chosen based on competing considerations of hydrodynamic instabilities and transmission of the target to ~1.5-keV x rays. Hydrodynamic instabilities due to target acceleration could compromise the spatial resolution of the measurement by mixing the Al layer with the CH.[29] Since the acceleration phase is delayed as the target thickness is increased, thicker targets are less susceptible to hydrodynamic instabilities than thinner ones; however, thicker targets attenuate the x-ray backlighter more than thinner ones. Choosing a drive foil with a 50-μm thickness was a good compromise. The buried depth of the layer was varied to probe the plasma conditions in different regions of the target. Al 1*s*–2*p* absorption spectroscopy of the drive foil was performed with a point-source Sm microdot backlighter irradiated with six tightly focused (~100-μm spot) laser beams having an overlapped intensity of ~10^{16} W/cm^2. This creates the well-defined Bragg reflection geometry necessary for this experiment. Source broadening can degrade the spectral resolution of the measurement. In contrast to the point-source Sm backlighter, the CH coronal plasma of the drive foil having an ~1-mm diameter does not create a well-defined Bragg reflection geometry. The coronal plasma emission contributes a background signal that degrades the contrast of the absorption features. The size of the Sm backlighter source was monitored with an x-ray framing camera and found to be less than 100 μm. The Sm M-shell emission provided a relatively smooth continuous spectrum in the 1.4- to 1.7-keV range, which overlaps the Al 1*s*–2*p* absorption features around 1.5 keV and probes the uniformly driven portion of the target (see Fig. 116.23).[20] The transmitted spectrum was recorded with an x-ray streak camera[30] outfitted with a Bragg crystal spectrometer that used a flat RbAP crystal[31] to disperse the spectrum onto a low-density (fluffy) CsI photocathode.[32] Each of the three components was positioned independently to ensure that the driven portion of the target was being probed with the Al 1*s*–2*p* absorption spectroscopy. Since alignment of the experiment was based on mechanical references, it was extremely reproducible. In a contrast measurement calibration using a Pb slit plate on the x-ray photocathode of the streaked x-ray spectrometer, a spectral resolution of 2.0 eV ($E/\mathrm{d}E \sim 750$) was estimated from the sharpness of the measured step function.[33] The dynamic range of the x-ray streak camera was measured to be ~50. The relative time axis of the x-ray streak spectra was established using the UV timing fiducial on OMEGA. The x-ray streak camera has a uniform streak speed with an average speed of 115 ps/mm.[34] It uses a microchannel-plate (MCP)[35] image intensifier, and the streaked spectrum is recorded on Kodak TMAX 3200 film. The film is converted from optical density to a linear intensity scale using the step wedge imprinted on each roll of film. The frequency-dependent transmission of a shocked Al layer was obtained from the ratio of transmitted Sm spectra through CH drive foils with and without an Al tracer layer.

One-Dimensional Simulations

Direct-drive plastic foils with a buried Al tracer layer were simulated with the 1-D hydrodynamics code *LILAC*[5] using either a flux-limited[6] or a nonlocal thermal transport model.[10] A flux-limited transport model calculates heat flux with either the classical Spitzer thermal conduction ($q_{\mathrm{SH}} = \kappa \nabla T_{\mathrm{e}}$) or a fraction of free-streaming flux ($q_{\mathrm{FS}} = n_{\mathrm{e}} T_{\mathrm{e}} v_{\mathrm{th}}$). The Spitzer transport model is valid only when the mean free path of electrons (λ_{e}) is much shorter than the electron-temperature scale length $\left[L_T = T_{\mathrm{e}} \big/ \left(\mathrm{d}T_{\mathrm{e}} / \mathrm{d}x\right)\right]$. When λ_{e} is comparable to L_T such as in a conduction zone with a steep temperature gradient, a flux-limited free-streaming flux ($q = f \bullet q_{\mathrm{FS}}$) is used to model the heat flux. The flux limiter was either 0.06 (lower heat flux) or 0.1 (higher heat flux) in these simulations. A higher flux limiter in the model allows more energy to flow from the critical density to the ablation surface, producing a stronger shock wave compared to a flux limiter with a lower value. A nonlocal model developed by Goncharov[10] does not require a flux limiter to calculate heat flux. It solves a simplified Boltzmann equation using the Krook collision model and calculates heat flux using a convolution with the Spitzer heat flux and a delocalization kernel. This nonlocal treatment of the thermal transport includes time dependence of a reduced heat flux from the Spitzer model in plasmas with a steep temperature gradient and nonlocal preheat due to long-range electrons from the coronal plasma. Details of the nonlocal electron-transport model are described in Refs. 10 and 36. The radiation transport is modeled in *LILAC* with multigroup diffusion using the Los Alamos National Laboratory astrophysical tables[37] for the opacities. The equation of state (EOS) is modeled using the *SESAME* tables[38] for both CH and Al. The serial numbers of *SESAME* EOS used in *LILAC* for these experiments are 7593 for CH and 3720 for Al.

Figure 116.24 shows the 1-D spatial profiles of the electron temperature and mass density predicted by *LILAC* in a drive foil during shock-wave heating and heat-front penetration using a flux limiter of 0.06. As the shock wave launched by laser ablation propagates through the Al layer, it compresses the layer and creates uniform plasma conditions in the target behind the shock wave [Fig. 116.24(a)]. The predicted electron temperatures due to shock-wave heating in the experiment are in the range of 10 eV to 40 eV. The uniform plasma approximation is valid until the ablation surface reaches the Al. Once the heat front penetrates into the Al layer, it creates strong gradients of T_e and ρ as shown in Fig. 116.24(b). The *LILAC* predictions are post-processed with *Spect3D*[25] to simulate the Al 1*s*–2*p* absorption spectral line shapes. Both *Spect3D* and the atomic physics code *PrismSPECT*[23] use level populations of detailed configuration accounting (DCA) to compute absorption spectra. The Stark-broadened line shapes are calculated using the Multi-Electron Radiator Line Shape (MERL) code.[39] MERL uses the adjustable parameter exponential approximation (APEX)[40] for ion microfield calculation and a quantum-mechanical relaxation approximation for electron broadening.[41] Figures 116.24(c) and 116.24(d) show Al absorption spectra post-processed *LILAC* profiles of uniform conditions and strong gradients shown in Figs. 116.24(a) and 116.24(b). The spatial profiles of the electron temperature and density from *LILAC* simulations are taken into account in calculating the Al absorption spectra. As shown in Fig. 116.24(c), a few absorption features (F-like, O-like, and N-like features) are created in the uniform condition, while the strong T_e gradient in the Al creates a wide range of 1*s*–2*p* absorption features from F-like to Li-like in Fig. 116.24(d). Both synthetic and measured absorption spectra were analyzed with *PrismSPECT* to infer T_e and ρ during the shock-wave heating and to establish a range of upper and lower limits of T_e during heat-front penetration, as described in the next section.

Analysis of Measured Absorption Spectra

Figure 116.25 shows examples of the x-ray streak images recorded from CH targets (a) with and (b) without an Al layer (shot 48232 and 48233, respectively). The drive and backlighter beams were co-timed at $t = 0$ ns. The drive foil was irradiated with a shaped laser pulse having a foot intensity of 3×10^{14} W/cm^2 and a peak intensity of 8×10^{14} W/cm^2. The time

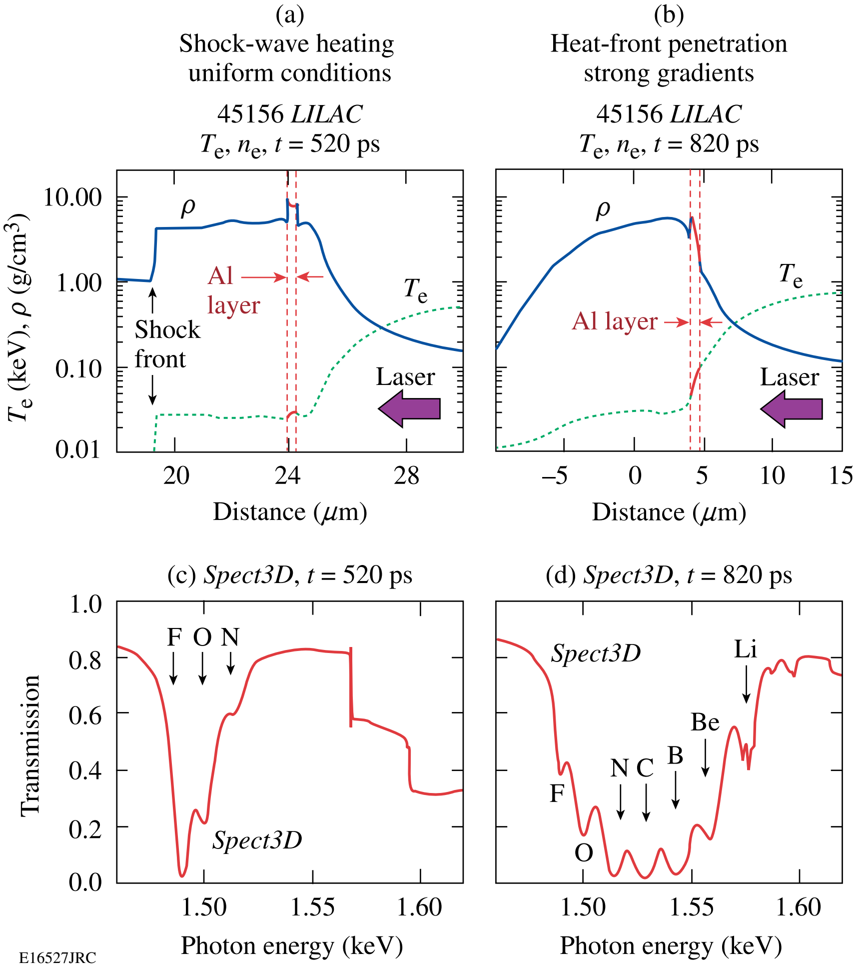

Figure 116.24
Simulated spatial profiles of electron temperature (dotted) and mass density (solid) during (a) shock-wave heating and (b) heat-front penetration. The Al absorption spectra simulated by post-processing *LILAC* with *Spect3D* are shown in (c) and (d). The prominent Al 1*s*–2*p* absorption features are identified.

axis of the streak images was established based on the average measured sweep speed (115 ps/mm) of the x-ray streak camera. The time $t = 0$ ns represents the time on the rising edge of the x-ray intensity when each measured streak reached 2% of the peak intensity. The absolute timing of the measured x-ray streak was established by synchronizing the measured onset of shock-wave heating in the buried Al layer with that predicted by the *LILAC* simulation. The experimental signature of shock-wave heating in the Al layer is a shift in the photon energy of the Al K edge at 1.56 keV. If the electron temperature is above ~10 eV, the shifting K edge is accompanied by the appearance of the F-like Al 1*s*–2*p* absorption. In this experiment, the shifting K edge was used as a timing fiducial in the measured spectra for synchronization with the *LILAC* simulations. The difference in shock timings predicted by *LILAC* using $f = 0.06$ and $f = 0.1$ is less than the experimental temporal resolution of 60 ps. A good timing fiducial around $t = 0$ in the x-ray streak does not exist for most of the drive conditions studied because the initial x-ray emission from the coronal plasma of the drive foil is usually below detection threshold of the streaked x-ray spectrometer. The spectral dispersion for the streak data was calibrated using the K-shell emission from a point-source Mg backlighter. Shortly after the laser irradiates the drive foil, the shock heats and compresses the buried Al layer. As shown in Fig. 116.25(a), the experimental signature of the shock-wave heating is the appearance of the Al 1*s*–2*p*, F-like absorption feature and a blue shift in the Al K edge. When the heat front penetrates the Al layer, a wide range of the higher charge states up to the Be-like feature appears as seen after 1.0 ns. None of these features appear in Fig. 116.25(b) since the CH drive foil does not have an Al layer. The streak images were temporally binned and averaged over a temporal resolution of 60 ps. The apparent absorption-like feature observed at 1.58 keV is an artifact caused by a portion of the photocathode with low sensitivity for this particular shot.

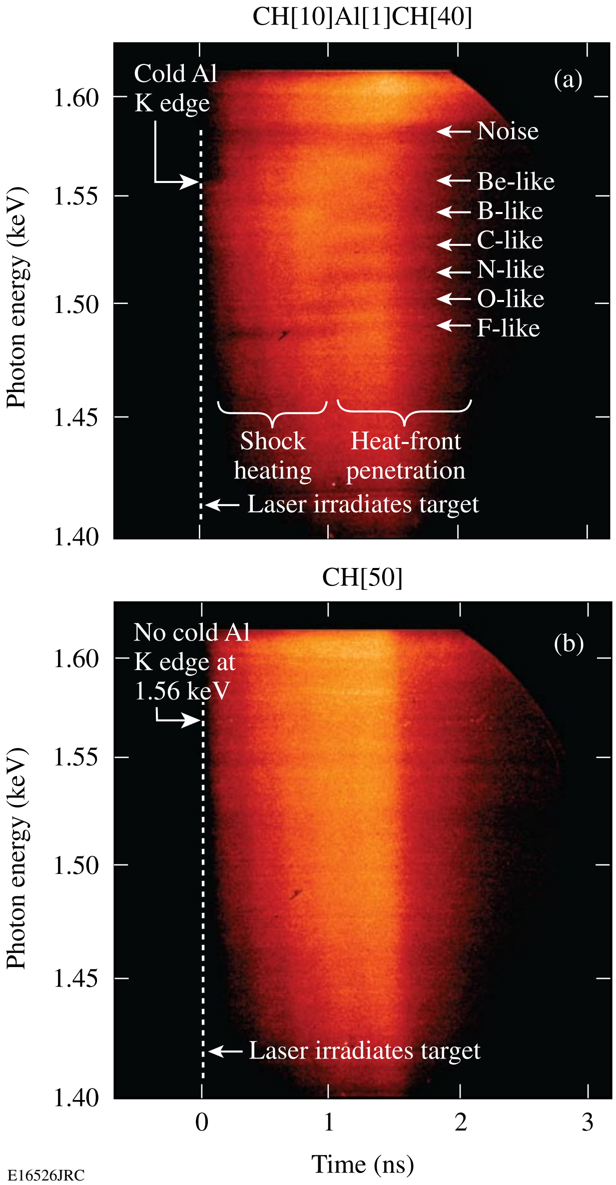

Figure 116.25
Measured streak images from (a) a CH foil with a buried Al layer and (b) a pure CH foil driven by the $\alpha = 3$ drive with a peak intensity of 8×10^{14} W/cm^2.

An *in-situ* calibration of the x-ray streak spectrometer was performed to eliminate contamination of background light from the measured intensity signals. An examination of the measured cold Al K edge at 1.56 keV from an undriven CH/Al/CH foil showed a degradation in contrast compared to the modeled contrast of the cold Al K edge.[42] Since there is no coronal plasma emission from the undriven target and the dynamic range of the detector (~50) does not limit the measured contrast, the cause of the degraded contrast was attributed to secondary fluorescence that occurs when intense x rays interact with a Bragg crystal or device parts of the spectrometer.[43,44] The fluorescence level was assumed to be proportional to a fraction of peak x-ray intensity and to contribute a constant background across the x-ray photocathode. This background light must be subtracted from the measured signals to calculate the transmission of the CH/Al/CH drive foil. There are two sources of background light for a driven target shot: x-ray fluorescence of the Bragg crystal and x-ray emission from the coronal plasma of the drive foil. For a driven target shot, the level of background was estimated prior to the shock arrival at the buried Al layer based on corrections of the measured contrast at the K edge. After the shock propagated through the Al layer, the total background level from the coronal plasma and x-ray fluorescence was estimated based on comparisons of measured Al 1*s*–2*p* absorption to *LILAC*/*Spect3D* predictions. A constant background was subtracted for both the absorption and the incident spectra.

The measured spectra with background corrections were fit with *PrismSPECT*[23] assuming uniform conditions for various combinations of T_e and ρ. *PrismSPECT* is a nonlocal-thermodynamic-equilibrium (NLTE), collisional-radiative code that calculates the absorption spectrum assuming a uniform slab plasma for a given T_e, ρ, and ΔL. The product of ρ and ΔL (areal density) for an Al layer is assumed to be conserved throughout the planar experiment. Figure 116.26 shows measured spectra fit with *PrismSPECT* at (a) $t = 360$ ps during shock-wave heating and (b) $t = 1224$ ps during heat-front penetration for shot 48232 shown in Fig. 116.25. The best fit to the measured spectra during shock-wave heating was determined based on a least-squares-fitting routine, which inferred T_e and ρ simultaneously. The plasma condition inferred from the fit in Fig. 116.26(a) is 22 eV (±2 eV) and 6 g/cm^3 (±3 g/cm^3). The ionization caused by shock-wave heating and compression can be obtained with different combinations of electron temperature and density; therefore, the inference of electron temperature is limited by the uncertainty in compressed density. The error estimates from the spectral-fitting routine were determined by doubling the minimum χ-squared value.[45] The uncertainty of the inference of T_e due to background subtraction has been considered by varying the estimated background levels for the drive intensity of 1×10^{14} W/cm^2 (Ref. 33). The uncertainties in the T_e and ρ inferences in this experiment were estimated to be ~10% and ~20% to 50%, respectively.

The experimental signature of heat-front penetration is the onset of absorption from a wide range of higher charge states of Al. The measured spectra at the time of the heat-front penetration were qualitatively compared to the product of two calculated spectra as shown in Fig. 116.26(b). Because of the strong gradients in T_e and ρ when heat front penetrates, the absorption spectrum cannot be fit by a calculated spectrum with a single T_e and ρ. Spatially resolved measurements of electron-temperature and density profiles in the conduction zone are challenging. To identify the time of heat-front penetration, it was assumed that the Al layer has two regions that determine a range of the plasma conditions: (1) a lower-density and higher-temperature region characteristic of matter ablated into the conduction zone, and (2) a higher-density and lower-temperature region characteristic of the shock-heated and compressed matter. The inferred ranges of T_e and ρ from the measured spectrum shown in Fig. 116.26(b) are 47 eV < T_e < 70 eV and 2.5 g/cm^3 < ρ < 3.5 g/cm^3. The initial areal density ($\rho\Delta L$) was equally divided into two parts. The total spectrum is a product of the calculated transmission spectra from each region and can be compared with the overall shape of measured spectra to roughly deter-

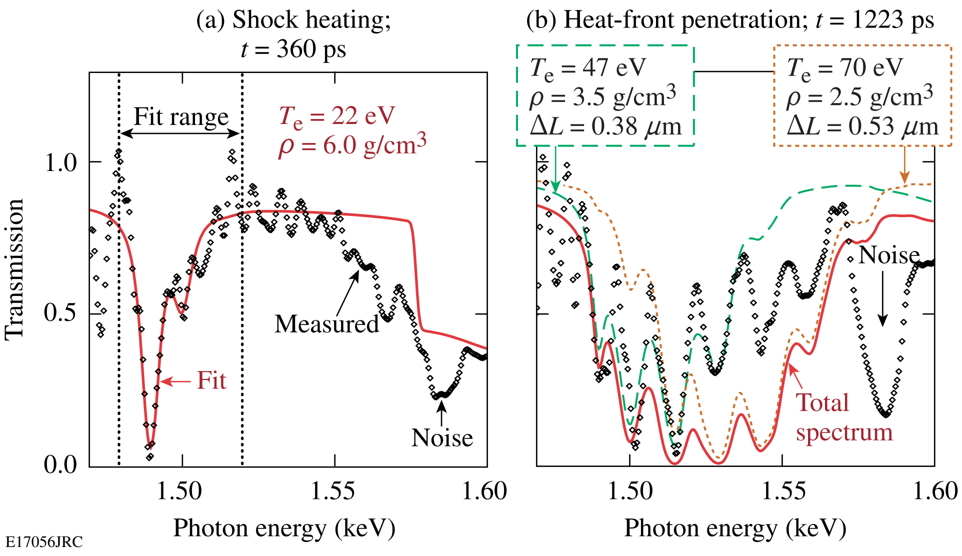

Figure 116.26
(a) A measured spectrum during shock-wave heating (diamond) and fit (thick black curve) obtained in a least-squares-fitting routine to infer T_e of 22 eV and ρ of 6.0 g/cm^3. (b) A measured spectrum during heat-front penetration and spectral analysis using two calculated spectra to determine upper and lower limits of T_e for shot 48232. The modeled spectra are calculated with $T_e = 47$ eV and $\rho = 3.5$ g/cm^3 for the lower limit (thin dashed black curve) and $T_e = 70$ eV and $\rho = 2.5$ g/cm^3 for the upper limit (thin dotted black curve). The total modeled spectrum (thick solid black curve) is obtained by the product of the two spectra.

mine the upper and lower limits of T_e. Although this is not a quantitative fitting, the procedure satisfies the experimental objective to identify the time of heat-front penetration by finding when a wide range of temperatures (greater than the shock-heated temperature) exists in the Al layer.

Results and Discussion

Time-resolved electron temperatures inferred from the experiments during shock-wave heating and heat-front penetration were compared with post-processed *LILAC* simulations using a nonlocal thermal-transport model,[10] as well as flux-limited models[5] with $f = 0.06$ and $f = 0.1$. The laser pulse shapes used in the experiment—1 ns square (1×10^{15} W/cm^2 and 4×10^{14} W/cm^2), 3 ns square (1×10^{14} W/cm^2), $\alpha = 3$ (peak intensities of 8×10^{14} W/cm^2 and 1×10^{15} W/cm^2), and $\alpha = 2$ pulses—are shown in Fig. 116.27. The target adiabat in this experiment is predicted to be $1.5 < \alpha < 5$. Square laser pulses launch a single shock wave through a CH/Al/CH foil, and a shell adiabat of 5 is created by the 1-ns square pulse with a peak intensity of 1×10^{15} W/cm^2. A shaped laser pulse drive with a low-intensity foot pulse that gradually increases to a constant high-intensity main drive produces a lower adiabat in the target. The adiabat of a CH/Al/CH foil driven with a shaped pulse is set by the foot intensity. The slowly rising intensity of the main drive produces a series of hydrodynamic waves as the drive pressure slowly increases (i.e., a compression wave). Ideally, isentropic target compression is achieved with a shaped laser pulse. The observation of plasma conditions created with a weak shock and a compression wave in direct-drive planar targets is presented in this section. The laser pulse shape and the number of drive beams were selected to achieve a desired target adiabat α and peak intensity. The buried depth of the Al tracer layer was varied to probe different portions of the target.

1. Plasma Conditions Achieved with Square Laser Pulses

Peak laser intensities of 1×10^{14} W/cm^2, 4×10^{14} W/cm^2, and 1×10^{15} W/cm^2 were generated for the square laser pulses using either a 1-ns or 3-ns square laser pulse shape. *LILAC* predicted that the pressures of the single shock wave launched by these drive intensities were 15, 40, and 70 Mbar, respectively. The Sm backlighter target was irradiated with the same pulse shape as the CH/Al/CH drive foil. The absorption spectra recorded just after shock-wave heating are compared with the fitted line shapes in Fig. 116.28. The Al layer was buried at 10 μm for each of these shots. The lowest-intensity shot had an Al thickness of 2 μm and the other shots had an Al thickness of 1 μm. This improved the signal-to-noise ratio of the absorption spectra recorded with the lowest-intensity drive. As drive intensity is increased, the shock-wave pressure increases and higher Al charge states are observed in 1*s*–2*p* absorption. Only the F-like charge state was recorded for the lowest drive intensity (1×10^{14} W/cm^2), while F-like, O-like, N-like, and C-like charge states are observed for

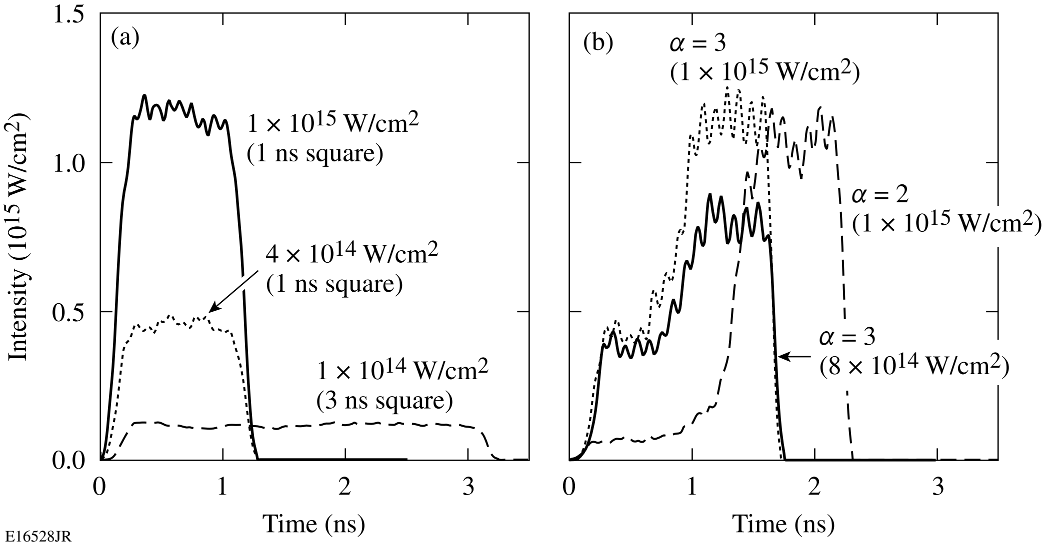

Figure 116.27
Laser pulse shapes for (a) square pulse shapes (1 ns square and 3 ns square) and (b) shaped pulse shapes ($\alpha = 3$ and $\alpha = 2$). The peak intensities for the square laser pulses are 1×10^{14} W/cm^2 (dashed), 4×10^{14} W/cm^2 (dotted), and 1×10^{15} W/cm^2 (solid). For the $\alpha = 3$ drives, the peak intensities are 8×10^{14} W/cm^2 (solid) and 1×10^{15} W/cm^2 (dotted); for the $\alpha = 2$ drives, peak intensity is 1×10^{15} W/cm^2 (dashed curve).

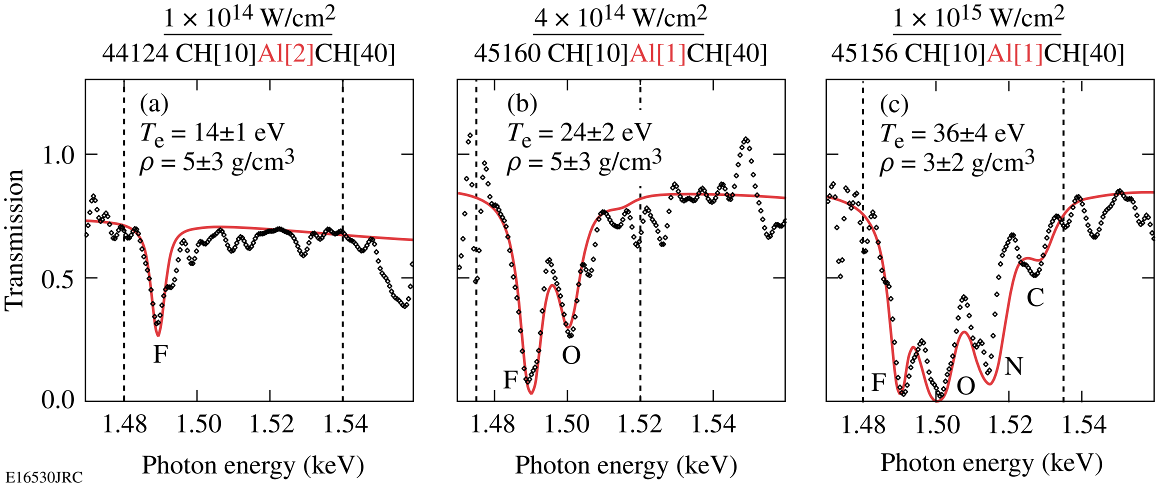

Figure 116.28

Measured Al absorption spectra (diamonds) and fits (solid curve) during shock heating and compression for the square laser pulse drives having intensities of (a) 1×10^{14} W/cm^2, (b) 4×10^{14} W/cm^2, and (c) 1×10^{15} W/cm^2. The buried depth of an Al layer was 10 μm for all three targets. The inferred condition from the fit is shown in each figure.

the highest drive intensity (1×10^{15} W/cm^2). Consequently, the inferred electron temperature increased from 14 eV to 24 eV to 36 eV (with 10% errors) as the drive intensities increased from 1×10^{14} W/cm^2 to 4×10^{14} W/cm^2 to 1×10^{15} W/cm^2. The mass densities inferred from measured spectra for the square laser pulses were ~5 g/cm^3 (±~2 g/cm^3).

Three buried depths—5, 10, and 15 μm—of the Al layer were studied for the 1-ns square pulse drive with a peak intensity of 1×10^{15} W/cm^2. A time history of the electron temperature in the Al layer inferred from the absorption spectroscopy for each of these buried depths is plotted in Fig. 116.29. The experimental data are presented with a single symbol during shock-wave heating and with a vertical line connecting two symbols that represent the range of upper and lower limits of inferred T_e after the heat front penetrates. Figure 116.29 also shows the *LILAC* simulations using $f = 0.06$, $f = 0.1$, and the nonlocal model. The post-processed electron temperatures were calculated as described in the previous section. The shock-breakout time from the rear surface of the target ($t = 0.72$ ns),

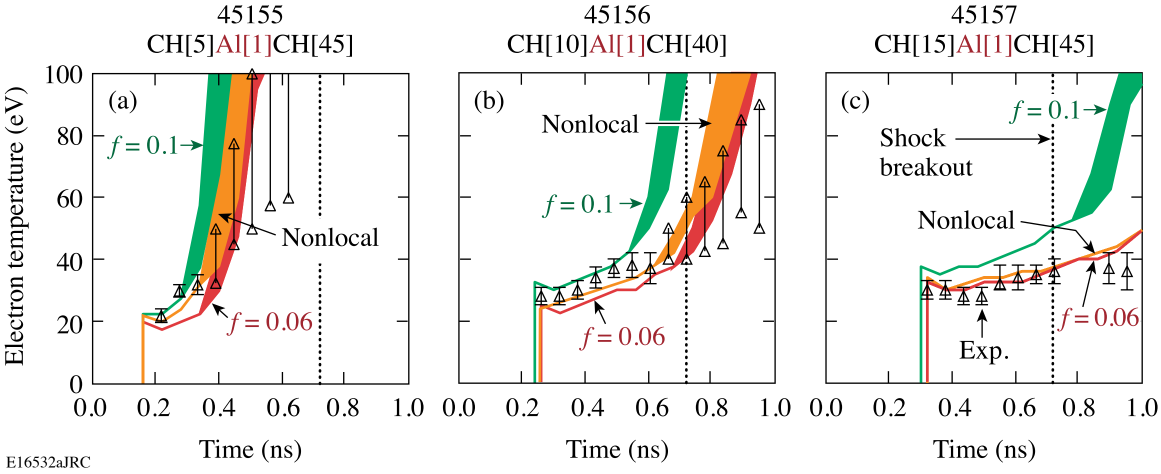

Figure 116.29

Time-resolved electron temperatures in the buried Al layer inferred from the experiment (triangles) for a 1-ns square laser drive with an intensity of 1×10^{15} W/cm^2 compared with the *LILAC* simulations using $f = 0.06$ (dark gray), $f = 0.1$ (black), and the nonlocal model (light gray). The depth of the buried Al layer was (a) 5 μm, (b) 10 μm, and (c) 15 μm. The shock-breakout time from the rear surface of the target ($t = 0.72$ ns), calculated with the nonlocal model for this drive intensity, is indicated by the dotted vertical line in each figure.

calculated with the nonlocal model for this drive intensity, is indicated by the dotted vertical line in each figure. The drive foil begins to accelerate and decompress after the shock wave breaks out of the rear surface of the target. An examination of Fig. 116.29 reveals the experimental delay in the onset of shock-wave heating as the buried depth of the Al layer is increased. A similar trend is observed for heat-front penetration. The simulation with the higher flux limiter predicts more shock-wave heating and an earlier penetration of the heat front than the other models. While the shock wave is transiting the drive foil (i.e., for times earlier than the shock-breakout time at $t = 0.72$ ns), the *LILAC* predictions using the nonlocal model agree with the experimental results for the 5-μm, 10-μm, and 15-μm buried depths. The nonlocal prediction is closer to the $f = 0.1$ prediction for the 5-μm buried depth, but it is similar to the $f = 0.06$ prediction for the deeper depths. This shows the time-dependent nature of the nonlocal heat transport.[46] For the 5-μm and 10-μm buried depths, the measured timing of heat-front penetration occurs before or around the predicted shock-breakout time. The prediction using the nonlocal model or $f = 0.06$ agrees with the measured heat-front penetration of the 5-μm and 10-μm buried depths. After the shock-wave breakout there are some minor discrepancies between the models and the measurements. The measured electron temperature for the 15-μm buried depth remains constant in time, while the prediction shows it should increase with time although it is close to the uncertainties. This discrepancy is likely due to the 2-D effects discussed in the next section. The $f = 0.1$ predictions do not agree with the measured heat-front penetration in the 10-μm- and 15-μm-buried-depth cases.

Two buried depths—5 and 10 μm—of the Al layer were studied for the 1-ns square pulse drive with a peak intensity of 4×10^{14} W/cm^2. A time history of the electron temperature in the Al layer inferred from the absorption spectroscopy for each of these buried depths is plotted in Fig. 116.30. The experimental data are presented with a single symbol during shock-wave heating and with a vertical line connecting two symbols that represent the range of upper and lower limits of inferred T_e after the heat front penetrates. Figure 116.30 also shows the *LILAC* simulations using $f = 0.06$, $f = 0.1$, and the nonlocal model. The post-processed electron temperatures were calculated as described in the previous section. The shock-breakout time from the target's rear surface ($t = 0.88$ ns) is calculated with the nonlocal model for this drive intensity and is indicated by the dotted vertical line in each figure. It occurs very late in the pulse. Timing of shock-wave heating and heat-front penetration on the buried depth is similar to Fig. 116.29. Nonlocal predictions are similar to those using $f = 0.06$. The simulation with the higher flux limiter predicts more shock-wave heating and an earlier penetration of the heat front than the other models. *LILAC* predictions using the nonlocal model or the $f = 0.06$ model agree with the experimental results for the 10-μm buried depth throughout the pulse. The initial level of shock-wave heating agrees with all three models for the 5-μm buried depth; however, the $f = 0.1$ model is closest to the heat-front penetration for this shallow depth. The advanced penetration of the heat front for the 5-μm

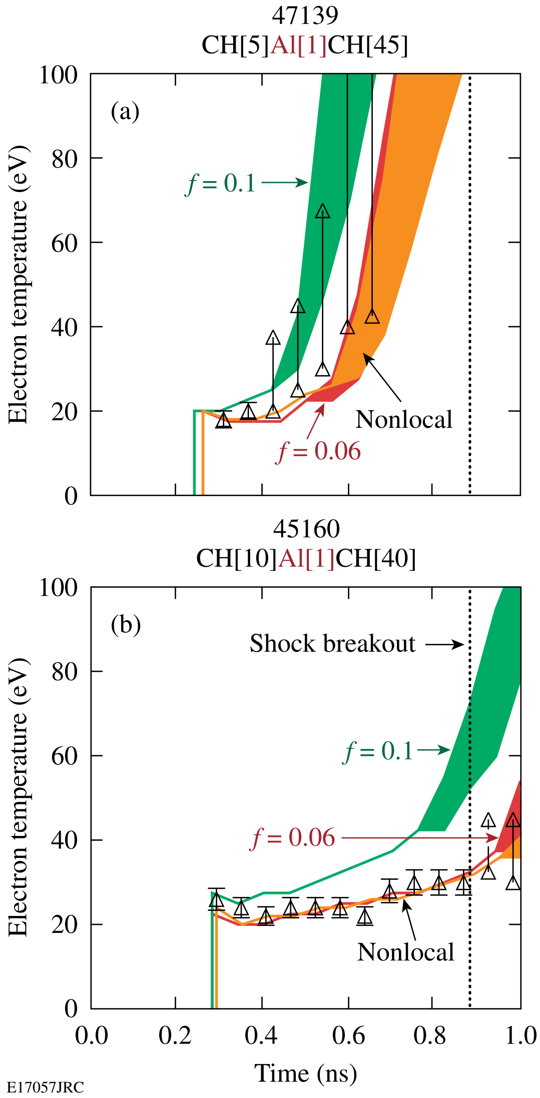

Figure 116.30
Time-resolved electron temperatures in the buried Al layer inferred from the experiment (triangles) for a 1-ns square laser drive with an intensity of 4×10^{14} W/cm^2 for (a) 5-μm and (b) 10-μm buried depths. The data are compared with *LILAC* simulations using $f = 0.06$ (dark gray), $f = 0.1$ (black) and the nonlocal model (light gray). The shock-breakout time from the rear target surface ($t = 0.88$ ns) is calculated with the nonlocal model for this drive intensity and is indicated by the dotted vertical line in each figure.

buried depth may be caused by spatial nonuniformities in the laser irradiation profile.

Two buried depths—5 and 10 μm—of the Al layer were studied for the 3-ns square pulse drive with a peak intensity of 1×10^{14} W/cm^2. The 2-D SSD system was not employed for this experiment to match the drive conditions used for the spectrally resolved x-ray scattering measurement presented in Ref. 22. Smoothing by spectral dispersion smoothes the spatial nonuniformities in the laser irradiation profile on a time scale that is short compared to the hydrodynamic time scales. The disadvantage of turning off 2-D SSD is an increase in the level of the laser irradiation nonuniformities. A time history of the electron temperature in the Al layer inferred from the absorption spectroscopy for each of these buried depths is shown in Fig. 116.31. The experimental data are presented with a single symbol during shock-wave heating and with a vertical line connecting two symbols that represent the range of upper and lower limits of inferred T_e after the heat front penetrates. Figure 116.31 also shows the *LILAC* simulations using $f = 0.06$, $f = 0.1$, and the nonlocal model. The post-processed electron temperatures were calculated as described in the previous section. The shock-breakout time ($t = 1.37$ ns) calculated with the nonlocal model for this drive intensity is indicated by the dotted vertical line in each figure. All of the models have similar predictions. The *LILAC* predictions agree with the experimental results for the 10-μm buried depth throughout the pulse [Fig. 116.31(b)]. This drive appears to be insensitive to the reduction of radiative heating caused by 2-D effects. The coronal plasma temperature predicted with *LILAC* remains relatively low (~2 keV) after shock-breakout time; consequently, the level of radiative heating is negligible. The initial level of shock-wave heating for the 5-μm buried depth is below detection threshold until just after $t = 0.4$ ns. The heat-front penetration for this shallow depth is much earlier than the *LILAC* predictions [Fig. 116.31(a)] and is most likely caused by the higher level of laser irradiation nonuniformities with the 2-D SSD turned off. The 10-μm buried depth does not appear to be influenced by this effect. Plasma smoothing of the laser irradiation nonuniformities reduces nonuniformities in the drive at the ablation surface.[47] Since the heat-front penetration time is delayed as the buried depth is increased, the 10-μm buried depth has more time to form a coronal plasma. Consequently, the plasma smoothing is more effective and early heat-front penetration is not observed for the 10-μm case. Further investigation to understand the cause of the early heat-front penetration for this drive condition is needed. The measured level of shock-wave heating of ~13 eV for the 3-ns square pulse drive with a peak intensity of 1×10^{14} W/cm^2 is close to the simulations. This is consistent with the results from noncollective spectrally resolved x-ray scattering experiment on OMEGA using the same drive condition.[22]

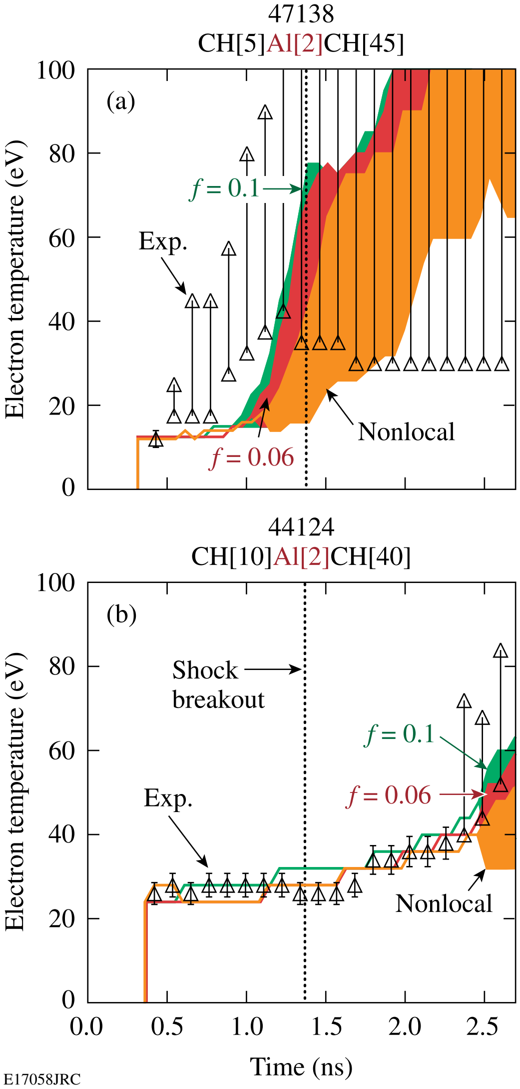

Figure 116.31
Comparisons of time-resolved electron temperatures in the buried Al layer inferred from the experiment (triangles) for a 3-ns square laser drive with an intensity of 1×10^{14} W/cm^2 with the *LILAC* simulations using $f = 0.06$ (dark gray), $f = 0.1$ (black), and the nonlocal model (light gray) for (a) 5-μm and (b) 10-μm buried depths. The shock-breakout time ($t = 1.37$ ns) calculated with the nonlocal model for this drive intensity is indicated by the dotted vertical line in each figure.

2. Plasma Conditions Achieved with Shaped Laser Pulses

High target compression can be achieved in ICF using a shaped laser pulse drive that launches a weak shock wave during the foot pulse through the target followed by a compression wave during the rise to the main pulse. Three shaped laser drives were investigated using the following laser pulse shapes: $\alpha = 3$ drive with a peak intensity of 8×10^{14} W/cm^2, $\alpha = 3$ drive with a peak intensity of 1×10^{15} W/cm^2, and $\alpha = 2$ drive with a peak intensity of 1×10^{15} W/cm^2 [see Fig. 116.27(b)]. To realize the full effect of the compression wave on the buried Al layer in a planar target, the shock-breakout time needs to occur after the shaped laser pulse reaches peak intensity. The buried depth should be deep enough to avoid heat-front penetration until after the compression wave has propagated through the Al layer. This section demonstrates how higher target compression can be achieved with a shaped laser drive compared to a square laser drive.

The peak intensity of the $\alpha = 3$ drive was increased from 8×10^{14} W/cm^2 to 1×10^{15} W/cm^2 to investigate preheat of the buried Al layer by energetic electrons. The higher peak intensities were achieved by increasing the number of drive beams from 15 to 21. In the TPD instability,[11] the incident laser decays into two electron-plasma waves (plasmons) around the quarter-critical-density region, producing energetic electrons.[48] Preheat caused by these electrons usually occurs during the main drive of the shaped laser pulse.[49] Hard x-ray signals produced by the energetic electrons have been observed to increase exponentially with the overlapped laser intensities in the range from 0.5 to 1.0×10^{15} W/cm^2 range (Ref. 49). This experiment was designed to increase the energetic electron production by varying the peak intensity of the $\alpha = 3$ drive. The hard x-ray signals were monitored with the four-channel hard x-ray detector recording x-ray energies greater than 20 keV, 40 keV, 60 keV, and 80 keV (Ref. 49). In the absorption spectroscopy experiment, hard x rays can be produced in the coronal plasmas of the backlighter and the drive foil. Hard x-ray measurements of the drive foil alone are not available.

TPD is expected to occur for most of the drives under consideration based on the threshold parameter[48] given as $I_{14} \times L_{\mu\text{m}} / (230 \times T_\text{c})$, where I_{14} is the incident laser intensity at the quarter-critical density in units of 10^{14} W/cm^2, $L_{\mu\text{m}}$ is the density scale length in microns at the quarter-critical density, and T_c is the electron temperature at the quarter critical density in keV. When the threshold parameter is above 1, laser light from the drive may decay into two electron-plasma waves around the quarter-critical density. The predicted density scale length in a planar target is longer than in a spherical implosion with the same overlapped laser intensity, resulting in more-energetic electron production. The higher-intensity $\alpha = 3$ drive exceeds a threshold parameter of 1 at $t = {\sim}0.8$ ns, while the threshold parameter for the lower-intensity drive exceeds 1 around $t = 1.0$ ns.

Three buried depths—10, 15, and 20 μm—of the Al layer were studied for the $\alpha = 3$ drive with peak intensity of 8×10^{14} W/cm^2. A time history of the electron temperature in the Al layer inferred from the absorption spectroscopy for each of these buried depths is plotted in Fig. 116.32. The experimental data are presented with a single symbol during shock-wave

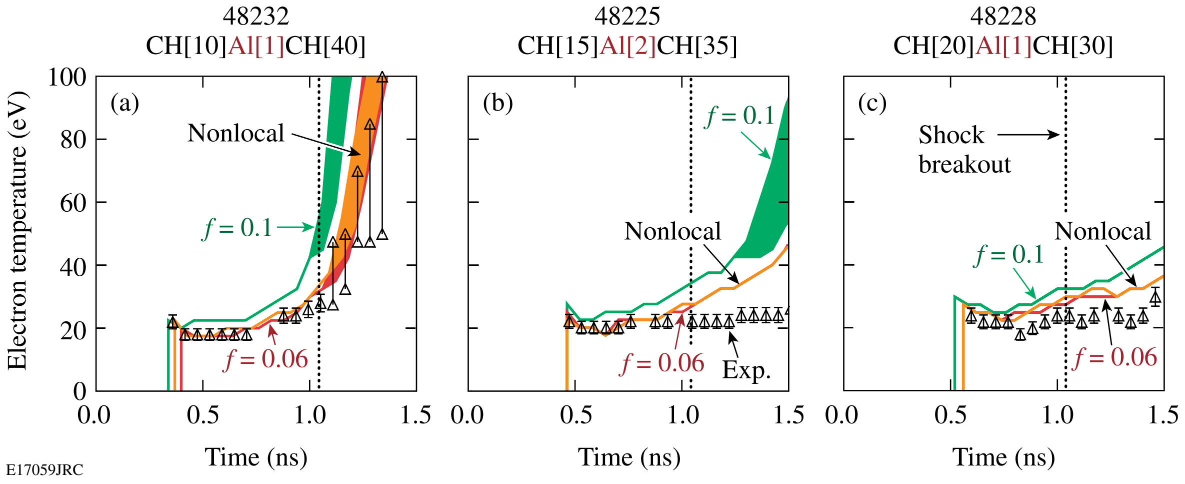

Figure 116.32
Comparisons of the measured electron temperatures in the buried Al layer (triangles) for the $\alpha = 3$ drive with peak intensity of 8×10^{14} W/cm^2 with the *LILAC* simulations using $f = 0.06$ (dark gray), $f = 0.1$ (black), and the nonlocal model (light gray) for (a) 10-μm, (b) 15-μm, and (c) 20-μm buried depths. The shock-breakout time ($t = 1.04$ ns) calculated with the nonlocal model for this drive intensity is indicated by the dotted vertical line in each figure.

heating and with a vertical line connecting two symbols that represent the range of upper and lower limits of inferred T_e after the heat front penetrates. Figure 116.32 shows the *LILAC* simulations using $f = 0.06$, $f = 0.1$, and the nonlocal model. The post-processed electron temperatures were calculated as described in the previous section. The timing of shock-wave heating and heat-front penetration is delayed as the buried depth of the Al layer is increased. The shock-breakout time (t = 1.04 ns) calculated with the nonlocal model for this drive intensity is indicated by the dotted vertical line in each figure. As can be seen in Fig. 116.27(b) the rising edge of the main drive of the $\alpha = 3$ drive with a peak intensity of 8×10^{14} W/cm^2 ends at 1.2 ns, which is after the shock-breakout time (t = 1.04 ns). While the shock wave is transiting the drive foil (i.e., for times earlier than the shock-breakout time at t = 1.04 ns), *LILAC* predictions using the nonlocal model or the $f = 0.06$ model agree with the experimental results for the 10-μm, 15-μm, and 20-μm buried depths. The $f = 0.1$ prediction is higher than the electron temperature inferred from the experiment during shock heating, and the predicted heat-front penetration occurs earlier than the experimental results. In Fig. 116.32(a) the *LILAC* predictions using the nonlocal model or the $f = 0.06$ model agree with the measured timing of heat-front penetration that occurs just after the shock-breakout time. The late time discrepancies observed in Figs. 116.32(b) and 116.32(c) are likely due to 2-D effects discussed below.

Similar plasma conditions were inferred in CH/Al/CH targets driven with the $\alpha = 3$ drive with a higher peak intensity of 1×10^{15} W/cm^2. The time-resolved electron temperatures in the Al layer inferred are presented in Fig. 116.33 for buried depths of 15 μm and 20 μm. The 10-μm depth was not studied with the higher drive intensity because the Al layer is ablated before peak compression is achieved in the target. The experimental data and the *LILAC* simulations in Fig. 116.33 are presented in a format similar to Fig. 116.32. The shock-breakout time (t = 1.02 ns) calculated by the nonlocal model for this drive intensity is indicated by the dotted vertical line in each figure. While the shock wave is transiting the drive foil (i.e., for times earlier than the shock-breakout time at t = 1.02 ns), *LILAC* predictions using the nonlocal model or the $f = 0.06$ model are close to the experimental results for the 15-μm and 20-μm buried depths. Prior to the shock-breakout time, however, the higher-intensity drive with the 20-μm buried depth shows slightly more discrepancy between simulation and measurement [see Fig. 116.33(b)] than the same case with the lower-intensity drive [see Fig. 116.32(c)]. The electron temperature predicted with $f = 0.1$ is higher than that measured for all times.

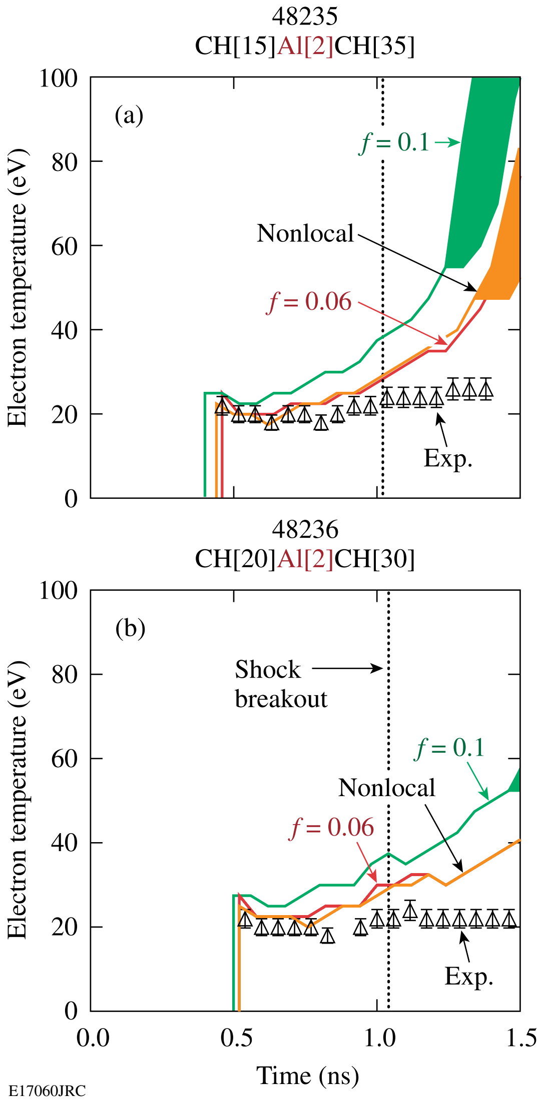

Figure 116.33
Comparisons of the measured electron temperatures in the buried Al layer (triangles) for the $\alpha = 3$ drive with a peak intensity of 1×10^{15} W/cm^2 with the *LILAC* simulations using $f = 0.06$ (dark gray), $f = 0.1$ (black), and the nonlocal model (light gray) for (a) 15-μm and (b) 20-μm buried depths. The shock-breakout time (t = 1.02 ns) calculated with the nonlocal model for this drive intensity is indicated by the dotted vertical line in each figure.

After the shock wave breaks out of the rear surface of the target, the *LILAC* simulation does not accurately predict the experimental results. This can be seen in Figs. 116.32(b), 116.32(c), 116.33(a), and 116.33(b). Although rising electron temperatures are predicted for 15- and 20-μm depths due to radiative heating, the experimental data remain at a constant value of ~20 eV. Measured and simulated absorption spectra are examined for times before and after the shock-wave breakout time in Fig. 116.34.

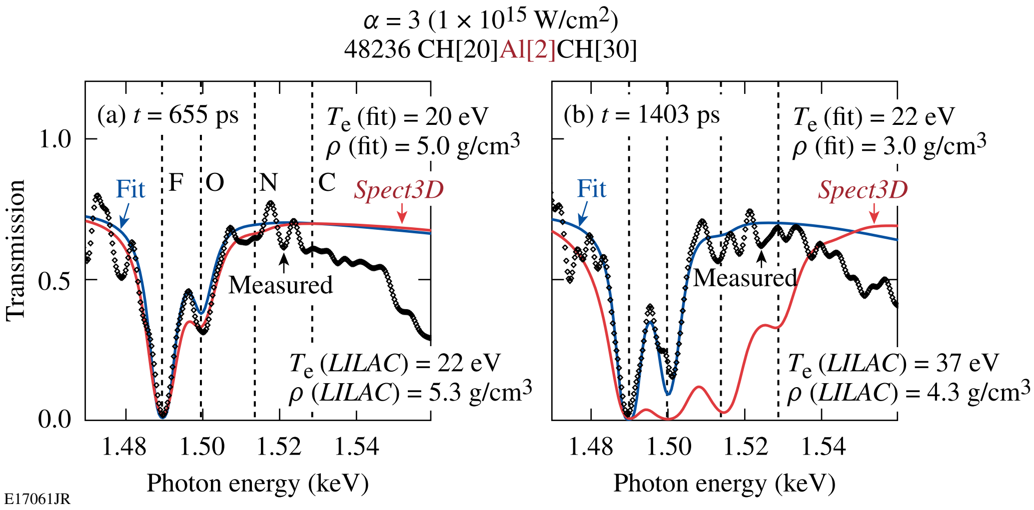

Figure 116.34
Measured (diamonds) and simulated Al absorption spectra before and after the shock-breakout time for the $\alpha = 3$ drives with a peak intensity of 1×10^{15} W/cm^2 (shot 48236). The fitted spectra assuming uniform conditions are shown in gray and *LILAC*/*Spect3D* spectra in black.

The simulated spectra are calculated using *LILAC* and *Spect3D* as described in **One-Dimensional Simulations** (p. 187). The spectral fitting calculated with *PrismSpect* is also shown. The simulated absorption spectrum is close to the measured one before shock breakout, for the $\alpha = 3$ drive with peak intensity of 1×10^{15} W/cm^2 [Fig. 116.34(a)], but after shock breakout, the measured spectrum has virtually no N-like and C-like absorption features indicating a lower electron temperature than the simulated one [Fig. 116.34(b)]. Quantitatively, the T_e and ρ inferred from the spectral fitting are 20 eV and 5.0 g/cm^3 and compare favorably to the predicted conditions of 22 eV and 5.3 g/cm^3. After the shock breakout, the T_e and ρ inferred from the spectral fitting are 22 eV and 3.0 g/cm^3 and are lower than the predicted conditions of 37 eV and 4.3 g/cm^3. If the mass density in the fits were increased, the peak of the O-like absorption is predicted to increase in transmission. Therefore, the differences between the simulated and measured spectra can be explained only by a lower measured electron temperature compared to the prediction.

The significant discrepancies between the measured and predicted plasma conditions in the Al layer after the shock wave breaks out of the rear surface of the foil are attributed to 2-D effects in the planar experimental geometry. The laser drive does not produce a planar shock front. The spatial-intensity profile of the laser drive incident on the target is defined by the single-beam super-Gaussian profile[50] and the overlap of beams having an angle of incidence up to ~60°. It causes the ablation front to have curvature and it creates a coronal plasma with lateral gradients in the temperature and density profiles, leading to a lateral heat flow. The resulting lower coronal plasma temperatures reduce the radiated x-ray power of the corona compared to the case with only radial gradients (i.e., the 1-D prediction). As a consequence the radiative heating of the Al layer is reduced. Nonuniform acceleration of the drive foil can bow the target, further enhancing the 2-D effects.

A 2-D hydrodynamic simulation *DRACO*[51] was performed to estimate the amount of lateral heat flow caused by 2-D effects. Figure 116.35 shows the simulated mass-density contours from *DRACO* for the $\alpha = 3$ with a peak intensity of 1×10^{15} W/cm^2 at (a) $t = 0$ ns, (b) $t = 0.6$ ns, and (c) $t = 1.4$ ns. The calculation was performed with cylindrical symmetry around the horizontal axis and the laser is incident on the target from the right. The vertical axis corresponds to the radial dimension of the target. The Al 1*s*–2*p* absorption spectroscopy probes radial locations up to 200 μm, which corresponds to the uniform drive region. The 2-D simulation includes the experimental configuration of beam angles and the single-beam intensity profiles. At $t = 0.6$ ns, curvature in the shock front and deformation of the shocked planar target are evident. The curvature becomes more pronounced at $t = 1.4$ ns. This creates 2-D gradients in the temperature and density profile in the coronal plasma, leading to a lateral heat flow. Figure 116.36 compares 1-D *LILAC* and 2-D *DRACO* simulations for (a) the maximum corona plasma temperatures and (b) the electron temperatures in the Al layer along with the measurement. The 2-D simulation shows a lower corona plasma temperature by ~1 keV and a lower electron temperature in the buried Al layer by ~10 eV than the 1-D simulation at the 1-D predicted time of shock breakout (t = 1.02 ns). The minimum and maximum temperatures in the Al layer predicted by the 2-D simulation are closer to the experimental results than the 1-D prediction as shown in Fig. 116.36(b).

Preheat by energetic electrons is expected to be observed in the drive foil having the Al layer buried at 20 μm and driven with the α = 3 drive with a peak intensity of 1×10^{15} W/cm^2 [Fig. 116.34(b)]. The 1-D *LILAC* prediction does not simulate the TPD instability; therefore, evidence of preheat would be an

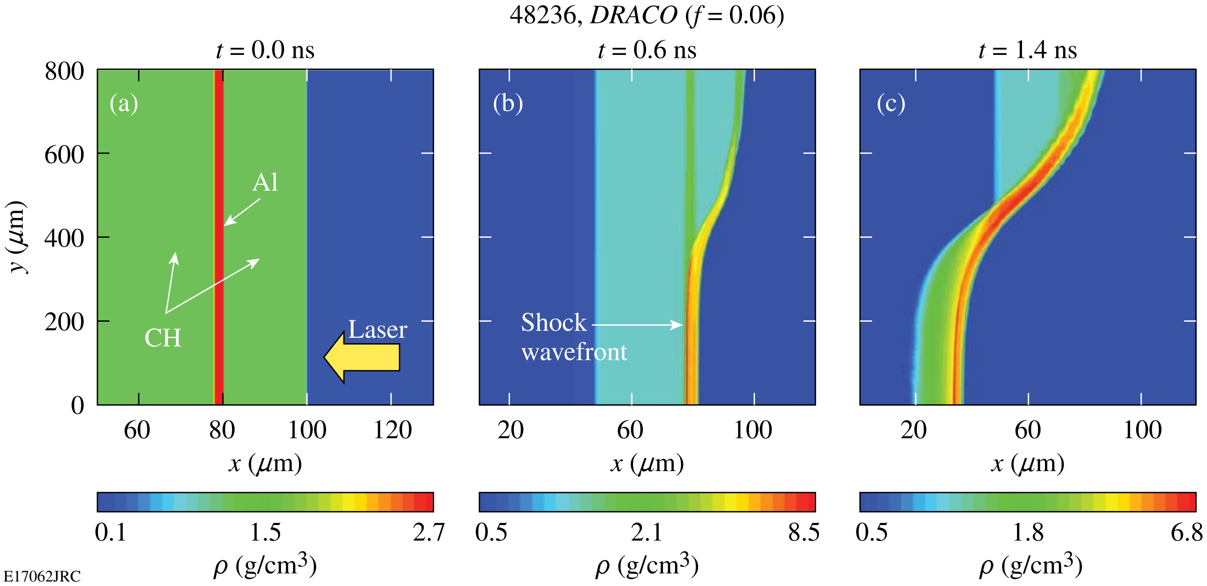

Figure 116.35
Mass-density contours of the driven CH/Al/CH planar target simulated with 2-D hydrodynamics code *DRACO* for shot 48236 at (a) t = 0, (b) t = 0.6 ns, and (c) t = 1.4 ns. The calculation was performed with cylindrical symmetry around the horizontal axis and the laser is incident on the target from the right.

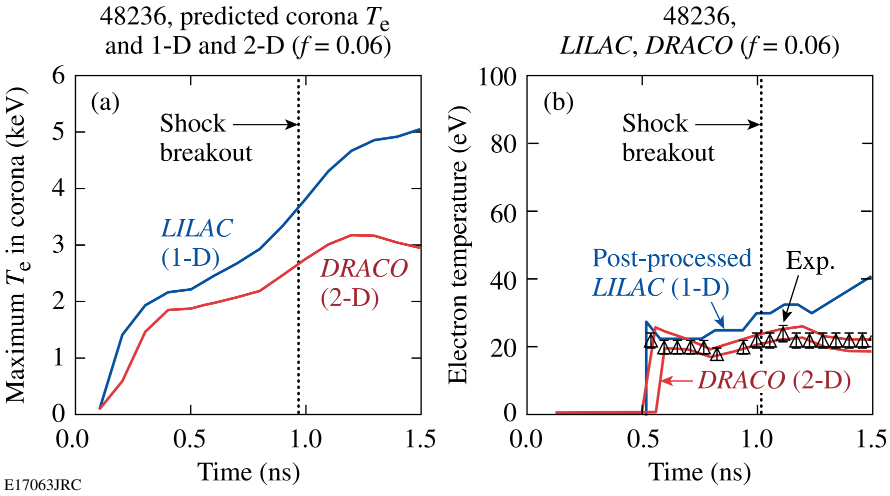

Figure 116.36
(a) A comparison of the maximum coronal plasma temperatures predicted by 1-D and 2-D simulations for a planar CH/Al/CH target driven with the α = 3 drive with a peak intensity of 1×10^{15} W/cm^2. (b) Time histories of predicted electron temperatures in the Al layer using *LILAC* and *DRACO* compared with the experimental data for shot 48236. The 1-D, post-processed T_e is shown in black, and the minimum and maximum predicted temperatures with *DRACO* are shown in gray.

inferred electron temperature in the Al layer that is higher than 1-D prediction. The 2-D effects, however, cause the electron temperature in the Al layer to be less than the 1-D prediction after the shock-breakout time ($t = 1.04$ ns). The 2-D effects mask any signature of increased electron temperature due to preheat from energetic electrons late in the drive pulse. Therefore, the evidence for preheat due to energetic electrons is inconclusive in this experiment.

Three buried depths—10, 15, and 20 μm—of the Al layer were studied for the $\alpha = 2$ drive with a peak intensity of 1×10^{15} W/cm^2. A time history of the electron temperature in the Al layer inferred from the absorption spectroscopy for each of these buried depths is plotted in Fig. 116.37. The experimental data are presented with a single symbol during shock-wave heating and with a vertical line connecting two symbols that represent the range of upper and lower limits of inferred T_e after the heat front penetrates. The foot intensity of the $\alpha = 2$ drive pulse was $\sim 4 \times 10^{13}$ W/cm^2 [Fig. 116.27(b)], producing ~8-Mbar pressure in the Al layer. The shock-wave strength was too weak to increase the T_e in the Al layer enough to generate F-like Al; however, a shifting spectral position of the Al K edge was observed. The absolute timing of the measurement could be established with the shifting Al K edge. The observed Al 1*s*–2*p* absorption lines appeared as the electron temperature in the Al layer increased due to radiative heating during the main laser drive and the compression wave. Figure 116.37 shows *LILAC* simulations using $f = 0.06$, $f = 0.1$, and the nonlocal model. The post-processed electron temperatures were calculated as described in the previous section. The timing of shock-wave heating and heat-front penetration are delayed as the buried depth of the Al layer is increased. The shock-breakout time ($t = 1.6$ ns) calculated with the nonlocal model for this drive intensity is indicated by the dotted vertical line in each figure. As can be seen in Fig. 116.27 the rising edge of the main drive of the $\alpha = 2$ drive with a peak intensity of 1×10^{15} W/cm^2 ends at 1.5 ns, which is just before the shock-breakout time ($t = 1.6$ ns). The predicted peak compression of the Al occurs at 1.5 ns. *LILAC* simulations with different thermal-transport models are close to each other for this drive condition. The *LILAC* simulations accurately model the experimental data before shock-breakout time of 1.6 ns. The inferred mass density from the Stark-broadened spectrum at the peak compression is 11 g/cm^3 (±5 g/cm^3). As described before, the 2-D effects lower the electron temperature in the coronal plasma, reducing the radiative heating of the Al. The 2-D predictions for 15- and 20-μm depths are in good agreement with the measurements before the shock-breakout times, but lower than the measurements by ~5 eV after the shock breakout. The TPD threshold parameter for the $\alpha = 2$ drive exceeds 1 at $t = 1.3$ ns, indicating that the difference between the measured and 2-D predicted temperatures in the Al at late time of the drive could be heating due to energetic electrons from the TPD instability. Further work is required to identify the level of preheating and to include the nonlocal electron thermal transport model in the 2-D simulations for a consistent explanation of the experimental results for the square and shaped laser drives after the shock-breakout time.

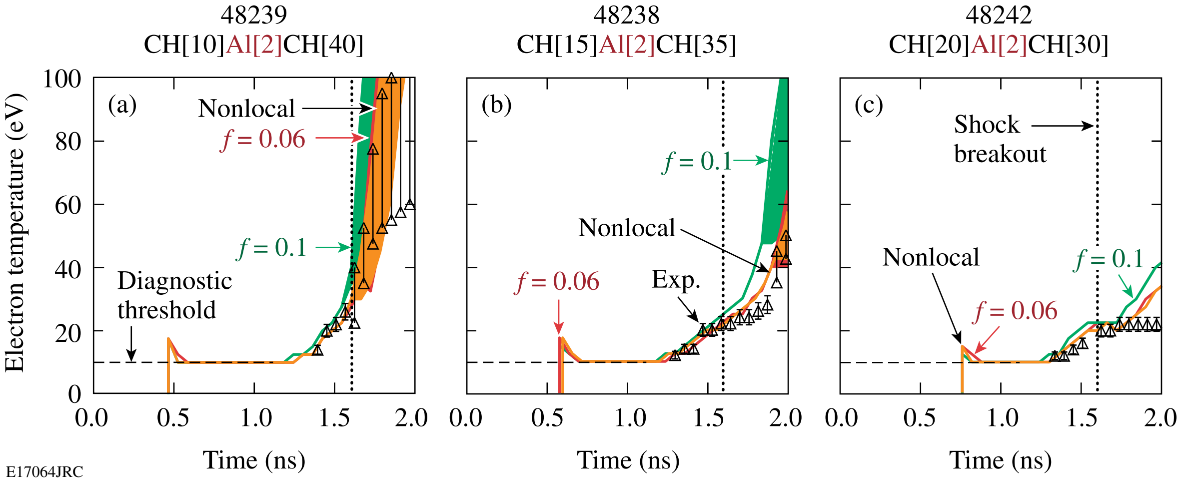

Figure 116.37
Comparisons of the measured electron temperatures in the buried Al layer for the $\alpha = 2$ drive with *LILAC* simulations using $f = 0.06$ (dark gray), $f = 0.1$ (black), and the nonlocal model (light gray) for (a) 10-μm, (b) 15-μm, and (c) 20-μm buried depths. The shock-breakout time ($t = 1.6$ ns) calculated with the nonlocal model for this drive intensity is indicated by the dotted vertical line in each figure.

Higher target compression has been achieved with a shaped laser pulse drive compared to a square laser pulse drive. A single shock wave launched by the square laser pulse creates a nearly constant mass density in the shocked Al. The shaped laser pulse launches a shock wave by the foot laser intensity and multiple hydrodynamic waves coalescing to form a compression wave with increasing pressure during the ramp of the laser intensity. A mass density of 11 g/cm^3 (±5 g/cm^3) and an electron temperature of 20 eV were created in the buried Al layer with the $\alpha = 2$ drive. Figure 116.38 presents a comparison of Al 1*s*–2*p* absorption spectra for two drive conditions. Both spectra have F-like and O-like absorption features. This is the first measurement of the plasma temperature and density in a direct-drive target created by multiple shock waves (i.e., a weak shock and a compression wave).[24] The best fit to each spectrum is represented by the black curve. The mass densities inferred are between 5 and 7 g/cm^3 for the 1-ns square laser pulse [Fig. 116.38(a)] and between 6 and 16 g/cm^3 for the $\alpha = 2$ drives [Fig. 116.38(b)]. The simulated spectra for the upper and lower limits of the mass density are plotted in Fig. 116.38. The predicted mass density of 14 g/cm^3 is consistent with the measured density of 11 g/cm^3 at the peak compression for the shaped laser pulse. The lower predicted mass density of 8 g/cm^3 for the 1-ns square pulse is consistent with the lower inferred value of 6 g/cm^3. Although the difference in the mass densities is just resolved with the Al 1*s*–2*p* absorption spectroscopy, this experiment shows that higher target compression is achieved with the shaped laser pulse drive compared with the square laser pulse drive.

Future Work and Application

The experimental results presented here demonstrate the diagnostic capability of measuring shock-wave heating and timing of heat-front penetration using the time-resolved Al 1*s*–2*p* absorption spectroscopy of a direct-drive, shock-wave–heated and compressed planar plastic foil for a wide range of drive conditions. Understanding electron thermal transport in a spherical geometry is the ultimate goal of this research. A spherical or hemispherical CH target with a buried Al layer will be investigated. Shifting to a spherical geometry eliminates the 2-D effects observed in the planar geometry and would pave the way for a conclusive preheat experiment. The CH foil is a surrogate for a deuterium–tritium (DT) cryogenic layer for a direct-drive ICF capsule. Measurements of plasma conditions in a shock-wave–heated planar DT or DD cryogenic layer with x-ray absorption spectroscopy will be a next step to understanding the shell condition of a laser-driven cryogenic ICF target. The target development will be challenging since a direct-drive, cryogenic deuterium planar experiment using x-ray absorption spectroscopy will require an Al foil in a liquid deuterium.

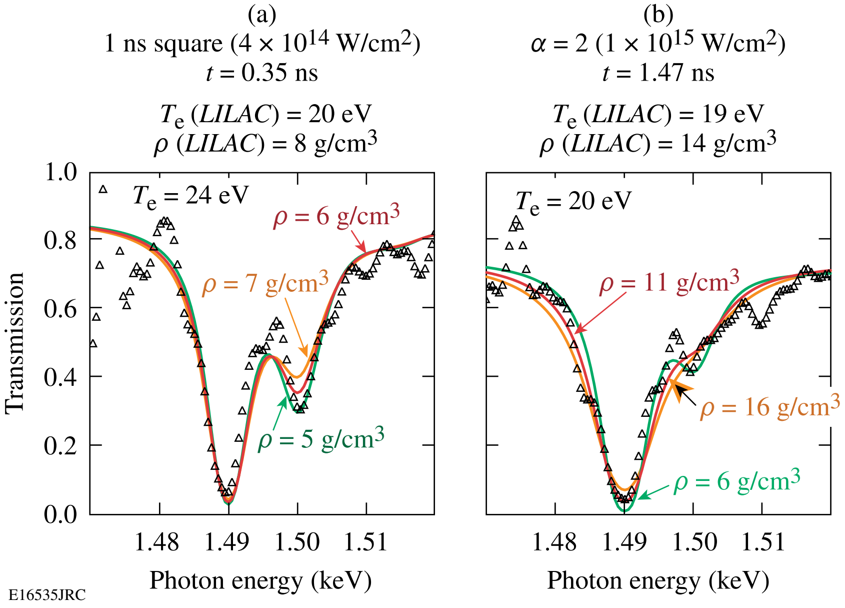

Figure 116.38
Spectral fits to the measured spectra for (a) a square laser pulse (4 × 10^{14} W/cm^2) taken at t = 0.35 ns and (b) shaped laser pulse (α = 2 drive) taken at 1.47 ns. Inferred mass densities from fitting the Stark-broadened Al 1*s*–2*p* absorptions are between 5 g/cm^3 (light gray) and 7 g/cm^3 (dark gray) for the square laser pulse and between 6 g/cm^3 (light gray) and 16 g/cm^3 (dark gray) for the shaped laser pulse. The modeled spectra for the best fit are shown in black.

Conclusion

The plasma conditions of a direct-drive, shock-wave–heated and compressed planar target comprising warm dense matter[13] were diagnosed using time-resolved Al $1s$–$2p$ absorption spectroscopy. A 50-μm planar CH foil with a buried tracer layer of Al was irradiated with intensities of 10^{14} to 10^{15} W/cm^2, and ~1.5 keV x rays from a point-source Sm backlighter were transmitted through the drive foil. Local shell conditions of T_e and ρ during the shock-wave heating and heat-front penetration were inferred from the measured absorption spectra analyzed with *PrismSPECT*, assuming uniform conditions in the Al layer. The drive foil was simulated with the 1-D hydrodynamic code *LILAC* using flux-limited ($f = 0.1$ and $f = 0.06$) or a nonlocal thermal transport model. The experimental results showed that 1-D simulations using the nonlocal model or $f = 0.06$ accurately predict the timing of heat-front penetration and the level of shock-wave heating for square and shaped laser pulses while the shock transits the target. The accuracy of the electron temperatures inferred from the experiments was sufficient to distinguish between the two flux-limited hydrodynamics predictions. The predicted plasma conditions of a shocked Al layer using the nonlocal model were similar to the ones using $f = 0.06$ in this experiment. Significant discrepancies between measured and predicted shock-wave heating were observed at late times in the drive, which can be explained by reduced radiative heating due to lateral heat flow in the corona. An early burnthrough observed for 5-μm buried depth could be caused by high laser irradiation nonuniformity levels without laser-beam smoothing with 2-D SSD. Preheat experiments of the buried Al layer due to energetic electron production by the two-plasmon-decay instability were inconclusive since the 2-D effects masked any experimental signature of preheat.

ACKNOWLEDGMENT

The authors are grateful to M. J. Bonino and S. G. Noyes for their target fabrication expertise and to R. E. Bahr and S. Mott for diagnostic expertise as well as to the OMEGA operations crew for providing the highly reproducible laser performance. The authors appreciate the insightful discussions with A. Ng and D. Hoarty. This work was supported by the U.S. Department of Energy Office of Inertial Confinement Fusion under Cooperative Agreement No. DE-FC52-08NA28302, the University of Rochester, and the New York State Energy Research and Development Authority. The support of DOE does not constitute an endorsement by DOE of the views expressed in this article.

REFERENCES

1. J. Nuckolls *et al.*, Nature **239**, 139 (1972); J. D. Lindl, R. L. McCrory, and E. M. Campbell, Phys. Today **45**, 32 (1992); R. L. McCrory, J. M. Soures, C. P. Verdon, F. J. Marshall, S. A. Letzring, S. Skupsky, T. J. Kessler, R. L. Kremens, J. P. Knauer, H. Kim, J. Delettrez, R. L. Keck, and D. K. Bradley, Nature **335**, 225 (1988); R. L. McCrory, S. P. Regan, S. J. Loucks, D. D. Meyerhofer, S. Skupsky, R. Betti, T. R. Boehly, R. S. Craxton, T. J. B. Collins, J. A. Delettrez, D. Edgell, R. Epstein, K. A. Fletcher, C. Freeman, J. A. Frenje, V. Yu. Glebov, V. N. Goncharov, D. R. Harding, I. V. Igumenshchev, R. L. Keck, J. D. Kilkenny, J. P. Knauer, C. K. Li, J. Marciante, J. A. Marozas, F. J. Marshall, A. V. Maximov, P. W. McKenty, J. Myatt, S. Padalino, R. D. Petrasso, P. B. Radha, T. C. Sangster, F. H. Séguin, W. Seka, V. A. Smalyuk, J. M. Soures, C. Stoeckl, B. Yaakobi, and J. D. Zuegel, Nucl. Fusion **45**, S283 (2005).

2. P. W. McKenty, V. N. Goncharov, R. P. J. Town, S. Skupsky, R. Betti, and R. L. McCrory, Phys. Plasmas **8**, 2315 (2001); P. W. McKenty, T. C. Sangster, M. Alexander, R. Betti, R. S. Craxton, J. A. Delettrez, L. Elasky, R. Epstein, A. Frank, V. Yu. Glebov, V. N. Goncharov, D. R. Harding, S. Jin, J. P. Knauer, R. L. Keck, S. J. Loucks, L. D. Lund, R. L. McCrory, F. J. Marshall, D. D. Meyerhofer, S. P. Regan, P. B. Radha, S. Roberts, W. Seka, S. Skupsky, V. A. Smalyuk, J. M. Soures, K. A. Thorp, M. Wozniak, J. A. Frenje, C. K. Li, R. D. Petrasso, F. H. Séguin, K. A. Fletcher, S. Padalino, C. Freeman, N. Izumi, J. A. Koch, R. A. Lerche, M. J. Moran, T. W. Phillips, G. J. Schmid, and C. Sorce, Phys. Plasmas **11**, 2790 (2004).

3. M. C. Herrmann, M. Tabak, and J. D. Lindl, Phys. Plasmas **8**, 2296 (2001); R. Betti, K. Anderson, V. N. Goncharov, R. L. McCrory, D. D. Meyerhofer, S. Skupsky, and R. P. J. Town, Phys. Plasmas **9**, 2277 (2002).

4. L. Spitzer, Jr. and R. Härm, Phys. Rev. **89**, 977 (1953).

5. J. Delettrez, R. Epstein, M. C. Richardson, P. A. Jaanimagi, and B. L. Henke, Phys. Rev. A **36**, 3926 (1987); J. Delettrez, Can. J. Phys. **64**, 932 (1986).

6. R. C. Malone, R. L. McCrory, and R. L. Morse, Phys. Rev. Lett. **34**, 721 (1975).

7. S. P. Regan, R. Epstein, V. N. Goncharov, I. V. Igumenshchev, D. Li, P. B. Radha, H. Sawada, W. Seka, T. R. Boehly, J. A. Delettrez, O. V. Gotchev, J. P. Knauer, J. A. Marozas, F. J. Marshall, R. L. McCrory, P. W. McKenty, D. D. Meyerhofer, T. C. Sangster, D. Shvarts, S. Skupsky, V. A. Smalyuk, B. Yaakobi, and R. C. Mancini, Phys. Plasmas **14**, 056305 (2007).

8. T. R. Boehly, D. L. Brown, R. S. Craxton, R. L. Keck, J. P. Knauer, J. H. Kelly, T. J. Kessler, S. A. Kumpan, S. J. Loucks, S. A. Letzring, F. J. Marshall, R. L. McCrory, S. F. B. Morse, W. Seka, J. M. Soures, and C. P. Verdon, Opt. Commun. **133**, 495 (1997).

9. O. Gotchev, V. N. Goncharov, J. P. Knauer, T. R. Boehly, T. J. B. Collins, R. Epstein, P. A. Jaanimagi, and D. D. Meyerhofer, Phys. Rev. Lett. **96**, 115005 (2006).

10. V. N. Goncharov, O. V. Gotchev, E. Vianello, T. R. Boehly, J. P. Knauer, P. W. McKenty, P. B. Radha, S. P. Regan, T. C. Sangster, S. Skupsky, V. A. Smalyuk, R. Betti, R. L. McCrory, D. D. Meyerhofer, and C. Cherfils-Clérouin, Phys. Plasmas **13**, 012702 (2006).

11. W. L. Kruer, *The Physics of Laser−Plasma Interactions*, Frontiers in Physics, Vol. 73, edited by D. Pines (Addison-Wesley, Redwood City, CA, 1988).

12. B. Yaakobi, C. Stoeckl, T. Boehly, D. D. Meyerhofer, and W. Seka, Phys. Plasmas **7**, 3714 (2000); B. Yaakobi, T. R. Boehly, T. C. Sangster, D. D. Meyerhofer, B. A. Remington, P. G. Allen, S. M. Pollaine, H. E. Lorenzana, K. T. Lorenz, and J. A. Hawreliak, Phys. Plasmas **15**, 062703 (2008).

13. National Research Council (U.S.) Committee on High Energy Density Plasma Physics, *Frontiers in High Energy Density Physics: The X-Games of Contemporary Science* (National Academies Press, Washington, DC, 2003), p. 84.

14. S. Ichimaru, Rev. Mod. Phys. **54**, 1017 (1982).

15. A. Ng *et al.*, Laser Part. Beams **23**, 527 (2005).

16. S. H. Glenzer *et al.*, Phys. Plasmas **6**, 2117 (1999).

17. O. L. Landen *et al.*, J. Quant. Spectrosc. Radiat. Transf. **71**, 465 (2001).

18. S. H. Glenzer *et al.*, Phys. Rev. Lett. **90**, 175002 (2003).

19. T. R. Boehly, J. A. Delettrez, J. P. Knauer, D. D. Meyerhofer, B. Yaakobi, R. P. J. Town, and D. Hoarty, Phys. Rev. Lett. **87**, 145003 (2001).

20. D. J. Hoarty *et al.*, J. Quant. Spectrosc. Radiat. Transf. **99**, 283 (2006).

21. S. H. Glenzer *et al.*, Phys. Rev. Lett. **98**, 065002 (2007).

22. H. Sawada, S. P. Regan, D. D. Meyerhofer, I. V. Igumenshchev, V. N. Goncharov, T. R. Boehly, R. Epstein, T. C. Sangster, V. A. Smalyuk, B. Yaakobi, G. Gregori, S. H. Glenzer, and O. L. Landen, Phys. Plasmas **14**, 122703 (2007).

23. Prism Computational Sciences, Inc., Madison, WI 53711.

24. S. P. Regan, H. Sawada, V. N. Goncharov, D. Li, P. B. Radha, R. Epstein, J. A. Delettrez, S. X. Hu, V. A. Smalyuk, B. Yaakobi, T. C. Sangster, D. D. Meyerhofer, R. L. McCrory, and R. C. Mancini, "Spectroscopic Observations of Fermi-Degenerate Aluminum Compressed and Heated to Four Times Solid Density and 20 eV," submitted to Physical Review Letters.

25. J. J. MacFarlane *et al.*, High Energy Density Phys. **3**, 181 (2006).

26. T. J. Kessler, Y. Lin, J. J. Armstrong, and B. Velazquez, in *Laser Coherence Control: Technology and Applications*, edited by H. T. Powell and T. J. Kessler (SPIE, Bellingham, WA, 1993), Vol. 1870, pp. 95−104.

27. S. Skupsky, R. W. Short, T. Kessler, R. S. Craxton, S. Letzring, and J. M. Soures, J. Appl. Phys. **66**, 3456 (1989).

28. T. R. Boehly, V. A. Smalyuk, D. D. Meyerhofer, J. P. Knauer, D. K. Bradley, R. S. Craxton, M. J. Guardalben, S. Skupsky, and T. J. Kessler, J. Appl. Phys. **85**, 3444 (1999).

29. J. P. Knauer, R. Betti, D. K. Bradley, T. R. Boehly, T. J. B. Collins, V. N. Goncharov, P. W. McKenty, D. D. Meyerhofer, V. A. Smalyuk, C. P. Verdon, S. G. Glendinning, D. H. Kalantar, and R. G. Watt, Phys. Plasmas **7**, 338 (2000).

30. D. H. Kalantar *et al.*, in *22nd International Congress on High-Speed Photography and Photonics*, edited by D. L. Paisley and A. M. Frank (SPIE, Bellingham, WA, 1997), Vol. 2869, pp. 680−685.

31. B. L. Henke, E. M. Gullikson, and J. C. Davis, At. Data Nucl. Data Tables **54**, 181 (1993).

32. B. L. Henke, J. P. Knauer, and K. Premaratne, J. Appl. Phys. **52**, 1509 (1981).

33. H. Sawada, "Experimental Investigation of a Direct-Drive Shock Wave Heated and Compressed Planar Target Relevant to ICF," Ph.D. thesis, University of Rochester, 2008.

34. S. P. Regan, Laboratory for Laser Energetics, private communication (2008).

35. D. K. Bradley, P. M. Bell, J. D. Kilkenny, R. Hanks, O. Landen, P. A. Jaanimagi, P. W. McKenty, and C. P. Verdon, Rev. Sci. Instrum. **63**, 4813 (1992).

36. V. N. Goncharov, T. C. Sangster, P. B. Radha, R. Betti, T. R. Boehly, T. J. B. Collins, R. S. Craxton, J. A. Delettrez, R. Epstein, V. Yu. Glebov, S. X. Hu, I. V. Igumenshchev, J. P. Knauer, S. J. Loucks, J. A. Marozas, F. J. Marshall, R. L. McCrory, P. W. McKenty, D. D. Meyerhofer, S. P. Regan, W. Seka, S. Skupsky, V. A. Smalyuk, J. M. Soures, C. Stoeckl, D. Shvarts, J. A. Frenje, R. D. Petrasso, C. K. Li, F. Séguin, W. Manheimer, and D. G. Colombant, Phys. Plasmas **15**, 056310 (2008).

37. W. F. Huebner *et al.*, Los Alamos National Laboratory, Los Alamos, NM, Report LA-6760-M (1977).

38. S. P. Lyon and J. D. Johnson, Los Alamos National Laboratory, Los Alamos, NM, Report LA-UR-92-3407 (1992).

39. R. C. Mancini *et al.*, Comput. Phys. Commun. **63**, 314 (1991).

40. C. A. Iglesias, J. L. Lebowitz, and D. MacGowan, Phys. Rev. A **28**, 1667 (1983).

41. D. A. Haynes, Jr., D. T. Garber, C. F. Hooper, Jr., R. C. Mancini, Y. T. Lee, D. K. Bradley, J. Delettrez, R. Epstein, and P. A. Jaanimagi, Phys. Rev. E **53**, 1042 (1996).

42. B. L. Henke, E. M. Gullikson, and J. C. Davis, At. Data Nucl. Data Tables **54**, 181 (1993).

43. P. A. Jaanimagi, Laboratory for Laser Energetics, private communication (2008).

44. C. I. Szabó, *et al.*, Radiat. Phys. Chem. **75**, 1824 (2006).

45. P. R. Bevington, *Data Reduction and Error Analysis for the Physical Sciences* (McGraw-Hill, New York, 1969), p. 53.

46. A. Sunahara, J. A. Delettrez, C. Stoeckl, R. W. Short, and S. Skupsky, Phys. Rev. Lett. **91**, 095003 (2003).

47. S. E. Bodner, J. Fusion Energy **1**, 221 (1981).

48. A. Simon, R. W. Short, E. A. Williams, and T. Dewandre, Phys. Fluids **26**, 3107 (1983).

49. C. Stoeckl, R. E. Bahr, B. Yaakobi, W. Seka, S. P. Regan, R. S. Craxton, J. A. Delettrez, R. W. Short, J. Myatt, A. V. Maximov, and H. Baldis, Phys. Rev. Lett. **90**, 235002 (2003).

50. S. P. Regan, J. A. Marozas, J. H. Kelly, T. R. Boehly, W. R. Donaldson, P. A. Jaanimagi, R. L. Keck, T. J. Kessler, D. D. Meyerhofer, W. Seka, S. Skupsky, and V. A. Smalyuk, J. Opt. Soc. Am. B **17**, 1483 (2000).

51. P. B. Radha, V. N. Goncharov, T. J. B. Collins, J. A. Delettrez, Y. Elbaz, V. Yu. Glebov, R. L. Keck, D. E. Keller, J. P. Knauer, J. A. Marozas, F. J. Marshall, P. W. McKenty, D. D. Meyerhofer, S. P. Regan, T. C. Sangster, D. Shvarts, S. Skupsky, Y. Srebro, R. P. J. Town, and C. Stoeckl, Phys. Plasmas **12**, 032702 (2005).

A Measurable Lawson Criterion and Hydro-Equivalent Curves for Inertial Confinement Fusion

Introduction

In inertial confinement fusion[1,2] (ICF), a shell of cryogenic deuterium and tritium ice is imploded at high velocities (~2 to 4×10^7 cm/s) and low entropy to achieve high central temperatures and high areal densities. The final fuel assembly consists of a relatively low density (~30 to 80 g/cc), high-temperature (~4 to 8 keV) core (the hot spot) surrounded by a dense (~300 to 1000 g/cc), cold (~100 eV) fuel layer (the compressed shell). The Lawson criterion[3] determining the onset of thermonuclear ignition is usually expressed through the product $p\tau > 10$ atm × s, where p is the plasma pressure in atm and τ is the energy confinement time in seconds. In magnetic fusion devices, both the pressure and confinement time are routinely measured, and the performance of each discharge can be assessed by comparing the value of $p\tau$ with respect to the ignition value (10 atm × s). In inertial confinement fusion, both p and τ cannot be directly measured and the performance of sub-ignited ICF implosions cannot be assessed with respect to the ignition condition. Often, the Lawson criterion is extended to ICF by simply restricting its application to the hot spot and by replacing p with the ideal gas equation of state $p = 2\rho_h T_h / m_i$ (ρ_h is the hot-spot mass density, T_h is the hot-spot temperature, and m_i is the DT average ion mass) and τ with the sound wave's traveling time through the hot spot, $t \sim R_h / C_s$ (here R_h is the hot-spot radius and C_s is the hot-spot sound speed, $C_s \sim \sqrt{T_h}$). This leads to the hot-spot–ignition condition $\left(\rho_h R_h\right)\sqrt{T_h} >$ const, where $\rho_h R_h$ is the hot-spot areal density. Such a simple derivation creates two problems: (a) the confinement time is incorrect since it neglects the inertial confinement of the surrounding cold shell, and (b) the hot-spot areal density cannot be experimentally measured.

A more accurate form of the hot-spot–ignition condition is given in Refs. 1 and 4–6 with the alpha heating balancing all the hot-spot power losses (thermal conduction and radiation losses). Our approach to ignition is somewhat different than the one in Ref. 4. First, our ignition model is dynamic since it includes both the compression and expansion phases of the shell motion. Second, our ignition condition is given in terms of the total areal density rather than the hot-spot areal density. Third, the ignition condition is viewed as an instability of both the pressure and the temperature rather than only the temperature. This causes the heat conduction losses to enter the ignition condition in a fundamentally different way. A more detailed discussion of this point is provided in the next section. It is important to emphasize that the presence of a cold, dense shell surrounding the hot spot significantly alters the onset of the thermonuclear instability (a similar point is made in Refs. 4, 7, and 8). Since the heat conductivity is negligible in the cold shell, most of the heat leaving the hot spot is recycled back into the hot spot in the form of internal energy and pdV work of the plasma ablated off the inner shell surface. Much of the radiation losses are also recycled back through ablation since the cold shell is opaque to the low-energy portion of the x-ray bremsstrahlung spectrum (only the high-energy x rays can penetrate the dense shell). As argued in Ref. 7, the heat conduction and, to some extent, the radiation losses do not appreciably change the hot-spot pressure (i.e., energy). Instead, those losses raise the density and lower the temperature while keeping $p \sim \rho T$ approximately constant. The fusion rate scales as $n^2 \langle \sigma v \rangle$, where n is the ion density and $\langle \sigma v \rangle$ is the fusion reactivity. Since $\langle \sigma v \rangle \sim T^{3-4}$ for $T < 6$ to 8 keV and $\langle \sigma v \rangle \sim T^2$ for 6 to $8 < T < 25$ keV, it follows that the alpha self-heating is degraded by heat conduction and radiation losses only at low temperatures less than 6 to 8 keV but unchanged at high temperatures $T > 6$ to 8 keV. This occurs because at high temperatures, the fusion rates depend only on the hot-spot pressure $\left(n^2 \langle \sigma v \rangle \sim p^2\right)$, which is independent of the heat losses. While these recycling effects (described in details in Ref. 7) improve the ignition threshold, the expansion losses, which are often not included in the ignition condition, causes a transfer of internal energy to kinetic energy and degrade the ignition conditions. Since hot-spot expansion occurs against the dense shell, the ignition conditions depend on the inertia of the dense shell. Furthermore, the hot spot's internal energy comes from the shell's kinetic energy, which is also used to assemble the shell's areal density. As shown in Ref. 9, there is a direct correlation between the hot spot areal density and the shell's areal density. Thus one can expect that the ICF Lawson criterion depends on the shell's areal density.

In this article, we derive a form of the Lawson criterion that can be directly measured in ICF implosions and includes the confinement of the surrounding cold shell. One can use such a new criterion to assess how far current and future sub-ignited ICF implosions are from achieving ignition. Such a new ignition criterion depends on the only two measurable quantities in the ICF fuel assembly: the total areal density and the hot-spot ion temperature. Note that the total areal density comes mostly from the cold shell surrounding the hot spot and is directly related to the inertial confinement time. In cryogenic implosions, the total areal density can be measured through charged-particle spectroscopy or x-ray radiography. The ion temperature is measured with neutron time-of-flight (nTOF) diagnostics.[10] For instance, recent cryogenic implosions[11] of D_2 targets on the OMEGA laser[12] have achieved a fusion burn–averaged areal density exceeding 200 mg/cm^2 and burn-averaged ion temperature of 2 keV—the highest performance for a cryogenic implosion to date. The burn-averaged areal density has been measured through the energy downshift of the proton spectrum from secondary D + He^3 reactions.[13] The ion temperature was measured through the nTOF diagnostics. The ion temperature used in the ignition condition is computed without alpha-particle heating. Thus, our measurable Lawson criterion is applicable to D_2 surrogate targets and DT sub-ignited implosions. Obviously, ignited DT implosions do not need a theoretical ignition criterion to verify that ignition conditions have been achieved.

We also show that hydro-equivalent curves can be represented on the same $\left(\rho R_{\text{tot}}, T_i^h\right)$ plane. Hydro-equivalent curves are defined as curves with constant adiabat and implosion velocity. Since the laser energy is the only parameter varying along such curves, they can be used to predict how a given implosion would perform when scaled up to a larger laser. For example, any implosion carried out on OMEGA[12] is represented by a point on a hydro-equivalent curve. By increasing the laser energy and keeping the implosion hydro-equivalent, the point on the diagram moves along the hydro-equivalent curve. If that point ends up within the ignition region for NIF-like energies, one can then conclude that particular OMEGA implosion scales to one-dimensional ignition on the National Ignition Facility (NIF).[14]

The remaining sections of this article (1) describe the analytic ignition model and derive its initial conditions; (2) derive the ignition condition from the analytic model and compare it with the results of one-dimensional hydrodynamic simulation; (3) discuss the assumptions concerning the alpha-particle confinement and compare with previous forms of ignition condition; and (4) derive the hydro-equivalent curves and discuss them in the conclusions.

Dynamic Model of Thermonuclear Ignition

The dynamic model described in this section includes standard energy losses and sources (heat conduction, radiation losses, alpha heating) as well as compression and expansion dynamics of a hot spot surrounded by a dense shell. The model describes the assembly phase of the hot spot up to ignition. It does not include the propagation of the burn wave or the disassembly of the ignited fuel. As such, energy gains are not calculated and the focus is restricted to the onset of thermonuclear instability in the hot spot (i.e., ignition).

In the derivation of ignition conditions, the hydrodynamic model of Refs. 7 and 8 is closely followed. During assembly of the hot spot, its temperature is high and the flow velocity is less than the hot spot's sound speed. Thus, the subsonic model of Refs. 7 and 8 is adopted and the kinetic energy with respect to the internal energy inside the hot spot is neglected. It is assumed that most of the alpha particles generated from the fusion reactions deposit their energy into the hot spot, requiring that the size of the hot spot exceeds the alpha particle's mean free path. This condition depends on the hot spot's areal density and temperature and is verified *a posteriori*. Energy losses in the hot spot include heat conduction and bremsstrahlung radiation. Conservation of the hot spot's energy including the *pdV* work of the shell, the alpha-particle heating, and the conduction and radiation energy losses, can be written in the following simple form:

$$\frac{\partial}{\partial t}\left(\frac{p}{\gamma-1}\right)+\nabla\times\left[\vec{u}\left(\frac{\gamma p}{\gamma-1}\right)\right]=\nabla\times\kappa(T)\nabla T+\frac{\theta\rho^2}{4m_i^2}\langle\sigma v\rangle\varepsilon_\alpha-\nabla\cdot\vec{F}, \quad (1)$$

where $\rho(r,t)$, $p(r,t)$, $\vec{u}(r,t)$ are the hot-spot density, pressure, and velocity, respectively. Here γ is the ratio of specific heats or adiabatic index ($\gamma = 5/3$) and $\kappa(T) = \kappa_0 T^\nu$ is the Spitzer thermal conductivity with $\nu = 5/2$. The second term on the right-hand side of Eq. (1) represents the alpha particle's energy deposition, with θ being the absorbed alpha-particle fraction depending on the hot spot's areal density and temperature, m_i the ion mass for DT, $\varepsilon_\alpha = 3.5$ MeV the alpha-particle energy from DT reactions, and $\langle\sigma v\rangle$ the fusion reaction rate as a function of the ion temperature T. The last term is the bremsstrahlung radiation. The radiation flux $\vec{F}$ is the first moment of the radiation field over angle[15] integrated over all frequencies. The radiation flux $\vec{F}$ depends on both the bremsstrahlung radiation and absorption processes. The bremsstrahlung emission[1,16] for the hot-spot plasma is expressed in terms of its pressure and temperature as $j = C_1 p^2 T^{-3/2}$, where $C_1 \approx 3.88 \times 10^{-29}\, Z^3/(1+Z)^2$ in $\mathrm{m} \times \mathrm{J}^{5/2} \times \mathrm{s}^{-1} \times \mathrm{N}^{-2}$, pressure p in $\mathrm{N/m^2}$, temperature T in J, and j in $\mathrm{W/m^3}$.

Inside the hot spot, the temperature is high and the plasma is optically thin. At the interface of the hot spot and the cold shell, the temperature drops significantly and much of the radiation energy escaping the hot spot is absorbed near the inner shell surface. The mean free path (l) of photons[1,16] with energy $h\nu$ in a DT plasma is

$$l \approx 2.25 \times 10^4 \frac{\sqrt{T}\,(h\nu)^3}{\rho^2}, \tag{2}$$

where l is in μm, ρ is the plasma density in g/cm^3, T is the plasma temperature in keV, and $h\nu$ is in keV. Consider the free–free emission in a marginal's ignited hot spot of typical radius ~50 μm, temperature 5 keV, and density ~50 g/cm^3. Most of the radiation energy is carried by photons with energy below 5 keV. According to Eq. (2), the mean free path of 5-keV photons ($l \sim 2500\ \mu$m) is much longer than the size of the hot spot. Therefore, typical hot spots are transparent to bremsstrahlung radiation. On the contrary, a 5-keV photon has a very short mean free path in the cold shell surrounding the hot spot. For typical compressed shell densities of ~600 g/cm^3 and temperatures of ~200 eV, the mean free path of a 5-keV photon is only 3.5 μm, much shorter than the typical dense shell thickness of 50 μm. This shows that in the fuel assembly of typical ICF implosions, the hot spot is optically thin and the opacity increases sharply near the shell's inner surface, resulting in a narrow absorption zone with strong attenuation at the hot spot/shell interface.

For typical ICF plasmas near stagnation, the hot-spot temperature is high enough that its sound speed exceeds the flow velocity. The fuel assembly develops an isobaric configuration,[7,8,17] and the hot spot has a flat pressure profile with $p \approx p(t)$. The temperature of the high-density shell is much less than that of the low-density hot spot. By neglecting the radiation energy, a self-similar solution for the hot-spot temperature[7] is obtained as $T = T_0 \hat{T}(\hat{r})$, where T_0 is the central temperature in the hot spot and $\hat{r}$ is the radius r normalized to the hot-spot radius R_h as $\hat{r} = r/R_h$,

$$\hat{T} \approx \left(1 - \hat{r}^2\right)^{2/5} \Big/ \left(1 - 0.15\hat{r}^2\right).$$

This profile indicates $T(\hat{r} = 1) \to 0$ at the boundary between the hot spot and the shell. The radiation flux reaching the hot-spot boundary is

$$F(R_h) = \int_0^{R_h} j r^2 \mathrm{d}r = C_1 p^2 T_0^{-3/2} R_h^3 \int_0^1 \hat{T}^{-3/2} \hat{r}^2 \mathrm{d}\hat{r}.$$

This radiation flux is absorbed and recycled back into the hot spot with the ablated material at the shell's inner surface. As the heat conduction losses are also recycled back into the hot spot via the ablated shell material, both effects alter the hot-spot temperature's evolution without appreciably changing the pressure.

After integrating Eq. (1) from 0 to the hot-spot radius $R_h(t)$, the heat conduction and radiation terms vanish since, as stated above, most of the heat and radiation fluxes are absorbed near the shell's inner surface; thus, the volume integral of the energy in Eq. (1) yields

$$\frac{1}{2}\dot{p}R_h^3 + \frac{5}{2}pR_h^2 u\left(R_h,t\right) = \frac{p^2 R_h^3}{(1+Z)^2}\int_0^1 \hat{r}^2 \frac{\theta\varepsilon_\alpha \langle\sigma v\rangle}{4T^2}\mathrm{d}\hat{r}, \tag{3}$$

where $\dot{p}$ is the time derivative of the pressure and $u(R_h,t)$ is the flow velocity at the shell's inner surface. The shell material is ablated into the hot spot as a result of the heat and radiation energy deposited at the shell's inner surface. The flow velocity resulting from the combination of the inner surface motion and the ablative flow is

$$u\left(R_h,t\right) = \dot{R}_h - V_a, \tag{4}$$

where V_a is the ablation velocity and $\dot{R}_h$ scales with the implosion velocity. Since $V_a \ll \dot{R}_h$, the ablation velocity can be neglected and Eq. (3) can be rewritten as

$$\frac{\mathrm{d}}{\mathrm{d}t}\left(pR_h^3\right) + 2pR_h^2\dot{R}_h = \frac{2p^2R_h^3}{(1-Z)^2} f(T). \tag{5}$$

Notice that pR_h^3 is proportional to the total internal energy of the hot spot and $pR_h^2\dot{R}_h$ to the pdV work. The function $f(T)$, defined as $f(T) \equiv \left(\theta\varepsilon_\alpha/4\right)\int_0^1 \hat{r}^2\left(\langle\sigma v\rangle/T^2\right)\mathrm{d}\hat{r}$ represents the alpha-particle heating with the fusion reactivity being a function of the temperature T. Observe that $f(T)$ is constant if $\langle\sigma v\rangle$ is approximated with a quadratic power-law dependence on the temperature.

Some of the points made here about the recycling of the heat-conduction losses into the hot spot were also highlighted in Refs. 7, 8, and 17. In Ref. 17, it was also argued that a similar effect applies to the alpha particles leaving the hot spot. That is, the alpha particles leaving the hot spot are efficiently stopped by the dense shell within a narrow layer, thus causing the dense shell material to ablate into the hot spot. The ablated material would recycle the alpha particle's energy back into the hot spot in the form of internal energy of the ablated material. As argued in Ref. 17, similarly to the heat conduction, alpha-particle losses do not lead to a lower hot-spot energy (i.e., pressure) but only to a lower temperature. In this optimistic scenario, the parameter θ in Eq. (1) would be close to unity since all the alpha-particle energy is retained within the hot spot. In our model, we set $\theta \approx 1$ and verify *a posteriori* whether or not the hot spot's areal density is large enough to confine most of the alphas (see the **Alpha-Particle Confinement** section, p. 213).

To simplify the analysis, we use a simple numerical fit of $f(T)$ as a power of the temperature $f(T) = \left(\varepsilon_\alpha T_*^\sigma \big/ 4c_k^2 + \sigma\right) C_0 \hat{T}^\sigma$ after integration over the hot-spot volume, where $c_k = 1.6 \times 10^{-16}$ J/keV, $\varepsilon_\alpha = 5.6 \times 10^{-13}$ J, $C_0 \approx 2.6 \times 10^{-26}$ m$^3 \times$ keV$^{-3} \times$ s^{-1} for $\sigma = 1$ and T_* in J is defined later in Eq. (8). A comparison between the numerical fit and the accurate values of the fusion-reaction rate from Ref. 18 is shown in Fig. 116.39 for temperatures in the range of 3 to 8 keV. It is important to notice that the fusion reactivity follows a T^3 power law for temperatures $3 < T < 8$ keV and a T^2 power law for $8 < T < 25$ keV. To accurately capture the onset of the thermonuclear instability, we use a T^3 fit that is more accurate near the ignition threshold temperatures below 8 keV. Using the power-law dependence of fusion reactivity also helps to define the onset of the ignition process. In the power-law model, the thermonuclear instability does not saturate since the fusion burn continues until the fuel is depleted. This causes the solution of the ignition model to develop an explosive instability or mathematical singularity. It follows that one can identify the onset of ignition with the development of mathematical singularity. This can be easily explained by observing that in the absence of plasma motion $\left(\dot{R}_h = 0\right)$ and T^2 dependence of the reactivity, Eq. (5) reduces to

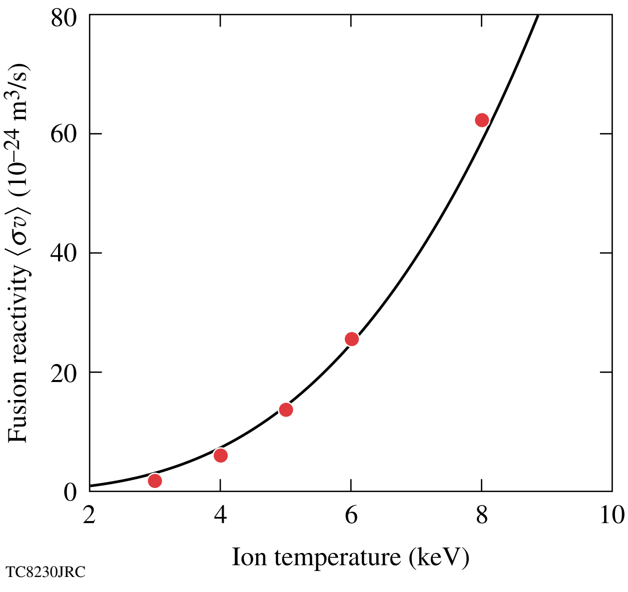

Figure 116.39

Fusion reactivity $\langle \sigma v \rangle$ is plotted as T^3 (solid curve). The dots are data taken from Ref. 18.

$$\frac{\mathrm{d}p}{\mathrm{d}t} = C_\alpha p^2, \tag{6}$$

where the right-hand side represents alpha-particle heating and $C_\alpha > 0$. Equation (6) yields the explosive solution for $t > t_0$,

$$p(t) = \frac{p(t_0)}{1 - C_\alpha p(t_0)(t - t_0)}. \tag{7}$$

If ignition occurs, our model develops an explosive solution even in the presence of energy losses. Equation (6) also helps to explain the difference in the heat-conduction treatment in Ref. 17 as compared to our model. Reference 17 makes the same argument made here (and in Ref. 7), that the heat conduction losses do not cause a net energy loss (p is not dependent on heat conduction) but do lead to a loss of temperature. Since in Ref. 17 ignition is defined as the condition for $\mathrm{d}T/\mathrm{d}t > 0$ [Eq. (26) of Ref. 17], the heat losses do enter into the ignition condition; however, the authors of Ref. 17 also realize that ignition can occur when $\mathrm{d}T/\mathrm{d}t < 0$. In this case, the temperature initially decreases but eventually reverses its course and increases rapidly. This form of ignition [which is not included in Eq. (26) of Ref. 17] can be included by defining ignition in terms of pressure increase ($\mathrm{d}p/\mathrm{d}t > 0$) rather than temperature increase ($\mathrm{d}T/\mathrm{d}t > 0$) as the pressure can increase even if the temperature decreases. Since our ignition model is dynamic, all the different paths to ignition are included with both pressure and temperature explosive growth.

It is useful to rewrite Eq. (5) in dimensionless form by defining the following normalization factors:

$$\begin{gathered} \tau = \frac{V_i t}{R_s}, \hat{p}(\tau) = \frac{p}{p_s}, \hat{R}(\tau) = \frac{R_h}{R_s}, \\ \hat{T}(\tau) = \frac{T_0}{T_*}, T_* = \left(\frac{25\mu_1}{48\pi\kappa_0} p_s R_s V_i\right)^{2/7}, \end{gathered} \tag{8}$$

where p_s and R_s are the hot-spot pressure and radius at stagnation and V_i is the implosion velocity. As will be shown in the **Solution of the Ignition Model and Marginal Ignition Condition** section (p. 209), T_* represents the stagnation temperature resulting from an adiabatic compression of the hot spot (in the absence of alpha heating and radiation losses). Here

T_* has the units of J with $\mu_1 \approx 0.55$ and $\kappa_0 = 3.7 \times 10^{69}$ m^{-1} × s^{-1} × J$^{-5/2}$ for $\ln\Lambda \approx 5$. For typical ICF implosion parameters, $T_*^{\mathrm{keV}} \equiv T_*/c_k$ falls in the range of 5 ~ 8 keV.

Using the power-law fit for $\langle \sigma v \rangle$ in Eq. (5) and substituting the dimensionless variables leads to the following simplified form of the energy equation:

$$\frac{\mathrm{d}}{\mathrm{d}\tau}\left(\hat{p}\hat{R}^5\right) = \gamma_\alpha \hat{p}^2 \hat{R}^5 \hat{T}^\sigma, \tag{9}$$

where $\gamma_\alpha = \left(\varepsilon_\alpha C_0 p_s R_s \big/ 2(1+Z)^2 c_k^{2+\sigma} V_i\right) T_*^\sigma$ is a parameter related to the initial shell condition at the beginning of the deceleration phase (see the **Initial Conditions** section, p. 209). Notice that Eq. (9) indicates that as long as the fusion reactivity $\langle \sigma v \rangle$ is proportional to ~T^2 and the alpha heating rate depends only on the pressure ($n^2 \langle \sigma v \rangle \sim p^2$), the temperature does not enter into the ignition condition. This is not the case for $\langle \sigma v \rangle \sim T^{3-4}$ since the fusion-reaction rate will depend on pressure *and* temperature ($n^2 \langle \sigma v \rangle \sim p^2 T^{1-2}$). Here, an additional equation describing the evolution of the temperature is required.

Since the pressure is determined by the *pdV* work and the alpha-particle heating, one can use mass conservation and the equation of state to evaluate the temperature. The evolution of the hot-spot density depends on the mass ablation rate off the shell. This was first calculated in Refs. 7 and 8 and later in Ref. 19. The ablation rate can be determined by integrating the energy in Eq. (1) across the hot-spot boundary. All divergent-free terms vanish as both temperature and radiation flux approach zero at the hot-spot boundary. A straightforward integration leads to

$$\frac{5}{2A}\dot{m}_a T_0 R_h^2 = \frac{6}{5}\kappa_0 T_0^{\nu+1} R_h + \mu_0 C_1 p^2 T_0^{-3/2} R_h^3, \tag{10}$$

where the ablative mass rate is $\dot{m}_a = \rho V_a = ApV_a \big/ T$, $A = m_i \big/ (1+Z)$, and $\mu_0 = \int_0^1 \hat{r}^2 \hat{T}^{-3/2} \mathrm{d}\hat{r} \approx 0.85$. Notice that Eq. (10) is derived by approximating the temperature profile with a step function, the correct limit of a $\nu \gg 1$ expansion. Equation (10), accurate to order $1/\nu$, describes the energy flux balance at the hot-spot boundary where the radiation and conduction energy flows are recycled back by the ablated material.

The total hot-spot mass can be expressed as

$$M_{\mathrm{hs}} = \int_0^{R_h} 4\pi\rho r^2 \mathrm{d}r = 4\pi\mu_1 A p R_h^3 \big/ T_0,$$

where $\mu_1 \approx 0.55$ is the value of the integral $\mu_1 = \int_0^1 \hat{r}^2 \big/ \hat{T} \mathrm{d}\hat{r}$ and T_0 is the hot spot's central temperature. Due to mass conservation, the change of the hot spot's mass is caused by mass ablation off the shell, $\mathrm{d}M_{\mathrm{hs}} \big/ \mathrm{d}t = 4\pi R_h^2 \dot{m}_a$. Substituting the above results into Eq. (10) yields

$$\frac{\mathrm{d}}{\mathrm{d}t}\left(\frac{pR_h^3}{T_0}\right) = \frac{12\kappa_0}{25\mu_1} R_h T_0^{5/2} + \frac{2\mu_0 C_1}{5\mu_1} \frac{p^2 R_h^3}{T_0^{5/2}}. \tag{11}$$

Notice that this equation governs the hot-spot temperature. Terms on the right-hand side represent heat conduction and radiation effects on the hot-spot temperature.

After a straightforward manipulation, the dimensionless form of the temperature equation can be written as

$$\frac{\mathrm{d}}{\mathrm{d}\tau}\left(\frac{\hat{p}\hat{R}^3}{\hat{T}}\right) = \hat{R}\hat{T}^{5/2} + \beta \frac{\hat{p}^2 \hat{R}^3}{\hat{T}^{5/2}}, \tag{12}$$

where $\beta = 2\mu_0 C_1 p_s^2 T_*^{-3/2} R_s \big/ 5\mu_1 p_s V_i$. Notice that β is proportional to the ratio between the total radiation energy emitted from the hot spot and the imploding shell's kinetic energy. The radiation energy is proportional to $C_1 p_s^2 T_s^{-3/2} R_s^3 \tau_c$ and the shell's kinetic energy is proportional to the hot spot's internal energy $MV_i^2 \sim p_s R_s^3$. As shown below, the time $\tau_c \sim R_s \big/ V_i$ represents the confinement time of the hot spot surrounded by a dense shell imploded with velocity V_i. Ignited ICF capsules require that the radiation energy be smaller than the compression work so that high temperatures can be reached in the hot spot. Furthermore, the bremsstrahlung losses are also smaller than the heat-conduction losses and do not appreciably alter the temperature profile, which is determined mostly by heat conduction.

The third and last equation of our ignition model governs the conservation of momentum of the thin shell surrounding the hot spot. The thin-shell approximation (discussed in Ref. 7) assumes that the entire shell kinetic energy is transferred to the internal energy of the hot spot upon stagnation. Even though the thin-shell model overestimates the stagnation energy, it yields the correct ignition scaling. This is shown in Ref. 8 where a more accurate shell model, the so-called "thick-shell" model, is compared with the "thin-shell" one. In the thick-shell model, the shell is treated as a finite-thickness, compressible gas, including the presence of a return shock driven by the rapid increase of the hot-spot pressure. A similar model was also later adopted in Ref. 19. While the thick shell is a more realistic (but more complicated) model than the thin-shell one, the ignition scaling is virtually the same. Furthermore, we will use the results of Refs. 9 and 20 to heuristically limit the transfer of kinetic energy from the shell to the hot spot, which, in the thin-shell model, is overestimated (100% transfer). Within the frame of the thin-shell model, the shell compresses the hot spot like a spherical piston and the equation of motion for the shell is simply the shell Newton's law $M_s\ddot{R} = 4\pi pR^2$. In dimensionless form, this equation can be rewritten using Eq. (8) as

$$\frac{\mathrm{d}^2\hat{R}}{\mathrm{d}\tau^2} = \hat{p}\hat{R}^2. \tag{13}$$

The shell Newton's law shows that the shell confinement time at stagnation scales as $\tau_c \sim \sqrt{M_s / p_s R_s}$. Since $M_s V_i^2 \sim p_s R_s^3$, the confinement time can be rewritten as $\tau_c \sim R_s / V_i$. During this time the hot spot's hydrodynamic pressure is at its peak value (in the absence of alpha heating). The shell's confinement time should not be confused with the burn time that depends on the shell's areal density (Ref. 1).

Equations (9), (12), and (13) represent a dynamic model of thermonuclear ignition. The next step is to determine the relevant set of initial conditions for the system of equations.

Initial Conditions

Based on the definition of the dimensionless variables, the initial condition of the thin-shell model requires that $\hat{R}(0) = R(0)/R_s$, $\dot{\hat{R}}(0) = -1$, $\hat{p}(0) = p(0)/p_s$, and $\hat{T}(0) = T_0(0)/T_*$, where $R(0)$, $p(0)$, $T_0(0)$ are the values of the radius, pressure, and central temperature at the beginning of the deceleration phase ($\tau = 0$) when the shell is imploding inward with its maximum velocity [$\mathrm{d}R/\mathrm{d}t(0) = -V_i$]. The stagnation values R_s and p_s can be defined through the energy conservation and adiabatic compression in the absence of alpha heating and radiation losses. In this case, energy conservation requires that $(1/2)M_s V_i^2 = (4\pi/3)p_s R_s^3$, while adiabatic compression requires that $p_s V_s^{5/3} = p(0)V(0)^{5/3}$ or $p_s R_s^5 = p(0)R(0)^5$. Using these relations, the initial conditions for the dimensionless variables can be rewritten as $\hat{R}(0) = \varepsilon_0^{-1/2}$, $\dot{\hat{R}}(0) = -1$, and $\hat{p}(0) = \varepsilon_0^{-5/2}$, where $\varepsilon_0 \equiv (1/2)M_s V_i^2 / (4\pi/3)p(0)R(0)^3$ is the ratio between the shell's kinetic energy and the hot spot's internal energy at the beginning of the deceleration phase. Notice that $\varepsilon_0 \gg 1$ in typical ICF implosions where the hot spot's energy is amplified many times during the deceleration of the shell. The initial condition for the temperature requires a special treatment. We start by integrating in Eq. (12) from the beginning of the deceleration phase ($\tau = 0$) to stagnation (τ_s). The stagnation values for the dimensionless variables are $\tau_s = \varepsilon_0^{1/2}$, $\hat{p}(\tau_s) = 1$, $\hat{R}(\tau_s) = 1$, and $\hat{T}(\tau_s) = 1$. The initial temperature $\hat{T}(0)$ can be inferred from an analysis of the temperature in Eq. (12). At the beginning of the deceleration phase, both pressure and temperature are small and the radiation losses can be neglected with respect to heat losses. Neglecting the alpha-particle heating during the hot-spot assembly phase (that is, $\gamma_\alpha = 0$) results in the adiabatic compression of the hot spot, leading to $\hat{p}\hat{R}^5 = 1$. Thus, the temperature defined in Eq. (12) can be rewritten as

$$\frac{\mathrm{d}\hat{\phi}}{\mathrm{d}\tau} = \hat{\phi}^{-5/2}\hat{R}^{-4}, \tag{14}$$

where $\hat{\phi} \equiv \hat{p}\hat{R}^3/\hat{T}$. The solution of Eq. (14) is

$$\hat{\phi}(\tau)^{7/2} = \hat{\phi}(0)^{7/2} + (7/2)\int_0^\tau \hat{R}^{-4}\mathrm{d}\tau.$$

For large $\varepsilon_0 \gg 1$, one expects the stagnation temperature to be independent of its value at the beginning of the deceleration phase (as long as the initial value is much smaller than the stagnation value). Thus, one requires that $I \equiv (7/2)\int_0^\tau \hat{R}^{-4}\mathrm{d}\tau \gg \hat{\phi}(0)^{7/2}$. Defining $\dot{\hat{R}} = \mathrm{d}\hat{R}/\mathrm{d}\tau$, the integral I can be rewritten as $I = (7/2)\int_0^\infty \hat{R}^{-4}\dot{\hat{R}}^{-1}\mathrm{d}\hat{R}$. Notice that most of the contribution to the integral I comes from the stagnation values $\hat{R} \approx \hat{R}(\tau_s) = 1$ and $\dot{\hat{R}} \approx \hat{R}(\tau_s) \approx 0$. By using the shell Newton's law [Eq. (13)], one finds that $\dot{\hat{R}}(\tau_s) \approx 1$ and the shell velocity $\dot{\hat{R}}$ can be approximated by $\dot{\hat{R}} \approx \sqrt{2(\hat{R}-1)}$ near stagnation. Substituting into I and integrating over $\hat{R}$ yields $I = \left(5\pi/16\sqrt{2}\right)$. At the beginning of the deceleration phase, the initial value of $\hat{\phi}$ is $\hat{\phi}(0) = \hat{p}(0)\hat{R}(0)^3/\hat{T}(0) = \left[\varepsilon_0\hat{T}(0)\right]^{-1}$. To guarantee a stagnation temperature independent of its initial value, one needs to choose $\varepsilon_0^{-1} \ll \hat{T}(0) \ll 1$. Any value of $\hat{T}(0) = \varepsilon_0^\omega$ with $-1 < \omega < 0$ satisfies this condition, and the resulting solution of the ignition model is independent of ε_0 and ω as long as $\varepsilon_0 \to \infty$. Here we choose $\omega = 1/2$ and $\hat{T}(0) = \varepsilon_0^{-1/2} \ll 1$.

Solution of the Ignition Model and Marginal Ignition Condition

Our ignition model consists of the three equations [(9), (12), and (13)] representing mass, momentum, and energy conservation, with the initial conditions derived in the **Initial Conditions** section (p. 209). For convenience, the equations and initial conditions are summarized below:

$$\begin{gathered}
\frac{\mathrm{d}}{\mathrm{d}\tau}\left(\hat{p}\hat{R}^5\right) = \gamma_\alpha \hat{p}^2\hat{R}^5 T^\sigma \\
\frac{\mathrm{d}}{\mathrm{d}\tau}\left(\frac{\hat{p}\hat{R}^3}{\hat{T}}\right) = \hat{R}\hat{T}^{5/2} + \beta\frac{\hat{p}^2\hat{R}^3}{\hat{T}^{5/2}} \\
\frac{\mathrm{d}^2\hat{R}}{d\tau^2} = \hat{p}\hat{R}^2 \\
\hat{p}(0) = \varepsilon_0^{-5/2}, \hat{T}(0) = \varepsilon_0^{-1/2}, \hat{R}(0) = \varepsilon_0^{1/2}, \hat{R}(0) = -1.
\end{gathered} \tag{15}$$

Equations (15) are numerically solved up to the stagnation time $\tau \sim \tau_s = \varepsilon_0^{1/2}$ for a large value of $\varepsilon_0 \gg 1$, and $\sigma = 1$ is used in the computation. The solution develops an explosive instability when the parameter γ_α exceeds a critical value for a preset value of β. Here, we are interested in the asymptotic value of γ_α for $\varepsilon_0 \to \infty$ (we use $\varepsilon_0 = 10^4$ in the numerical integration). Physically, this instability corresponds to the onset of ignition. The critical values of γ_α and β are obtained through a series of numerical solutions of the system of Eqs. (15) and shown in Fig. 116.40, where each dot represents a single pair of γ_α and β such that the solution of the equations turns singular for both pressure and temperature. The ignition curve in Fig. 116.40 can be accurately fitted by the following simple formula:

$$\gamma_\alpha = 1.12 + \beta^2 + 0.28\beta^3. \tag{16}$$

Within the frame of the thin-shell model, the shell thickness is negligible. The effects of finite thickness can be included, however, by noticing that only a fraction of the shell's kinetic energy is converted into hot-spot internal energy. That fraction is related to the ratio of the hot spot and shell volume at stagnation and can be written as $(1 + A^{-1})^{-3}$, where A is the aspect ratio defined as the hot-spot radius R_h over the shell thickness Δ, $A = R_h/\Delta$. The total mass is expressed as $M = 4\pi(\rho\Delta)R_s^2\Sigma(A)$ (Ref. 20) with the volume factor Σ defined as $\Sigma(x) = 1 + (1/x) + 1/(3x^2)$.

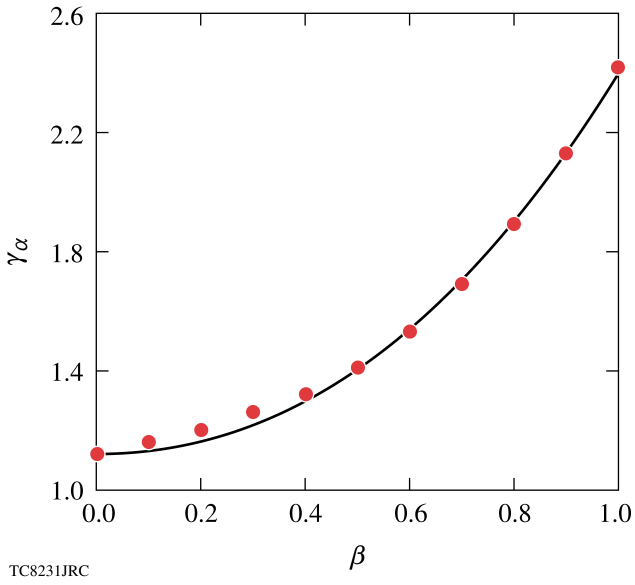

Figure 116.40
Relation between γ_α and β. Each dot represents a single pair of γ_α and β such that the solution of Eqs. (15) turns singular. The solid curve is the fitting formula $\gamma_\alpha(\beta)$ in Eq. (16).

Thus, the important parameter γ_α in the ignition condition can be rewritten as

$$\gamma_\alpha = \frac{\varepsilon_\alpha C_0 T_*^\sigma}{2(1+Z)^2 c_k^{2+\sigma}} \frac{\sqrt{M}\sqrt{MV_i^2\Big/\left(1+A^{-1}\right)^3}}{4\pi R_s^2}$$

$$= \frac{\varepsilon_\alpha C_0 T_*^\sigma}{2(1+Z)^2 c_k^{2+\sigma}} \frac{\Sigma(A)}{\left(1+A^{-1}\right)^{3/2}}(\rho\Delta)V_i. \tag{17}$$

Similarly, the temperature normalization factor T_* can be written as

$$T_* = \left(\frac{25\mu_1}{48\pi\kappa_0} \times \frac{M_s V_i^3}{R_s^2}\right)^{2/7}$$

$$= \left(\frac{25\mu_1}{12\kappa_0} \times \frac{\Sigma(A)(\rho\Delta)V_i^3}{\left(1+A^{-1}\right)^{9/2}}\right)^{2/7}. \tag{18}$$

For typical ICF implosions, the stagnation aspect ratio A usually falls within the range of $1 < A < 4$ (Ref. 20). Within this interval, the function $\Sigma(A)/(1 + A^{-1})^{9/2}$ can be approximated by the power law, $\Sigma(A)/(1 + A^{-1})^{9/2} \approx 0.12A^{1.045}$. Since the stagnation aspect ratio scales with the implosion velocity and shell adiabat as $A \approx 8.2 \times 10^{-6} V_i^{0.96}/\alpha^{0.19}$ (Ref. 9), the function $\Sigma(A)$ can be approximated as

$$\Sigma(A)\Big/\left(1+A^{-1}\right)^{9/2} \approx \delta_0 V_i\Big/\alpha^{0.2},$$

with the constant $\delta_0 = 5.7 \times 10^{-7}$ s/m. Substituting into Eq. (18) and solving for the implosion velocity yields

$$V_i = \left(\frac{12\kappa_0}{25\mu_1\delta_0}\right)^{1/4} \alpha^{0.05}(\rho\Delta)^{-1/4} T_*^{7/8}. \tag{19}$$

Notice that the adiabat dependence is very weak, so it is neglected in the following derivation. Furthermore, the aspect ratio's dependence in Eq. (17) can be approximated with a constant, $\Sigma(A)/(1 + A^{-1})^{3/2} \approx 0.85$ for $1 < A < 4$. Substituting this result and Eq. (19) into Eq. (17), one finds the γ_α dependence on the areal density $\rho\Delta$ and temperature T_*:

$$\gamma_\alpha = \frac{0.85\varepsilon_\alpha C_0}{2(1+Z)^2 c_k^{2+\sigma}} \left(\frac{12\kappa_0}{25\mu_1\delta_0}\right)^{1/4} (\rho\Delta)^{3/4} T_*^{\sigma+7/8}. \tag{20}$$

The parameter β can be expanded in the same manner as above. Notice that $\beta/\gamma_\alpha \sim T_*^{-\sigma-3/2}$ and β can be written in the following form:

$$\beta = \frac{0.34\,\mu_0 C_1}{\mu_1}\left(\frac{12\,\kappa_0}{25\,\mu_1\delta_0}\right)^{1/4}(\rho\Delta)^{3/4}T_*^{-5/8}. \tag{21}$$

In both Eqs. (20) and (21), the units of $\rho\Delta$ and T_* are in kg/m^2 and J, respectively. To express T_* in keV in these equations, γ_α and β can be rewritten as

$$\begin{aligned}
\gamma_\alpha &= C_3(\rho\Delta)^{3/4}\left(T_*^{\mathrm{keV}}\right)^{15/8},\\
C_3 &= \frac{0.85\varepsilon_\alpha C_0}{2(1+Z)^2 c_k^{9/8}}\left(\frac{12\,\kappa_0}{25\,\mu_1\delta_0}\right)^{1/4},\\
\beta &= C_4(\rho\,\Delta)^{3/4}\left(T_*^{\mathrm{keV}}\right)^{-5/8},\\
C_4 &= \frac{0.34\,\mu_0 C_1}{\mu_1 c_k^{5/8}}\left(\frac{12\,\kappa_0}{25\,\mu_1\delta_0}\right)^{1/4},
\end{aligned} \tag{22}$$

where $Z = 1$ for DT plasma, $\varepsilon_\alpha = 3500$, $c_k = 5.6 \times 10^{-13}$ J, $C_0 = 2.6 \times 10^{-26}$ m^3 × keV^{-3} × s^{-1}, $\mu_0 = 0.85$, $\mu_1 = 0.55$, $\kappa_0 = 3.7 \times 1069$ m^{-1} × s^{-1} × J$^{-5/2}$, $\delta_0 = 5.7 \times 10^{-7}$ m^{-1} × s. Using $C_1 = 9.7 \times 10^{-30}$ m × J$^{5/2}$ × s^{-1} × N^{-2} for $Z = 1$ leads to $C_4 \approx 0.327$ keV$^{5/8}$ m$^{3/2}$ × kg$^{-3/4}$, and the parameter $\beta \le 1$ for typical values of areal density and temperature. Using $C_0 \approx 2.6 \times 10^{-26}$ m^3 × keV^{-3} × s^{-1} into the first equation of (22) yields $C_3 \approx 7.6 \times 10^{-3}$ keV$^{-15/8}$ × m$^{3/2}$ × kg$^{-3/4}$ for DT fuel.

The next step is to relate the parameter T^* to the maximum temperature in the absence of alpha heating $\left(T_{\max}^{\text{no }\alpha}\right)$. Such a temperature is approximately equal to the temperature measured in D$_2$ targets or sub-ignited DT implosions where the self-heating plays a negligible role in the hot-spot energy balance. A more detailed discussion of the validity of $T_{\max}^{\text{no }\alpha}$ as a measurable parameter is included in the **Conclusions** (p. 216). The value of $T_{\max}^{\text{no }\alpha}$ is found by setting $\gamma_\alpha = 0$ and by solving Eq. (15) for various values of β. The maximum of the solution for $\hat{T}$ corresponds to $T_{\max}^{\text{no }\alpha}/T_*$. A series of numerical solutions lead to the following relations between the parameter β and the maximum hot-spot temperature $\hat{T}_{\max}^{\text{no }\alpha}$ without alpha heating:

$$\begin{aligned}
\hat{T}_{\max}^{\text{no }\alpha} &= \frac{T_{\max}^{\text{no }\alpha}}{T_*} = \frac{0.78}{\Pi(\beta)},\\
\Pi(\beta) &= 1 + 0.42\beta^{0.9} + 1.7\times 10^{-3}\beta^{1.8},
\end{aligned} \tag{23}$$

as shown in Fig. 116.41. Using Eq. (23) and the definitions of γ_α and β in Eqs. (22), one can easily rewrite the ignition condition as

$$(\rho\Delta)\left(T_{\max}^{\text{no }\alpha}\right)^{5/2} = 33.5\,\frac{\left[\gamma_\alpha(\beta)\right]^{4/3}}{\Pi(\beta)^{5/2}}, \tag{24}$$

where $\rho\Delta$ is in g/cm^2, $T_{\max}^{\text{no }\alpha}$ is in keV, γ_α is given in Eq. (16), and β can be determined in terms of $T_{\max}^{\text{no }\alpha}$ from the following equation:

$$\frac{\beta\Pi(\beta)^{5/2}}{\lambda_\alpha(\beta)}\left[\frac{3.4}{T_{\max}^{\text{no }\alpha}}\right]^{5/2}. \tag{25}$$

Notice that for large temperatures $T_{\max}^{\text{no }\alpha} \gg 3.4$ keV, β is small and the ignition condition reduces to

$$(\rho\Delta)\left(T_{\max}^{\text{no }\alpha}\right)^{5/2} = 33.5\ \mathrm{g/cm^2 keV^{2.5}}.$$

Numerically solving Eq. (25) for various $T_{\max}^{\text{no }\alpha}$ in the range $2.5 < T_{\max}^{\text{no }\alpha} < 8$ keV to find β and substituting $\beta\left(T_{\max}^{\text{no }\alpha}\right)$ into

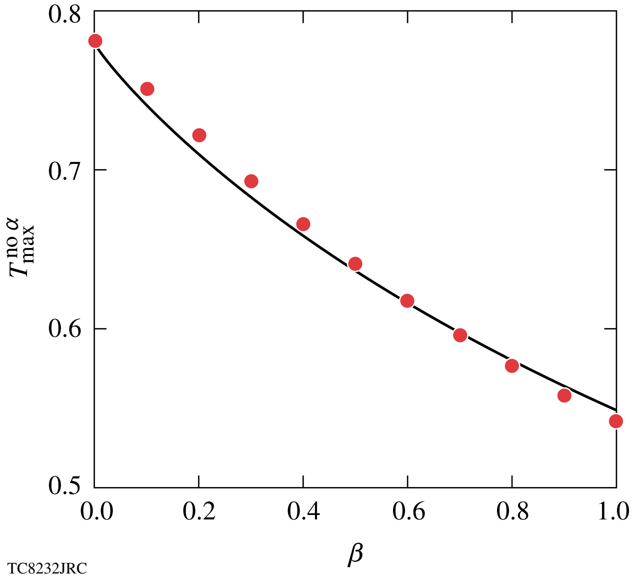

Figure 116.41
Relation between $\hat{T}_{\max}^{\text{no }\alpha}$ and β. Each dot represents a single pair of $\hat{T}_{\max}^{\text{no }\alpha}$ and β by solving Eqs. (15) with $\gamma_\alpha = 0$ for various β. $\hat{T}_{\max}^{\text{no }\alpha}$ is the maximum value of $\hat{T}$ in the solution. The solid curve is the fitting formula $\hat{T}_{\max}^{\text{no }\alpha}(\beta)$ in Eq. (23).

Eq. (24) yields the ignition condition in terms of the two measurable parameters $\rho\Delta$ and $T_{\max}^{\text{no}\,\alpha}$. Figure 116.42 shows the ignition condition in the $\rho\Delta$, $T_{\max}^{\text{no}\,\alpha}$ plane. A simple fit of the ignition condition, accurate to within ±10% in the range $4 < T_{\max}^{\text{no}\,\alpha} < 8$, is given by

$$(\rho\,\Delta)\approx\frac{2.5}{\left(T_{\max}^{\text{no}\,\alpha}\right)^{1.18}\left[1-\left(\frac{3}{T_{\max}^{\text{no}\,\alpha}}\right)^{2.5}\right]}\,. \qquad (26)$$

The solid curve in Fig. 116.42 shows the numerical fit in relation to the exact numerical solution of the ignition model (dots). Notice that Eq. (26) exhibits a singularity for $T_{\max}^{\text{no}\,\alpha}\approx 3$ keV, indicating that at such low temperatures, ignition requires very large areal densities. The areal density in Eq. (26) refers to the shell's areal density without including the hot spot's contribution. The hot spot's contribution to the areal density is typically small except for marginally ignited targets at high temperatures. As shown in Fig. 116.42, when the $T_{\max}^{\text{no}\,\alpha}$ temperatures increase, the shell's areal density required for marginal ignition falls below 0.5 g/cm^2. At such low values, the areal densities of both the shell and the hot spot are of the same order and the hot spot's contribution is a significant portion of the total areal density. In the next section, the total areal density from a set of hydrodynamic simulations is used to generate an ignition curve similar to the one in Fig. 116.42. Therefore, significant discrepancies between the theoretical and numerical results are expected at high ignition temperatures. A detailed discussion of the validity of Eq. (26) and a comparison with the results of numerical simulations are the subjects of the next section.

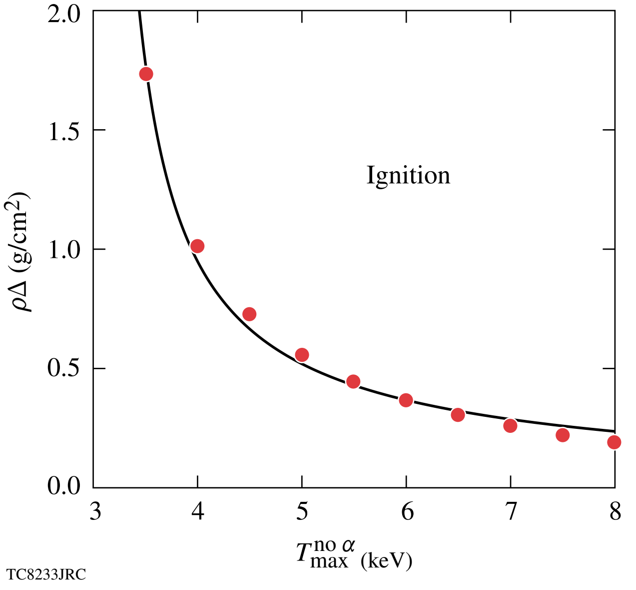

Figure 116.42
Relation between $\rho\Delta$ and $T_{\max}^{\text{no}\,\alpha}$ according to the ignition model of Eq. (15). Each dot represents a single pair of $\rho\Delta$ and $T_{\max}^{\text{no}\,\alpha}$ from the solution of Eqs. (24) and (25) for $4 < T_{\max}^{\text{no}\,\alpha} < 8$. The solid curve is the fitting formula in Eq. (26) and represents the marginal ignition condition.

Hydrodynamic Simulations

About 20 marginally ignited direct-drive targets have been simulated with the one-dimensional Lagrangian radiation-hydrodynamic code *LILAC*.[21] *LILAC* is routinely used for ICF target design studies at the Laboratory for Laser Energetics. It includes *SESAME*[22] equation-of-state tables, flux-limited Spitzer thermal conduction (the value of the flux limiter is set at $f = 0.06$), multigroup radiation transport, multigroup alpha-particle transport, and 3-D laser ray tracing. The targets used in the simulations were spherical shells consisting of a single DT-ice layer or two layers of wetted-foam [$(\text{DT})_6\text{CH}$] and pure-DT ice. All targets were filled with 1 atm of DT gas at 2.1×10^{-4} g/cm^3, and the initial aspect ratio of the targets varied from 2.0 to 5.5. The relaxation (RX) adiabat shaping[23] technique was used to design most of the laser pulse shapes for these implosions. The relaxation (RX) laser pulse consisted of a prepulse followed by an interval of laser shut-off and the main pulse. Such a laser pulse is used to shape the adiabat in the ablator. In these simulations, the UV driver energy varies from 35 kJ to 10 MJ, adiabat from 0.7 to 4, and implosion velocity from 1.75 to 5.3×10^7 cm/s. These targets are designed to achieve marginal ignition with minimum laser energy. In the simulations, marginal ignition is defined as gain = 1 (fusion energy = laser energy on target). These implosions are also simulated without alpha energy deposition to compute the areal density and the no-alpha ion temperature used in the ignition condition (previous section).

Each dot in Figs. 116.43 and 116.44 shows the areal density and ion temperature of each marginally ignited target. Figure 116.43 shows the maximum total areal density and the maximum hot-spot-volume–averaged, no-alpha ion temperature (the volume average is carried out over the hot-spot volume). Observe that all the points lie on a curve (i.e., the ignition curve). The latter can be accurately approximated (Fig. 116.43) by the following fitting formula:

$$\rho R_{\max}\approx\frac{33.5}{\langle T^{\text{no}\,\alpha}\rangle_v^{5/2}\left[1-\left(\frac{1.2}{\langle T^{\text{no}\,\alpha}\rangle_v}\right)^{5/2}\right]^{4/3}}\,, \qquad (27)$$

where $\rho R_{\max}$ is in g/cm^2 and $T^{\text{no}\,\alpha}$ is in keV. Similarly, Fig. 116.44 shows the ignition points in terms of the burn-

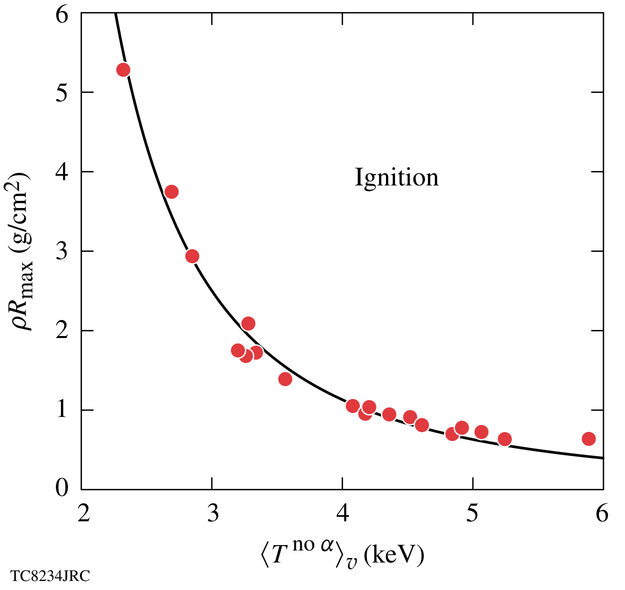

Figure 116.43
Relation between the maximum total areal density (ρR_{max}) and the maximum hot-spot volume-averaged, no-alpha ion temperature ($\langle T^{\text{no}\,\alpha}\rangle_v$) for marginally ignited targets. Each dot represents a single simulation from the 1-D hydrocode *LILAC*. The solid curve is the fitting formula in Eq. (27).

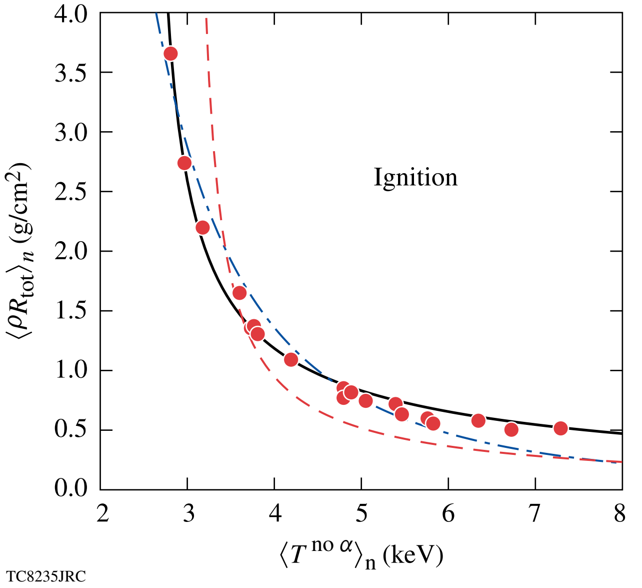

Figure 116.44
Relation between neutron-averaged, no-alpha temperature ($\langle T_i^{\text{no}\,\alpha}\rangle_\text{n}$) and neutron-averaged total areal density ($\langle \rho R_{\text{tot}}\rangle_\text{n}$) for marginally ignited targets. Each dot represents a single simulation from 1-D hydrocode. The solid curve is the fitting formula in Eq. (28). The dashed–dotted curve is the approximation of the ignition curve in Eq. (29). The dashed curve is the ignition model given in Eq. (26) of the **Solution of the Ignition Model and Marginal Ignition Condition** section (p. 209).

averaged areal density and the burn-averaged ion temperature. The burn-averaged areal density is defined as the total areal density weighted in time with the neutron rate. The burn-averaged temperature is the temperature weighted in time and space with the fusion reaction rate. Even in the $\langle \rho R_{\text{tot}}\rangle_\text{n}$, $\langle T_i^{\text{no}\,\alpha}\rangle_\text{n}$ plane the simulated marginal ignition points lie on an ignition curve. This curve is of particular importance since $\langle \rho R_{\text{tot}}\rangle_\text{n}$, $\langle T_i^{\text{no}\,\alpha}\rangle_\text{n}$ are the only two measurable parameters of the fuel assembly in an ICF implosion. The burn-averaged total areal density can be inferred from the downshift of the spectrum of charged fusion products,[13] and the burn-averaged ion temperature can be measured with the neutron time-of-flight diagnostics (nTOF's).[10] One can argue that the measurements give $\langle T_i\rangle_\text{n}$ instead of $\langle T_i^{\text{no}\,\alpha}\rangle_\text{n}$. The two parameters are virtually identical, however, for D_2 surrogate implosions or sub-ignited DT implosions with gain $\ll 1$. The ignition curve in Fig. 116.44 can also be approximated with a simple fitting formula

$$\langle \rho R_{\text{tot}}\rangle_\text{n} = \frac{3.4}{\langle T^{\text{no}\,\alpha}\rangle_\text{n}^{0.97}\left[1-\left(\dfrac{2.5}{\langle T^{\text{no}\,\alpha}\rangle_\text{n}}\right)^{2.5}\right]^{0.79}}, \qquad (28)$$

where $\langle \rho R_{\text{tot}}\rangle_\text{n}$ is in g/cm^2 and $\langle T^{\text{no}\,\alpha}\rangle_\text{n}$ is in keV. Equation (28), plotted as the solid curve in Fig. 116.44, is the most useful form of the ignition condition that can be directly measured. A rough approximation of the ignition curve can be cast into a simple power law

$$\langle \rho R_{\text{tot}}\rangle_\text{n} \times \langle T_i^{\text{no}\,\alpha}\rangle_\text{n}^{2.6} > 50 \text{ g} \times \text{cm}^{-2} \times \text{keV}^{2.6}. \qquad (29)$$

The dashed–dotted line in Fig. 116.44 shows the simple fit [Eq. (29)] in relation to the simulation results (dots). To compare the ignition condition from the analytic model in the previous section with the simulation results, we plot Eq. (26) in the $\langle \rho R_{\text{tot}}\rangle_\text{n}$ $\langle T_i^{\text{no}\,\alpha}\rangle_\text{n}$ plan of Fig. 116.44. The dashed curve in Fig. 116.44 shows the ignition model results as given in Eq. (26). This suggests that in spite of its simplicity, the ignition model captures the essential physics and the ignition condition [Eq. (26)] is in reasonable agreement with the simulation results. Notice that, as expected, the model prediction (dashed curve) falls below the simulation results at high temperatures since the hot-spot areal density is not accounted for.

Alpha-Particle Confinement

An important assumption used in the analytic model in the **Solution of the Ignition Model and Marginal Ignition Condition** section (p. 209) concerns the alpha-particle confinement. The assumption was made that most of the alpha particles slow down within the hot spot, and that the alpha-particle energy deposited inside the hot spot is close to 100% ($\theta \approx 1$). Since the alpha-energy deposition in the hot spot depends on its areal density and temperature,[24] we have computed the hot-spot areal densities and hot-spot temperature for the marginal ignited targets in our simulation database. Figure 116.45 shows the hot-spot areal density and temperature at marginal ignition from the 1-D simulations discussed in the previous section. Observe that all the marginally ignited targets have a hot-spot areal density above the critical value of 0.3 g/cm^2 often cited in the literature.[1,2] To estimate the fraction of absorbed alpha particles (θ), we use the results of Ref. 24 to find that

$$\theta = \frac{3\tau}{2} - \frac{4}{5}\tau^2,\ \tau \le \frac{1}{2};$$

$$\theta = 1 - \frac{1}{4\tau} + \frac{1}{160\tau^2},\ \tau \ge \frac{1}{2}; \qquad (30)$$

$$\tau \approx 92(\rho R)_{\text{hs}} \Big/ T_h^{3/2},$$

where $(\rho R)_{\text{hs}}$ is the hot-spot areal density in g/cm^2 and T_h is the hot-spot temperature in keV. Substituting the areal densities and temperatures from Fig. 116.45 into Eq. (30) shows that the fraction of alpha energy deposited within the hot spot ranges from about 87% to 99% ($0.87 < \theta < 0.99$). Thus, our assumption that $\theta \approx 1$ seems to be satisfied at marginal ignition. It is also interesting to observe that, as shown in Fig. 116.45, ignition at no-alpha temperatures $\langle T_h^{\text{no}\,\alpha}\rangle$ below 4 keV requires a hot-spot areal density well above the 0.3-g/cm^2 critical value.

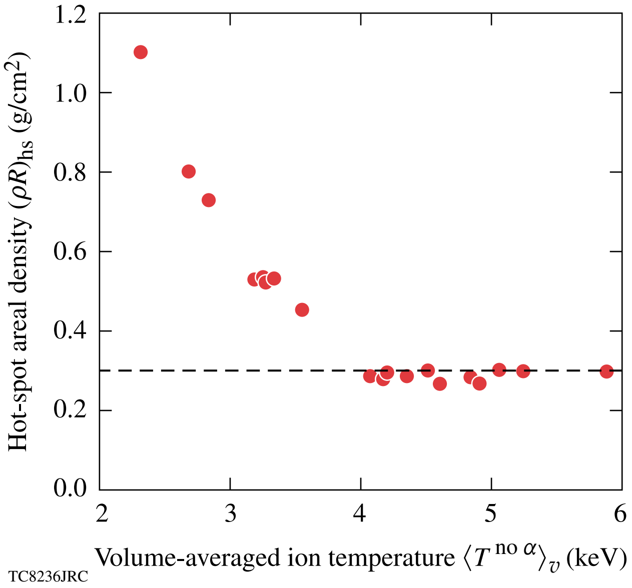

Figure 116.45
Hot-spot areal density $\left[(\rho R)_{\text{hs}}\right]$ and volume-averaged, no-alpha hot-spot ion temperature $\left(\langle T^{\text{no}\,\alpha}\rangle_v\right)$. Each dot represents a single simulation from 1-D hydrocode. The dashed line marks the hot-spot areal density of 0.3 g/cm^2.

For large hot-spot areal densities and low hot-spot temperatures, a significant fraction of the bremsstrahlung radiation and conductive heat flux is absorbed within the hot spot, thus preventing a severe temperature degradation. For these targets, the only confinement issue is with the hydrodynamic disassembly of the surrounding shells. Since high hot-spot areal densities are correlated with high shell areal densities,[9] the inertial confinement of such shells is very long and ignition can occur at very low no-alpha temperatures, as shown in Fig. 116.45.

Comparison with the HTL Ignition Condition

To test the validity of the ignition condition derived in this article, we compare it to the ignition criterion derived by Herrmann *et al.* in Ref. 25. We refer to the criterion of Ref. 25 as the Herrmann–Tabak–Lindl (HTL) ignition condition. The HTL condition is a more accurate extension of the ignition scaling of Levedahl and Lindl,[26] and it correlates the minimum shell kinetic energy required for ignition with the implosion velocity, shell adiabat, and ablation pressure. Since all our simulations are for direct-drive targets with maximum intensity around 10^{15} W/cm^2, we will use the form of the HTL condition rewritten in terms of laser energy on target rather than the shell kinetic energy as shown in Eq. (53) of Ref. 9. The relation between laser energy and kinetic energy is $E_{\text{L}} = E_\kappa / \eta$, where η is the overall hydrodynamic efficiency. For intensities of 10^{15} W/cm^2, our 1-D hydrodynamic simulations show an ablation pressure close to 200 Mbar at the end of the acceleration phase in spherical implosions. Using $I_{15} = 1$ and $P_L = 200$ Mbar into Eq. (53) of Ref. 9, we find the following modified HTL ignition criterion:

$$E_{\text{L}} \approx 5.9 \times 10^2 \alpha_{\text{if}}^{1.9} \left(\frac{3 \times 10^7}{V_i}\right)^{6.6}, \qquad (31)$$

where the laser energy E_{L} is in kJ and the implosion velocity V_i in cm/s. Since our ignition criterion uses the areal density and the ion temperature, a relation between these variables and those in Eq. (31) is required. For simplicity, we will consider the simplest (and the least accurate) form of our criterion, $\langle T^{\text{no}\,\alpha}\rangle_{\text{n}}^{2.6} \times \langle \rho R\rangle_{\text{n}} > 50\ \text{keV}^{2.6} \times \text{g}/\text{cm}^2$. The scaling relations derived in Ref. 9 provide accurate formulas relating the maximum areal density and the maximum volume-averaged, no-alpha temperature to the laser energy, shell adiabat, and implosion velocity. We will use the same scaling relation in Ref. 9 and simply adjust the proportionality constant to fit the neutron-averaged quantities in our ignition criterion. A simple fit of the numerical results from our implosion database leads to

$$\langle \rho R \rangle_{\mathrm{n}}(E_{\mathrm{L}}) = \frac{0.78}{\alpha_{\mathrm{if}}^{0.54}} \left(\frac{V_i}{3 \times 10^7}\right)^{0.06} \left(\frac{E_{\mathrm{L}}}{100}\right)^{0.33}$$

$$\left\langle T_i^{\mathrm{no}\,\alpha} \right\rangle_{\mathrm{n}}(E_{\mathrm{L}}) = \frac{3.5}{\alpha_{\mathrm{if}}^{0.15}} \left(\frac{V_i}{3 \times 10^7}\right)^{1.25} \left(\frac{E_{\mathrm{L}}}{100}\right)^{0.07}. \tag{32}$$

Figures 116.46 and 116.47 compare the results of the simulations with the above fitting formulas. Substituting Eq. (32) into our ignition criterion yields the minimum energy required for

$$E_{\mathrm{L}}(\mathrm{kJ}) > 5.9 \times 10^2 \alpha_{\mathrm{if}}^{1.8} \left(\frac{3 \times 10^7}{V_i}\right)^{6.5}. \tag{33}$$

Notice that the power indices and the proportionality constants in Eq. (33) are virtually identical to those in Eq. (31). This shows that our ignition criterion reproduces the HTL scaling quite accurately.

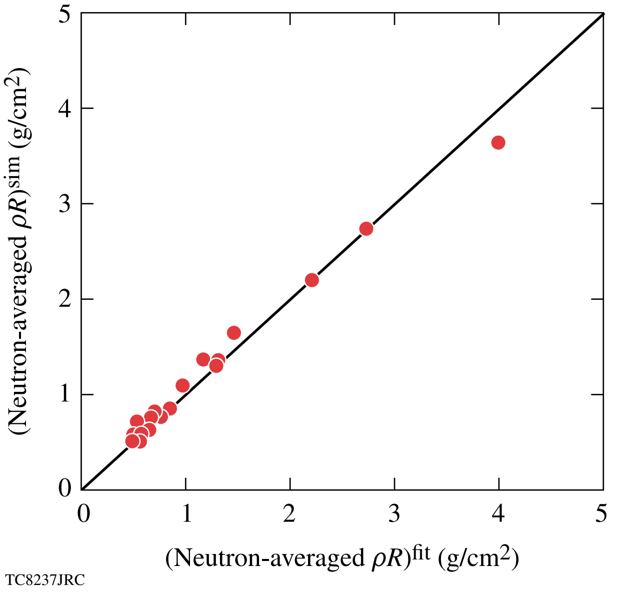

Figure 116.46
Neutron-averaged areal density $\langle \rho R \rangle_{\mathrm{n}}$ from simulations (dots) compared to the numerical fit in Eq. (32) (solid line).

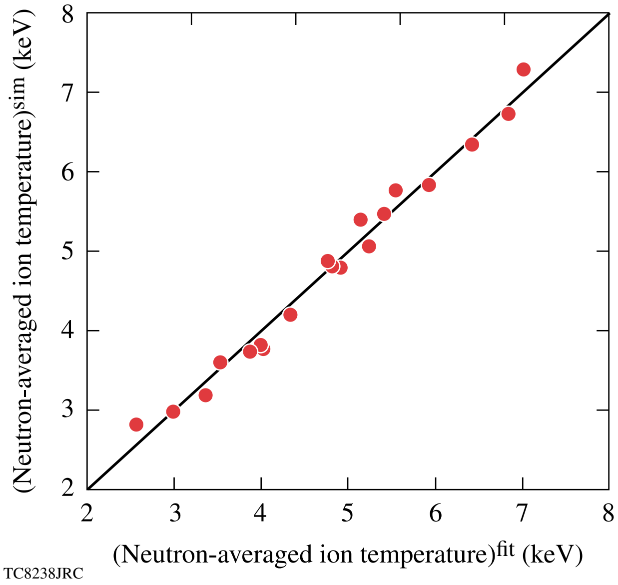

Figure 116.47
Neutron-averaged, no-alpha ion temperature $\langle T_i^{\mathrm{no}\,\alpha} \rangle_{\mathrm{n}}$ from simulation (dots) compared to the numerical fit in Eq. (32) (solid line).

Hydro-Equivalent Curves

In this section we introduce the concept of hydro-equivalency and hyro-equivalent curves in the ρR, T_i plane. ICF targets with similar in-flight hydrodynamic variables, but different driver energy and gain, are considered hydrodynamically equivalent. Hydro-equivalent targets are expected to exhibit the same hydrodynamic behavior with respect to their hydrodynamic performance not only in 1-D but also in 3-D. Here, we relate the hydrodynamic performance to the peak pressure of the stagnating core and to the hydrodynamic stability of the implosion. If a set of targets is scaled in mass (M), radius (R), thickness (Δ), adiabat (α), implosion velocity (V_i), laser intensity (I), and energy (E_{L}) according to the simple scaling $M \sim E_{\mathrm{L}}$, $R \sim E_{\mathrm{L}}^{1/3}$, $\Delta + E_{\mathrm{L}}^{1/3}$, $I \sim$ constant, $\alpha \sim$ constant, and $V_i \sim$ constant, then the target implosions yield the same peak pressure and the same hydrodynamic stability properties. The latter is related to the magnitude of the in-flight aspect ratio (IFAR), which depends on the implosion velocity, adiabat, and laser intensity (Ref. 9). Assuming the same relative size of the initial perturbations on targets, hydro-equivalent targets have the same Rayleigh–Taylor (RT) growth factor (Ref. 9) and the same RT amplitude with respect to their thicknesses. As shown in Eqs. (32) (and in Ref. 9), due to the dependence on the laser energy E_{L}, hydro-equivalent targets will produce different areal densities and slightly different no-alpha temperatures. Obviously, targets imploded by larger drivers (larger E_{L}) will achieve greater ρR and T_i.

Using Eqs. (32), one can easily plot hydro-equivalent curves on the $\langle \rho R \rangle_{\mathrm{n}}$, $\langle T^{\mathrm{no}\,\alpha} \rangle_{\mathrm{n}}$ ignition plane, by fixing α and V_i in Eqs. (32) and letting E_{L} vary. In Fig. 116.48, we plot two hydro-equivalent curves for the direct-drive NIF point design[27] and the current best-performing cryogenic D_2 implosion on OMEGA to date.[11] The direct-drive NIF point design

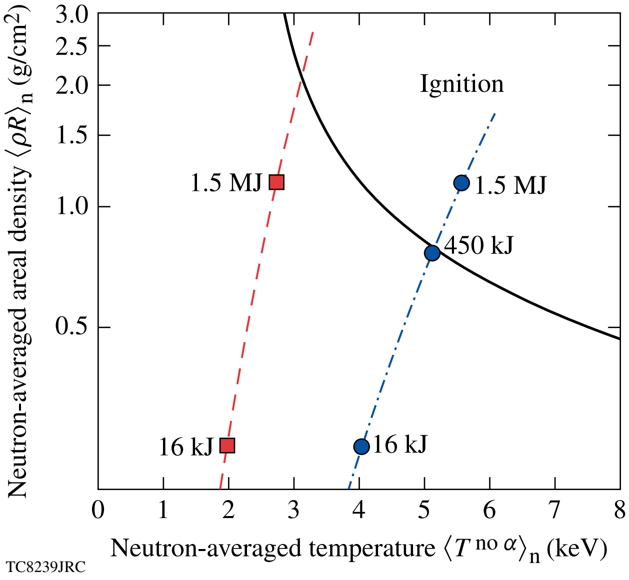

Figure 116.48
Hydro-equivalent curves in the $(\langle \rho R\rangle_n, \langle T^{\text{no}\,\alpha}\rangle_n)$ plane. The solid curve is the ignition condition in Eq. (28). The dashed curve is the hydro-equivalent curve for implosions with $\alpha_{\text{if}} = 2.5$, $V_i = 2.4 \times 10^7$ cm/s in Eq. (32). The lower square represents an implosion at 16 kJ and the upper one at 1.5 MJ. The dashed–dotted curve is the hydro-equivalent curve for implosions with $\alpha_{\text{if}} = 2.7$, $V_i = 4.25 \times 10^7$ cm/s. The three dots are implosions at 16 kJ, 450 kJ, and 1.5 MJ, respectively.

has an in-flight adiabat of 2.7 and implosion velocity of 4.25×10^7 cm/s. The hydro-equivalent curve for such values of α_{if} and V_i is the dashed–dotted curve in Fig. 116.48. The bottom dot on such a curve is the hydro-equivalent point for a 16-kJ implosion. The areal density and no-alpha temperature corresponding to that point are $\langle \rho R\rangle_n \approx 0.25$ g/cm^2 and $\langle T^{\text{no}\,\alpha}\rangle_n \approx 4.1$ keV, respectively. The top dot on the same curve represents the same implosion scaled up to NIF-like energies of 1.5 MJ. The middle dot is the same implosion scaled up to 450 kJ. Notice that the 450-kJ implosion is right on the 1-D marginal ignition curve (the solid curve in Fig. 116.48). This shows that the full NIF energy of 1.5 MJ is approximately three times larger than required for 1-D marginal ignition. The plots in Fig. 116.48 mainly imply that if a 16-kJ cryogenic implosion is carried out on OMEGA to achieve areal densities and temperatures as indicated on the bottom point, then one can use such a result to theoretically conclude that the same implosion scaled up to the NIF will have three times more energy as required by the 1-D Lawson criterion. While this is not absolute proof that such a target will ignite on the NIF, it will establish some confidence in the achievement of ignition.

The point representing the highest areal density cryogenic implosion on the OMEGA laser to date is the bottom square on the dashed curve. The point represents a neutron-averaged areal density slightly exceeding 0.2 g/cm^2 and neutron-averaged temperature of 2 keV. The corresponding implosion had an in-flight adiabat of about 2.5 and implosion velocity of about 2.4×10^7 cm/s. The upper square on that hydro-equivalent curve is below the marginal ignition curves and represents the same implosion scaled up to the full NIF energy of 1.5 MJ. Obviously, such an implosion would fail to ignite. This is explained by the relatively low implosion velocity ($V_i \approx 2.4 \times 10^7$ cm/s) and by the sensitivity on V_i of the minimum energy required for ignition [see Eq. (33)]. Current OMEGA cryogenic targets are massive shells (430-μm outer diam) with a 95-μm-thick cryogenic layer and a 10-μm-thick plastic ablator used to study high compression while reducing the effect of hydrodynamic instabilities. A point worth making is that current OMEGA targets have been imploded with ignition-relevant adiabats that are even slightly below the value required for the direct-drive point design.

In summary, hydro-equivalent curves plotted on the ρR, T_i ignition plane are useful in predicting 1-D performance for different laser energies. An immediate conclusion is that OMEGA-size capsules will have to be imploded at higher implosion velocities (for the same adiabat) to achieve a hydro-equivalent demonstration of ignition.

Conclusions

Equation (28) provides an accurate representation of a measurable Lawson criterion for inertial confinement fusion with DT fuel. Such an ignition condition is found using an analytical dynamic model of ignition, and it is confirmed by the results of one-dimensional simulations of marginally ignited direct-drive targets (gain ≈ 1). A simple fit of the ignition condition can be written as

$$\left\langle T_i^{\text{no}\,\alpha}\right\rangle_n^{2.6} \times \left\langle \rho R_{\text{tot}}\right\rangle_n > 50\ \text{keV}^{2.6} \times \text{g}\big/\text{cm}^2. \qquad (34)$$

This ignition condition is given in terms of the only two measurable parameters of the compressed fuel: (1) the burn-averaged total areal density $\langle \rho R_{\text{tot}}\rangle_n$, and (2) the neutron-averaged hot-spot ion temperature $\langle T_i^{\text{no}\,\alpha}\rangle_n$ without accounting for the α-particle energy deposition. The burn-averaged total areal density can be measured through the detection of the spectrum of fusion products such as protons from secondary reactions.[13] The neutron-averaged temperature is measured through the neutron time-of-flight diagnostic.[10] In our ignition condition, the neutron-averaged ion temperature is computed without the contribution of the fusion alpha particles. This is done to avoid using the actual temperature that undergoes extremely large and sudden variations when the compressed fuel assembly approaches the ignition condition. The so-called no-alpha temperature $T^{\text{no}\,\alpha}$ used in this article is a slowly varying hydrodynamic parameter that is well suited to measure the implosion performance with respect to the ignition condition. The only drawback for using $T^{\text{no}\,\alpha}$ rather than T is that $T^{\text{no}\,\alpha}$ is not always equal to the actual measurable temperature. The no-alpha temperature and the real temperature are virtually identical for cryogenic implosions with surrogate fuel (such as D_2) and for sub-ignited DT implosions with gains much less than unity. In both cases, the fusion self-heating is negligible and $T^{\text{no}\,\alpha} \approx T$. For DT implosions approaching ignition (gains ≥ 0.1), the alpha heating plays an important role in determining the hot-spot temperature and our form of the Lawson criterion cannot be used. In this case, however, the neutron-yield measurement alone is sufficient to determine that the implosion is approaching ignition. Because of the large excursion in neutron yield of a target approaching ignition (commonly referred to as the "ignition cliff"), the neutron yield rather than a formula like Eq. (34) is a much better indicator of target performance.

The measurable Lawson criterion, Eq. (34), favorably compares with the Herrmann–Tabak–Lindl ignition scaling when the areal density and temperature are rewritten in terms of the implosion velocity, in-flight adiabat, and driver energy by using the conversion formulas Eqs. (32) (also from Ref. 9). Furthermore, hydro-equivalent curves [Eqs. (32)] are plotted on the ignition diagram to show how hydro-equivalent implosions would perform with respect to the ignition condition when scaled up in laser energy.

It is worth mentioning that the ignition model presented here could be modified according to the results in Ref. 28 to include the effects of hydrodynamic instabilities developing at the hot-spot/shell interfaces. Such an extension of the ignition model could lead to a more accurate ignition condition that is valid in multidimensions.

ACKNOWLEDGMENT

This work was supported by the U.S. Department of Energy Office of Inertial Confinement Fusion under Cooperative Agreement Nos. DE-FC52-08NA28302 and DE-FC02-04ER54789, the University of Rochester, and the New York State Energy Research and Development Authority. The support of DOE does not constitute an endorsement by DOE of the views expressed in this article.

REFERENCES

1. S. Atzeni and J. Meyer-ter-Vehn, *The Physics of Inertial Fusion: Beam Plasma Interaction, Hydrodynamics, Hot Dense Matter*, International Series of Monographs on Physics (Clarendon Press, Oxford, 2004).
2. J. D. Lindl, *Inertial Confinement Fusion: The Quest for Ignition and Energy Gain Using Indirect Drive* (Springer-Verlag, New York, 1998).
3. J. D. Lawson, Proc. Phys. Soc. Lond. **B70**, 6 (1957).
4. S. Atzeni and A. Caruso, Phys. Lett. A **85**, 345 (1981).
5. S. Yu. Gus'kov, O. N. Krokhin, and V. B. Rozanov, Nucl. Fusion **16**, 957 (1976).
6. R. Kishony, E. Waxman, and D. Shvarts, Phys. Plasmas **4**, 1385 (1997).
7. R. Betti, M. Umansky, V. Lobatchev, V. N. Goncharov, and R. L. McCrory, Phys. Plasmas **8**, 5257 (2001).
8. R. Betti, K. Anderson, V. N. Goncharov, R. L. McCrory, D. D. Meyerhofer, S. Skupsky, and R. P. J. Town, Phys. Plasmas **9**, 2277 (2002).
9. C. D. Zhou and R. Betti, Phys. Plasmas **14**, 072703 (2007).
10. V. Yu. Glebov, D. D. Meyerhofer, C. Stoeckl, and J. D. Zuegel, Rev. Sci. Instrum. **72**, 824 (2001).
11. T. C. Sangster, V. N. Goncharov, P. B. Radha, V. A. Smalyuk, R. Betti, R. S. Craxton, J. A. Delettrez, D. H. Edgell, V. Yu. Glebov, D. R. Harding, D. Jacobs-Perkins, J. P. Knauer, F. J. Marshall, R. L. McCrory, P. W. McKenty, D. D. Meyerhofer, S. P. Regan, W. Seka, R. W. Short, S. Skupsky, J. M. Soures, C. Stoeckl, B. Yaakobi, D. Shvarts, J. A. Frenje, C. K. Li, R. D. Petrasso, and F. H. Séguin, Phys. Rev. Lett. **100**, 185006 (2008).
12. T. R. Boehly, D. L. Brown, R. S. Craxton, R. L. Keck, J. P. Knauer, J. H. Kelly, T. J. Kessler, S. A. Kumpan, S. J. Loucks, S. A. Letzring, F. J. Marshall, R. L. McCrory, S. F. B. Morse, W. Seka, J. M. Soures, and C. P. Verdon, Opt. Commun. **133**, 495 (1997).
13. J. A. Frenje, C. K. Li, F. H. Séguin, J. Deciantis, S. Kurebayashi, J. R. Rygg, R. D. Petrasso, J. Delettrez, V. Yu. Glebov, C. Stoeckl, F. J. Marshall, D. D. Meyerhofer, T. C. Sangster, V. A. Smalyuk, and J. M. Soures, Phys. Plasmas **11**, 2798 (2003).
14. E. M. Campbell and W. J. Hogan, Plasma Phys. Control. Fusion **41**, B39 (1999).
15. D. Mihalas and B. Weibel-Mihalas, *Foundations of Radiation Hydrodynamics* (Oxford University Press, New York, 1984).
16. Ya. B. Zel'dovich and Yu. P. Raizer, in *Physics of Shock Waves and High-Temperature Hydrodynamic Phenomena*, edited by W. D. Hayes and R. F. Probstein (Dover Publications, Mineola, NY, 2002).

17. S. Atzeni and A. Caruso, Nuovo Cimento B **80**, 71 (1984).

18. H.-S. Bosch and G. M. Hale, Nucl. Fusion **32**, 611 (1992).

19. Y. Saillard, Nucl. Fusion **46**, 1017 (2006).

20. R. Betti and C. Zhou, Phys. Plasmas **12**, 110702 (2005).

21. M. C. Richardson, P. W. McKenty, F. J. Marshall, C. P. Verdon, J. M. Soures, R. L. McCrory, O. Barnouin, R. S. Craxton, J. Delettrez, R. L. Hutchison, P. A. Jaanimagi, R. Keck, T. Kessler, H. Kim, S. A. Letzring, D. M. Roback, W. Seka, S. Skupsky, B. Yaakobi, S. M. Lane, and S. Prussin, in *Laser Interaction and Related Plasma Phenomena*, edited by H. Hora and G. H. Miley (Plenum Publishing, New York, 1986), Vol. 7, pp. 421–448.

22. S. P. Lyon and J. D. Johnson, Los Alamos National Laboratory, Los Alamos, NM, Report LA-UR-92-3407 (1992).

23. K. Anderson and R. Betti, Phys. Plasmas **11**, 5 (2004).

24. O. N. Krokhin and V. B. Rozanov, Sov. J. Quantum Electron. **2**, 393 (1973).

25. M. C. Herrmann, M. Tabak, and J. D. Lindl, Nucl. Fusion **41**, 99 (2001).

26. W. K. Levedahl and J. D. Lindl, Nucl. Fusion **37**, 165 (1997).

27. P. W. McKenty, V. N. Goncharov, R. P. J. Town, S. Skupsky, R. Betti, and R. L. McCrory, Phys. Plasmas **8**, 2315 (2001).

28. J. Sanz *et al.*, Phys. Plasmas **12**, 112702 (2005).

Pulsed-THz Characterization of Hg-Based, High-Temperature Superconductors

Introduction

Superconductivity is still regarded as a very promising technology to be applied in high-performance electronics (e.g., Josephson junction digital circuits, ultrasensitive magnetometers) and optoelectronics (broadband x-ray-to-visible-light photodetectors, optical single-photon and photon-number–resolving detectors). The discovery of high-temperature superconductors (HTS's)[1] made those applications technically easier to achieve, at least from the cryogenics point of view, since most HTS's require only liquid nitrogen cooling. Among them, the $HgBa_2Ca_{n-1}Cu_nO_{2n+2+\delta}$ (HBCCO, Hg-based) compound, with its record high superconducting critical temperature T_c of 134 K at ambient pressure,[2] has attracted special attention. However, it is a very complicated system and its complete understanding from the physics, chemistry, and materials science points of view is needed in order to overcome the technological barriers facing HBCCO, and HTS's in general, in their quest for widespread applications.

This work presents comprehensive studies of time-resolved dynamics of Cooper pairs and quasiparticles in Hg-based superconductors. Our experiments implement a femtosecond optical system to perform the time-domain spectroscopy (TDS), using either pulses with 1-THz bandwidth for transmission measurements or the ultrafast optical-pump THz-probe (OPTP) characterization method. In the case of the transmission-type THz-TDS experiments, our sample is put into the path of a subpicosecond-in-duration, THz radiation burst and the transmitted electric-field waveform is measured. After performing the fast Fourier transform (FFT) of the time-domain transient, the frequency-dependent magnitude and phase components of the signal are obtained. By comparing the obtained data to the reference signal collected without the sample present in the system, either the frequency-dependent complex index of refraction $n(\omega)$ or conductivity $\sigma(\omega)$ of the sample's material can be deduced without resorting to Kramers–Kronig analysis. Since various pairing theories predict the different temperature behavior of the complex $\sigma = \sigma_{re} - i\sigma_{im}$ in HTS's,[3] by measuring the temperature- and frequency-dependent components of σ (σ_{re} and σ_{im}), we are able to provide insight on the intrinsic relaxation dynamics of quasiparticles in the HBCCO material.

Sample Fabrication and Experimental Setup

1. Sample Fabrication

Our Hg-based thin films were synthesized from 200 to 600-nm-thick Re-Ba-Ca-Cu-O precursor films, rf-magnetron sputtered at the room temperature on $LaAlO_3$ substrates, then followed by an *ex-situ* mercuration process in a sealed, evacuated quartz ampoule, using an un-reacted (Hg, Re)-1223 pellet as the source of mercury, prepared by a sol-gel method. The ampoule was placed inside a furnace, kept at 800°C for 5 h, and later cooled at a rate of 120°C/h to the ambient temperature.[4]

The x-ray-diffraction analyses demonstrated that our films were predominantly composed of a *c*-axis–oriented Hg-1212 phase, together with a Hg-1223 phase. Four-point resistance measurements of chemically etched, 20-μm-wide microbridges, showed that the samples used in this study exhibited the onset of the superconducting transition $T_{c,on}$ at ~122 K and the zero-resistance $T_{c,0}$ at ~110 K.[4]

2. Experimental Setup

Figure 116.49 shows our experimental setup. A 1-kHz, 800-nm-wavelength, 50-fs-duration commercial Ti:sapphire amplifier system was used as a laser source with a total output of ~500 mW. The output from the laser was split into three beams: one beam was used to optically pump the Hg-based sample and generate photoexcited quasiparticles; the second beam was used to generate THz radiation via optical rectification in a ZnTe emitter; and the third one (very weak) detected the THz transmission signal via a free-space, electro-optic sampling in a ZnTe sensor. The generated THz transient was formed and focused on the HBCCO sample (marked by an arrow in Fig. 116.49) using two sets of metallic parabolic mirrors. The sample was mounted on a cold finger inside an optical, continuous-flow, liquid-helium cryostat with the temperature controlled between 8 K and 293 K. The computer-based data-acquisition system monitored current flow through two balanced photodetectors using a lock-in amplifier. The

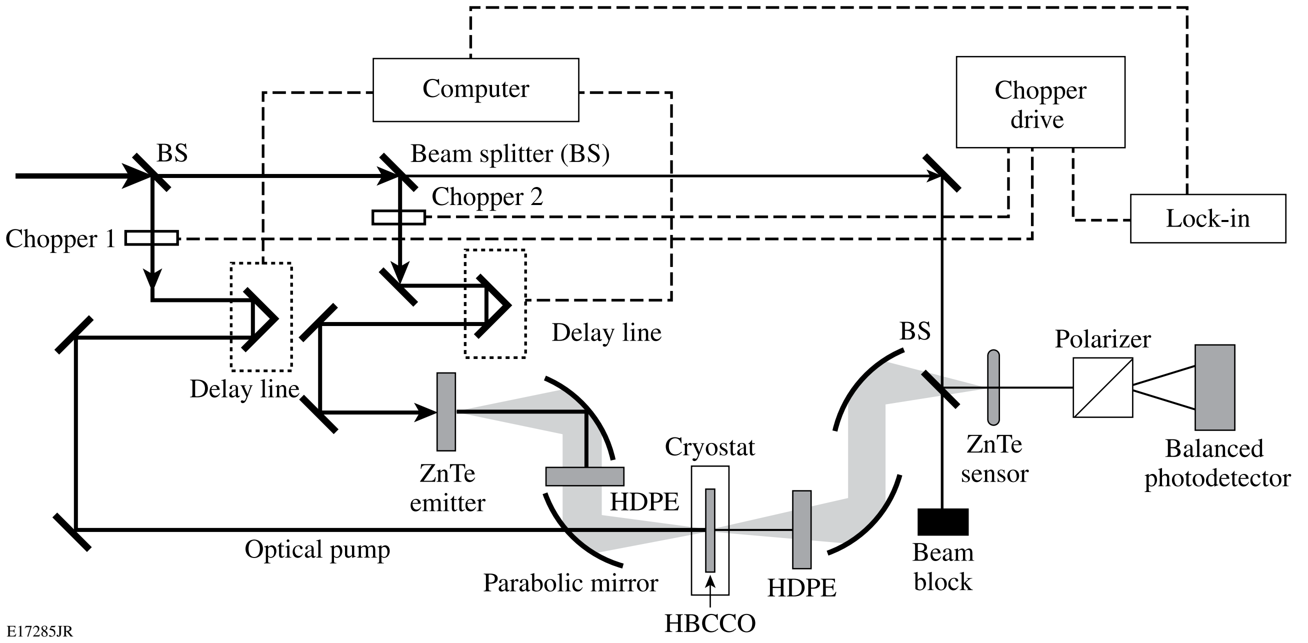

Figure 116.49
THz-TDS/OPTP experimental setup.

same setup was used for both the transmission THz-TDS and OPTP measurements, but, of course, the optical pump beam was blocked when performing transmission THz-TDS experiments. Further technical details of the experimental setup and OPTP spectroscopy can be found in Ref. 5.

Experimental Results and Discussion

1. THz-TDS Experiments

The transmission THz-TDS experiments were performed in the temperature range between 8 K and 293 K on both the HBCCO thin film and the bare $LaAlO_3$ substrate. Figure 116.50 shows the transmitted THz signals for a nominally (before annealing) 500-nm-thick HBCCO film at different temperatures. The THz transient amplitude decreases and the peak position slightly shifts as the temperature drops below T_c, indicating that Cooper pairs contribute to both the increased reflectivity and the phase shift via the imaginary component of the conductivity. We stress that the observed temperature-related changes in the THz transient are solely due to the change in the HBCCO superconducting properties since the reference THz-TDS studies performed on the bare $LaAlO_3$ did not reveal any changes, indicating no substrate absorption. The refractive index of $LaAlO_3$ remained constant and was ~4.85 for frequencies below 1 THz, which agrees with the results reported by Zhang.[6] As shown in the inset in Fig. 116.50, above T_c, the amplitude of the transmitted electric field decreased slowly with the temperature decrease, due to the progressive increase of the film's conductivity. When the temperature crossed T_c, there was a sharp drop in the THz transmission, as we will show later, directly related to the strong increase in σ_{im}.

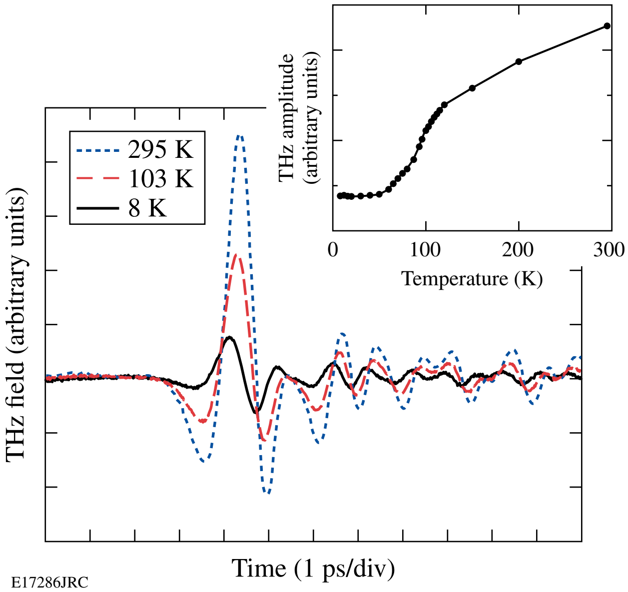

Figure 116.50
Transmitted THz field through a HBCCO film at different temperatures. The inset shows temperature dependence of the THz field amplitude.

2. THz-TDS Experiments—Complex Conductivity Analysis

Our HBCCO film on the $LaAlO_3$ substrate was put in the experimental THz optical path at the normal incidence to the THz beam as is schematically illustrated in Fig. 116.51(a). Therefore, the transmitted waveform can be expressed as

$$E_{\text{sam + sub}} = Et(\omega)\, t_{31} \exp\left[i n_3 (\omega/c)\, d_3 \right], \tag{1}$$

with the transmission coefficient t of the air/HBCCO/$LaAlO_3$ system equal to[7]

$$t(\omega) = \frac{t_{12} t_{23} \exp\left[i n_2 (\omega/c)\, d_2 \right]}{1 + r_{12} r_{23} \exp\left[2 i n_2 (\omega/c)\, d_2 \right]}, \tag{2}$$

where $t_{ij} = 2n_i \big/ \left(n_i + n_j\right)$, $r_{ij} = \left(n_i - n_j\right) \big/ \left(n_i + n_j\right)$, E is the incident THz field, d_2 and d_3 are thicknesses of the thin film and the substrate, respectively, and n_i and n_j are complex refraction indexes. In general, we should consider a Fabry–Pérot effect due to multiple reflections from the interferences.[8] However, the thickness of $LaAlO_3$ is ~0.5 mm, so even the first-reflection signal is going to be outside the time window of interest associated with the transmitted signal; therefore, reflections can be ignored.

In the case of the bare $LaAlO_3$ substrate illuminated with the Thz radiation [Fig. 116.51(b)], the transmitted waveform can be expressed as

$$E_{\text{air + sub}} = E t_{13} t_{31} \exp\left[i n_3 (\omega/c)\, d_3 \right] \exp\left[i (\omega/c)\, d_2 \right]. \tag{3}$$

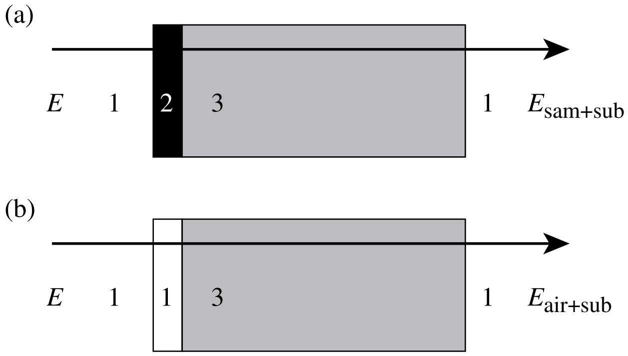

E17287JR

Figure 116.51
Schematic of THz wave transmission through (a) an HBCCO thin-film sample + $LaAlO_3$ substrate (sam+sub) and (b) air + a bare $LaAlO_3$ substrate (air+sub). The numbers 1, 2, and 3 correspond to air, HBCCO sample, and $LaAlO_3$ substrate, respectively.

Thus, dividing Eqs. (1) and (3), we get

$$\frac{E_{\text{sam + sub}}}{E_{\text{air + sub}}} = t(\omega) \Big/ \left\{ t_{13} \exp\left[i (\omega/c)\, d_2 \right] \right\}$$

$$= A(\omega) \exp\left[i \phi(\omega) \right], \tag{4}$$

where $A(\omega)$ is the frequency-dependent magnitude of $E_{\text{sam+sub}}$ divided by that of $E_{\text{air+sub}}$, and $\varphi(\omega)$ is the frequency-dependent phase of $E_{\text{sam+sub}}$ subtracted by that of $E_{\text{air+sub}}$. Since, in our case, $\left| n_2 (\omega/c)\, d \right| \ll 1$, and $\left| n_2 \right| \gg n_3 \gg 1$, therefore[7]

$$\frac{1 + n_3}{1 + n_3 Z_0 d_2 \sigma(\omega)} = A(\omega) \exp\left\{ i \left[\phi(\omega) + \omega d_2 \big/ c \right] \right\}, \tag{5}$$

where Z_0 is the impedance of free space. Equation (5) shows that now we can directly relate the experimentally measured THz-TDS spectra given by Eq. (4) to the tested complex $\sigma(\omega)$ of our sample.

The complex $\sigma(\omega)$ of superconductors can be described by the two-fluid model[1] and is composed of two parts: (1) an imaginary part that is dominant below T_c and related to the superfluid fraction f_s of electrons and (2) a Drude component proportional to the quasiparticle (normal electron) fraction f_n (Ref. 3):

$$\sigma(\omega, T) = \sigma_{\text{re}} + i\sigma_{\text{im}} = \frac{ne^2}{m^*} \left[\frac{f_n(T)}{\tau(\omega, T)^{-1} - i\omega} - \frac{f_s(T)}{i\omega} \right], \tag{6}$$

where $f_n + f_s = 1$ and $\tau(\omega, T)$ is the quasiparticle scattering time.

The temperature dependences of σ_{re} and σ_{im} are presented in Fig. 116.52. Figure 116.52(a) shows that σ_{re} increases with the decrease of temperature, exhibits a small cusp at ~T_c, and reaches the main peak below T_c, which is due to a competition of the quasiparticle density decrease and simultaneous increase of their scattering rate. The main σ_{re} peak [see Fig. 116.52(a)] shifts to lower temperatures with lower frequencies, and its amplitude becomes larger. On the other hand, Fig. 116.52(b) demonstrates that the σ_{im} component increases dramatically below T_c, which is due to the presence and increase of the superconducting condensate (Cooper pairs). There is a small nonzero σ_{im} in the normal state, apparently due to a residual kinetic-inductive effect. The latter can be speculated as evidence of the pseudogap state, but more systematic studies are needed.

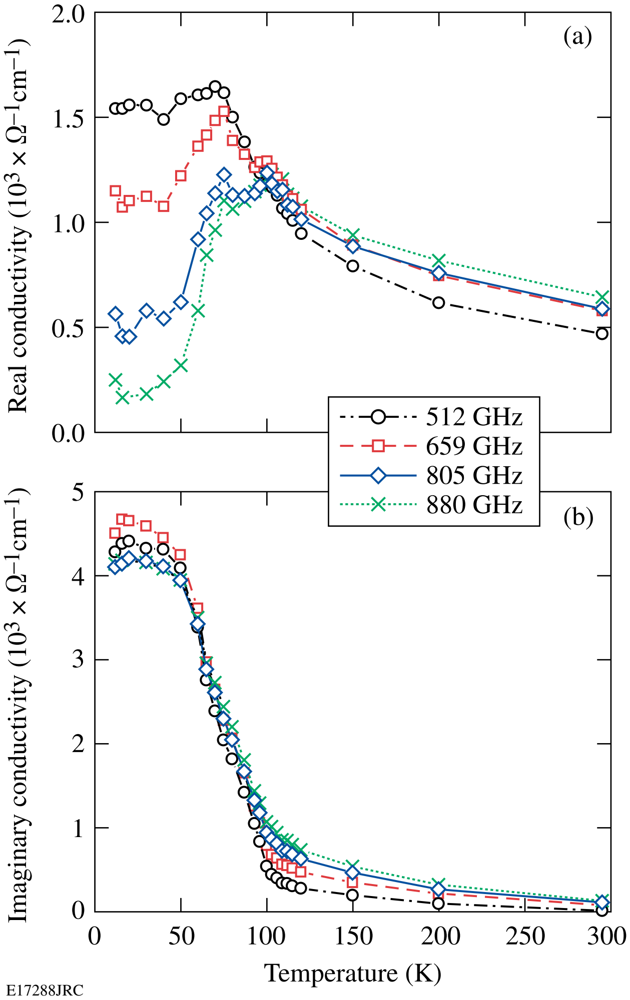

E17288JRC

Figure 116.52
(a) Temperature-dependent real conductivity at different frequencies; (b) temperature-dependent imaginary conductivity at different frequencies.

3. Time-Resolved OPTP Experiments

Optical excitation of a superconductor induces $\Delta\sigma_{re}$ and $\Delta\sigma_{im}$ changes, which result in a change of the transmitted transient THz electric field $\Delta E(t)$. As we mentioned before, the $\Delta\sigma_{im}$ component contains information about the superconducting condensate density, while the quasiparticle (normal electron) density is probed by $\Delta\sigma_{re}$. In our OPTP measurements, optical excitation increases the amplitude of the transient THz signal. Thus, we can fix the THz-probe-signal optical-delay line at the position where the positive, maximum peak of the THz electric-field waveform occurs [$\Delta E(t = t_{max})$] and, subsequently, vary the arrival time of the femtosecond optical excitation pump pulse (see Fig. 116.49). This way we can obtain the time-resolved $\Delta\sigma(t)$ dynamics and the corresponding quasiparticle dynamics.

Figure 116.53 shows our OPTP results at different temperatures below T_c with an optical fluence of the pump beam equal to 2 μJ/cm^2. The measured THz $\Delta E(t)$ transients have their decay times of the order of 2 ps and represent the quasiparticle relaxation (Cooper-pair formation) dynamics. We note that the above observation is contrary to the common, slow relaxation process in photoinduced superconductors, typical for conventional (e.g., metallic) superconductors, where the quasiparticle relaxation speed is limited by the acoustic-phonon escape time for the film to the substrate. The latter is called the phonon-bottleneck effect[9] and is due to the secondary pair-breaking by the acoustic phonons emitted during the process of two-quasiparticle recombination into a Cooper pair. The corresponding phonon escape time is in the nanosecond range, depending linearly on the superconductor thickness. In HBCCO superconductors, 2Δ is estimated to be in the 50- to 70-meV range and the acoustic phonons predominantly relax enharmonically; thus, they are decoupled from the carriers, resulting in the direct intrinsic quasiparticle recombination process. According to Fig. 116.53, far below T_c, our HBCCO material relaxes back to the fully superconducting (equilibrium) state in less than 2 ps. The latter observation is in direct agreement with our earlier, all-optical, pump–probe spectroscopy studies[10] and confirms that, far below T_c, thermal (phonon) contribution is negligible in the relaxation dynamics of the nonequilibrium HBCCO superconductors.

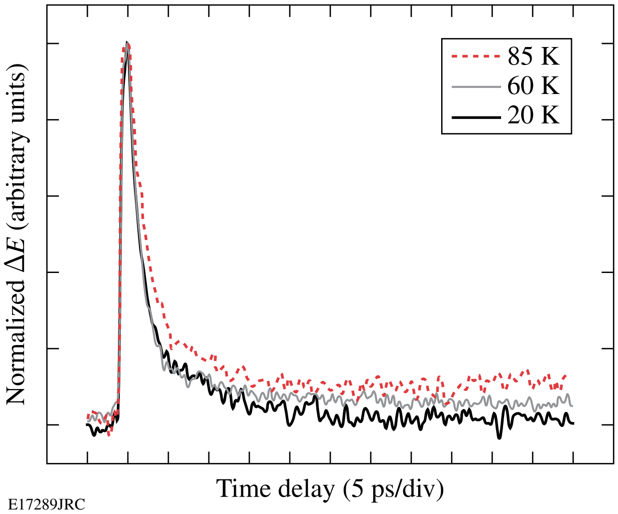

E17289JRC

Figure 116.53
Normalized transient transmitted electrical field signals at different temperatures below T_c obtained from OPTP experiments.

Conclusion

We presented our complex conductivity studies of HBCCO HTS thin films using the THz-TDS and OPTP techniques. THz studies are the volume measurements; thus, they are insensitive to the sample roughness or granularity, which are much smaller in size compared to the THz radiation wavelength. The latter is important in the case of our *ex-situ*-grown HBCCO films, which have a rough surface and are to some extent multi-phased specimens. From the transient THz transmission measurements, one observed that $\Delta\sigma_{\mathrm{re}}$ shows a peak below T_{c}, which shifts to lower temperatures with lower frequencies. At the same time, $\Delta\sigma_{\mathrm{im}}$ has a sharp increase below T_{c} due to the increase in Cooper-pair density and formation of a superconducting condensate. Both findings are in general agreement with the complex conductivity model for low-energy excitations (far below the material's 2Δ) in superconductors. The time-resolved quasiparticle relaxation of HBCCO, measured directly by the OPTP techniques, exhibits an intrinsic single-picosecond dynamics with no phonon bottleneck, or a substantial bolometric signal plateau, which is a unique feature among both LT and HT nonequilibrium superconductors, and makes this material very promising for ultrafast photodetector applications.

ACKNOWLEDGMENT

This work was supported by the US AFOSR grant FA9550-06-1-0348 (Rochester), the Slovak Research and Development Support Agency grants 2/0139/08 and LPP-0078-07 (Bratislava), and the NSF Center on Materials and Devices for Information Technology Research (CMDITR), DMR-0120967 (Baltimore).

REFERENCES

1. See, e.g., M. Tinkham, *Introduction to Superconductivity*, 2nd ed., International Series in Pure and Applied Physics (McGraw-Hill, New York, 1996), pp. 108–381.
2. C. W. Chu, Chin. J. Phys. **34**, 166 (1996).
3. R. D. Averitt *et al.*, J. Opt. Soc. Am. B **17**, 327 (2000).
4. Š. Chromik, M. Valeriánová, V. Štrbík, Š. Gaži, P. Odier, X. Li, Y. Xu, R. Sobolewski, F. Hanic, G. Plesch, and Beňačka, Appl. Surf. Sci. **254**, 3638 (2008).
5. P. D. Cunningham and L. M. Hayden, J. Phys. Chem. **112**, 7928 (2008).
6. Z. M. Zhang *et al.*, J. Opt. Soc. Am. B **11**, 2252 (1994).
7. T.-R. Tsai, C.-C. Chi, and S.-F. Horng, Physica C **391**, 281 (2003).
8. L. Duvillaret, F. Garet, and J.-L. Coutaz, IEEE J. Sel. Top. Quantum Electron. **2**, 739 (1996).
9. A. Rothwarf and B. N. Taylor, Phys. Rev. Lett. **19**, 27 (1967).
10. X. Li, Y. Xu, Š. Chromik, V. Štrbík, P. Odier, D. De Barros, and R. Sobolewski, IEEE Trans. Appl. Supercond. **15**, 622 (2005).

LLE's Summer High School Research Program

During the summer of 2008, 15 students from Rochester-area high schools participated in the Laboratory for Laser Energetics' Summer High School Research Program. The goal of this program is to excite a group of high school students about careers in the areas of science and technology by exposing them to research in a state-of-the-art environment. Too often, students are exposed to "research" only through classroom laboratories, which have prescribed procedures and predictable results. In LLE's summer program, the students experience many of the trials, tribulations, and rewards of scientific research. By participating in research in a real environment, the students often become more excited about careers in science and technology. In addition, LLE gains from the contributions of the many highly talented students who are attracted to the program.

The students spent most of their time working on their individual research projects with members of LLE's technical staff. The projects were related to current research activities at LLE and covered a broad range of areas of interest including experimental diagnostic development and analysis, computational modeling of implosion hydrodynamics and radiation physics, database development, materials science, cryogenic target characterization, target vibration analysis, and engineering device development (see Table 116.II).

The students attended weekly seminars on technical topics associated with LLE's research. Topics this year included laser physics, fusion, holography, fiber optics, optical manufacturing, the physics of music, and electronic paper. The students also received safety training, learned how to give scientific presentations, and were introduced to LLE's resources, especially the computational facilities.

The program culminated on 27 August with the "High School Student Summer Research Symposium," at which the students presented the results of their research to an audience including parents, teachers, and LLE staff. The students' written reports will be made available on the LLE Web site and bound into a permanent record of their work that can be cited in scientific publications.

Two hundred and thirty three high school students have now participated in the program since it began in 1989. This year's students were selected from approximately 50 applicants.

At the symposium LLE presented its 12th annual William D. Ryan Inspirational Teacher Award to Ms. Jane Bowdler, a mathematics teacher at Brockport High School. This award is presented to a teacher who motivated one of the participants in LLE's Summer High School Research Program to study science, mathematics, or technology and includes a $1000 cash prize. Teachers are nominated by alumni of the summer program. Ms. Bowdler was nominated by Priya Rajasethupathy, a participant in the 2000 Summer Program. Priya recognized Ms. Bowdler as an exceptional teacher who inspired and nurtured her intellectual curiosities: "She is able to bring structure into a classroom and make a difficult subject more manageable… She understands her students and their needs and is able to provide individualized attention… She goes beyond the call of duty by leading the math club and constantly innovating ways to recruit students and sustain their interest in math… Her unbounded patience toward students is one of her unique qualities." Mr. Glen Levandowski, principal of Brockport High School, added: "Her knowledge of math is outstanding and she has the ability to make it interesting and fun to all students, even those who may not generally favor the subject. Overall, Jane is an outstanding educator and serves as a wonderful role model for her students."

Table 116.II: High School Students and Projects—Summer 2008.

Name	High School	Supervisor	Project Title
Jay Amin	Rush-Henrietta	C. Dorrer	Development of an Optical Pulse Characterization Device Based on Spectral Shearing Interferometry
Chris Baldwin	Honeyoye Falls-Lima	R. W. Kidder	Exploring Metadata for Laser Diagnostics and Control Systems
Husain Bawany	Brighton	R. Janezic	Development of the Cryogenic Target Information System
Krysta Boccuzzi	Mercy	E. Kowaluk	Investigation of the Causes of and Possible Remedies for Damage to Sensors Used on the OMEGA Laser System
David Brummond	Honeyoye Falls-Lima	C. Stoeckl	Controlling a PC-Based Data Acquisition System with Java
Nicholas Hensel	Fairport	D. Jacobs-Perkins	High-Speed Measurements of Target-Support Vibrations Using Linescan Cameras
Rachel Kurchin	Harley	R. S. Craxton, M. D. Wittman	Characterization of a Cryogenic Target in a Transparent Cylindrical Hohlraum
Alexis Kurmis	Greece Arcadia	T. C. Sangster, T. Duffy	Counting System for the Carbon Activation Diagnostic
Mangala Patil	Pittsford Mendon	K. L. Marshall	Contamination-Resistant Sol-Gel AR Coatings by Vapor-Phase Silylation
Angela Ryck	Fairport	R. S. Craxton	Optimization of Cone-in-Shell Implosions
Collin Sowinski	Penfield	W. T. Shmayda	Minimization of the Tritium Contamination of Surfaces
Jack Stokes	Fairport	S. Ingraham, D. J. Lonobile	Investigation of Brushless dc Motor Commutation Techniques
James Tsay	Phillips	R. Epstein	K-Shell Emission-Line Backlighter Source Optimization
Brian Wang	Webster Thomas	J. F. Myatt, P. Jaanimagi	The Effects of Space Charge on Electron Pulse Broadening in Streak Cameras
Bradley Wideman	Fairport	F. J. Marshall	Automated Determination of Crystal Reflectivity in the X-Ray Laboratory

FY08 Laser Facility Report

OMEGA Laser Facility

During FY08 the OMEGA Laser Facility conducted 1169 target shots on OMEGA and 85 target shots on OMEGA EP for a variety of users (see Table 116.III). A total of 50 D_2 and 8 DT low-adiabat cryogenic target implosions were performed. Double- and triple-picket pulse-shaping developments highlighted the ongoing development of direct-drive cryogenic implosion capability. The OMEGA Availability and Experimental Effectiveness averages for FY08 were 91.3% and 96.1%, respectively. Highlights of other achievements for FY08 include the following:

Pulse-shaping capability has evolved to meet the demands of producing double- and triple-picket shaped pulses for cryogenic experiments (see Fig. 116.54). The picket-generation hardware has been upgraded to allow for the creation and independent timing/amplitude control of three picket channels. Pulse-shape measurement diagnostics and analysis software have also become more sophisticated to accurately predict picket energies and UV pulse shapes.

A new harmonic energy detector (HED) system was designed and installed to replace the legacy system that was based on aging CCD technology and controlled by dated software.

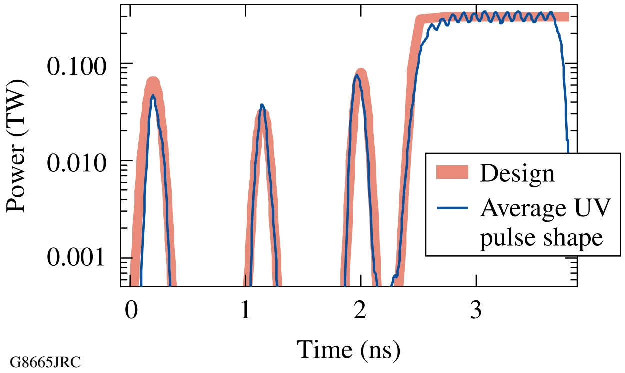

Figure 116.54
OMEGA average pulse shape from cryogenic target implosions (shot 53066) using pulse shape SG3801T.

The Fiducial Laser System has been upgraded to solid-state, diode-pumped regenerative amplifier technology with increased capacity for fiducial signal outputs. This upgrade improves fiducial pulse stability, provides greater reliability, and requires less maintenance than the dated technology that it replaced. Additionally, the fourth-harmonic UV fiducial repetition rate increased from once every 10 min to rates as high as 0.1 Hz, resulting in more-efficient timing of experimental diagnostics.

Table 116.III: The OMEGA target shot summary for FY08.

Laboratory	Planned Number of Target Shots	Actual Number of Target Shots	IDI NIC	DDI NIC	Total NIC	Non-NIC
LLE	607	600	145	409	554	46
LLNL	221	237	117	0	117	120
NLUF	114	125	0	0	0	125
LANL	85	85	22	0	22	63
LBS	50	51	0	0	0	51
CEA	35	39	0	0	0	39
AWE	30	32	0	0	0	32
Total	1142	1169	284	409	693	476

All rod amplifier power-conditioning-unit control systems were upgraded with improved trigger boards. These upgrades mitigate the recently observed increased failure rates associated with the aging control system hardware.

A new Target Viewing System (TVS) was installed on the OMEGA target chamber in June of this year, greatly enhancing target-viewing performance and capability. The new TVS features real-time image processing, up to a 50-mm field of view, up to 2000-frames/s data collection, cryogenic target imaging improvements, remote focus capability, and target detection improvements.

New environmental controls were added to the pulse-generation room (PGR) and the driver electronics room (DER) to improve temperature and humidity stability. The thermal stability improvements resulted in better stability for both the temporal pulse shape and spatial profile.

OMEGA EP Laser Facility

The OMEGA EP Laser Facility completed the integration to target of two short-pulse beamlines and two long-pulse UV beamlines. A total of 85 target shots were taken. Beamline 1 was activated in short-pulse mode to the OMEGA EP target chamber via both the backlighter and sidelighter paths as well as to the OMEGA target chamber. Beamline 2 was activated in short-pulse mode to the OMEGA EP target chamber via the backlighter path and to the OMEGA target chamber. Beamlines 3 and 4 were activated to the OMEGA EP target chamber in long-pulse UV mode. On 16 September 2008, an OMEGA EP beamline provided greater than 1.3 kJ of infrared light to target in a 10-ps laser pulse. This energy to target is more than a factor of 2 higher than has ever been achieved with a high-energy, short-pulse laser system.

Two additional ten-inch manipulators (TIM's) were commissioned on the OMEGA EP target chamber, bringing the total to three. A suite of initial target diagnostics have been qualified for use, including

- NRL – Dual-Crystal Spectrometer
- LLE – Yaakobi X-Ray Spectrometer
- LLE – Ultrafast X-Ray Streak Camera
- LLE – X-Ray Monitor and Neutron Time-of-Flight Detectors
- LLNL – Proton Film Pack
- CEA – Static Penumbral Imager and Fixed Activation Devices
- LLNL – High-Energy Radiography Imager for OMEGA EP

A NIF preamplifier module (PAM) was installed in the Laser Sources Bay. Preliminary engineering of a 2-D SSD module improvement as well as connection and diagnostic hardware necessary to seed Beamline 4 with the PAM has been accomplished.

National Laser Users' Facility and External Users' Programs

During FY08, a governance plan was implemented to formalize the scheduling of the OMEGA Laser Facility as an NNSA User Facility. Under this plan, OMEGA shots are allocated by campaign. The majority of the FY08 target shots were allocated to the National Ignition Campaign (NIC), and integrated experimental teams from LLNL, LANL, SNL, and LLE conducted a variety of NIC-related experiments primarily at the OMEGA Laser Facility. Shots were also allocated in FY08 to the high-energy-density (HED) physics programs from LLNL and LANL.

Under the governance plan, 25% of the facility shots are allocated to Basic Science experiments. Roughly half of these are dedicated to University Basic Science under the National Laser Users' Facility program, and the remaining shots are allotted to Laboratory Basic Science, comprising peer-reviewed basic science experiments conducted by the national laboratories and LLE/FSC.

The OMEGA Facility is also being used for several campaigns by teams from the Commissariat à l'Énergie Atomique (CEA) of France and AWE of the United Kingdom. These programs are conducted at the facility on the basis of special agreements put in place by DOE/NNSA and the participating institutions.

The external users during this year included six collaborative teams participating in the National Laser Users' Facility (NLUF) program; many collaborative teams from the national laboratories conducting experiments for the National Ignition Campaign (NIC); investigators from LLNL and LANL conducting experiments for HED physics programs; and scientists and engineers from CEA of France and AWE of the United Kingdom.

In this section, we briefly review all the external user activity on OMEGA during FY08, including NLUF programs and experiments conducted by users from LLNL, LANL, CEA, and AWE.

NLUF Program

In FY08, the Department of Energy (DOE) issued a solicitation for NLUF grants for the period of FY09–FY10. A total of 13 proposals were submitted to DOE for the NLUF FY09–FY10 program. An independent DOE Technical Evaluation Panel comprised of Dr. Steven Batha (LANL), Dr. Gilbert (Rip) Collins (LLNL), Dr. Ramon Leeper (SNL), Prof. Howard Milchberg (University of Maryland), and Prof. Donald Umstadter (University of Nebraska, Lincoln) reviewed the proposals on 18 April 2006 and recommended that 11 of the proposals receive DOE funding and shot time on OMEGA in FY09–FY10. Table 116 IV lists the successful proposals.

FY08 NLUF Experiments

FY08 was the second of a two-year period of performance for the NLUF projects approved for the FY07–FY08 funding and OMEGA shots. Six of these NLUF projects were allotted OMEGA shot time and received a total of 125 shots on OMEGA in FY08. Some of this work is summarized in this section.

Experimental Astrophysics on the OMEGA Laser

Principal Investigator: R. P. Drake (University of Michigan)
Co-investigators: D. Arnett (University of Arizona); T. Plewa (Florida State University); A. Calder (University of Chicago); J. Glimm, Y. Zhang, and D. Swesty (State University of New York–Stony Brook); M. Koenig (LULI, École Polytechnique, France); C. Michaut (Observoratorie de Paris, France); M. Busquet (France); J. P. Knauer and T. R. Boehly (LLE); P. Ricker (University of Illinois); and B. A. Remington, H. F. Robey, J. F. Hansen, A. R. Miles, R. F. Heeter, D. H. Froula, M. J. Edwards, and S. H. Glenzer (LLNL)

The OMEGA laser, with its ability to produce pressures greater than 10 Mbars, can create conditions of very high energy density that are relevant to astrophysical phenomena. This project explores two such issues: the contribution of hydrodynamic instabilities to the structure in supernovae and the dynamics of radiative shock waves. The study of radiative shock dynamics is a continuation of successful campaigns at LLE that have employed x-ray radiography to quantify the average shock velocity and the structure of the dense, shocked matter. Of primary importance to understanding the role played

Table 116.IV: FY09–FY10 NLUF Proposals.

Principal Investigator	Affiliation	Proposal Title
F. Beg	University of California, San Diego	Systematic Study of Fast Electron Transport and Magnetic Collimation in Hot Plasmas
R. P. Drake	University of Michigan	Experimental Astrophysics on the OMEGA Laser
R. Falcone	University of California, Berkeley	Detailed *In-Situ* Diagnostics of Multiple Shocks
U. Feldman	ARTEP, Inc.	EP-Generated X-Ray Source for High Resolution 100–200 keV Point Projection Radiography
Y. Gupta	Washington State University	Ramp Compression Experiments for Measuring Structural Phase Transformation Kinetics on OMEGA
P. Hartigan	Rice University	Dynamics of Shock Waves in Clumpy Media
R. Jeanloz	University of California, Berkeley	Recreating Planetary Core Conditions on OMEGA, Techniques to Produce Dense States of Matter
K. Krushelnick	University of Michigan	Intense Laser Interactions with Low Density Plasmas Using OMEGA EP
R. Mancini	University of Nevada, Reno	Three-Dimensional Studies of Low-Adiabat Direct-Drive Implosions at OMEGA
M. Meyers	University of California, San Diego	Response of BCC Metals to Ultrahigh Strain Rate Compression
R. D. Petrasso	Massachusetts Institute of Technology	Monoenergetic Proton and Alpha Radiography of Laser-Plasma-Generated Fields and of ICF Implosions

by radiation in the shock dynamics is the electron temperature throughout the shocked material. We have used x-ray Thomson scattering to make such temperature measurements.

In the experiment, ten OMEGA laser beams irradiate a Be drive disk with UV light for 1 ns. The beams deposit a total energy of ~3.8 KJ, giving an average irradiance of ~4.8×10^{14} W/cm^2, corresponding to an ablation pressure of ~46 Mbar in the Be drive disk. The enormous pressure first launches shocks and then accelerates the Be material, which in turn drives a shock into a cylinder filled with Ar gas. The shock moves through the Ar with an average velocity of the order of ~150 km/s, which is fast enough that radiative effects play a significant role in the shock dynamics. An additional eight OMEGA laser beams irradiate a Mn foil for 1 ns to create the x rays needed to probe the shocked Ar system. The x rays are scattered through an average angle of 100° before being spectrally resolved by a crystal spectrometer and then detected by a four-strip gated microchannel plate.

Figure 116.55 shows some of the resulting data. The probe for these data was offset from the drive beams by 15 ns, placing the measurement in the precursor region of the shock. Additional measurements were made at different times, corresponding to different regions in the shock system. The signal includes two peaks produced by elastic scattering from tightly bound electrons and a broad red-shifted feature expected from

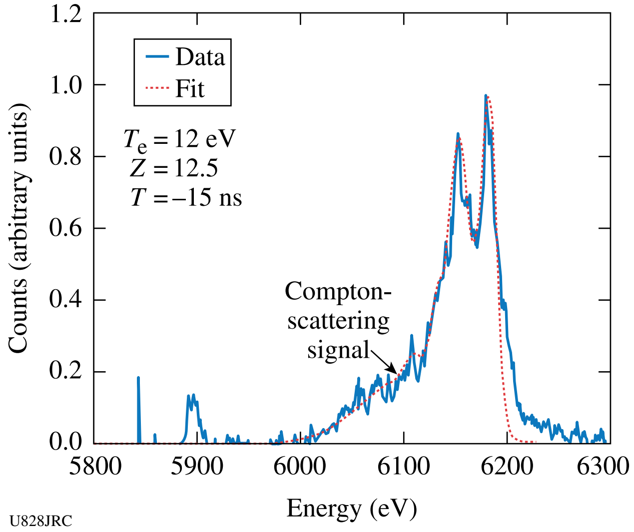

Figure 116.55
Spectrum of x-ray Thomson-scattered light from the precursor region of radiative shock, showing peaks from elastic scattering and a shifted feature from free electrons.

photons that are Compton scattered from the free electrons. By fitting a theoretical line to the observed signal, the electron temperature and average ionization can in principle be deduced. The fit shown is preliminary.

Laboratory Experiments of Supersonic Astrophysical Flows Interacting with Clumpy Environments

Principal Investigator: P. Hartigan (Rice University)
Co-investigators: R. Carver and J. Palmer (Rice University); J. Foster, P. Rosen, and R. Williams (AWE); B. Wilde and M. Douglas (LANL); A. Frank (University of Rochester); and B. Blue (General Atomics)

Strong shock waves occur in many astrophysical systems, and the morphology of the emission lines that occur from the hot gas behind these shocks is often highly clumpy. The objective of this sequence of NLUF experiments is to develop scaled laboratory experiments to study the hydrodynamics of clumpy supersonic flows. The laboratory work complements new astrophysical images from the Hubble Space Telescope (HST) that were motivated by the results of the NLUF program.

Our work in the past year has concentrated first on developing and implementing an experimental design that could follow the destruction of a single clump by the passage of a strong shock and then expanding this work to include two clumps that are close enough that shadowing significantly affects the dynamics of the interactions. A sample of the results from these successful experiments appears in Fig. 116.56. Upper panels (a) and (b) show how a single clump flattens and the bow shock widens as time progresses in the interaction. Remarkably, we have now seen this exact phenomenon in our most-recent image of one of the knots in a Herbig–Haro object (HH 2). The bottom panels show H_α images obtained with HST in 1994, 1997, and 2007. The new bow shock clearly expands as a result of the strong wind that passes from right to left in the figure.

A large complex region of multiple clumps within HH 2 shown in the figure appears to have significant morphological changes. In several cases significant differential motions exist between adjacent clumps, and it now appears that shadowing and merging are probably common in such flows. We see

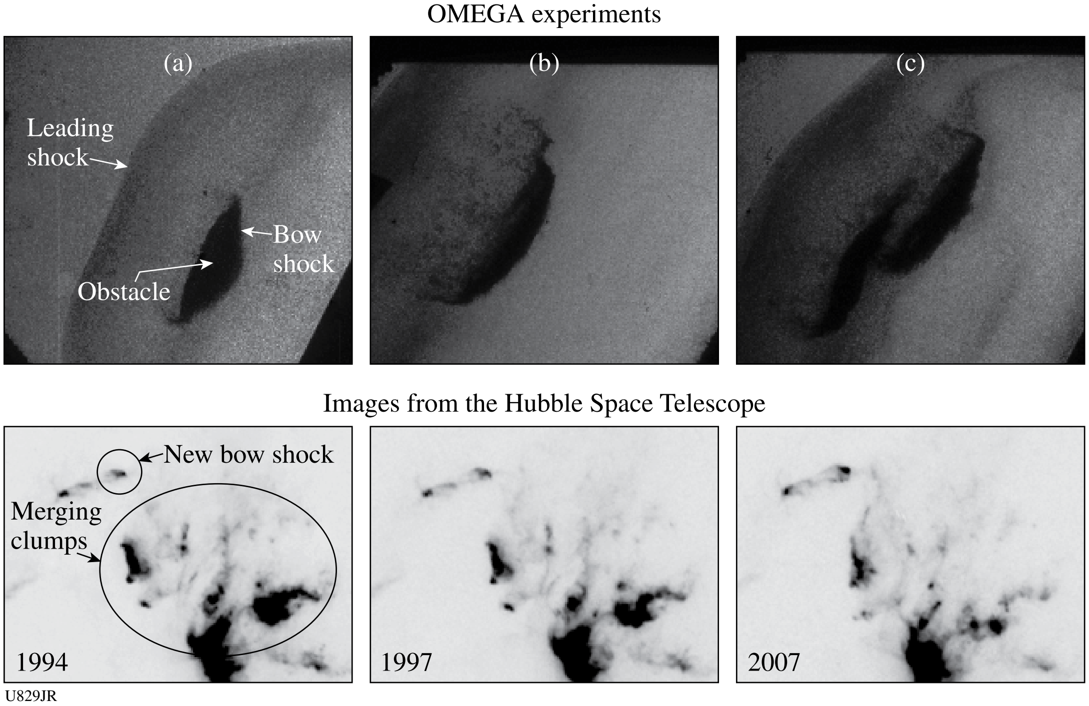

Figure 116.56
OMEGA experiments (top) and three astronomical images (bottom) of shock waves around single and multiple clumps. The experimental images (a) and (b) show how a shock wave flattens and tears apart an obstacle. Analogous behavior has just been observed unambiguously for the first time with a third-epoch Hubble Space Telescope image of shocks in HH 2 (bottom). Note how the new bow shock widens in the most-recent 2007 image. The third experimental image (c) shows how shadowing affects two clumps. Multiple clump interactions also occur in HH 2.

analogous behavior in the laboratory experiment labeled (c) where shadowing effects have created a bumpy bow shock around two closely spaced obstacles in the flow. In the coming year we will be evolving this design to address shocked flow through a medium with dozens of small clumps. Two additional third-epoch HST images will complement the experimental work in the coming year.

Multiview Tomographic Study of OMEGA Direct-Drive-Implosion Experiments

Principal Investigators: R. Mancini (University of Nevada, Reno), R. Tommasini (LLNL)

Co-investigators: N. Izumi (LLNL); I. E. Golovkin, (Prism Computational Sciences); D. A. Haynes and G. A. Kyrala (LANL); and J. A. Delettrez, S. P. Regan, and V. A. Smalyuk (LLE)

The determination of the spatial structure of inertial confinement fusion implosion cores is an important problem of high-energy-density physics. To this end, three identical multimonochromatic x-ray imagers (DDMMI's), designed and built as part of this project, are currently being used in direct-drive OMEGA implosion experiments to perform simultaneous observations along three quasi-orthogonal lines of sight (LOS). The implosions are driven with 60 OMEGA beams using high- and low-adiabat laser pulses, and the targets are gas-filled plastic shells. At the collapse of the implosion, the hot and dense core plasma achieves temperatures in the 1-keV to 2-keV range and electron number densities in the 1×10^{24} cm^{-3} to 3×10^{24} cm^{-3} range. X-ray K-shell line emission from a tracer amount of argon added to the deuterium fuel is a suitable spectroscopy diagnostic for this temperature and density range. In addition, x-ray absorption from a titanium tracer layer embedded in the plastic yields information about the compressed shell.

Core images recorded by DDMMI instruments are formed by a large array of 10-μm-diam pinholes, with an ~100-μm separation between pinholes, and are reflected off a depth-graded WB$_4$C multilayer mirror with an average bilayer thickness of 15 Å. The instrument is equipped with 10-cm-long mirrors that permit the observation of narrowband x-ray images over a 3-keV to 5-keV photon energy range. They have a magnification of 8.5, provide spatial resolution of approximately 10 μm, and record gated (framed) images characteristic of a 50-ps time interval. The broad photon energy range, afforded by the use of long mirrors, covers the K-shell line emission from argon ions as well as the K-shell line absorption from titanium L-shell ions. As an illustration of the data recorded by DDMMI instruments, Fig. 116.57 displays gated argon Ly$_\beta$ ($1s\ ^2S$–$3p\ ^2P$, $h\nu$ = 3936 eV) narrowband core images observed simultaneously along three quasi-orthogonal LOS: TIM-3, TIM-4, and TIM-5. These images are taken close to the state of maximum compression of the core. The photon energy range of these narrowband images is given by the (mainly) Stark-broadening widths of the line shape, which for the plasma conditions achieved in these cores is in the 60-eV to 70-eV range. The multiview data recorded with DDMMI instruments make it possible to study the three-dimensional structure of the implosion core. It is interesting to observe the differences in distribution of brightness associated with the Ly$_\beta$ core images along different LOS, which depends on both temperature and density conditions in the core. In addition to differences in intensity distributions, there are differences in shapes: the image observed along TIM-4 is the most-elongated one (i.e., oval of largest eccentricity), while the shapes observed along TIM-3 and TIM-5 are less elongated. Argon Ly$_\alpha$ ($1s\ ^2S$–$2p\ ^2P$, $h\nu$ = 3320 eV) and He$_\beta$ ($1s^2\ ^1S$–$1s3p\ ^1P$, $h\nu$ = 3684 eV) images are also recorded, thus providing data that will determine the temperature and density distribution in the core. Several analysis methods initially developed and tested for single LOS data analysis are now being extended to consider the analysis of data simultaneously observed along three LOS for a three-dimensional reconstruction of the spatial structure in the core.

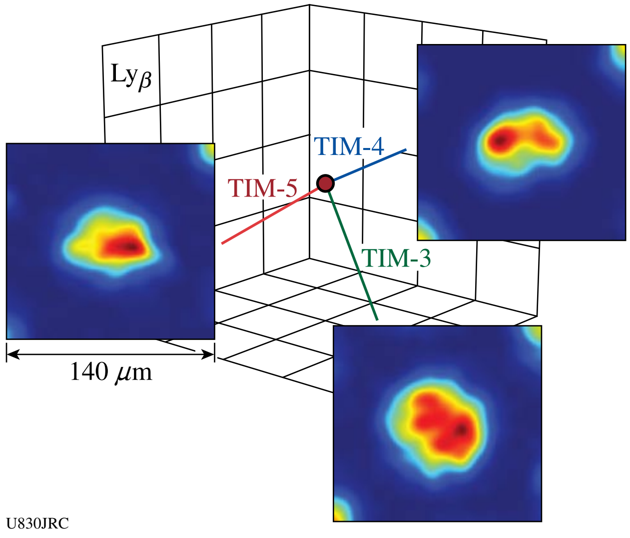

Figure 116.57
Gated argon Ly$_\beta$ narrowband images of the implosion core simultaneously recorded by DDMMI instruments along three quasi-orthogonal lines of sight: TIM-3, TIM-4, and TIM-5 for OMEGA shot 49956.

Monoenergetic Proton Radiography of ICF Implosions

Principal Investigators: R. D. Petrasso and C. K. Li (Massachusetts Institute of Technology)
Co-investigators: F. H. Séguin and J. A. Frenje (MIT); J. P. Knauer and V. A. Smalyuk (LLE); and J. R. Rygg and R. P. J. Town (LLNL)

MIT's NLUF program has continued an ongoing series of experiments using monoenergetic charged-particle radiography in the study of plasmas and transient electromagnetic fields generated by the interactions of OMEGA laser beams with plastic foils and ICF target capsules. This work, involving novel studies of field instabilities, magnetic reconnection, ICF implosion dynamics, and self-generated electromagnetic fields in ICF implosions, has already resulted in many publications, including four in Physical Review Letters[1–4] and one in Science,[5] as well as several invited talks at conferences.[6–9]

Figure 116.58 shows the basic experimental setup for imaging of implosions (see Ref. 10 for more general details of the radiography method). Up to 40 OMEGA laser beams interact with a target capsule, which has a spherical plastic shell with or without a gold cone inserted for "fast-ignition" studies. A radiographic image of the imploded capsule is made by using a special backlighter and a matched imaging detector. The backlighter is a glass-shell ICF capsule filled with D^3He gas and imploded by ~20 OMEGA laser beams, producing D^3He protons (14.7 MeV) and other fusion products. CR-39 nuclear track detectors are used in conjunction with appropriate filters and processing techniques to record individual charged particles and their energies in the detector plane. Since the burn duration of the D^3He implosion is short (~130 ps) relative to the nanosecond-scale duration of the capsule illumination (1 ns) and subsequent evolution, and since the relative timing of the backlighter and the capsule illumination was adjustable, it is possible to record images at different times during implosions.

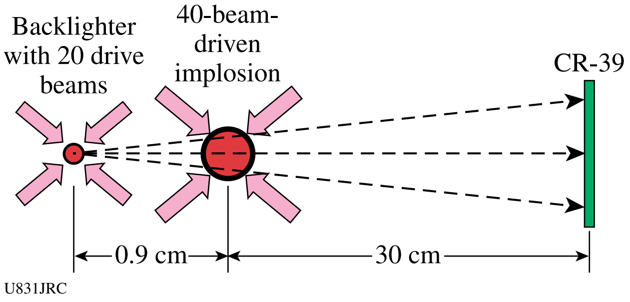

Figure 116.58
Experimental setup with proton backlighter, subject implosion, CR-39 imaging detector, and laser beams. The subject implosion shown here has a spherical plastic shell, but images were also made with "cone-in-shell" capsules (see Fig. 116.59).

The experiments resulted in the discovery and characterization of two distinctly different types of electromagnetic configurations in ICF implosions (Fig. 116.59), as well as the measurement of capsule radius and areal-density (ρR) temporal evolution (Fig. 116.60).[4,5] Proton radiography reveals field structures through deflection of proton trajectories. The two field structures evident in Fig. 116.59 consist of (1) many radial filaments with complex striations and bifurcations, permeating the entire field of view, of magnetic field magnitude 60 T; and (2) a coherent, centrally directed electric field of the order of 10^9 V/m within the capsule, leading to the central concentration of protons in Fig. 116.59(b). Figure 116.60 shows the values of capsule radius and ρR at various times during the implosions of spherical capsules studied in images similar to those in Fig. 116.59.[4] The size was inferred from the spatial structure of the images, while ρR was determined from the energy loss of the imaging protons while passing through the capsule center.

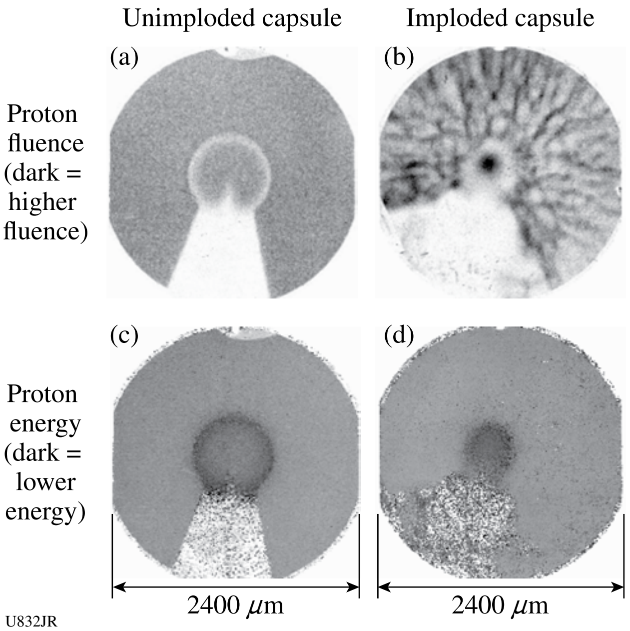

Figure 116.59
Images of a 430-μm-radius spherical CH capsule with attached gold cone, before and during implosion. Images (a) and (c) show the unimploded capsule used in OMEGA shot 46531. Images (b) and (d) show a capsule at 1.56 ns after the onset of the laser drive (shot 46529). In (a) and (b) dark areas correspond to regions of higher proton fluence, while in (c) and (d) dark areas correspond to regions of lower proton energy. The energy image values in the region shadowed by the cone are mostly noise since very few protons were detected in that region.

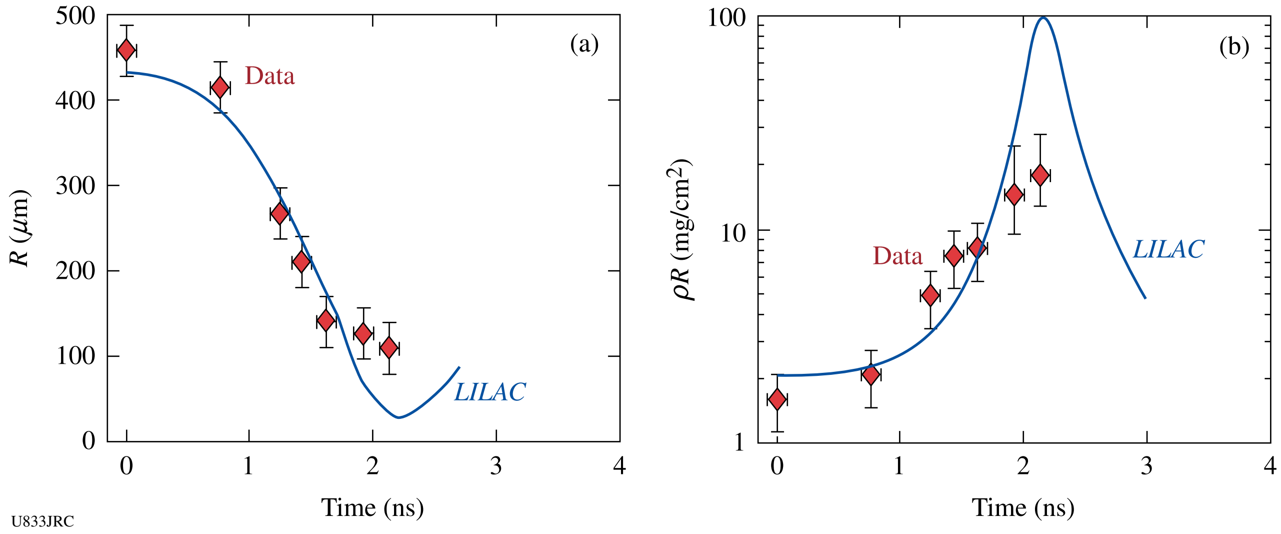

Figure 116.60
Measured capsule radius (a) and ρR (b) as a function of time,[4] from a series of images of spherical implosions (40 drive beams in a 1-ns flat-top pulse). The curves show *LILAC* 1-D simulations.

The relationship of the measured sizes and ρR's to predictions of the 1-D code *LILAC* are also shown.

X-Ray Thomson-Scattering Spectra in Shock-Compressed Beryllium

Principal Investigators: R. Falcone and H. J. Lee (University of California, Berkeley), P. Neumayer and S. H. Glenzer (LLNL)

Direct measurement of the exact thermodynamic and physical properties of dense matter is of great interest to test dense plasma modeling and to address fundamental physics questions such as the equation of state and the structure of dense matter. Powerful laser-produced x-ray sources have been used to probe dense matter, which has enabled a quantitative *in-situ* diagnostic of densities and temperatures using x-ray Thomson scattering measurements.[11] We have continued x-ray scattering experiments in shock-compressed beryllium to measure the electron temperature and density for varying drive-beam conditions.

Two types of planar targets coupled with Mn backlighters were deployed for the x-ray Thomson-scattering measurements of 25° and 90° scattering angles on the OMEGA laser. A 250-μm-thick beryllium foil was driven by 12 beams smoothed with distributed phase plates (SG-4) overlapped in a ~1-mm-diam focal spot. Laser intensities of 10^{14} W/cm^2 < I < 10^{15} W/cm^2 in a 4-ns-long constant or 5-ns shaped pulse were applied. Radiation-hydrodynamic calculations performed using Helios[12] indicate that under these irradiation conditions, a strong shock wave is launched in the solid target, compressing it homogeneously at pressures in the range of 20 to 60 Mbar. Twelve additional focused beams (~200-μm spot) illuminate a Mn foil to produce ~6.18-keV He$_\alpha$ x rays for 25° scattering (17 backlighter beams are used for 90° scattering). Figures 116.61(a) and 116.61(b)

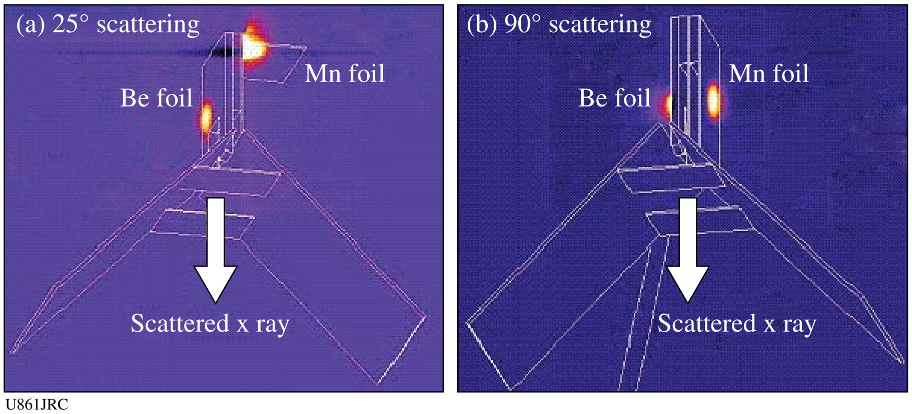

Figure 116.61
Time-integrated images for $E > 2$ keV show the emission produced by heater and probe beams for (a) 25° scattering and (b) 90° scattering.

present time-integrated images showing the emission by drive and backlighter beams. A highly oriented pyrolytic graphite (HOPG) crystal spectrometer coupled to a gated microchannel plate detector in TIM-3 has been used as a spectrometer and a detector. The scattered photon fraction is determined by the product $n_e\sigma_{TS}l$, where σ_{TS} is the Thomson-scattering cross section and l is the length of the scattering volume.

Figures 116.62(a) and 116.62(b) show the scattering spectra (solid lines) and fits (dotted lines) for a 25° and a 90° scattering angle from 4-ns-long constant drive beams, which give a pressure of 30 Mbar. Two small plasmon features in addition to the two elastic peaks from the 6.18-keV Mn He_α line and the 6.15-keV intercombination line are measured at a 25° scattering angle, indicating a collective scattering regime with a scattering parameter $\alpha = 1/k\lambda_s = 1.56$ and λ_s being the screening length and k the scattering vector with $k = 4\pi\left(E_0/hc\right)\sin g\left(\theta/2\right) = 1.36\ \mathring{\mathrm{A}}^{-1}$. The frequency shift of the plasmon is determined by the frequency of plasma oscillations. Calculated spectra using the theoretical form factor indicate that the solid beryllium is compressed by a factor of 3 with $7 \times 10^{23}\ \mathrm{cm}^{-3} < n_e < 8 \times 10^{23}\ \mathrm{cm}^{-3}$.

The Compton-scattering spectrum measured at a scattering angle of $\theta = 90°$ accessing the noncollective scattering regime with $\alpha = 0.5$ and $k = 4.4\ \mathring{\mathrm{A}}^{-1}$ shows a parabolic spectrum downshifted in energy from the incident radiation by the Compton effect; the shift is determined by the Compton energy $E_C = h^2k^2/2m_e = 74$ eV. The theoretical fit to the measured spectrum indicates the same densities and temperatures as obtained for collective scattering. Details may be found in Ref. 13.

To generate higher compression, the intensity of nanosecond laser beams was shaped to have (1) a 4-ns-long step-like foot,

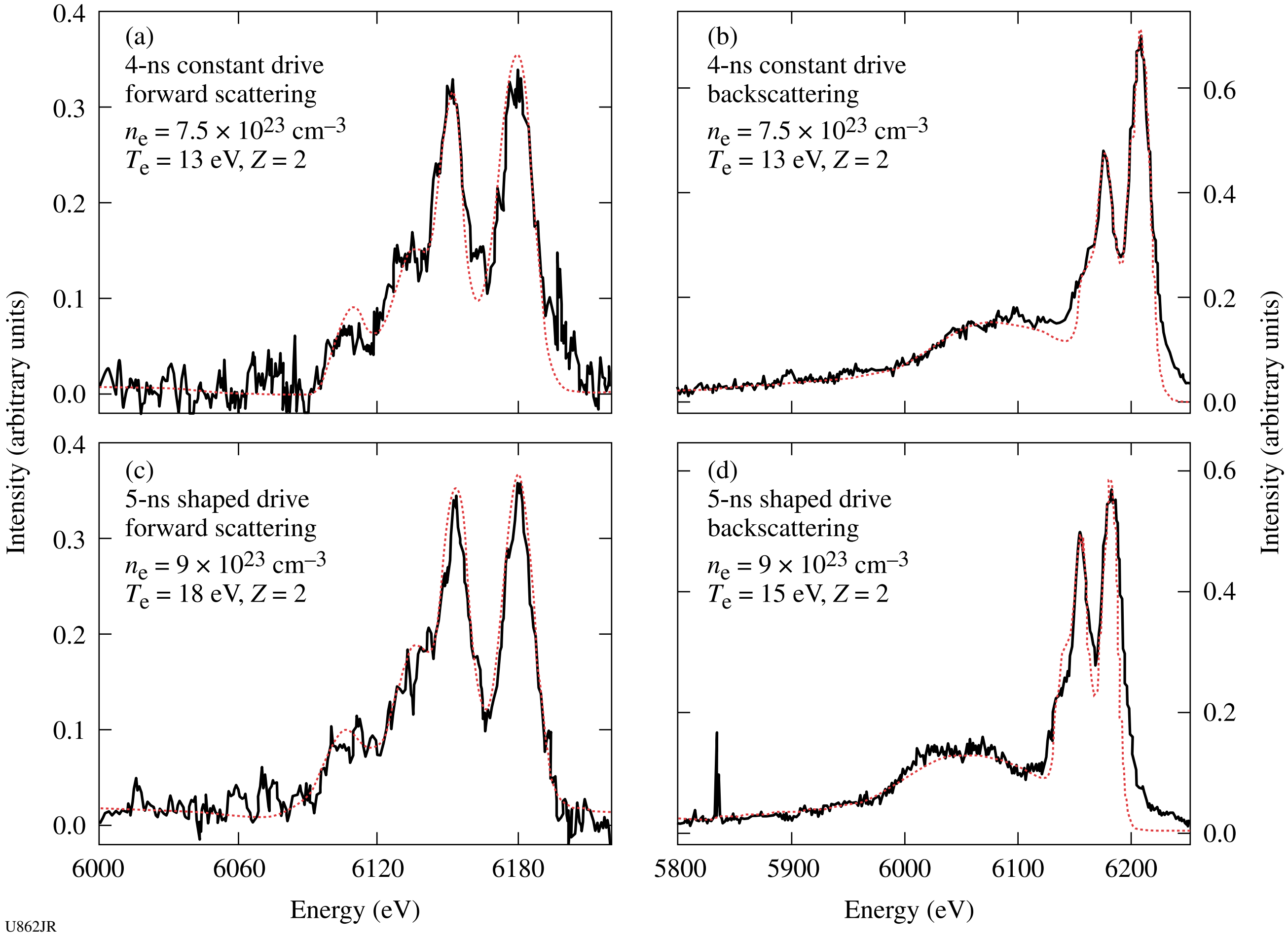

Figure 116.62
X-ray scattering data (solid lines) and fits (dotted lines) of 25° forward scattering [(a) and (c)] and 90° backscattering [(b) and (d)] with different driving beams.

with a 2-ns first foot at 8×10^{13} W/cm^2 and a 2-ns second foot at 1.6×10^{14} W/cm^2 and (2) a 1-ns-long peak at 4.8×10^{14} W/cm^2 following a 4-ns step-like foot. Radiation-hydrodynamic simulations show that the three shock waves from each step merge at about 6 ns after the beginning of drive beams and compress the target by more than a factor of 3.5.

Figures 116.62(c) and 116.62(d) show the experimental scattering spectra (solid lines) at a 25° and a 90° scattering angle and fits (dotted lines) from 5-ns-long shaped drive beams that drive a strong shock reaching ~60 Mbar. The calculated spectrum with $n_e = 9 \times 10^{23}$ cm^{-3}, $T_e = 15$ eV, and $Z = 2$ gives a best fitting to the Compton-scattering data. The parameters from the fit to the data in the collective scattering regime are in good agreement with the ones from the noncollective scattering data within error bars of ±20% in temperature. Theoretical x-ray scattering spectra have been calculated in a random phase approximation for the free-electron feature and density-functional theory for the ion feature.

Through this campaign, we have successively accomplished the measurement of the Compton and plasmon resonance on shock-compressed Be. In addition to the accurate measurement within ±7% in density, we have demonstrated that we can characterize multiply shocked matter by changing the drive pulse shape and intensity. This opens up the possibility of obtaining a compression of $n_e > 1.0 \times 10^{24}$ cm^{-3} by co-propagating and counter-propagating the geometry of driving beams. In future research, the Thomson-scattering method will be used to investigate the equation of state in the multiple-shock-compressed matter.

FY08 LLNL OMEGA Experimental Programs

In FY08, Lawrence Livermore National Laboratory (LLNL) led 238 target shots on the OMEGA Laser System. Approximately half of these experiments were dedicated to the National Ignition Campaign (NIC); the other half were dedicated to supporting the high-energy-density stewardship experiments (HEDSE's).

Objectives of the LLNL-led NIC campaigns on OMEGA included the following:

- *Laser–plasma interaction studies of physical conditions relevant for the National Ignition Facility (NIF) ignition targets*
- *Studies of the x-ray flux originating from the laser entrance hole (LEH) window of a hohlraum, which might impact the performance of a fusion capsule*
- *Characterization of the properties of warm dense matter—specifically radiatively heated Be*
- *Studies of the physical properties of capsules based on Cu-doped Be, high-density carbon, and conventional plastics, including new high-resolution shock-velocimetry measurements*
- *Determining ablator performance during the implosion of NIC-candidate ablators*
- *Experiments to study the physical properties (thermal conductivity) of shocked fusion fuels*
- *High-resolution measurements of velocity nonuniformities created by microscopic perturbations in NIF ablator materials*
- *Demonstration of $T_r = 100$-eV foot-symmetry tuning using a re-emission sphere*
- *Demonstration of $T_r = 100$-eV foot-symmetry tuning using a backlit thin-shell capsule*
- *Quantification of x-ray foot preheat caused by laser–window interaction*

The LLNL HEDSE campaigns included the following:

- *Quasi-isentropic [isentropic compression experiment (ICE)] drive used to study material properties such as strength, equation of state, phase, and phase-transition kinetics under high pressure*
- *Development of long-duration, point-apertured, point-projection x-ray backlighters*
- *Development of an experimental platform to study nonlocal thermodynamic equilibrium (NLTE) physics using direct-drive implosions*
- *Opacity studies of high-temperature plasmas under LTE conditions*
- *Development of multikilovolt x-ray sources using underdense NLTE plasmas for x-ray source applications*
- *Studies of improved hohlraum heating efficiency using cylindrical hohlraums with foam walls*

- *Laser-driven dynamic-hohlraum (LDDH)-implosion experiments*

- *High-speed hydrodynamic jets for code validation*

1. NIC Experiments

Laser–Plasma Interactions: The laser–plasma interaction experiments continued to emulate the plasma conditions expected along the laser-beam path in inertial confinement fusion designs. An interaction beam (beam 30) aligned along the axis of a gas-filled hohlraum is used to study laser-beam propagation. Figure 116.63 shows the results of laser–plasma interaction experiments that were performed to study the propagation of laser light through high-density $\left(N_e/N_{cr} > 10\%\right)$, millimeter-long, high-temperature (T_e > 2.5 keV) plasmas. These results provide limits on the intensity of the inner-cone beams to maintain stimulated Raman scattering (SRS) backscatter below the 5% requirements for ignition on the NIF.

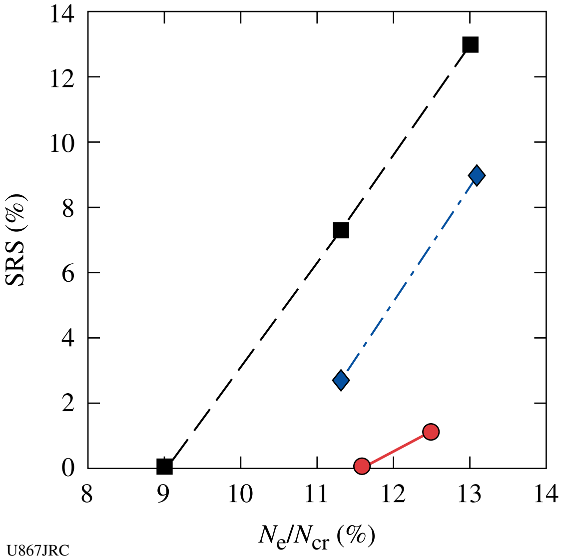

Figure 116.63
Measured time-integrated backscatter as a function of density in a high-temperature millimeter-long plasma at three interaction-beam intensities: 10 × 10^{14} W/cm^2 (squares), 5 × 10^{14} W/cm^2 (diamonds), and 2.5 × 10^{14} W/cm^2 (circles). For densities above 10%, the backscatter is dominated by stimulated Raman scattering (SRS); the measured time-integrated stimulated Brillouin scattering (SBS) is less than 1%.

These experiments also quantified the effect of polarization smoothing in high-density plasmas where SRS dominates, providing further guidance for the design of a low-backscatter, indirect-drive ICF experiment. Figure 116.64 shows that adding polarization smoothing increases the intensity threshold for SRS by a factor of 1.5, which was predicted by *pf3D* code simulations completed prior to these experiments.

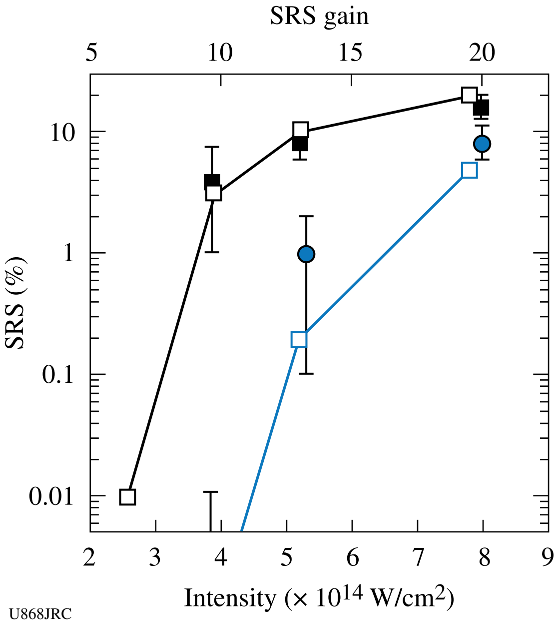

Figure 116.64
Instantaneous SRS reflectivities measured 700 ps after the rise of the heater beams in a 11.5% N_{cr} plasma. Experiments without polarization smoothing (squares) show a threshold (reflectivity of 5%) for SRS at an intensity of 4.5 × 10^{14} W/cm^2 and a corresponding gain of 11. Adding polarization smoothing increases this threshold to an intensity of 6.8 × 10^{14} W/cm^2, which corresponds to an SRS gain of 17. *pf3D* simulations performed prior to the experiments are shown (open symbols) and predicted the main results of these experiments. The gains are calculated by post-processing hydrodynamic simulations using *LIP*.

Prior work on stimulated Brillouin scattering (SBS) mitigation was documented and published in Refs. 14 and 15.

X-Ray Preheat from an LEH Window: The NIF ignition hohlraum was gas filled with polyimide windows over the laser entrance holes. During the early part of the laser pulse, the beams had to burn through the windows and fill-gas before reaching the hohlraum walls. As a result, the x rays generated during window burnthrough occured ~300 ps before the hohlraum x rays. There was concern that the resultant early deposition of energy at the capsule poles could have generated an asymmetric pressure wave, or that asymmetric preheat could have seeded instabilities in crystalline Be. Initial *LASNEX* calculations predicted that x-ray production would not be high enough to significantly perturb the capsule, but an extrapolation of existing experimental data suggested that *LASNEX* might have underestimated the flux from the windows. A short series of OMEGA shots were carried out to measure the absolute x-ray spectrum generated during burnthrough of polyimide windows of various thicknesses, and the inner- to outer-beam cone delay and intensities spanning those expected to be used on the NIF. The primary diagnostic on these shots was the Dante x-ray diode array.

Figure 116.65 shows the measured flux from Channel 5 (centered from 600 to 800 eV) for a series of five shots, together with *LASNEX* simulations for each shot. The results showed that in all cases the measured flux integrated over the first nanosecond was ~2× lower than predicted by *LASNEX*. The x-ray flux scaled as expected—approximately linearly with window thickness.

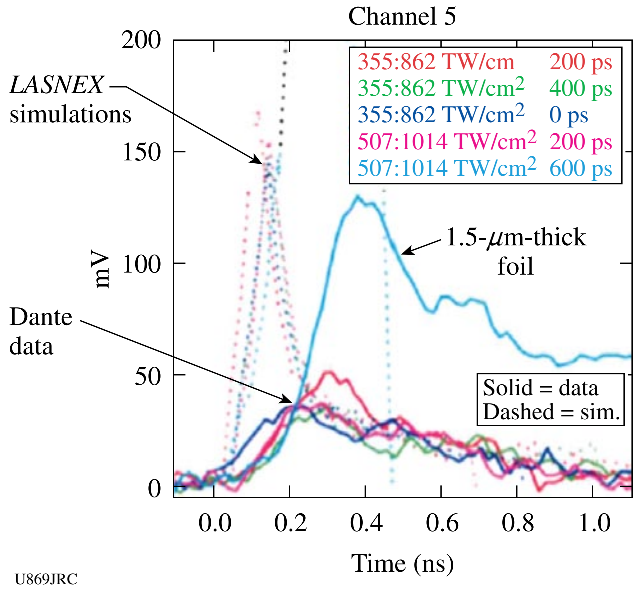

Figure 116.65
A measured signal from Dante Channel 5 for the window preheat shots. The legend shows an intensity of cone-1 beams in TW/cm^2 (first number), cone-2 intensity (second number), and the delay between beams (third number). The indicated curve depicts a 1.5-μm-thick foil; all others have 0.5-μm thickness.

Since no adverse effect was expected on the capsule even with nominal x-ray production, the low measured x-ray flux indicated that the ignition point design was robust to perturbations imposed on the capsule during window burnthrough.

Symmetry Diagnosis by a Re-emission Sphere: The NIC proposes to set the first 2 ns of hohlraum radiation symmetry by observing the instantaneous soft x-ray re-emission pattern from a high-*Z* sphere in place of the ignition capsule.[16] To assess this technique under NIC conditions, we used the OMEGA Laser Facility to image the re-emission of Bi-coated spheres with 200-ps temporal, 50- to 100-μm spatial, and 30% spectral resolution. The sphere was driven by 70% NIC-scale vacuum Au hohlraums heated to T_r = 100 eV using two cones/side laser-beam illumination (Fig. 116.66). The laser beams smoothed with SG4 phase plates using 1-ns square pulses generated intensities at the hohlraum wall that were similar to the foot of the NIF ignition design.

Good re-emit images were acquired at 100- to 115-eV NIF foot temperatures for both 900- and 1200-eV energy bands (see Fig. 116.67). The re-emission patterns at 900 eV and 1200 eV were consistent with each other, but their sensitivity ratio was greater than expected; this will be confirmed in FY09. We also demonstrated the expected P_2/P_0 dependence to the laser-cone power ratio (Fig. 116.67). The experiments demonstrated the required accuracies of $<5(7\%)\ P_2/P_0\ (P_4/P_0)$ Legendre mode-flux asymmetry at both 900-eV and 1200-eV re-emission photon energies.

Viewfactor calculations were in agreement with the experimentally measured hohlraum radiation flux and re-emit images when assuming 50% inner-beam and 95% outer-beam coupling

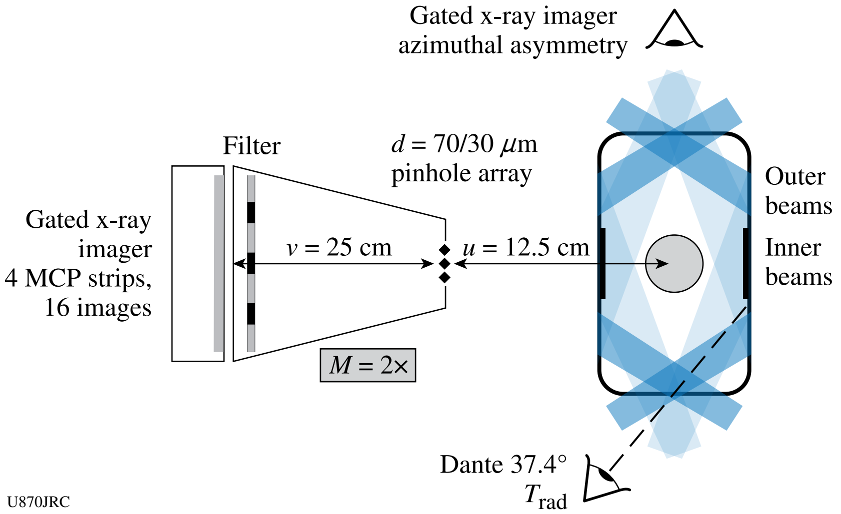

Figure 116.66
The re-emit experimental setup for the NIF and OMEGA.

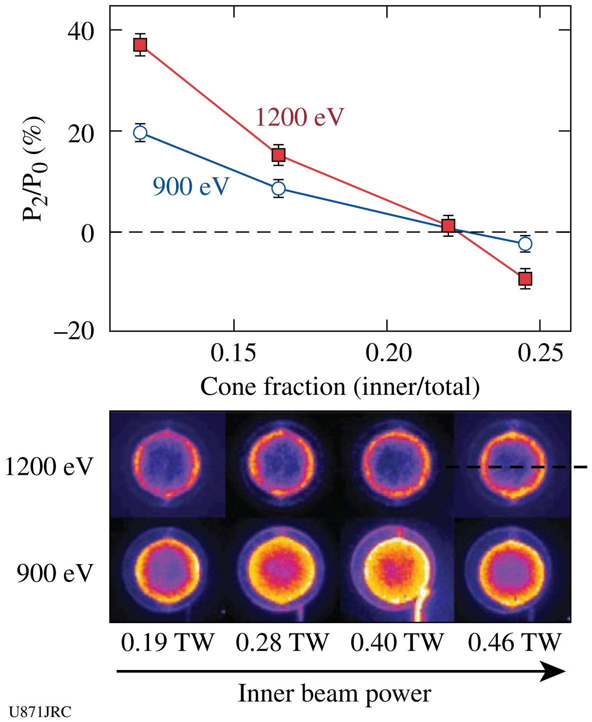

Figure 116.67
Re-emit images measured at 0.8 ns at 900-eV and 1200-eV energy bands for constant 0.28-TW outer-beam power and variable inner-beam power, and the corresponding measured re-emitted P_2/P_0 versus laser-cone power fraction.

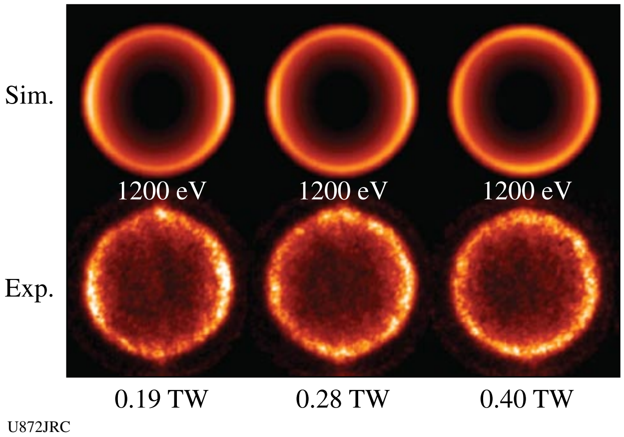

Figure 116.68
Simulated viewfactor versus measured re-emit images for different inner-beam powers (outer beams: 0.28 TW/beam).

into x rays at the hohlraum wall (Fig. 116.68). Radiation-hydrodynamic simulations used to design the NIC ignition target confirm the lower inner-beam coupling to within 10%, as do the thin-walled shell experiments described below.

Symmetry Diagnosis by Thin Shell: Should it prove necessary to further optimize the symmetry during the second and third shocks to obtain maximum yield, the shape of a thin-shell capsule in flight can be measured during this time period by x-ray backlit imaging. The thin shell will be made of the ignition ablator material with its thickness adjusted to optimize its sensitivity to drive at different times during the foot of the pulse. Recent experiments at the OMEGA Laser Facility demonstrated the viability of area backlit images of 0.6-scale Be capsules doped with 2% Cu under NIC foot conditions by using a 1-ns pulse shape for both drive and backlighter beams, as shown in Fig. 116.69.

To determine the drive symmetry during the foot of the pulse, a scale-0.6 hohlraum was illuminated with a 1.0-ns pulse, giving a drive peaking at 125 eV early in time. Sixteen high-precision images of the converged shell were then recorded on each shot with a 4.7-keV (Ti) foil backlighter, at times between 6.6 and 7.4 ns; an example is shown in Fig. 116.70.

The sensitivity of the measured P_2 distortions to changes in the fraction of the power in the inner and outer cones of beams confirmed the predictions of simulations, as shown in Fig. 116.71, albeit with an offset consistent with 10% less inner-cone absorption than predicted by this simulation. The

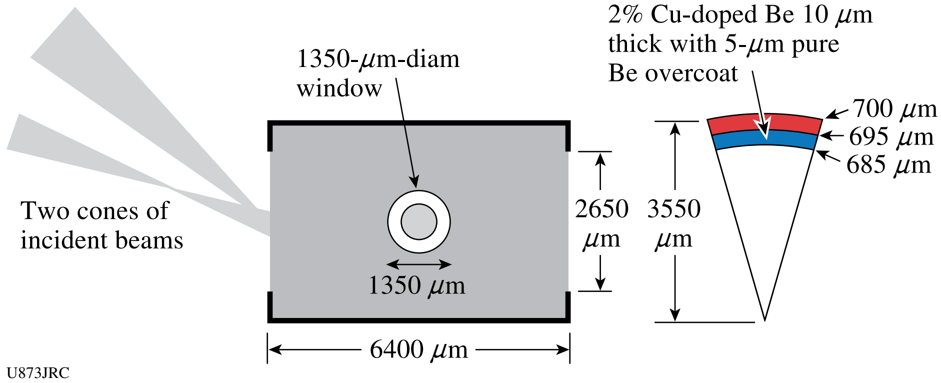

Figure 116.69
Schematic of the scale-0.6 NIC hohlraum and thin-shell capsule used on OMEGA to validate the plans to control the drive symmetry during the foot of the ignition pulse where $T_r \gtrsim 100$ eV. The obtained backlit images demonstrated that the measured ball distortion has the expected sensitivity to the $\ell = 2$ component of the drive and can measure the Legendre moments to the needed precision.

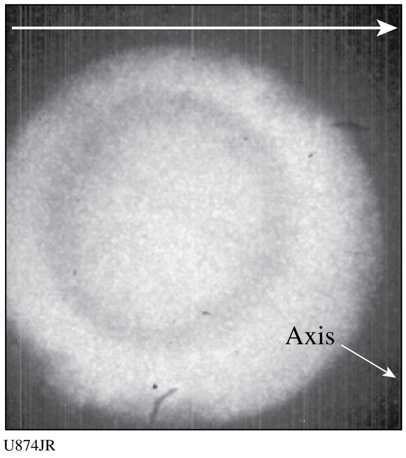

Figure 116.70
Image of a thin shell converged to half its initial radius by a 125-eV x-ray drive in the NIC-like hohlraum.

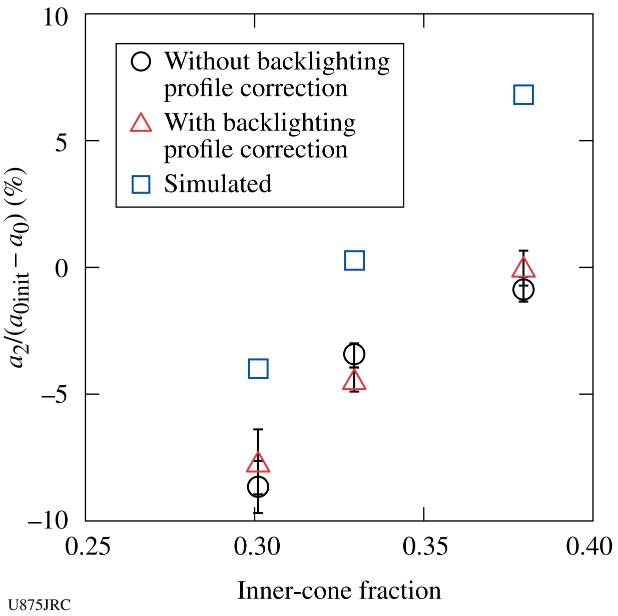

Figure 116.71
Measured versus simulated thin-shell P_2 relative to distance traveled versus cone fraction.

results verified that the overall measurement accuracy (±1% in P_2, extrapolating to ±0.3% at full NIC scale and larger distance traveled) is sufficient to meet the ±0.5% P_2 requirement for foot symmetry control in the NIC.[17]

X-Ray Thomson Scattering (XRTS) Conductivity: The ultimate goal of this campaign was to measure the plasmon broadening in collective x-ray Thomson scattering (XRTS) to extract the plasma collisionality and, therefore, conductivity, which is important to accurately model capsule performance on the NIF. For this purpose, 250-μm Be foils were driven at 3.5×10^{14} W/cm^2 over a total duration of 3 ns (see Fig. 116.72). From 1-D hydrodynamic simulations (*HELIOS*) we expected shock-compressed electron densities between 6 and 8×10^{23}/cc and electron temperatures in the range of 10 to 15 eV at times ≥4.25 ns after the start of the heater pulse at the Be rear surface. The Cl Ly-α line at 2.96 keV was employed to probe the plasma parameters. The scattered signal was dispersed by the GTS HOPG spectrometer in TIM-6 and recorded by XFRC4 coupled to the LLNL charge-coupled device (CCD).

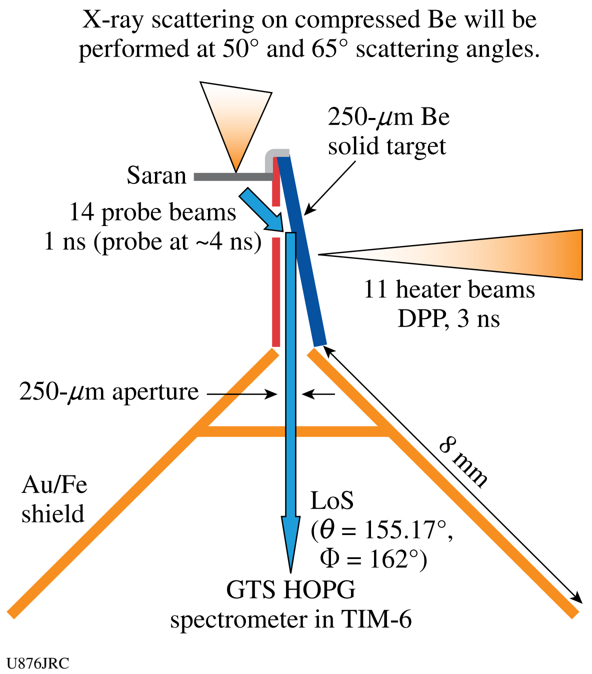

Figure 116.72
Schematic of the experimental configuration.

Figure 116.73 shows both the recorded spectrum from a 50° scattering shot fitted by a synthetically generated spectrum corresponding to a plasma density of $n_e = 1.5 \times 10^{23}$/cc and an electron temperature of 8 eV. We note that the shape of the red-shifted plasmon was sensitive to both n_e and T_e, and that T_e, on its own, was sensitive through detailed balance to the ratio of the blue- to red-shifted plasmon.

The density was 4× to 5× below the values predicted by the hydrodynamic simulations. This suggests that either the shock speed was slower than predicted, leaving an uncompressed, possibly preheated, region probed, or that a low-density blow-off plasma was generated at the back surface, delaying shock breakout. In either case, the 2.96-keV Cl Ly-α radiation was

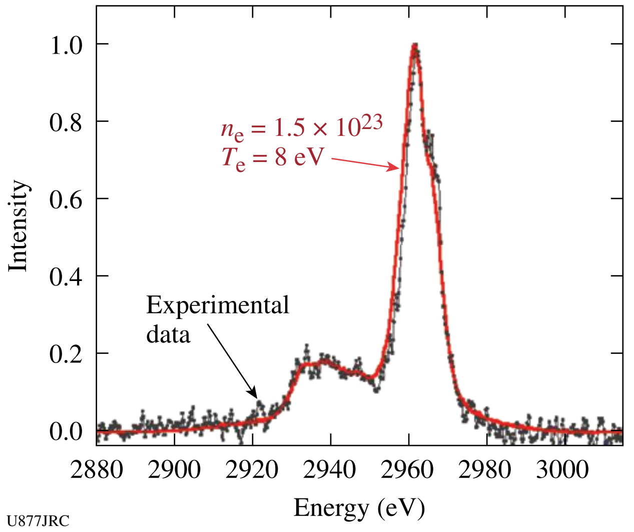

Figure 116.73
Experimental spectrum fitted to synthetic spectrum corresponding to n_e = 1.5 × 10^{23}/cc and T_e = 8 eV.

unable to penetrate to the shocked region and out of the target again. Future shots will optimize target and probe design.

Convergent Ablation: Determining ablator performance during an implosion was a critical part of the NIF tuning campaign. In particular, it was vital to have accurate, in-flight measurements of the velocity, areal density, and mass of the ablator. In tests on OMEGA, a new technique was developed that achieved time-resolved measurements of all these parameters in a single, area-backlit, streaked radiograph of an indirectly driven capsule (Fig. 116.74). Abel inverting the absorption profile to determine the density profile at each time step accomplished this. Results showed a clear difference in ablated mass for Cu-doped Be-capsule implosions with different initial shell thicknesses, illustrating that this technique was suitably precise to be used as a remaining mass diagnostic for the NIF tuning campaign.

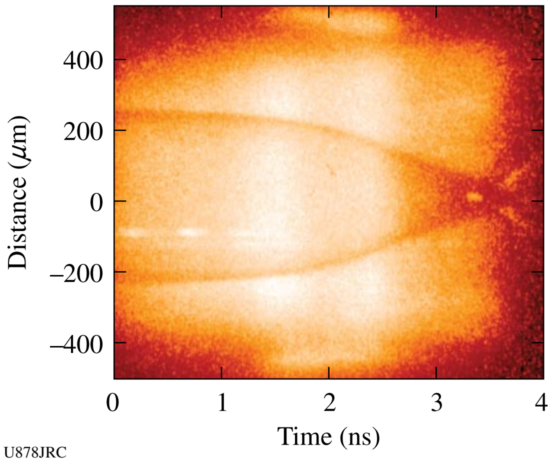

Figure 116.74
Streaked radiograph showing a converging capsule leading up to bang time at 3.3 ns.

Deuterium Thermal Conductivity: Multiple shocks reverberating in a thin layer of liquid deuterium made it possible to attain quasi-isentropic compression of deuterium. Simultaneous measurements of velocity, reflectivity, and emissivity were used to investigate the transport properties of compressed deuterium. As seen in Fig. 116.75, the onset of a more highly reflective state at a temperature of 4000 K and pressure of 1.5 Mbar demonstrated a phase transition to a highly conductive, metal-like phase.

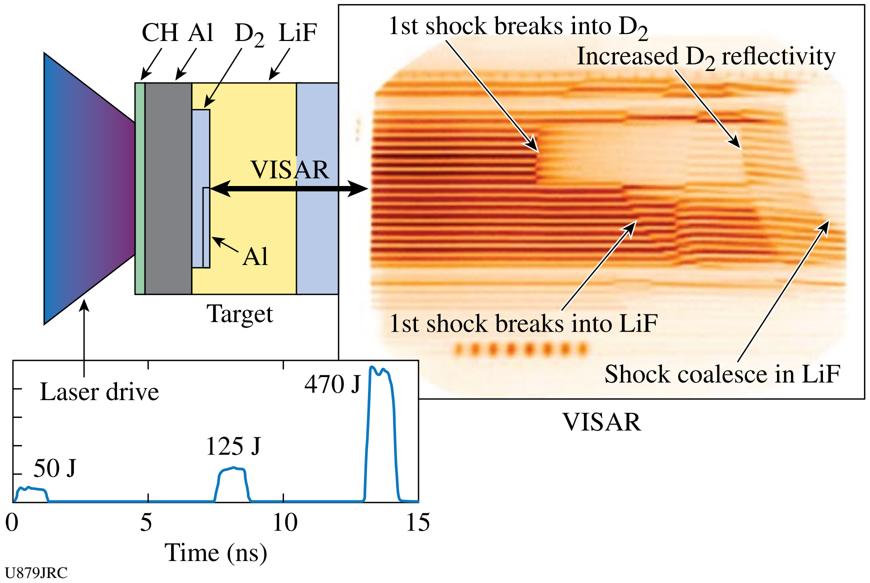

Figure 116.75
Experimental setup and VISAR record of shocked liquid D_2.

Capsule Instability Seeding by Shock Nonuniformity: The CAPSEED campaigns performed measurements of fluid-velocity nonuniformities created by microscopic perturbations in NIC ablator materials. Begun in FY07 and continued through FY08, these campaigns employed a newly commissioned instrument—the OMEGA high-resolution velocimeter (OHRV)—as the primary diagnostic. During FY08 we carried out a survey of the three candidate NIC ablators: Cu-doped Be, polycrystalline diamond, and Ge-doped CH. In addition, much progress was made on analyzing of the data sets and extracting quantitative results. The experiments in October 2007 focused on microcrystalline diamond samples, Be(Cu) targets with preimposed ripples, and sections of capsule shells made from both types of target. Analysis of the rippled Be(Cu) targets showed good agreement between the measured shock-ripple amplitude and simulations of the time evolution of the ripple perturbation (Fig. 116.76).

A surprising result was finding that the shock-front nonuniformities produced by diamond samples shocked below the melt transition were significantly higher than the nonuniformities produced by the same material shocked into the solid–liquid coexistence region (Fig. 116.77). Further experiments in February studied Be targets shocked into the solid–liquid coexistence region, on polycrystalline diamond samples with nanometer-sized grains and on CH(Ge) targets. A third campaign in April continued to examine the three ablator candidates, with a particular focus on Be(Cu) flats constructed with the layered Cu-doping scheme that is specified in the NIC point design for Be capsules. Results from these campaigns are being used to assess the different ablator candidates.

2. High-Energy Stewardship Experiments

Material Properties: In FY08, the Materials Strength Experimental Team performed two types of experiments on OMEGA: vanadium Rayleigh–Taylor (VRT) strength measurements and ramped-drive-development experiments that use indirect x-ray illumination from a hohlraum.

The VRT experiment tested models of material strength by measuring the Rayleigh–Taylor (RT) growth factors on accelerated sinusoidally rippled samples of polycrystalline vanadium.[18] When driven, the amplitude of the rippled interface will grow via the RT hydrodynamic instability, with the amount of growth depending on the drive conditions and vanadium material strength at high pressures and strain rates. The amount of growth will be derived from face-on radiographs taken with the laser-driven x-ray backlighter. Our experiments were conducted to confirm the drive and growth-factor measurements of the previous experiments and to understand the results in terms of various material-strength models. The ripple sample had a period of 60 μm with an initial amplitude of

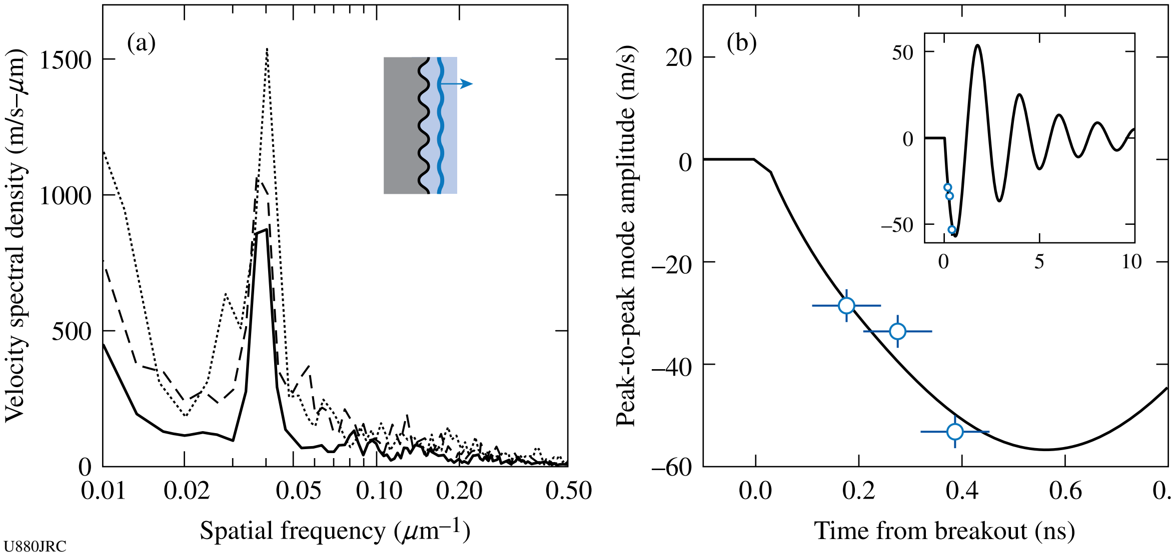

Figure 116.76
(a) Velocity spectra recorded at 180 ps (solid), 280 ps (dashed), and 390 ps (dotted) after shock breakout recorded from targets with a preimposed sinusoidal ripple of 25-μm wavelength and 125-nm initial amplitude at the interface between the Be(Cu) ablator and the PMMA indicator material. The 25-μm ripple mode occupies the spectral peak near a 0.04-μm^{-1} spatial frequency. (b) Velocity amplitude of the isolated ripple modes (symbols) compared to the prediction from a hydrodynamic simulation (curve). Inset: the same data on an expanded time scale.

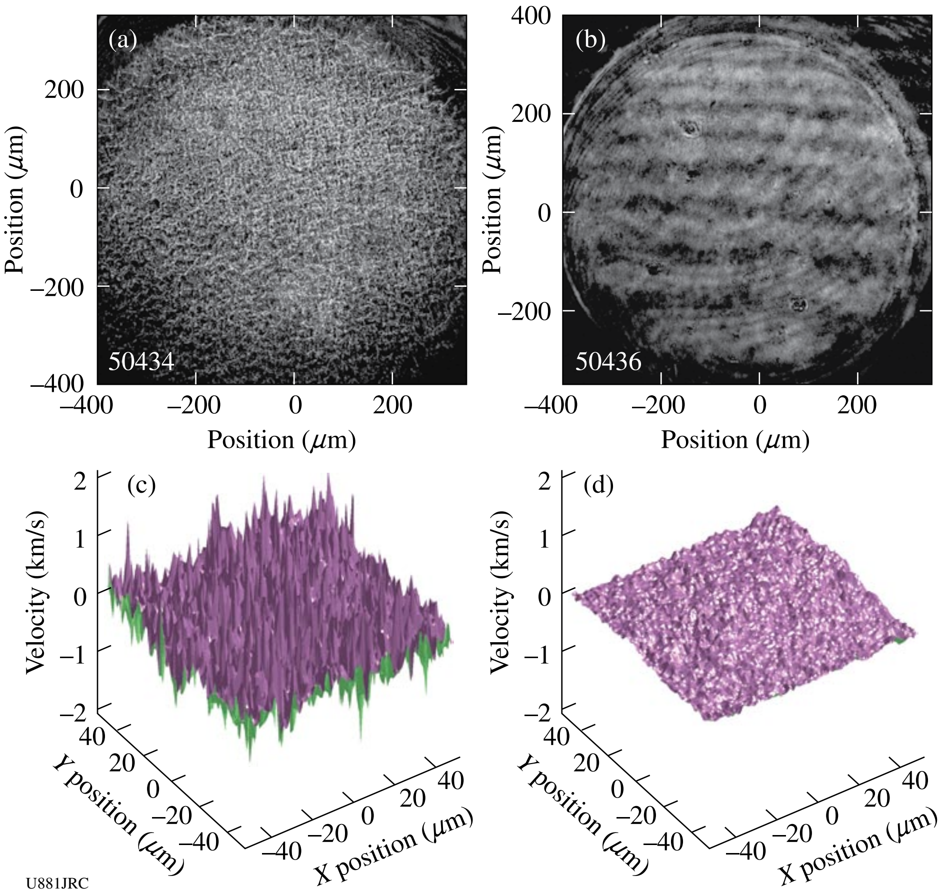

Figure 116.77

Intensity patterns of the probe beam reflected from shock fronts transmitted through polycrystalline diamond samples: (a) at ~300 GPa, which is below the melt, and (b) at ~800 GPa, which is in the solid–liquid coexistence region. Two-dimensional spatial-velocity fluctuations extracted from a 50 × 50 μm^2 region of these datasets are shown in (c) and (d), respectively.

0.6 μm. Figure 116.78 shows a radiograph of the ripples at 70 ns after the start of the drive using a vanadium He-α backlighter (~5.2 keV). From these data, we derived a measured growth factor of 12. Our data were compared with hydro simulations using three different strength models. The models we studied were Steinberg–Guinan (SG), Preston–Tonks–Wallace (PTW), and the new multiscale model that was developed at LLNL by Arsenlis and Becker. Figure 116.79 shows the results. We found that, in all cases, our measurements required modification to the model input parameters. With these modified input parameters, however, all three models were brought into agreement with the measurement. An experimental campaign over several different pressures and strain rates would now be required to distinguish between the models.

We performed three additional experiments that developed isentropic drives using hohlraums to drive a reservoir-gap-sample target package.[19] We employed an extended scale-2.5

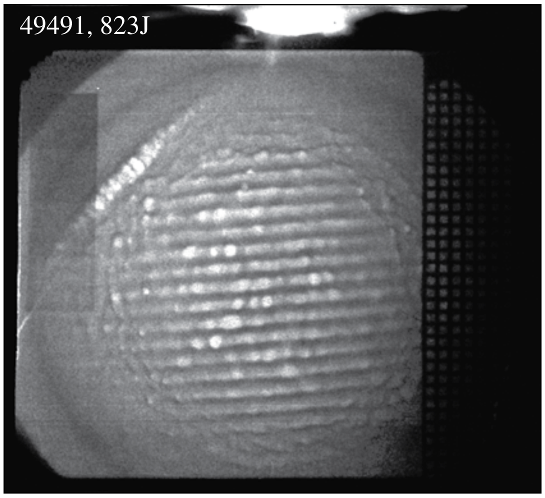

Figure 116.78

Vanadium Rayleigh–Taylor ripple-growth image taken 70 ns after the drive.

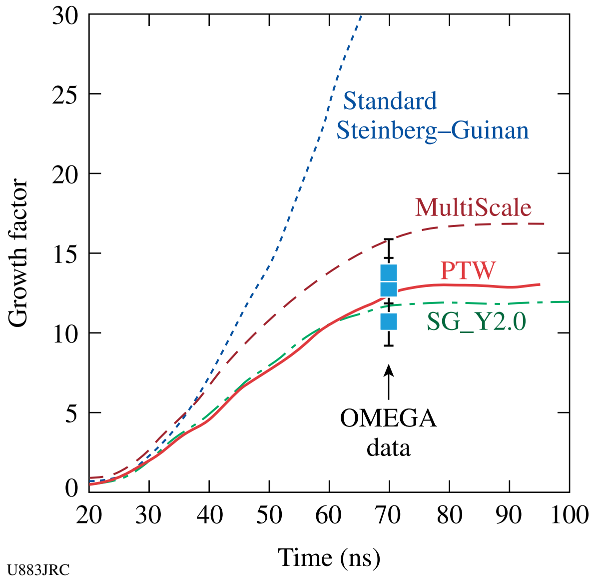

Figure 116.79
Experimental results (solid squares) of the vanadium ripple-growth factor versus the predictions from three different strength models. All models required changes to parameters to fit the data. Experiments at different pressure or strain rates will make it possible to distinguish the differences between the models.

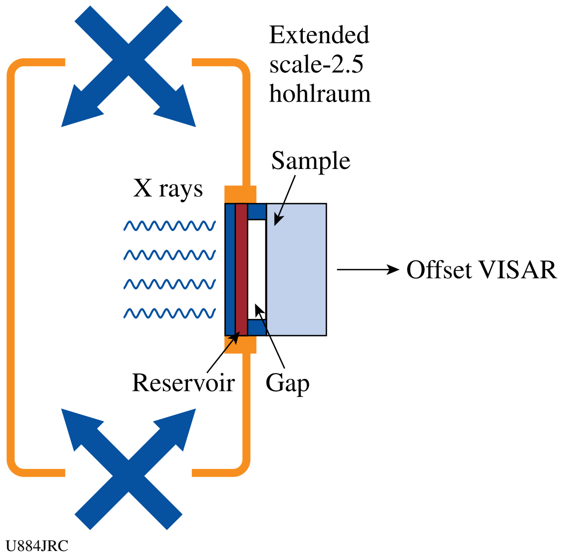

Figure 116.80
A schematic of a quasi-isentropic drive target package mounted on a scale-2.5 hohlraum.

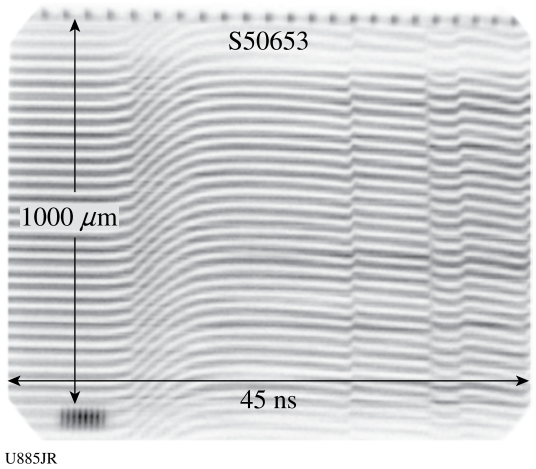

Figure 116.81
A VISAR image of the hohlraum-driven quasi-isentropic drive. The planarity yields resolution better than 150 ps across the 1-mm field of view.

hohlraum (7.0-mm length, 4.0-mm diam; and 2.4-mm-diam LEH) for the first time to create large enough planar regions to drive our samples in a ramp-loading configuration. We used the active shock breakout (ASBO) offset telescope that was specifically designed and commissioned to measure the pressure profile of samples mounted on the equator of the hohlraums. A schematic of our hohlraum package is shown in Fig. 116.80. The reservoir was a 75-μm-thick CH ablator glued to a 200-μm-thick 12% BrCH. An example of the resulting velocity interferometer for any reflector (VISAR) image from this hohlraum is shown in Fig. 116.81. Our measurements showed that the planarity in the measured data yielded resolution better than 150 ps across the entire 1-mm field of view. The peak radiation temperature (T_r) of 130 eV, measured by Dante, agreed well with the simulations. We also observed, however, unexpected second and third pressure rises and a late-time stagnation shock, as shown by the dashed–dotted curves in Fig. 116.82. Since our RT strength experiment requires taking radiographs at late times (>50 ns), these additional pressure waves and shock will cause undesirable increases in the growth factors. Our current understanding of these additional pressure rises is that they are caused by late-time hohlraum radiation, after the laser turns off. The experiments suggest that this late-time radiation (T_r) in the "tail" of the drive is ~15 eV higher than predicted by *LASNEX*.[20] This causes additional late-time ablation pressure, which recompresses the package and launches additional pressure waves. The strong, late-time shock indicated by the "up" arrows is thought to occur because the ablated plasma from the ablator is flowing into a confined volume (the hohlraum), which fills up with plasma and exerts a back pressure, as opposed to flowing into an infinite vacuum, as modeled by *LASNEX* (solid curve in Fig. 116.82). This is called the stagnation shock. We artificially modified the simulated T_r profile so that it preserved the peak T_r, but increased the late-time T_r profile; the drive profile was roughly reproduced from this experiment.

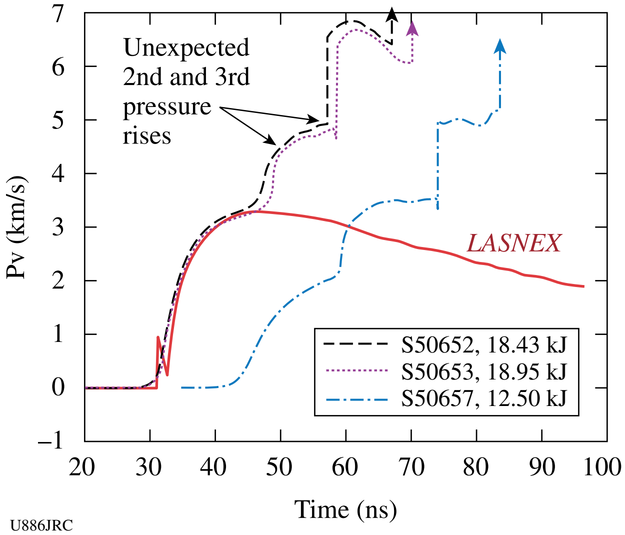

Figure 116.82
Drive profile from the hohlraum-driven ramped drive. The second and third rises are likely caused by late-time T_r that causes additional ablation pressure. We are now investigating the thin-walled hohlraums (<1-μm Au layer) to delay these late-time pushes.

We also tested a reservoir comprised of layers of high-density (1.98 g/cm^3 12% BrCH) to low-density (1.41 g/cm^3 4.3% BrCH) brominated plastic to test if hydrodynamic instabilities at the interfaces in the reservoir caused an unacceptable spatially nonuniform drive. The VISAR results showed that there is no spatial nonuniformity from these layers. We also tested quartz as a possible reservoir material. To reach very high pressure (>10 Mb), a high-density, high-sound-speed material will be needed as a part of the reservoir. These experiments will need to be performed on the NIF, where a high enough temperature can be achieved to generate the required plasma drive on release.

We studied a 500-mg/cm^3 foam layer that will be a part of the reservoir for the 5-Mb Ta strength experiment on the NIF. The low-density foam layers will make it possible for smoother loading of the initial ramp profile, thus mitigating the initial shock that may cause the sample to melt. It was demonstrated that the 500-mg/cm^3 CRF foam properly released into vacuum and did not display any spatial nonuniformity. The shock-breakout times from the foam, the release temperature, and arrival time across the gap matched the *LASNEX* predictions well.

In FY09, drive development will be continued using thin-walled hohlraums designed to lower the late-time T_r (Ref. 21). There are plans to perform Ta RT experiments using OMEGA EP's >20-keV backlighter capability.

Non-LTE Implosions: The goal of the nonlocal thermodynamic equilibrium (NLTE) campaign is to build a platform to study energy balance in implosions by measuring ion, electron, and radiation temperatures as a function of high-*Z* dopant concentration. In FY08 experiments, 60 beams of OMEGA were used for direct-drive implosions of thin (4-μm) glass capsules filled with 10 atm D^{3}He gas and 0.005 atm Kr gas as a spectroscopic tracer. The relative concentration of DD and ^{3}He was varied during the shots, and some capsules also contained as much as ~0.1 atm Xe. As a time-resolved electron-temperature (T_e) diagnostic, we fielded a mica conical crystal spectrometer coupled to a streak camera and viewed K-shell emission lines from the Kr dopant (see Fig. 116.83). Time-integrated spectra were also recorded with the HENEX spectrometer developed by NIST/NRL. We also fielded the direct-drive multispectral imager (DDMMI) to obtain 2-D images in the light of Li-like Kr lines. An increase in the DD/DT yield ratio with increasing DD concentration was observed, as well as an increase in the ion temperature, inferred from proton and neutron emission-time histories and spectra. The continuum emission spectra recorded from HENEX have been used to infer the time-integrated electron temperatures, which show a temperature decrease with an increase of dopant concentration. We used the time-resolved spectra from the conical crystal spectrometer to study the temporal evolution of the Kr He-β lines. The He-β2/He-β1 line ratio shows a peak in the central 50 ps of the Kr emission. Data analysis and comparison to simulations

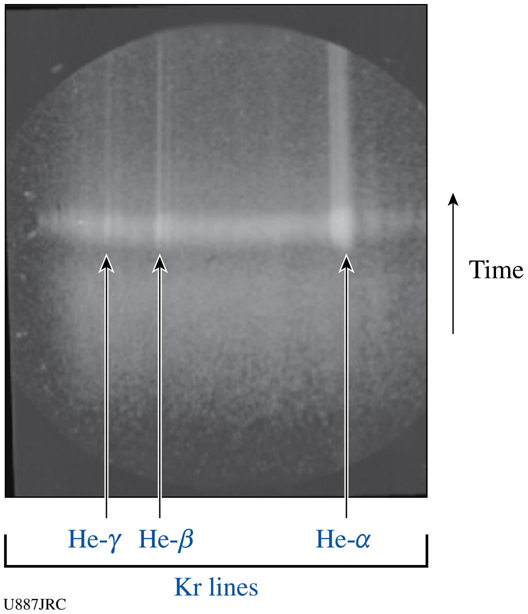

Figure 116.83
Typical time-resolved spectrum from the mica conical crystal spectrometer, for a capsule without Xe dopant.

is ongoing. For the next campaigns, we are building a Johann spectrometer, which will use the Doppler broadening of x-ray lines for measuring ion temperature (T_i), and a new multimonochromatic imager (MMI) designed for narrowband imaging in the 8- to 15-keV spectral region.

Long-Duration Backlighters: The long-duration backlighter campaign successfully demonstrated a pinhole-apertured point-projection backlighter lasting for 8 ns at both the Ni He-α-line energy (7.9 keV) and the Zn He-α-line energy (8.9 keV) (Ref. 22). Experiments on OMEGA used 20 beams with 1-ns square pulse shapes from P_7, with individual beams delayed such that the laser intensity on target was 2.6 to 2.9 × 10^{15} W/cm^2 for 7 ns, and 1.6 × 10^{15} W/cm^2 for an additional 1 ns. Beams irradiated either a zinc or nickel microdot, mounted on a 400-μm-thick high-density carbon substrate, centered over a 20-μm-diam pinhole or a 20-μm × 200-μm slot aperture in a 75-μm-thick tantalum substrate, with the target normal along the P_6–P_7 axis. The resulting x rays imaged a gold grid or wire array at 20× magnification on either a framing camera or streak camera in TIM-4. Diagnostics also monitored the emission spot, x-ray conversion efficiency, backscatter, and hard x-ray production.

Resolution studies on both gated and streaked diagnostics confirmed little-to-no pinhole closure over 8 ns for the nominal target and beam setup, which fired outer-cone beams first. Rearranging beams such that inner-cone beams fired first gave better conversion to x rays, which may have caused the pinhole to close faster, but gave a dimmer overall signal late in time, resulting in dim images that could not be analyzed for source resolution. Early-time results on those shots showed very little pinhole closure. Figure 116.84 shows a streaked image of a wire array, illuminated with a nickel microdot emitter with a slot-apertured backlighter over 8 ns, and a lineout in time of the signal. Notice the signal varies some as beams turn on and off over the 8 ns. The laser intensity on target is relatively constant over the image, but beams closer to normal to the target's surface convert better to x rays. This can be seen by comparing the signal level early in time in the image, when 58° beams were on, to late times in the image, when the 21° beams fired.

Additionally, gated tests were done to purposefully cause quick pinhole closure, to match *LASNEX* models of closure time. The standoff distance between the microdot emitter and the pinhole was reduced to 250 μm, which was irradiated with a 3 × 10^{15}-W/cm^2 laser source for 5 ns by 21° and 42° beams. Resolution of grid wires and change in signal level through the pinhole show that the pinhole was closed to a 7±2-μm-diam source in 2.25 ns.

X-Ray-Source Applications: Bright, tunable x-ray sources are necessary for radiography applications, radiation-effects experiments, and as backlighters for high-energy-density experiments. LLNL's x-ray-source development campaign had one full day of shots during which three varieties of a multi-keV x-ray source were shot.[23] The x rays from the laser targets were characterized as a function of different

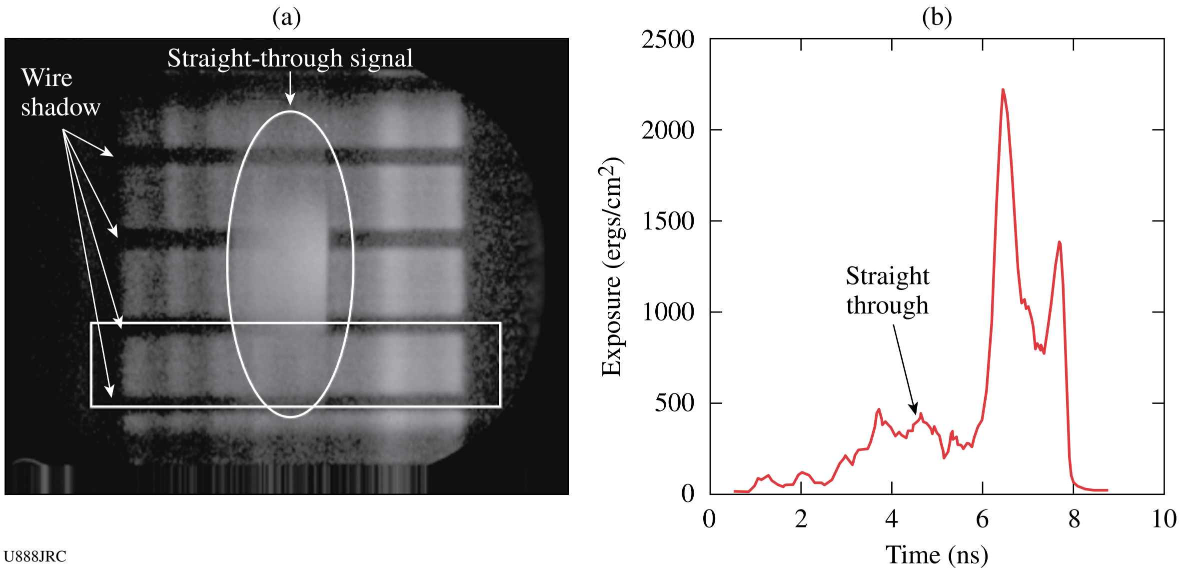

Figure 116.84
A streaked image of a wire array, illuminated with a slot-apertured backlighter over 8 ns with a nickel microdot emitter, and a lineout in time of the signal.

target geometries and volumes. Previous campaigns studied target yield as a function of laser intensity and target-plasma density. The x-ray sources were created by driving (using 20 kJ of laser energy) either ultralow-density (3- to 4-mg/cm^3) Ge-doped (20% atm) SiO_2 aerogels or Ge-foil-lined epoxy (CHNO) cavities. The laser-to-x-ray conversion efficiency in the 10- to 13-keV x-ray band was measured to be between 0.6% and 1.0% and in the 1.0- to 3.5-keV band between 35% and 40%. These shots compared output from aerogel targets that differed by 40% in volume and saw no difference in the measured x-ray yields. X-ray spectra and time-resolved images of the three types of targets are shown in Fig. 116.85. Analysis indicated that the laser-heated volume was the same in both targets, which resulted in the same number of emitting ions in the plasma. Similarly, and surprisingly, the foil-lined cavities produced measured yields, in all spectral bands, that did not differ from those of the aerogel targets. The measured yield for the foil-lined cavity target was consistent with trends observed with previous cavity targets, shot in 2007 by Commissariat à l'Énergie Atomique (CEA) researchers, that produced higher yields and had a better-optimized laser configuration. These experiments were conducted jointly with U.K.'s Atomic Weapons Establishment (AWE) Laboratory, Sandia National Laboratories, France's CEA, and the Department of Defense's (DoD) Missile Defense Agency and Defense Threat Reduction Agency. The x rays from these targets were applied to various test objects and the response was measured.

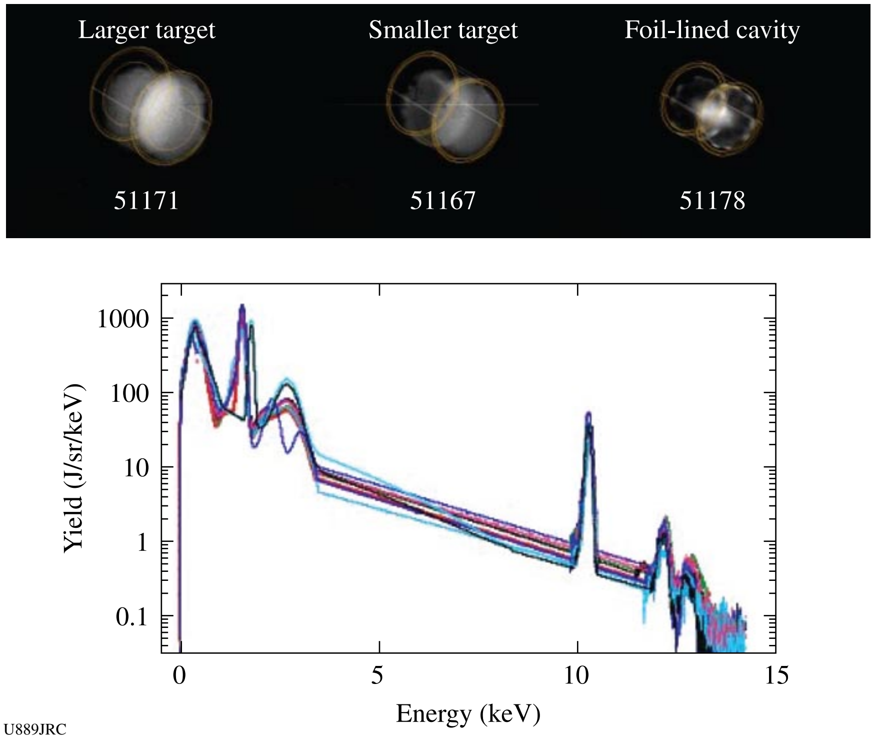

Figure 116.85
(a) Time-integrated x-ray pinhole-camera images, filtered for x rays above 3 keV, of the large and small aerogel targets shot on the x-ray source development day (8 May). (b) X-ray spectra reconstructed from data measured with the HENWAY spectrometer and the Dante diode array. Across the whole range shown, 35% to 45% of laser energy is converted into x rays.

Dynamic Hohlraums: Earlier experiments showed that laser-driven dynamic hohlraums (LDDH's) emit very bright, spectrally smooth bursts of x rays up to 3.5 keV, suitable as broadband backlighters for absorption spectroscopy experiments (Fig. 116.86). These experiments also demonstrated that LDDH's are robust

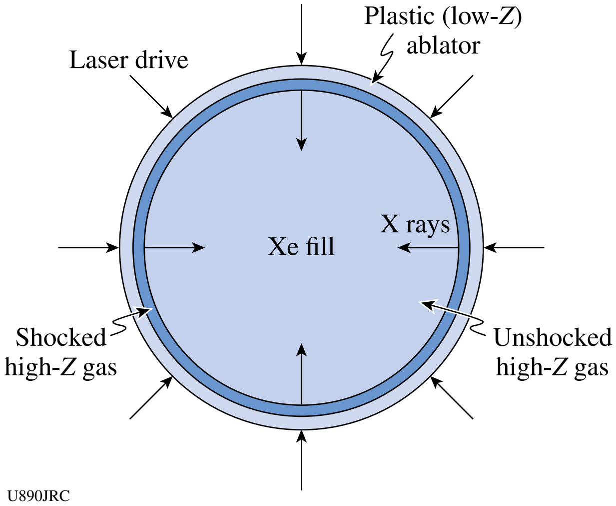

Figure 116.86
Concept of "dynamic hohlraum": shock-heated Xe gas forms a spherically converging shell that traps radiation inside. When the shell stagnates, radiation is released in a bright x-ray flash suitable as a backlighting source for opacity experiments. Data obtained of the converging dynamic hohlraum included x-ray streaked images of the self-emitted x rays, multiple x-ray images, and spectral data.

to the polar (nonspherically symmetric) laser configuration that will be used on the NIF as a continuum source backlighter. During FY08, these two aspects of LDDH's were combined in an experiment where a Xe-filled LDDH without an inner shell was driven by laser beams in a polar configuration and was used as a backlighter for absorption spectroscopy of heated Fe samples.[24] It was found that the LDDH emits a strong, 200-ps-long x-ray flash that is spectrally smooth from 4.5 keV to ~9 keV, enabling a significant expansion of the spectral range for future OMEGA and NIF opacity experiments. This year's LDDH experiments also completed a series of shots where capsules were filled with neopentane rather than xenon. These shots were experimentally difficult as the gaseous neopentane was near its boiling point just prior to the experiment and condensation had to be avoided. The successful completion of the experiment made it possible to measure the difference in yield and fuel density caused by the hohlraum effect (which is present in "standard" xenon-filled LDDH's but not in neopentane).

High-Speed Jets: The evolution of high-speed jets is an important benchmark for hydrodynamic simulations, e.g., the shape of the front of a jet penetrating into a surrounding medium can be either flat-topped or arrow-shaped, and this must be correctly predicted by simulations. An OMEGA experiment yielded a dramatic increase in the current data set of high-speed-jet images; the evolution of the jet was followed temporally ~2 to 2.5× longer than in previous experiments on OMEGA and in the NIF Early Light campaigns (see Fig. 116.87). A preliminary result from the experiment is the need to model foam material as two fluids in numerical simulations. A new two-fluid model for foams is currently under development at LLNL. In the new model, foam is treated both with LEOS (used for undisturbed foam) tables and with an ideal gas (used for foam that has been "reflected" by the shock, i.e., cast out ahead of the shock by shock–foam interaction forces).

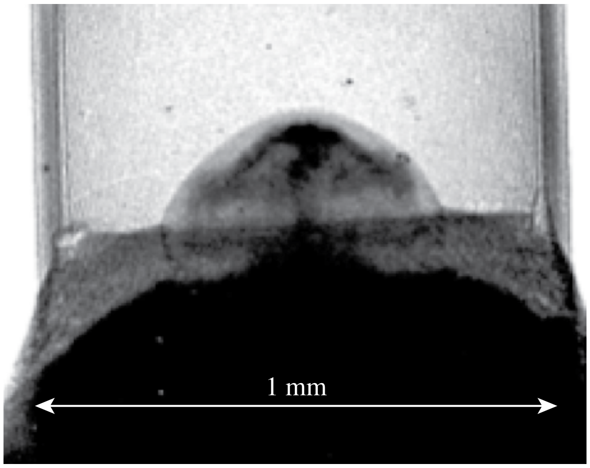

Figure 116.87
X-ray radiograph of an aluminum jet driven into a 0.1-g/cm^3 carbon foam. The image is taken 35 ns after the start of the experiment, and the jet has evolved ~2× longer than in previous experiments of this type. The jet structure is clearly visible, as is the location and shape of the bow shock.

Enhanced Efficiency Hohlraums: The hohlraum development campaign investigated the behavior of gold-foam–walled halfraums (ρ = 400 mg/cm^3), comparing the flux levels and temperature to solid-gold halfraums.[25] The layout of the foam-walled halfraum is shown in Fig. 116.88. By optimizing the wall

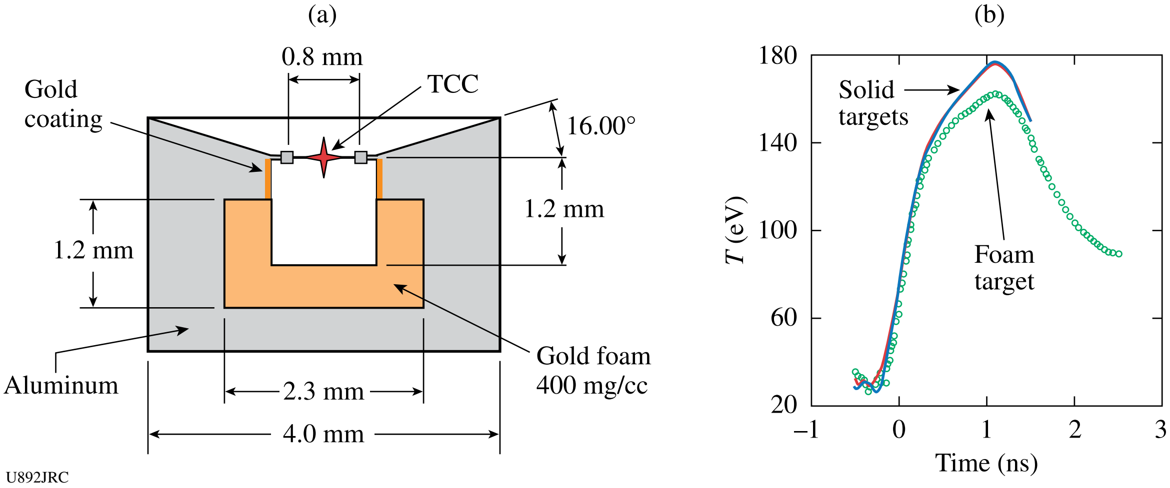

Figure 116.88
(a) Gold-foam–walled halfraum-target schematic. Beams hit a gold-coated plate near the LEH, while the rest of the cavity is lined with 400-mg/cm^3 foam. (b) Temperature as a function of time for two solid-gold targets and one foam target. Although lower-density gold was predicted to optimize target flux and temperature, the foam target had a lower temperature than the solid targets.

density for these hohlraums at temperatures near 200 eV, we expected to see an increase in flux by ~15%. These shots positioned the targets on the Dante axis and used 15 beams from the H16 direction, with the RR1001 reverse-ramp pulse shape and IDI-300 phase plates. Beams hit a 1200-μm-diam gold-coated solid surface near the 800-μm LEH on the foam targets, which hid the laser spots from the Dante view. The inner foam or solid surface was 1200 μm in diameter and 1200 μm in length. Dante measured flux while a soft x-ray camera in TIM-6 monitored the LEH. Over three shots, two solid targets were compared to one foam target. These shots showed a lower flux in the foam target than in the solid targets, contrary to our predictions [see Fig. 116.88(b)]. We are investigating whether the reverse-ramp pulse shape was the appropriate choice. Remaining targets will be used for future tests.

Opacity: In FY08, LLNL completed the development of a high-temperature laser-opacity platform. Thin-foil samples of co-mixed sodium chloride and titanium, tamped by plastic on all sides, were placed inside hohlraums, and heated to temperatures well above 100 eV in local thermodynamic equilibrium, or LTE, conditions. The samples were then backlit by two different broadband radiation sources. Separate shots used samples of co-mixed tantalum and titanium. The data in Fig. 116.89 show an edge-on view of the sample, backlit by a ten-beam Kr-filled dynamic hohlraum capsule backlighter, which was apertured down to 30 μm in one direction to improve the spatial resolution. The data are spectrally resolved in the horizontal direction using an MSPEC elliptical crystal spectrometer and a gated microchannel-plate detector. This was the first-ever laboratory measurement of a hot sample in the photon energy range above 4 keV. The expansion of the sample was consistent with pre-shot *LASNEX* simulations and established the sample density. The spectrum was well fit by the *VISTA* opacity code, using the known optical path length and measured density, at a temperature of 110±5 eV. Separate, nearly synchronous measurements were obtained in a 250- to 1600-eV spectral band using a variable-spaced grating spectrometer and a second backlighter. The latter data, including both absorption and self-emission spectra from the hot sample, provide detailed information on the sample's opacity in the spectral band contributing to the Rosseland mean opacity, which, in turn, controls the overall radiation flow through such a plasma. By simultaneously characterizing the sample's density, temperature, ionization balance, and Rosseland-band opacity, this new experimental platform makes possible detailed, photon-energy-specific investigations of the process of radiation transport in the hot plasmas found deep inside the sun and other stars.

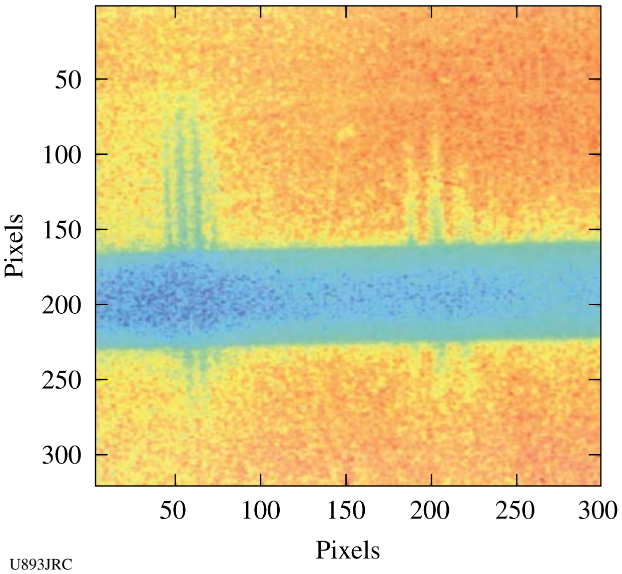

Figure 116.89
Gated space-resolved titanium absorption spectrum for photon energies around 5 keV. The horizontal bar is a gap between two strips on the detector. To the left are n = 1 to 2 absorption lines of F-like to C-like Ti. To the right are n = 1 to 3 lines of the same ions. The spatial expansion of the sample is determined by the vertical extent of the lines.

FY08 LANL OMEGA Experimental Programs

During FY08 Los Alamos National Laboratory (LANL) successfully fielded a range of experiments on OMEGA to study the physics relevant to inertial confinement fusion (ICF) and high-energy-density laboratory plasmas (HEDLP) in support of the national program. LANL conducted a total of 85 target shots on OMEGA. Collaborations with LLNL, LLE, MIT, and AWE remain an important component of LANL's program on OMEGA.

AGEX-EOS: The AGEX-EOS-09 campaign studies the role that radiative preheating plays in the Richtmyer–Meshkov mixing of a large-Atwood-number interface. The experiment uses a variant of the off-Hugoniot platform to produce a heated interface that is subsequently shocked. The resulting interface evolution is imaged radiographically.

The new platform, first tested in September 2008, employs an independently controlled shock and heating drive as well as a point-aperture pinhole backlighter configuration. The primary objectives for the September campaign were to exercise this new platform under every permutation of drive, identify sources of noise, and demonstrate the imaging viability of the experiment.

Figure 116.90 shows the target geometry and preliminary data obtained from shot 52215. The data clearly show the position of the heated and shocked Teflon interface as well as the positions of the main and preheat-side shocks at 25 ns. Drawing from the success of September's experiment, a number of imaging improvements have been initiated, giving us high confidence for the physics experiments planned in February 2009.

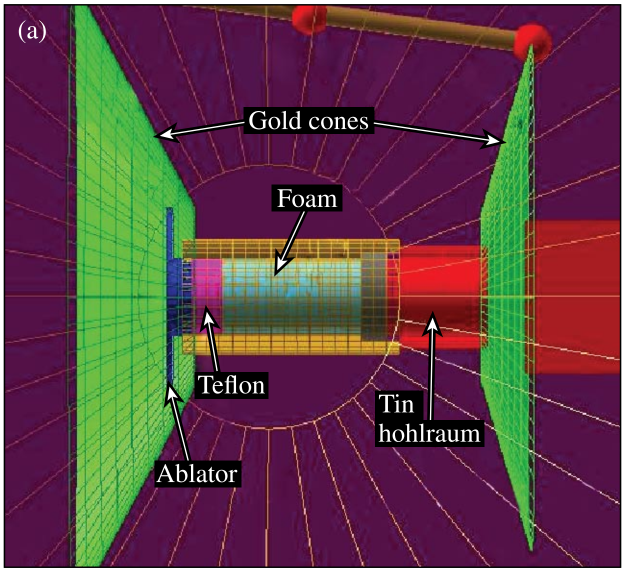

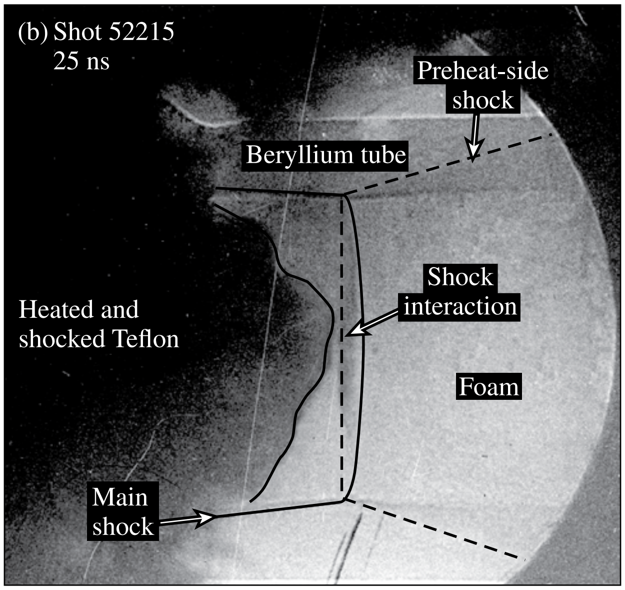

Figure 116.90
Overview of the (a) AGEX-EOS-09 target and the preliminary data from (b) shot 52215.

DTRat: In August 2008, LANL continued the *DT Ratio-^{3}He Addition* campaign, imploding glass capsules filled with DT/^{3}He using a 600-ps square laser pulse. Previous studies have looked at the effect of adding ^{3}He to the D_2-filled capsules (as a DT surrogate); this study is the first to look at the effect on DT. The use of DT also makes it possible to acquire high-quality reaction histories derived from the Gas Cherenkov Detector (GCD-1). From these reaction histories, it has been determined that the addition of ^{3}He degrades the compression component of yield more than expected. This is consistent with the conclusions of the study conducted by MIT using $D_2/^3$He-filled plastic capsules[26] and LANL's Hi-*Z* campaign utilizing glass capsules, also filled with $D_2/^3$He (Ref. 27). Contrary to the MIT study, however, the shock component does not appear to be significantly affected.

Figure 116.91 shows the reaction histories for three concentrations of ^{3}He addition. Overall, the measured neutron yield is ~37% of a clean calculation for *each* ^{3}He concentration. However, when the histories are decomposed into Gaussian components representative of shock and compression yields, the measured compression component goes from being a factor of 3 lower than calculated at 0% ^{3}He, to being a factor of 5 lower at 36% ^{3}He. This agrees well with the MIT study as seen in Fig. 116.92 (the factor of 3 at 0% ^{3}He is normalized out for the DTRat data set, whereas a factor of ~2.2 is normalized out for the "Rygg" data set). In contrast, the decomposed shock com-

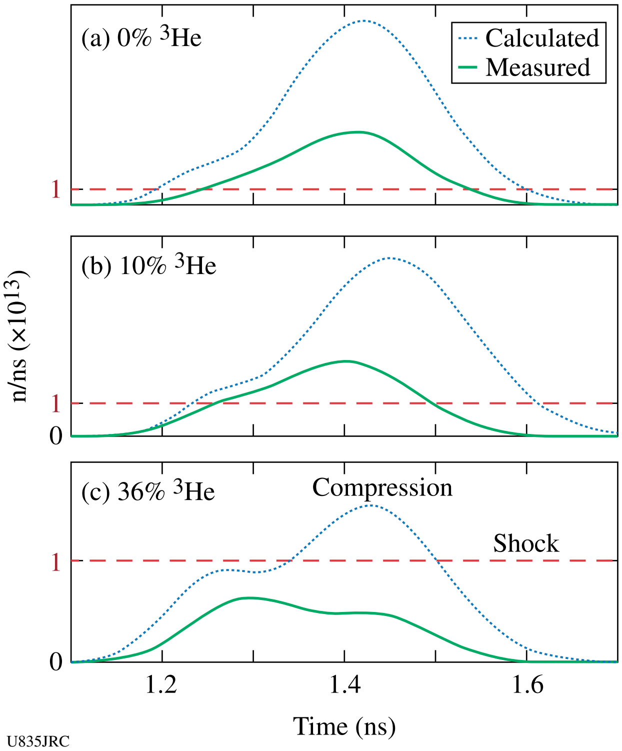

Figure 116.91
Calculated (convolved with residual instrument response) and measured (deconvolved GCD data) reaction histories for various ^{3}He concentrations.

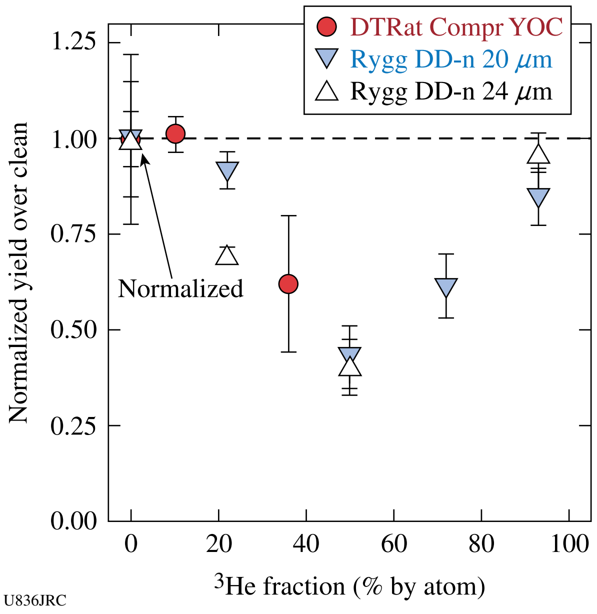

Figure 116.92
Scaled compression component of neutron yield normalized to 1 at 0% ^{3}He.

ponent from DTRat agrees quite well with the clean calculation for all three ^{3}He concentrations as shown in Fig. 116.93.

Shock-yield data for the 24-μm-wall-thickness capsules from MIT's "Rygg" study exhibit a parabolic dependence on ^{3}He fraction, with the minimum occurring near 50% ^{3}He, similar to what was observed for the compression component. The data set for 20-μm-thick walls, however, does not appear to support this trend. We suspect the degraded yield anomaly arises only after the shock has reflected from the center and has hit the incoming shell. After such time, the shock yield is diminishing while the compression yield is rising. X-ray imaging and ρR data from DTRat, Hi-Z, and the MIT study support the hypothesis that capsules with ~50% ^{3}He are not as compressed at the time of peak neutron production rate during the compression phase as those without ^{3}He (or those with nearly pure ^{3}He from the MIT study). It is not understood at this time what is degrading the compression.

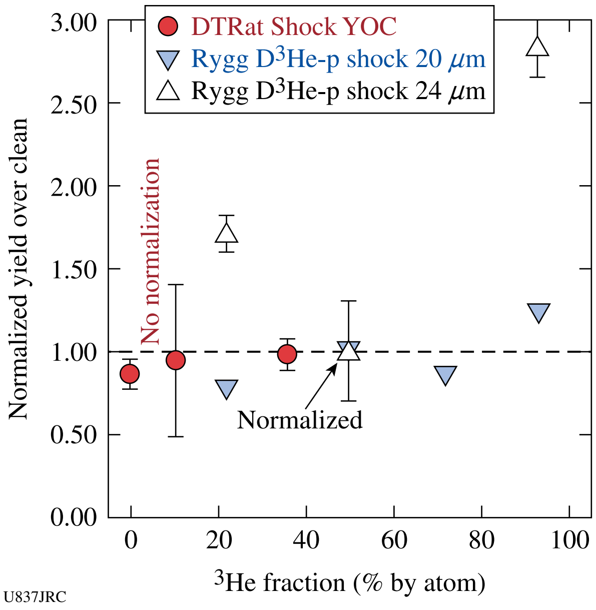

Figure 116.93
Scaled shock component of neutron yield normalized to 1 at 50% ^{3}He for "Rygg" data; no normalization for DTRat data.

High-Z: The High-*Z* project successfully completed its planned experiments for FY08 at the OMEGA Laser Facility. These experiments investigated what effect the addition of He to ICF implosions has on fusion yield. The experiment used the standard glass-shell targets we have used in the past and varied the concentration of ^{3}He in the target and measured the resulting yield. These were done for three different concentrations of ^{3}He: 0%, 10%, and 50% by atomic fraction. The gas fills were also designed to be hydrodynamically equivalent to try to ensure similar hydrodynamic behavior. In addition, we also planned to measure the change in yield for two different laser pulse lengths. We first used our standard pulse length of 1.0 ns and then conducted a second series of experiments using a shorter pulse length of 0.6 ns. The shorter pulse length should emphasize the differences in the compression component of the yield where we believe the ^{3}He is causing a significant impact.

On 23 April 2008, we successfully fired eight shots on OMEGA with 1-ns laser pulses and varied the concentration of He in the capsules. The neutron-yield results from these experiments are shown in Fig. 116.94, along with the expected degradation caused by less deuterium in the target. One can see in the figure that the observed yield does fall below the expected yield as the He is increased. We also see little difference in the ion temperature for these shots, which varies from 6.9 keV to 7.4 keV and increases only slightly as the He concentration is increased.

We also did two additional shots on 23 April with 4.0-μm-thick glass shells. These targets contained 50% atom fraction of He, but one was ^{4}He instead of the usual ^{3}He. The yields for these two shots were 4.8 × 10 and 4.3 × 10, respectively—a difference of 10%, which is similar to our standard shot-to-shot variation. The ion temperature for these shots was higher, ~8.2 keV, consistent with thinner glass and a more rapid implosion.

Four additional shots were conducted on a separate half-day, 17 June; the results from those shots are shown in Fig. 116.95. The behavior is similar to what was observed for the 1-ns drive shots with one exception: the ion temperatures for these experiments varied greatly, from 5.3 keV for no He to 7.8 keV for 50% He and bring into question whether the implosions are hydrodynamically equivalent. This would be consistent with an even greater degradation of the compression burn, reducing its importance compared to the shock burn and effectively elevating the average burn temperature.

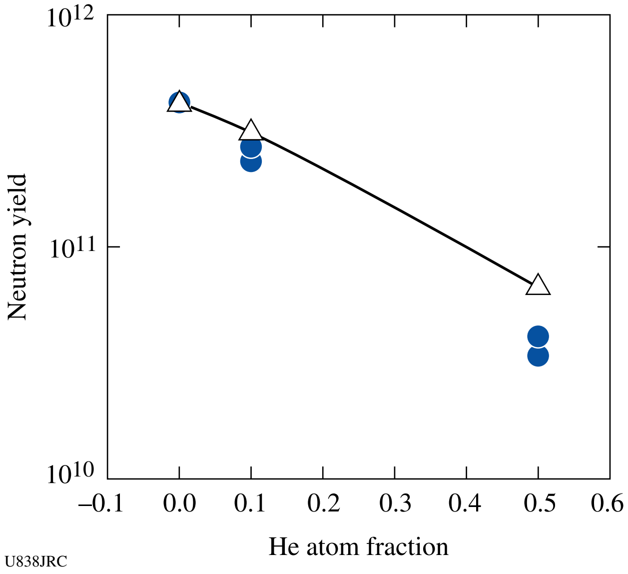

Figure 116.94
Neutron yield as a function of He atom fraction in the gas. The dots are data for a 1-ns pulse drive with 4.3-μm-thick walls and the curve represents the expected yield based on the deuterium concentration only.

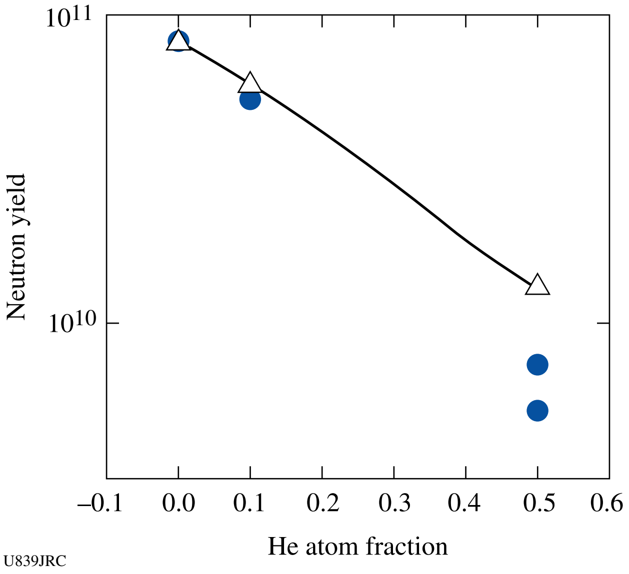

Figure 116.95
Neutron yield as a function of helium atom fraction in the gas. These experiments used 0.6-ns laser drive and the data are shown as dots. The curve represents the expected yield based on the deuterium concentration.

Overall, the results for doping the gas with ^{3}He were consistent with earlier results for Ar, Kr, and Xe, although a much larger atom fraction of ^{3}He was required to produce a similar effect.

NIF Platform #5: The NIF Platform #5 campaign continued experiments to develop diagnostic techniques for future NIF experiments. The FY08 experiments focused on backlighter source characterization and development as well as the successful execution of a new platform for the observation of absorption features due to heated materials.

One aspect of the backlighters that was examined was the conversion efficiency for L-shell and M-shell emitters. Over the course of the FY08 campaign, the studied laser irradiance varied from 10^{14} W/cm^2 up to nearly 10^{17} W/cm^2. The data obtained will assist in evaluating the expected photon fluxes at the NIF. An example of some of the data obtained from a CsI backlighter is shown in Fig. 116.96.

The platform for studying absorption spectroscopy is shown in Fig. 116.97. A Ti foil was heated inside a hohlraum. A CsI backlighter provided a quasi-continuum spectrum source, which passed through the sample and was recorded on by a spectrometer (Fig. 116.98). The recorded spectrum contains both the emission from the CsI backlighter and the absorption from the heated Ti foil. Although detailed analysis is still underway, these experiments provided valuable information on the absorption spectroscopy technique and have led to a number of improvements being implemented for future NIF experiments.

Symergy: We have used two cones of the OMEGA laser to irradiate a linear 0.7-scale NIF hohlraum to implode Be and CH capsules to measure the effect of beam phasing on the implosion symmetry. The vacuum hohlraums, with 2-mm-diam capsules, reached 105 eV using 1-ns laser pulses. The symmetry of the x-ray emission from the implosion was measured for both the CH and Be capsules. We were able to vary the symmetry at implosion time by varying the cone fraction or ratio of energy between the inner cones (21° or 42°) and the outer cone (59° beams) (Fig. 116.99). We found that the fraction where the best symmetry occurred was closest to those ratios that the re-emit

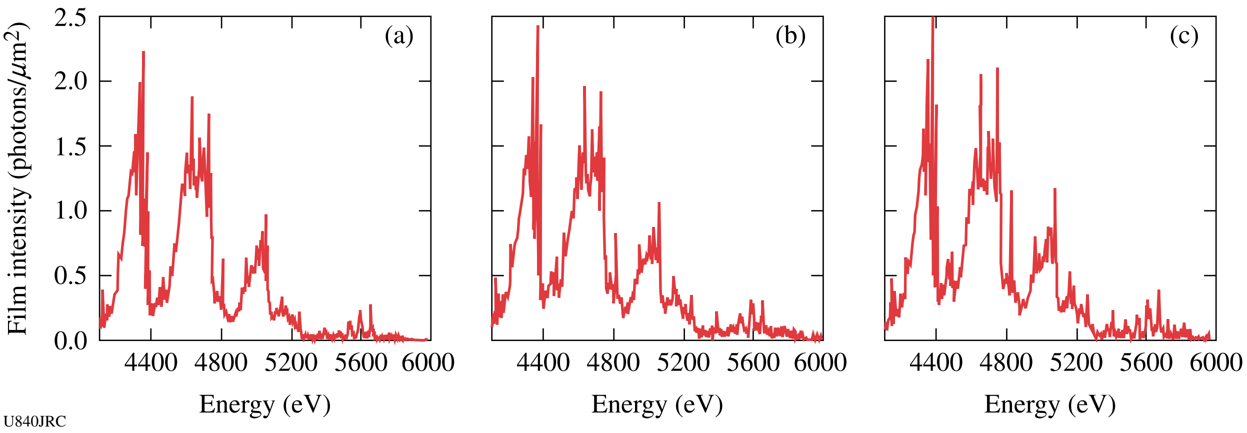

Figure 116.96
CsI spectra for (a) a nominal 600-, (b) nominal 400-, and (c) nominal 200-μm-diam spot. Note that although the laser irradiance spans an order of magnitude, the amount of emission stays essentially constant.

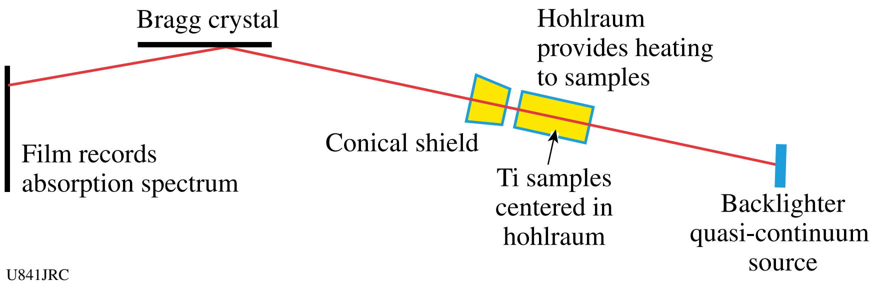

Figure 116.97
Schematic depicting the absorption spectroscopy configuration. Laser beams enter both sides of the hohlraum. A thin Ti foil sitting in the center of the hohlraum is then heated. The backlighter provides a quasi-continuum backlighter source, and its x rays pass through the Ti sample and are reflected off the Bragg crystal and recorded on film. Some of the backlighter emission is absorbed, depending on the temperature and density of the Ti. This schematic is not to scale.

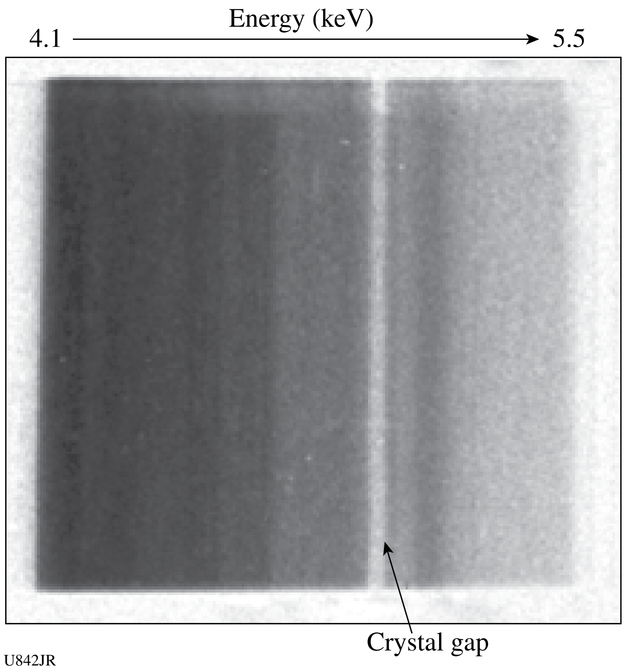

Figure 116.98
Spectrum containing the emission from a CsI backlighter and the absorption due to a thin, heated Ti foil.

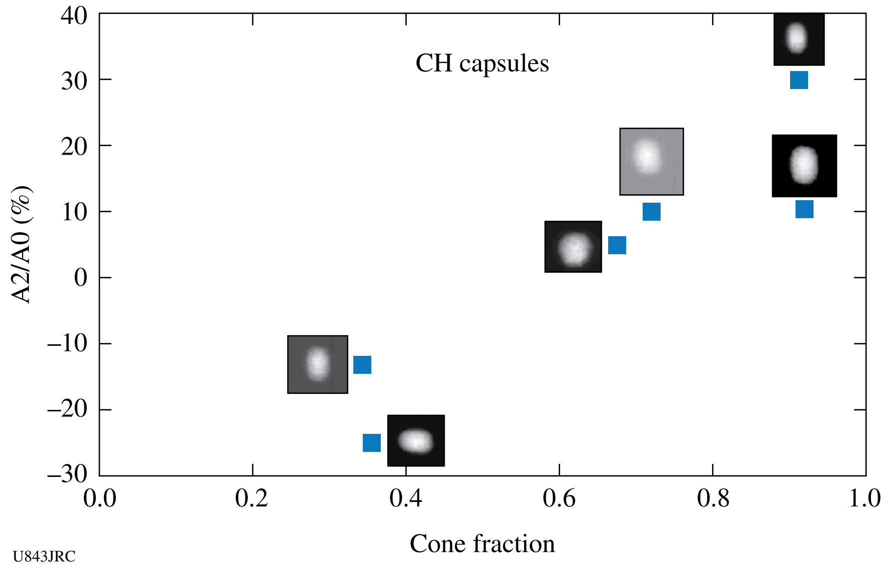

Figure 116.99
The measured second-order Legendre coefficient for the x-ray emission at the 30% level, measured at peak emission.

technique had found for the same pointing. When we replaced the 42° beams with the 21° beams and pointed to the same location in the hohlraum with the same laser irradiance, the hohlraum radiation was lower and the symmetry was affected, indicating some impaired propagation of the inner cone.

FY08 CEA OMEGA Experimental Programs

CEA conducted 39 target shots on the OMEGA Laser Facility in FY08. The CEA efforts included the following:

CEA Acquisition System and Software Developments for the OMEGA Facility: Since 1999 the development of specific CEA diagnostics for joint experiments with LLE, LANL, and LLNL on the OMEGA facility (for instance, DMX,[28] NIS,[29] or HRXI[30]) have used the same devices (single-shot oscilloscopes, CCD, HV supply, switches, fast triggering generators, electrical attenuators, etc.) to supply and record detectors placed inside the target chamber area. All these recording and control devices are quite sensitive to the radiative environment generated during the OMEGA high-yield neutron shots ($Y_n > 10^{13}$ n/4π) induced mainly by the hard x-ray components for every shot or the neutron and gamma ray flux for high-neutron-yield shots.[31] To protect these sensitive instruments, we decided to place them in a "quieter" radiative environment named "La Cave," located in the basement of the target chamber area and protected by 70 cm of concrete. Figure 116.100 shows FPE (Force de Projection d'Enregistrement)—the recording system installed in La Cave that presently includes

- fourteen high-bandwidth single-shot oscilloscopes (IN 7100 – 7 GHz)
- two digital oscilloscopes (TEKTRONIX TDS694 – 3 GHz)
- some HV supplies (used for biasing our detectors) and a related voltmeter
- a control system for our DMX high-bandwidth remotely controlled electrical attenuators

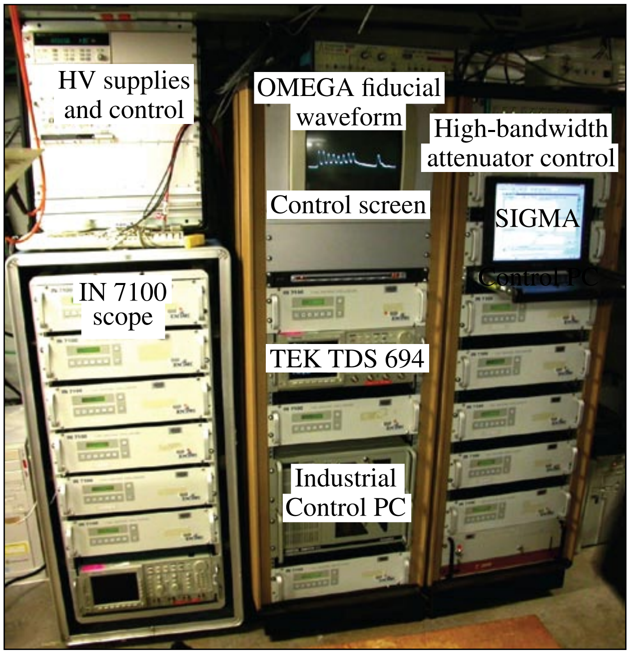

Figure 116.100
The CEA "FPE" acquisition system in the OMEGA "La Cave."

- a fast triggering system (not shown at the rear side of these cabinets)

- an automated control/command system

The CEA FPE control/command system, described in detail in the next paragraph, is based on PC hardware and is specially designed to automatically control our devices during the shot sequence when access to La Cave is closed for safety reasons. During that time (from 10 min prior to the shot to a few minutes after, depending on the radiative decay), each specific "order" generated during the OMEGA countdown process (during the capacitor bank charge), from a few minutes before until a few seconds after the shot, is recognized and used to automatically trigger some specific action on each device remotely controlled by the software (HV on, oscilloscope or CCD armed, data transfer and storage process, HV off, etc.). These actions can also be manually triggered by an operator if needed during the setup and preparation of the diagnostic. This system can be also be seen (for controlling its correct automated operation during the shot sequence) by the OMEGA experimental team operators when the relevant diagnostic is included as a "facility diagnostic" (as done, for example, for DMX).

<u>"FPE-SIGMA" Command/Control System.</u> Most of the deployment and tuning of the measurement chains of each CEA diagnostic is done by a "mobile" team (present at the OMEGA facility only during main CEA experiments) that uses a specific tool to manage the acquisition devices and their controlling network of computers.

Developed and improved over a decade, the "SIGMA" software tool solves computing issues going from manual to fully automated experiments. A distributed architecture—which also downsizes to fit into a single computer—is controlled at one place by human interface. The tool supports the diagnostic design and improvement process by making it possible to describe the system in a smart graphical interface (the Microsoft Visio diagram editor is shown in Fig. 116.101). The targets, filters, and mirrors (the main components of DMX) appear at the left side of a schematic view in which the signal paths and delays also appear and can be documented. Thus the settings definition of each remote-controllable device is postponed after the definition of its use case. In fact, in an automated diagnostic, settings are sets of logical data that are selectively recalled into a static physical layer. The versatility of a physical layer increases with the remote controllability of its key components.

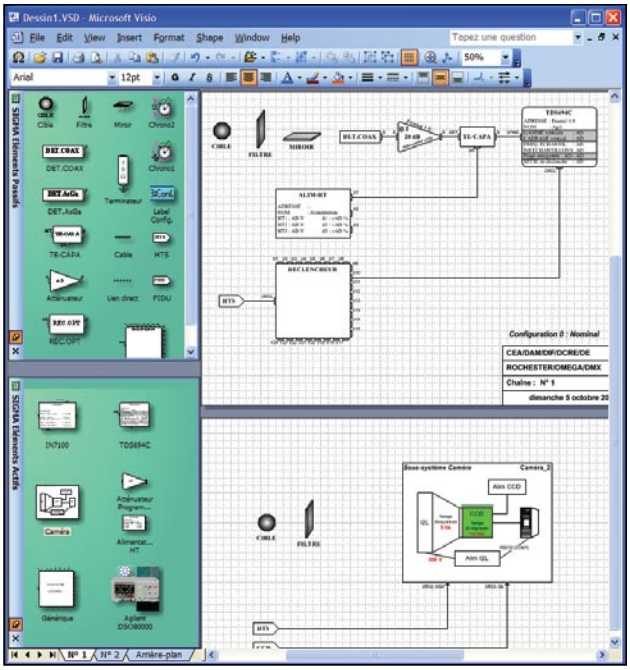

U853JRC

Figure 116.101
The diagnostic editor built over Microsoft Visio.

The underlying and hidden computing technologies include

- specific support of a few device drivers (GPIB controller, ISA/PCI imaging cards, USB devices)

- standard communication with serial ports, GPIB ports, TCP/IP connections, and ODBC databases

In addition, the complexity of some instrumental subsystems—e.g., based on more than one device connected to different ports, leading to advanced communication handshake or to advanced commands implementation—was hidden in high-level virtual device drivers that run on the device computers and expose a GPIB-like interface.

The supported classes of instruments come with a visual schematic footprint, an inline OCX front panel, a guarded OCX settings form, and a set of intrinsic commands provided by design. Intrinsic commands may generate specific event types that also come with their suite of *in-situ* viewers and commands.

Currently, the SIGMA software controls analog and digital oscilloscopes, power supplies, programmable attenuator banks, and neutronic imaging subsystems. At design time, the Visio multipage editor is fully automated to show the instrument settings according to the active configuration. At run time, the configuration variable is also maintained and its value can be automatically affected in order to influence the conduct of operations. For example, the active configuration can be retrieved from a database each time a shot number is received.

Ten configurations are currently supported, each being freely labeled. At the instrument level, four sets of settings are freely associated to the ten configurations. Settings factorization across configurations simplifies diagnostic management. At the diagnostic level, a matrix determines the physical subsets (measurement chain) that are active with each configuration.

An experiment can be controlled manually, in a semi-automatic manner (triggering scripted sequences), or fully automatic [involving the internal scheduler or listening to a hierarchical uplink (supervisor)]. Supervisors can also be notified when selected error levels occur.

During a run time, the software builds a single chronology of time-stamped and typed events. Each event type shows a specific icon and comes with a set of tools that makes possible inspection (texts, forms, curves, or pictures), event navigation, or procedure recall. Past-event inspection is possible at any time, as well as single command executions, script executions, and inspection/modification of instrument settings. The guarded variables cover every aspect of the system except the state of the user interface.

Recently, the SIGMA tool was qualified to be integrated into the OMEGA operations as the DMX diagnostic application controller. To make the startup and the stopdown of the diagnostic application easier, the tool was given a simplified alternate interface showing a strictly filtered set of notifications (Fig. 116.102). In addition, the non-specialist is guided from the first power up to the last shutdown thanks to a localized operator sheet (Fig. 116.103) and to the firing of some interactive checklists. In the meantime, the software monitors the presence of each component.

The SIGMA software developed and tested initially for OMEGA common experiments is also deployed at the LULI facility (Palaiseau, France) and the LIL facility (Cesta, France); CEA

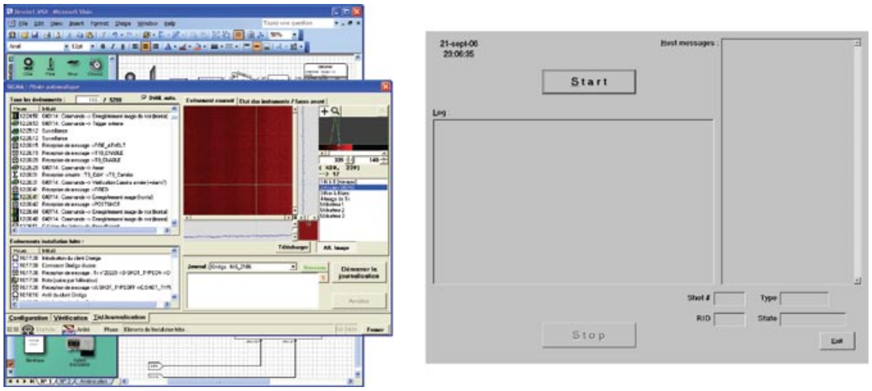

U854JRC

Figure 116.102
The complete versus the simplified run-time human interface.

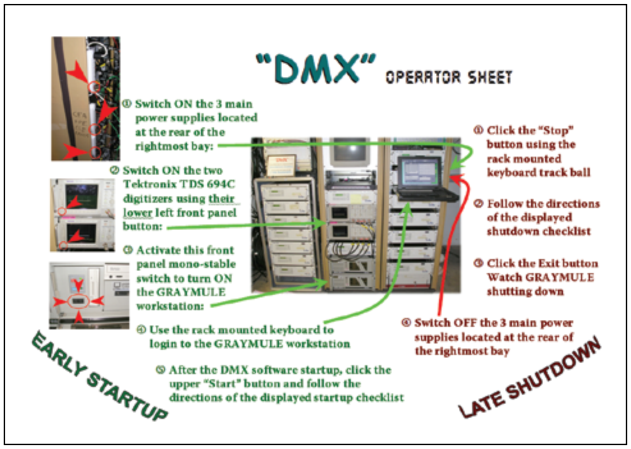

"DMX" OPERATOR SHEET

EARLY STARTUP

① Switch ON the 3 main power supplies located at the rear of the rightmost bay:

② Switch ON the two Tektronix TDS 694C digitizers using their lower left front panel button:

③ Activate this front panel mono-stable switch to turn ON the GRAYMULE workstation:

④ Use the rack mounted keyboard to login to the GRAYMULE workstation

⑤ After the DMX software startup, click the upper "Start" button and follow the directions of the displayed startup checklist

LATE SHUTDOWN

① Click the "Stop" button using the rack mounted keyboard track ball

② Follow the directions of the displayed shutdown checklist

③ Click the Exit button Watch GRAYMULE shutting down

④ Switch OFF the 3 main power supplies located at the rear of the rightmost bay

U855JRC

Figure 116.103
An operator sheet to properly start the minimum hardware and launch the checklist.

also uses it on its Gekko XII diagnostic (Osaka, Japan), justifying its given name of FPE for "Projected Force for Recording."

Monocrystalline CVD Diamond Detector: A Novel Tool for Neutron Yield and Duration Emission Measurement: Synthetic diamond detectors are now known to exhibit attractive characteristics to discriminate neutrons by the time-of-flight technique (nTOF), as well as to measure neutron bang time and ion temperature. Earlier work had, however, demonstrated how the quality of this material matters since the temporal properties of synthetic diamond devices (aiming to be in the 100-ps range) strongly differ from device to device and growth origins. For the record, sensitive CVD diamonds are usually too slow to be used for timing measurement, although such a development of sensitive and fast CVD diamonds would make it possible to perform simultaneously both neutron-yield and ion-temperature measurements, thus minimizing the number of nTOF detectors on the Laser Megajoule Facility.

More recently, and to complete the data acquired in 2007 (Ref. 32) for low-neutron-yield measurements, a new series of polycrystalline CVD diamonds (Element Six) and new monocrystalline CVD diamonds (CEA-LIST, Saclay) were implemented on the OMEGA Laser Facility during implosion experiments of DT capsules yielding 10^{13} to 10^{14} neutrons. These materials exhibited higher sensitivities. The goal was to determine how such novel materials could be relevant for neutron-yield, bang-time, and ion-temperature diagnostics.

On OMEGA, diamond detectors were inserted at distances of 30 cm, 1 m, and 2 m from the target chamber center using the TIM diagnostic insertion mechanisms. Other diamonds were placed outside the target chamber at 3.3 m from target chamber center (TCC). Distances and neutron-yield ranges provide the ability to probe the detectors' performances within two decades of the neutron flux (n/cm^2). The detectors exhibit a linear response over the dynamic range explored. To compare diamond materials, their sensitivities were normalized as a function of the sample volume: diamond sensitivity can often vary by several orders of magnitude, up to three decades previously observed. Table 116.V shows that the novel monocrystalline sample A260107B (from CEA-LIST) appears to be the most sensitive of all diamond material calibrated on OMEGA from the campaigns in 2007 and 2008.

Prior to the experiments, we had evaluated the temporal properties of these diamonds under 16-MeV electrons produced on a Linac accelerator at CEA (ELSA at Bruyères-le-Châtel). The pulse duration on ELSA is about 25 ps, making it possible to measure the main timing parameters. The monocrystalline diamond A260107B pulse shape has a 10% to 90% rise time that remains below 100 ps. Such temporal properties make this sensitive diamond a good candidate to measure the Doppler broadening of the neutron pulse along its propagation, thus enabling one to measure the ion temperature at bang time.

On OMEGA, the detector signal must propagate through 10 to 30 m of cable before it reaches the 7-GHz-bandwidth single-shot oscilloscope (IN7100). We have developed a software processing tool that makes it possible to deconvolve the pulse broadening produced by such a high cable length. It led to processed signals exhibiting rise times of 870 ps at 3.3 m from TCC with an ion temperature of 6.7 keV (Fig. 116.104). This signal rise time observed during DT implosions results from the 150-ps burn duration, convoluted with the temporal broadening induced by the DT ion's main energy at bang time.

Using the signal-processing technique already used in NTD diagnostics,[33] we can deduce the neutron pulse duration at 3.3 m from the target, which is mainly determined by the Doppler broadening produced by the ions. The resulting ion temperature and measured time duration are shown in the two last columns of Table 116.VI. The inferred ion temperatures from the CVD diamond signal are in good agreement with the standard OMEGA measurement performed at 5 m with a fast scintillator and an MCP photomultiplier and are presented for

Table 116.V: Diamond sensitivity measured under 14-MeV neutrons pulses.

CVD	Type	Thickness	Size	Gold Contact	High Voltage	Sensitivity (C/n/cm^3)
A260107B	Monocrystalline	500 μm	4 × 4 mm	3 × 3 mm	–1400 V	3.1×10^{-15}
A281103	Polycrystalline	260 μm	5 × 5 mm	4 × 4 mm	–360 V	1.8×10^{-15}
E6 300 μm	Polycrystalline	300 μm	ϕ 10 mm	ϕ 8 mm	–750 V	2.4×10^{-16}
E6 1 mm	Polycrystalline	1000 μm	ϕ 10 mm	ϕ 8 mm	–1000 V	1.3×10^{-16}
A270105	Polycrystalline	115 μm	5 × 5 mm	4 × 4 mm	–750 V	4.7×10^{-17}
A190106	Polycrystalline	450 μm	5 × 5 mm	4 × 4 mm	–500 V	4.9×10^{-18}

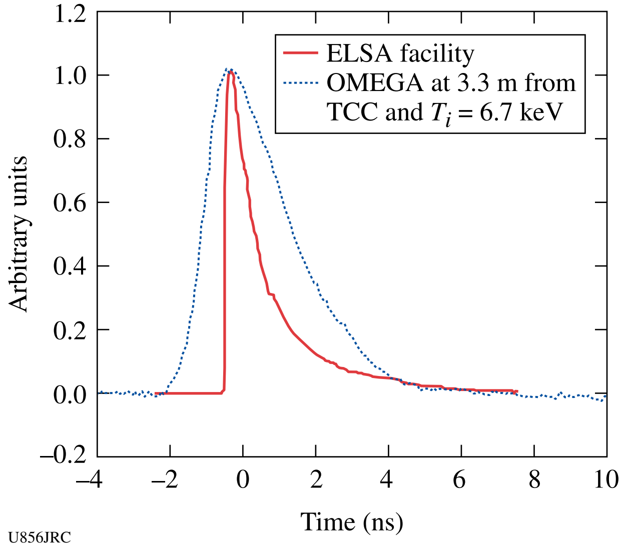

Figure 116.104
Comparison of a monocrystalline pulse shape measured on ELSA (solid curve) and OMEGA (dotted curve).

comparison in Table 116.VI. As predicted, monocrystalline CVD diamonds made by CEA-LIST (A260107B) are sensitive enough for neutron-yield measurements and fast enough for ion-temperature measurements.

Low-sensitivity diamonds are also required for neutron high-yield measurements. A polycrystalline diamond (A190106 from CEA-LIST) grown using a high level of nitrogen impurity was tested on OMEGA; it exhibited a very low sensitivity but also a very long pulse tail. A "black diamond" detector (from Applied Diamond) exhibiting high levels of "non-carbon impurities" was provided by V. Yu. Glebov of LLE. These two diamond samples were evaluated at the ELSA facility using 16-MeV electrons to compare their relative sensitivities and timing parameters (Fig. 116.105). Comparison with other diamonds tested on ELSA and OMEGA shows that those black diamonds are probably good "low-sensitivity" detectors for high neutron-yield measurements on MJ-class lasers.

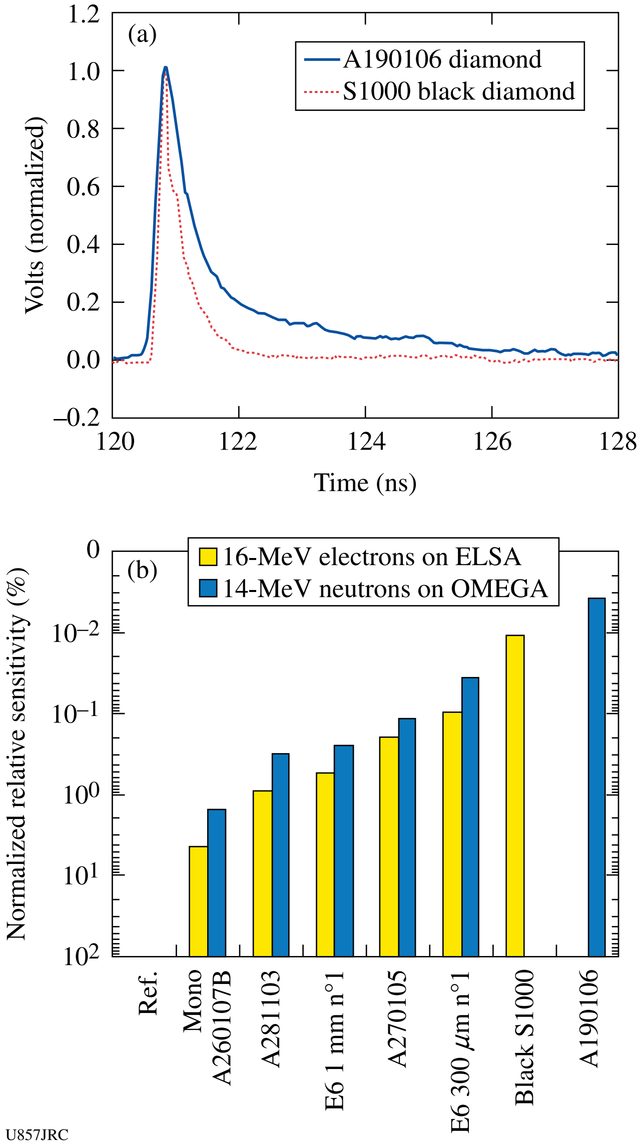

Figure 116.105
Comparison of pulse shape and electron–neutron relative sensitivity. Relative sensitivities are normalized to earlier measurements on one of the most-sensitive diamonds.

Table 116.VI: Ion-temperature measurement with monocrystalline CVD diamond at 3.3 m from TCC.

OMEGA Measurement			CVD Diamond Measurement		
Shot	Ti LLE (±0.5 KeV)	Δt	CVD reference	Ti measured	Δt measured
51301	6.4 keV	992 ps	A260107B	6.7 keV	1016 ps
51305	5.3 keV	903 ps	A260107B	5.2 keV	893 ps
51314	3.6 keV	744 ps	A260107B	3.7keV	729 ps
51315	3.7 keV	754 ps	A260107B	3.6 keV	740 ps
51322	5.5 keV	919 ps	A260107B	5.6 keV	926 ps
51325	5.1 keV	885 ps	A260107B	5.1 keV	882 ps

The 2008 campaigns have therefore enabled us to identify families of materials that appear suitable according to measurement objectives. This development of faster high- and low-sensitivity CVD diamond detectors is still being investigated with CEA-LIST and LLE. A new challenge will now be to demonstrate that a large, sensitive CVD diamond is capable of measuring the downscattered neutron yield for ρR determination.

Neutron Imaging on OMEGA: For several years, CEA has obtained neutron-imaging measurements on OMEGA with an overall resolution of 20 μm (Refs. 29 and 34). The imaging system is based on a small aperture (a 2-mm-diam hole made in a 10-cm-thick tungsten cylinder) placed 260 mm from TCC.[35] The detector (80-mm diameter) is then set 8 m from the target. In this setup, aligning the aperture is very difficult due to the fact that any small misalignment entails a large displacement of the target image on the detector plane at 8 m. As shown with the penumbral aperture last year, there is also the influence of the source position inside the field of view, which is 200 μm for a source size of approximately 50-μm FWHM.[35,36]

In FY07 we presented the effects of misalignment on both calculated and experimental unfolded images obtained with a penumbral aperture. Distortions entailed on the image shape revealed that aperture-positioning tolerance is about 50 μm within the field of view to prevent any effects from misalignment on unfolded images. Briefly, our alignment technique uses a telescope and a beam splitter to view the target through the aperture and the detector, thus fixing the detector–target axis. Next, the aperture is aligned using picomotors on this axis. This technique is very accurate but quite long and fastidious. To meet OMEGA repetition rate and shot plan requirements, a new technique for coarse alignment was tested this year to earn time for setting up before shots. For fine alignment, the old technique is then performed. The new technique relies on a laser beam being injected inside the TIM by a single-mode optical fiber. The laser is sent in two collinear directions via a semitransparent plate, one through the aperture and one to the detector. The first allows us to be sure that we are well centered both on the target and the aperture, the second on the detector. Such a system permits us to be ready for a shot in about 1 h, compared to approximately 2.5 h in the past. We have thus obtained a usable image well centered on the detector on the first shot (51295, see Fig. 116.106).

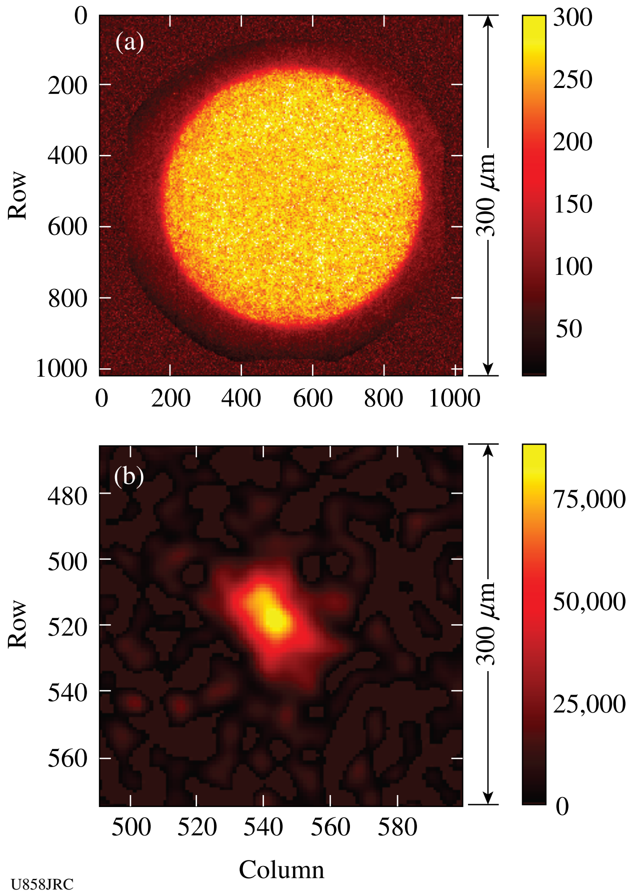

Figure 116.106
Image of DT implosion (shot 51295) yielding 4.0 × 10^{12} neutrons. (a) Raw image and (b) unfolded image using autocorrelation method[37] (SNR = 17).

For high SNR images, we use an annular aperture (see Fig. 116.107) to form neutron images.[34] This aperture is made with a biconical plug inserted in the penumbral aperture, but, in this case, there is no opportunity to send the laser through the aperture. Alignment precision then relies on the capability of reproducing two identical penumbral apertures that can be replaced with minimal misalignment. Aperture positioning tolerance and repeatability between these two apertures were quantified in our laboratory and verified during several campaigns on OMEGA. As for the penumbral aperture, this year (FY08) we studied image distortion as varying annular aperture alignment on OMEGA experiments. These results were compared to Monte Carlo calculations (Geant4)[38] and showed relatively good agreement with experimental results (see Fig. 116.108).

The oblate shape of Fig. 116.106(b) reveals that the aperture is not perfectly aligned; this image was ~200 μm off center. This misalignment was due to the TIM insertion/reinsertion cycle before the shot for adding tritium protection. Alignment control is impossible after tritium coverage addition. It was found that feedback springs on picomotors were not strong

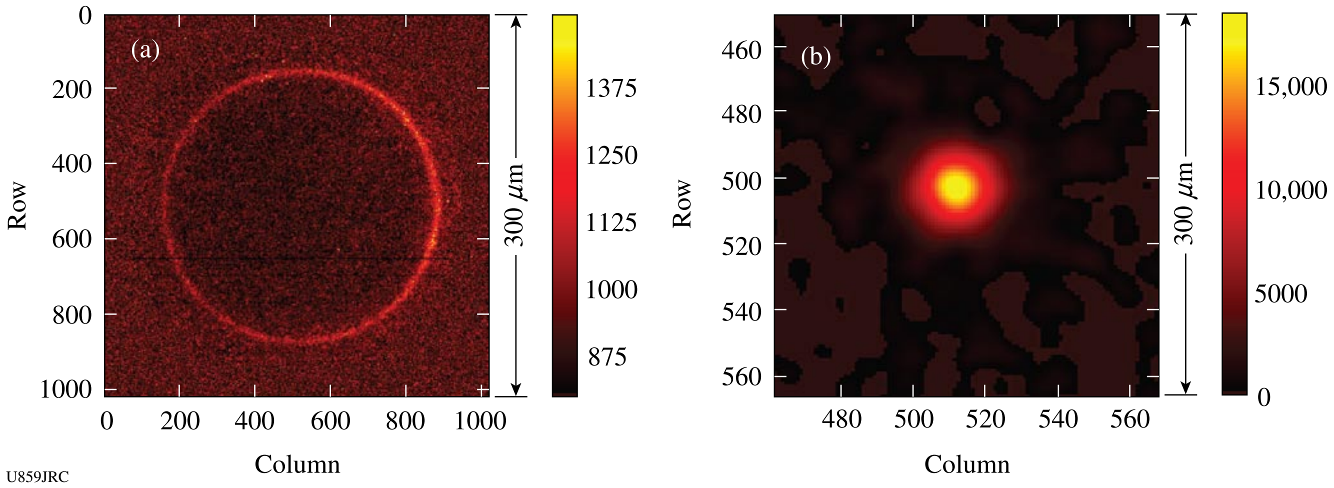

Figure 116.107
(a) Raw image of DT implosion (shot 51324) yielding 2.8 × 10^{13} neutrons. (b) Unfolded image using autocorrelation method[37] (SNR = 41).

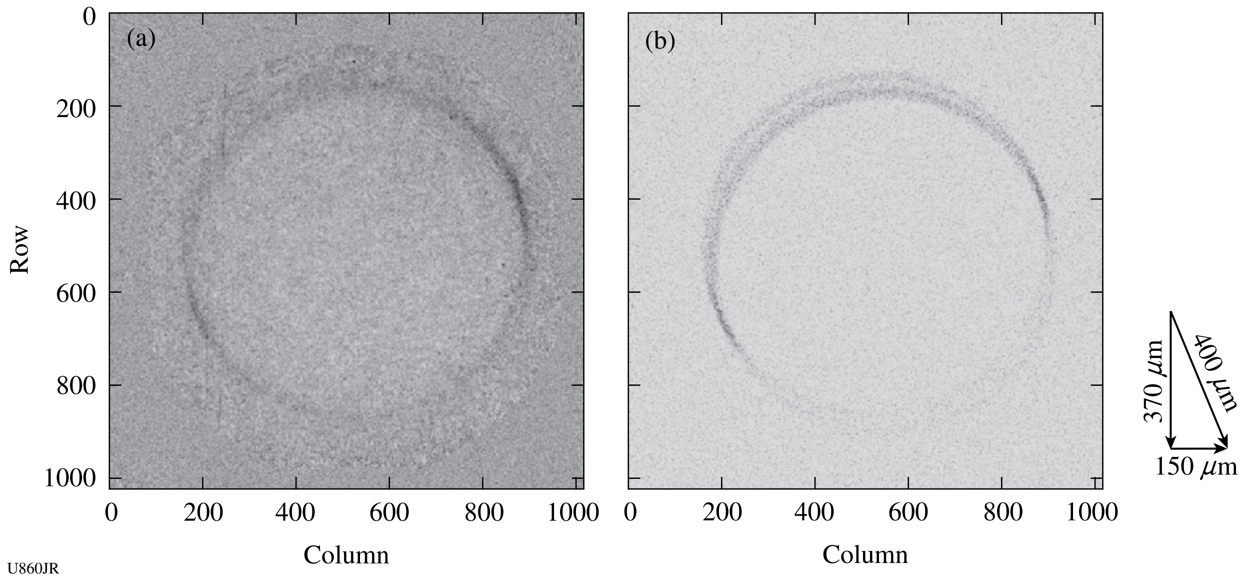

Figure 116.108
(a) Image of DT implosion (shot 51304) yielding 3.2 × 10^{13} neutrons. (b) Calculated image using Geant4 with 50-μm-diam neutron source off center by 400 μm (150 μm right and 370 μm down).

enough to recover the right position during insertion vibrations. Alignment technique was not responsible for this error.

The capability of being well aligned on a first shot is a crucial point for megajoule-class lasers with a 40-m line of sight. Misalignment contributors are now well known and can be reduced under acceptable values less than 50 μm. We are currently qualifying a 150-mm-diam camera for high-resolution measurements (down to 10 μm) that next year will be placed at 13 m from target.

FY08 AWE OMEGA Experimental Programs

Thirty-two target shots were taken for AWE-led experiments on OMEGA in FY08. Hohlraum symmetry was one of the principal topics of investigation.

Coupling laser energy into a hohlraum is a long-established method for generating a symmetric x-ray drive for high-convergence implosions. A number of studies of hohlraum symmetry have been undertaken to optimize the conditions for inertial confinement fusion;[39,40] therefore our codes are relatively well validated in this regime. In certain situations, it is necessary to perturb the symmetry of the driver, for example, where beams are required for diagnostic purposes. To validate our simulations in such conditions, AWE has commenced a campaign to study the energetics of asymmetric hohlraums.

A laser-heated hohlraum was used (Fig. 116.109) and driven either from both ends ("symmetric drive") or from only one end ("asymmetric drive"). The OMEGA Dante diagnostic is used to measure temporal evolution of the radiation temperature. A capsule located at the center of the hohlraum is used as a diagnostic of the flux uniformity radiographed with a titanium area backlighter. Two classes of capsules with a nominal diameter of 600 μm were fielded on the first shot day (September 2008). A silicon aerogel sphere ($\rho \sim$ 325 mg/cc) makes it possible to characterize the time-dependent drive as a function of angle via the steep x-ray transmission gradient just outside the converging ablation front. A plastic-coated, thin-shelled glass capsule provides a complementary measure of the angular variation in absorbed flux. The outer plastic layer serves to mitigate the backlighter attenuation from the ablated material, while the glass shell provides an opaque tracer layer for the radiography. For some targets a thin gold layer was applied over the diagnostic holes to maximize the albedo and reduce any azimuthal variation in the dynamics.

Figure 116.110 illustrates the late-time implosion dynamics of a thin-shell glass capsule driven from one side and synthetic radiographs produced from AWE's *NYM* radiation hydrocode. The experimental data indicate that the ablation is preferentially directed toward the laser spots, with a slightly reduced drive on axis adjacent to the laser entrance hole. This results in an inwardly propagating shock that converges on axis, driving a collimated jet ahead of the main shock front. The preliminary calculations of these targets qualitatively reproduce the macroscopic evolution of the implosion but overestimate the velocity of the shell. The radiographic images of the aerogel spheres show a clear departure from sphericity (Fig. 116.111). Contours of the backlighter transmission, coupled with the original location of the sphere, make a Legendre polynomial fit to the data possible. This indicates a significant P_1 mode resulting from the imposed drive imbalance within the hohlraum.

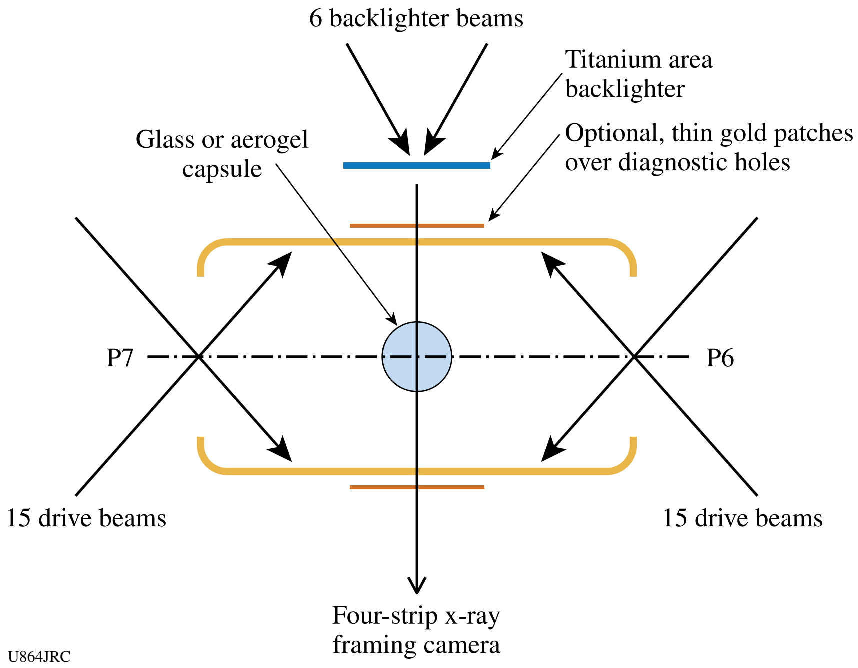

Figure 116.109
Schematic of the experiment to investigate the performance of an asymmetrically driven hohlraum. The 600-μm-diam spherical capsule is placed at the center of a 1.6-mm-diam hohlraum target that is heated through both laser entrance holes (symmetric-drive case) or through just one laser entrance hole (asymmetric-drive case). Radiographic measurements of the implosion are made using a titanium area backlighter and a four-strip x-ray framing camera.

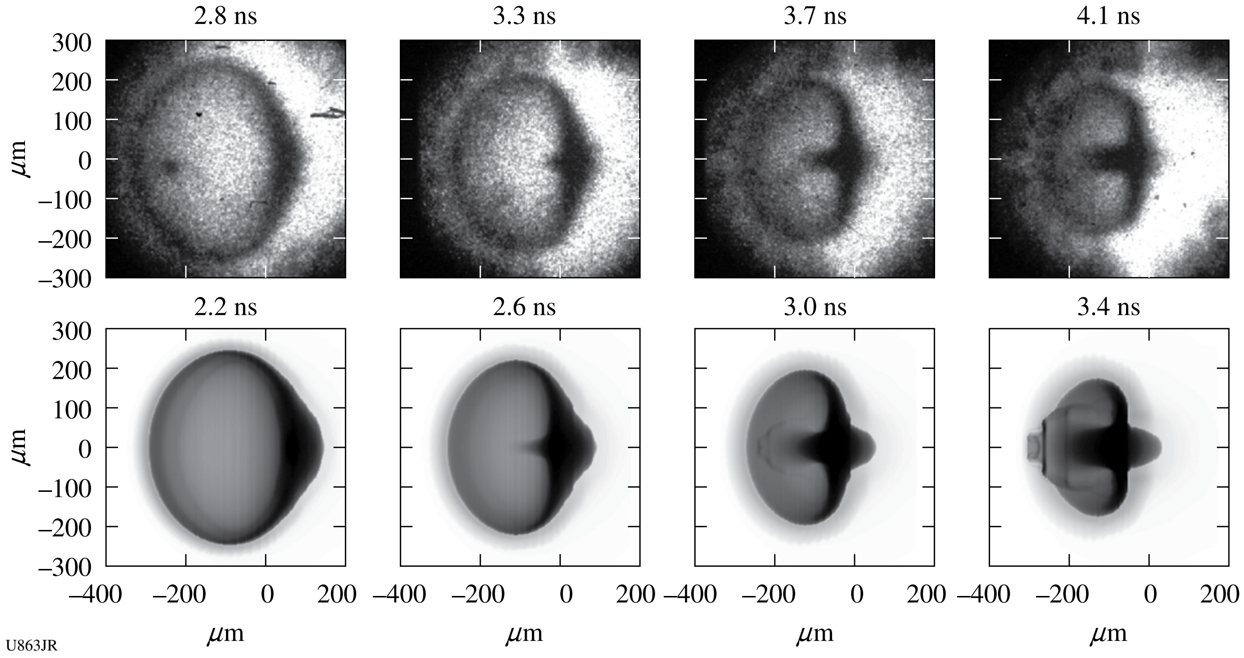

Figure 116.110
Radiographs of the capsule implosion (top) compared with synthetic radiographs (bottom) obtained by post-processing simulations using the AWE 2-D radiation hydrodynamics code *NYM*.

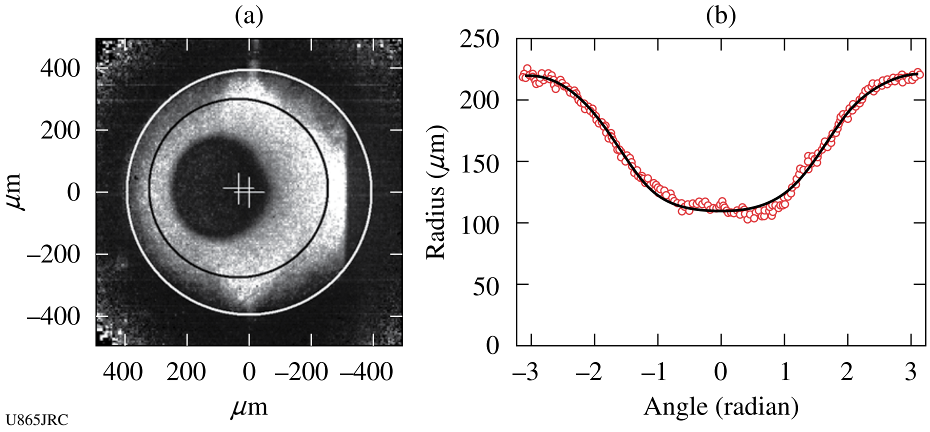

Figure 116.111
(a) Radiograph of an asymmetrically driven silica-aerogel sphere at 2.5 ns after onset of the radiation drive. The superimposed circles represent the initial positions of the aerogel sphere and diagnostic hole (the sphere and hole centers are shown by the crosses), and (b) Legendre-polynomial fit to the contour of transmitted backlighter intensity = 0.4. The inferred values of the first four Legendre coefficients are 156 μm (P_0), 62 μm (P_1), 4.3 μm (P_2), and 7.3 μm (P_3).

REFERENCES

1. C. K. Li, F. H. Séguin, J. A. Frenje, J. R. Rygg, R. D. Petrasso, R. P. J. Town, P. A. Amendt, S. P. Hatchett, O. L. Landen, A. J. Mackinnon, P. K. Patel, V. A. Smalyuk, T. C. Sangster, and J. P. Knauer, Phys. Rev. Lett. **97**, 135003 (2006).
2. C. K. Li, F. H. Séguin, J. A. Frenje, J. R. Rygg, R. D. Petrasso, R. P. J. Town, P. A. Amendt, S. P. Hatchett, O. L. Landen, A. J. Mackinnon, P. K. Patel, M. Tabak, J. P. Knauer, T. C. Sangster, and V. A. Smalyuk, Phys. Rev. Lett. **99**, 015001 (2007).
3. C. K. Li, F. H. Séguin, J. A. Frenje, J. R. Rygg, R. D. Petrasso, R. P. J. Town, O. L. Landen, J. P. Knauer, and V. A. Smalyuk, Phys. Rev. Lett. **99**, 055001 (2007).
4. C. K. Li, F. H. Séguin, J. R. Rygg, J. A. Frenje, M. Manuel, R. D. Petrasso, R. Betti, J. Delettrez, J. P. Knauer, F. Marshall, D. D. Meyerhofer, D. Shvarts, V. A. Smalyuk, C. Stoeckl, O. L. Landen, R. P. J. Town, C. A. Back, and J. D. Kilkenny, Phys. Rev. Lett. **100**, 225001 (2008).
5. J. R. Rygg, F. H. Séguin, C. K. Li, J. A. Frenje, M. J.-E. Manuel, R. D. Petrasso, R. Betti, J. A. Delettrez, O. V. Gotchev, J. P. Knauer, D. D. Meyerhofer, F. J. Marshall, C. Stoeckl, and W. Theobald, Science **319**, 1223 (2008).
6. C. K. Li, F. H. Séguin, J. A. Frenje, J. R. Rygg, R. D. Petrasso, R. P. J. Town, P. A. Amendt, S. P. Hatchett, O. L. Landen, A. J. Mackinnon, P. K. Patel, V. Smalyuk, J. P. Knauer, T. C. Sangster, and C. Stoeckl, Rev. Sci. Instrum. **77**, 10E725 (2006).
7. C. K. Li, F. H. Séguin, J. A. Frenje, M. Manuel, R. D. Petrasso, V. A. Smalyuk, R. Betti, J. Delettrez, J. P. Knauer, F. Marshall, D. D. Meyerhofer, D. Shvarts, C. Stoeckl, W. Theobald, J. R. Rygg, O. L. Landen, R. P. J. Town, P. A. Amendt, C. A. Back, and J. D. Kilkenny, Plasma Phys. Control. Fusion **51**, 014003 (2009).
8. R. Petrasso, Bull. Am. Phys. Soc. **52**, 97 (2007).
9. C. K. Li, Bull. Am. Phys. Soc. **53**, 20 (2008).
10. C. K. Li, F. H. Séguin, J. A. Frenje, J. R. Rygg, R. D. Petrasso, R. P. J. Town, P. A. Amendt, S. P. Hatchett, O. L. Landen, A. J. Mackinnon, P. K. Patel, V. Smalyuk, J. P. Knauer, T. C. Sangster, and C. Stoeckl, Rev. Sci. Instrum. **77**, 10E725 (2006).
11. S. H. Glenzer *et al*., Phys. Rev. Lett. **90**, 175002 (2003).
12. J. J. MacFarlane, I. E. Golovkin, and P. R. Woodruff, J. Quant. Spectrosc. Radiat. Transf. **99**, 381 (2006).
13. H. J. Lee *et al*., "X-Ray Thomson Scattering Measurements of Density and Temperature in Shock-Compressed Beryllium," to be published in Physical Review Letters.
14. D. H. Froula *et al*., Phys. Rev. Lett. **101**, 115002 (2008); D. H. Froula *et al*., Phys. Rev. Lett. **100**, 015002 (2008).
15. P. Neumayer *et al*., Phys. Rev. Lett. **100**, 105001 (2008); P. Neumayer *et al*., Phys. Plasmas **15**, 056307 (2008).
16. E. L. Dewald *et al*., Rev. Sci. Instrum. **79**, 10E903 (2008).
17. R. K. Kirkwood *et al*., Phys. Plasmas **16**, 012702 (2009).
18. H.-S. Park *et al*., "Experimental Tests of Vanadium Strength Models at High Pressures and High Strain Rates," International Journal of Plasticity (in preparation).
19. B. A. Remington *et al*., "A Path to Materials Science at Extreme Pressures," International Journal of Plasticity (in preparation).
20. S. Prisbrey *et al*., "3-D Hohlraum Simulations for an Indirect-Drive Strength Platform," International Journal of Plasticity (in preparation).
21. S. Pollaine *et al*., "Thin Walled Hohlraum Designs for High Pressure, Stagnation Free Loading," International Journal of Plasticity (in preparation).
22. A. B. Reighard *et al*., Rev. Sci. Instrum. **79**, 10E915 (2008).
23. K. B. Fournier *et al*., Absolute X-Ray Yields from Laser-Irradiated Ge-Doped Low-Density Aerogels," Physics of Plasmas (in preparation).
24. J. F. Hansen *et al*., Rev. Sci. Instrum. **79**, 013504 (2008).
25. P. E. Young *et al*., Phys. Rev. Lett. **101**, 035001 (2008).
26. J. R. Rygg, J. A. Frenje, C. K. Li, F. H. Séguin, R. D. Petrasso, J. A. Delettrez, V. Yu. Glebov, V. N. Goncharov, D. D. Meyerhofer, S. P. Regan, T. C. Sangster, and C. Stoeckl, Phys. Plasmas **13**, 052702 (2006).
27. D. C. Wilson, G. A. Kyrala, J. F. Benage Jr., F. J. Wysocki, M. A. Gunderson, W. J. Garbett, V. Yu. Glebov, J. Frenje, B. Yaakobi, H. W. Herrman, J. H. Cooley, L. Welser-Sherrill, C. J. Horsfield, and S. A. Roberts, J. Phys., Conf. Ser. **112**, 022015 (2008).
28. J. L. Bourgade *et al*., Rev. Sci. Instrum. **72**, 1173 (2001).
29. L. Disdier, A. Rouyer, A. Fedotoff, J.-L. Bourgade, F. J. Marshall, V. Yu. Glebov, and C. Stoeckl, Rev. Sci. Instrum. **74**, 1832 (2003).
30. J. L. Bourgade, P. Troussel, A. Casner, G. Huser, T. C. Sangster, G. Pien, F. J. Marshall, J. Fariaud, C. Redmond, D. Gontier, C. Chollet, C. Zuber, C. Reverdin, A. Richard, P. A. Jaanimagi, R. L. Keck, R. E. Bahr, W. J. Armstrong, J. Dewandel, R. Maroni, F. Aubard, B. Angelier, C. Y. Cote, and S. Magnan, Rev. Sci. Instrum. **79**, 10E904 (2008).
31. J. L. Bourgade, V. Allouche, J. Baggio, C. Bayer, F. Bonneau, C. Chollet, S. Darbon, L. Disdier, D. Gontier, M. Houry, H. P. Jacquet, J.-P. Jadaud, J. L. Leray, I. Masclet-Gobin, J. P. Negre, J. Raimbourg, B. Villette, I. Bertron, J. M. Chevalier, J. M. Favier, J. Gazave, J. C. Gomme, F. Malaise, J. P. Seaux, V. Yu. Glebov, P. Jaanimagi, C. Stoeckl, T. C. Sangster, G. Pien, R. A. Lerche, and E. Hodgson, Rev. Sci. Instrum. **75**, 4204 (2004).
32. *LLE Review Quarterly Report* **112**, 203, Laboratory for Laser Energetics, University of Rochester, Rochester, NY, LLE Document No. DOE/SF/19460-790 (2007).
33. R. A. Lerche, D. W. Phillion, and G. L. Tietbohl, Rev. Sci. Instrum. **66**, 933 (1995).

34. L. Disdier, A. Rouyer, I. Lantuéjoul, O. Landoas, J. L. Bourgade, T. C. Sangster, V. Yu. Glebov, and R. A. Lerche, Phys. Plasmas **13**, 056317 (2006).

35. *LLE Review Quarterly Report* **112**, 270, Laboratory for Laser Energetics, University of Rochester, Rochester, NY, LLE Document No. DOE/SF/19460-790 (2007).

36. M. C. Ghilea, T. C. Sangster, D. D. Meyerhofer, R. A. Lerche, and L. Disdier, Rev. Sci. Instrum. **79**, 023501 (2008).)

37. A. Rouyer, Rev. Sci. Instrum. **74**, 1234 (2003).

38. S. Agostinelli, *et al*., Nucl. Instrum. Methods Phys. Res. A **506**, 250 (2003); http://geant4.web.cern.ch/geant4.

39. S. G. Glendinning, P. Amendt, B. D. Kline, R. B. Ehrlich, B. A. Hammel, D. H. Kalantar, O. L. Landen, R. E. Turner, R. J. Wallace, T. J. Weiland, N. Dague, J.-P. Jadaud, D. K. Bradley, G. Pien, and S. Morse, Rev. Sci. Instrum. **70**, 536 (1999).

40. S. M. Pollaine *et al*., Phys. Plasmas **8**, 2357 (2001).

Publications and Conference Presentations

Publications

B. Ashe, K. L. Marshall, D. Mastrosimone, and C. McAtee, "Minimizing Contamination to Multilayer Dielectric Diffraction Gratings Within a Large Vacuum System," in *Optical System Contamination: Effects, Measurements, and Control 2008*, edited by S. A. Straka (SPIE, Bellingham, WA, 2008), Vol. 7069, Paper 706902.

S.-W. Bahk, J. Bromage, I. A. Begishev, C. Mileham, C. Stoeckl, M. Storm, and J. D. Zuegel, "On-Shot Focal-Spot Characterization Technique Using Phase Retrieval," Appl. Opt. **47**, 4589 (2008).

A. M. Cok, R. S. Craxton, and P. W. McKenty, "Polar-Drive Designs for Optimizing Neutron Yields on the National Ignition Facility," Phys. Plasmas **15**, 082705 (2008).

C. Dorrer, J. Bromage, and J. D. Zuegel, "High-Dynamic-Range Single-Shot Cross-Correlator Based on an Optical Pulse Replicator," Opt. Express **16**, 13,534 (2008).

T. Duffy, W. T. Shmayda, R. Janezic, S. J. Loucks, and J. Reid, "LLE's High-Pressure DT-Fill-Process Control System," Fusion Sci. Technol. **54**, 379 (2008).

D. H. Edgell, W. Seka, R. E. Bahr, T. R. Boehly, and M. J. Bonino, "Effectiveness of Silicon as a Laser Shinethrough Barrier for 351-nm Light," Phys. Plasmas **15**, 092704 (2008).

M. J. Guardalben, "Littrow Angle Method to Remove Alignment Errors in Grating Pulse Compressors," Appl. Opt. **47**, 4959 (2008).

S. X. Hu, V. A. Smalyuk, V. N. Goncharov, S. Skupsky, T. C. Sangster, D. D. Meyerhofer, and D. Shvarts, "Validation of Thermal-Transport Modeling with Direct-Drive, Planar-Foil Acceleration Experiments on OMEGA," Phys. Rev. Lett. **101**, 055002 (2008).

H. Irie, Q. Diduck, M. Margala, R. Sobolewski, and M. J. Feldman, "Nonlinear Characteristics of T-Branch Junctions: Transition from Ballistic to Diffusive Regime," Appl. Phys. Lett. **93**, 053502 (2008).

C. Kim, K. L. Marshall, J. U. Wallace, J. J. Ou, and S. H. Chen, "Novel Cholesteric Glassy Liquid Crystals Comprising Benzene Functionalized with Hybrid Chiral-Nematic Mesogens," Chem. Mater. **20**, 5859 (2008).

W. Manheimer, D. Colombant, and V. Goncharov, "The Development of a Krook Model for Nonlocal Transport in Laser Produced Plasmas. I. Basic Theory," Phys. Plasmas **15**, 083103 (2008).

K. L. Marshall, J. Gan, G. Mitchell, S. Papernov, A. L. Rigatti, A. W. Schmid, and S. D. Jacobs, "Laser-Damage-Resistant Photoalignment Layers for High-Peak-Power Liquid Crystal Device Applications," in *Liquid Crystals XII*, edited by I. C. Khoo (SPIE, Bellingham, WA, 2008), Vol. 7050, Paper 70500L.

P. M. Nilson, L. Willingale, M. C. Kaluza, C. Kamperidis, S. Minardi, M. S. Wei, P. Fernandes, M. Notley, S. Bandyopadhyay, M. Sherlock, R. J. Kingham, M. Tatarakis, Z. Najmudin, W. Rozmus, R. G. Evans, M. G. Haines, A. E. Dangor, and K. Krushelnick, "Bidirectional Jet Formation During Driven Magnetic Reconnection in Two-Beam Laser–Plasma Interactions," Phys. Plasmas **15**, 092701 (2008).

S. Papernov and A. W. Schmid, "Testing Asymmetry in Plasma-Ball Growth Seeded by a Nanoscale Absorbing Defect Embedded in a SiO_2 Thin-Film Matrix Subjected to UV Pulsed-Laser Radiation," J. Appl. Phys. **104**, 063101 (2008).

J. Qiao, A. Kalb, T. Nguyen, J. Bunkenburg, D. Canning, and J. H. Kelly, "Demonstration of Large-Aperture Tiled-Grating Compressors for High-Energy, Petawatt-Class, Chirped-Pulse Amplification Systems," Opt. Lett. **33**, 1684 (2008).

M. J. Quinlan, W. T. Shmayda, S. Lim, S. Salnikov, Z. Chambers, E. Pollock, and W. U. Schröder, "Effects of H_2O and H_2O_2 on Thermal Desorption of Tritium from Stainless Steel," Fusion Sci. Technol. **54**, 519 (2008).

A. Simon, "Response to 'Comment on "An Alternative Analysis of Some Recent Diffusion Experiments on the Large Plasma Device" ' [Phys. Plasmas **15**, 074701 (2008)]," Phys. Plasmas **15**, 074702 (2008).

V. A. Smalyuk, S. X. Hu, V. N. Goncharov, D. D. Meyerhofer, T. C. Sangster, D. Shvarts, C. Stoeckl, B. Yaakobi, J. A. Frenje, and R. D. Petrasso, "Rayleigh–Taylor Growth Stabilization in Direct-Drive Plastic Targets at Laser Intensities of $\sim 1 \times 10^{15}$ W/cm^2," Phys. Rev. Lett. **101**, 025002 (2008).

V. A. Smalyuk, S. X. Hu, V. N. Goncharov, D. D. Meyerhofer, T. C. Sangster, C. Stoeckl, and B. Yaakobi, "Systematic Study of Rayleigh–Taylor Growth in Directly Driven Plastic Targets in a Laser-Intensity Range of $\sim 2 \times 10^{14}$ to $\sim 1.5 \times 10^{15}$ W/cm^2," Phys. Plasmas **15**, 082703 (2008).

M. S. Wei, A. A. Solodov, J. Pasley, R. B. Stephens, D. R. Welch, and F. N. Beg, "Study of Relativistic Electron Beam Production and Transport in High-Intensity Laser Interaction with a Wire Target by Integrated LSP Modeling," Phys. Plasmas **15**, 083101 (2008).

Forthcoming Publications

Z. A. Ali, V. Yu. Glebov, M. Cruz, T. Duffy, C. Stoeckl, S. Roberts, T. C. Sangster, R. Tommasini, A. Throop, M. Moran, L. Dauffy, and C. Horsefield, "Tests and Calibration of NIF Neutron Time of Flight Detectors," to be published in Review of Scientific Instruments.

S.-W. Bahk, J. D. Zuegel, J. R. Fienup, C. C. Widmayer, and J. Heebner, "Spot-Shadowing Optimization to Mitigate Damage Growth in a High-Energy Laser Amplifier Chain," to be published in Applied Optics.

Z.-M. Bei, T. B. Jones, A. Tucker-Schwartz, and D. R. Harding, "Electric Field Mediated Droplet Centering," to be published in Applied Physics Letters.

J. L. Bourgade, P. Troussel, A. Casner, G. Huser, T. C. Sangster, G. Pien, F. J. Marshall, J. Fariaud, C. Redmond, D. Gontier, C. Chollet, C. Zuber, C. Reverdin, A. Richard, P. A. Jaanimagi, R. L. Keck, R. E. Bahr, W. J. Armstrong, J. Dewandel, R. Maroni, F. Aubard, B. Angelier, C. Y. Cote, and S. Magnan, "A Versatile High-Resolution X-Ray Imager (HRXI) for Laser-Plasma Experiments on OMEGA," to be published in Review of Scientific Instruments.

J. Bromage, S.-W. Bahk, D. Irwin, J. Kwiatkowski, A. Pruyne, M. Millecchia, M. Moore, and J. D. Zuegel, "A Focal Spot Diagnostic for On-Shot Characterization of High-Energy Petawatt Lasers," to be published in Optics Express.

V. Yu. Glebov, M. Moran, C. Stoeckl, T. C. Sangster, and M. Cruz, "Neutron Bang Time Detector Based on a Light Pipe," to be published in Review of Scientific Instruments.

V. N. Goncharov, "Ablative Richtmyer–Meshkov Instability: Theory and Experimental Results," to be published in the Proceedings of the Scottish Summer School.

V. N. Goncharov, "Direct-Drive Inertial Fusion: Basic Concepts and Ignition Target Designing," to be published in the Proceedings of the Scottish Summer School.

Z. Jiang and J. R. Marciante, "Comments on 'Beam Quality Factor of Higher Order Modes in a Step-Index Fiber,' " to be published in the Journal of Lightwave Technology.

J. R. Marciante, "Gain Filtering for Single-Spatial-Mode Operation of Large-Mode-Area Fiber Amplifiers," to be published in the IEEE Journal of Selected Topics in Quantum Electronics.

D. Pan, G. P. Pepe, V. Pagliarulo, C. DeLisio, L. Parlato, I. Khafizov, and R. Sobolewski, "Layered Ferromagnet/Superconductor Heterostructures: Nonequilibrium Quasiparticle Dynamics and Photodetector Applications," to be published in Physical Review B.

S. N. Shafrir, S. D. Jacobs, S. Adar, C. Miao, H. Romanofsky, and J. C. Lambropoulos, "Drag Force and Surface Texture in Material Removal with MRF on Optical Glass and Hard Ceramics," to be published in the Proceedings of the 12th Electromagnetic Windows Symposium.

A. A. Solodov, K. S. Anderson, R. Betti, V. Gotcheva, J. F. Myatt, J. A. Delettrez, S. Skupsky, W. Theobald, and C. Stoeckl, "Simulations of Electron Transport and Ignition for Direct-Drive Fast-Ignition Targets," to be published in Physics of Plasmas.

M. Storm, I. A. Begishev, R. J. Brown, C. Guo, D. D. Meyerhofer, C. Mileham, J. F. Myatt, P. M. Nilson, T. C. Sangster, C. Stoeckl, W. Theobald, and J. D. Zuegel, "A High-Resolution Coherent Transition-Radiation Diagnostic for Laser-Produced Electron Transport Studies," to be published in Review of Scientific Instruments.

A. Trajkovska-Petkoska and S. D. Jacobs, "Effect of Different Dopants on Polymer Cholesteric Liquid Crystals," to be published in Molecular Crystals and Liquid Crystals.

C. D. Zhou and R. Betti, "A Measurable Lawson Criterion and Hydro-Equivalent Curves for Inertial Confinement Fusion," to be published in Physics of Plasmas.

Y. Zhu, J. D. Zuegel, J. R. Marciante, and H. Wu, "Distributed Waveform Generator: A New Circuit Technique for Ultra-Wideband Pulse Generation, Shaping, and Modulation," to be published in the IEEE Journal of Solid-State Circuits.

Conference Presentations

T. Pfuntner and S. D. Jacobs, "The Optics Suitcase and Liquid Crystal Mood Patches," Boulder Workshop on Light-Controlled Liquid Crystalline Complex Adaptive Materials, Boulder, CO, 6 August 2008.

The following presentations were made at SPIE Optics and Photonics, San Diego, CA, 10–14 August 2008:

B. Ashe, G. Myhre, D. Mastrosimone, and C. McAtee, "Minimizing Contamination to Multilayer Dielectric Diffraction Gratings Within a Large Vacuum System."

K. L. Marshall, J. Gan, G. Mitchell, S. Papernov, A. L. Rigatti, A. W. Schmid, and S. D. Jacobs, "Laser-Damage Resistant Photoalignment Layers for High-Peak-Power Liquid Crystal Device Applications."

The following presentations were made at the HEDLP FESAC Workshop, Washington, DC, 25–27 August 2008:

W. Theobald, R. Betti, C. Stoeckl, K. S. Anderson, T. R. Boehly, J. A. Delettrez, J. A. Frenje, V. N. Goncharov, V. Yu. Glebov, C. K. Li, R. L. McCrory, D. D. Meyerhofer, L. J. Perkins, R. D. Petrasso, P. B. Radha, T. C. Sangster, W. Seka, A. A. Solodov, B. Yaakobi, and C. D. Zhou, "Driving Gigabar Shocks with High-Power Lasers and Their Applications to Shock Ignition."

W. Theobald, C. Stoeckl, R. Betti, K. S. Anderson, T. R. Boehly, J. A. Delettrez, R. R. Freeman, J. A. Frenje, V. N. Goncharov, V. Yu. Glebov, D. R. Harding, M. H. Key, A. J. MacKinnon, R. L. McCrory, D. D. Meyerhofer, J. F. Myatt, P. M. Nilson, A. V. Okishev, P. K. Patel, R. D. Petrasso, C. Ren, T. C. Sangster, W. Seka, R. B. Stephens, A. A. Solodov, L. Van Woerkom, B. Yaakobi, and C. D. Zhou, "Fast Ignition with OMEGA/OMEGA EP."

The following presentations were made at the Boulder Damage Symposium, Boulder, CO, 22–24 September 2008:

J. B. Oliver, S. Papernov, A. W. Schmid, and J. C. Lambropoulos, "Optimization of Laser-Damage Resistance of Evaporated Hafnia at 351 nm."

S. Papernov and A. W. Schmid, "Laser-Induced Surface Damage of Optical Materials: Absorption Sources, Initiation, Growth, and Mitigation."

The following presentations were made at the 18th Topical Meeting on the Technology of Fusion, San Francisco, CA, 28 September–2 October 2008:

R. Betti, P. W. McKenty, W. Theobald, C. D. Zhou, C. Stoeckl, K. S. Anderson, J. A. Delettrez, D. D. Meyerhofer, V. N. Goncharov, P. B. Radha, T. C. Sangster, A. A. Solodov, V. A. Smalyuk, S. Skupsky, C. K. Li, R. D. Petrasso, J. A. Frenje, L. J. Perkins, D. Shvarts, and A. Schmitt, "Shock Ignition of Thermonuclear Fuel with High Areal Density."

S. F. B. Morse, J. Bromage, C. Dorrer, M. J. Guardalben, J. H. Kelly, B. E. Kruschwitz, S. J. Loucks, R. L. McCrory, D. D. Meyerhofer, J. Qiao, and L. J. Waxer, "OMEGA Extended Performance Short-Pulse Laser: Technology and Operational Flexibility."

J. M. Soures, "The OMEGA Facility: Providing Unique Capabilities for Inertial Fusion and High-Energy-Density Physics Experiments."

UNIVERSITY of ROCHESTER